3D PRINTING OF BIOLOGICAL MACHINES FOR BIOLOGY AND MEDICINE

BY
VINCENT CHAN

DISSERTATION
Submitted in partial fulfillment of the requirements
for the degree of Doctor of Philosophy in Bioengineering
in the Graduate College of the
University of Illinois at Urbana-Champaign, 2013

Urbana, Illinois

Doctoral Committee:
Professor Rashid Bashir, Chair
Assistant Professor Hyunjoon Kong, Co-Chair
Professor M. Taher A. Saif
Professor Lawrence B. Schook

ABSTRACT

A cell-based biological machine is a set of sub-components consisting of living cells and cell-instructive micro-environments that interact to perform a prescribed task. Cell types such as neurons, muscle cells, and endothelial cells can be programmed for sensing, information processing, actuation, protein expression, or transport. By combining clusters of these different cell types, complex biological machines can be created for specific applications in health, security, and the environment. The potential benefits and social implications of these systems are enormous. In health, biological machines can enhance tissues and organs by engineering a collection of cells to sense drug levels in the bloodstream, process it, and instruct secretory cells to counteract it. In security, 'noses' can be grown that are comparable or even more sensitive than that of dogs to identify explosives or toxic substances during airport screenings. In the environment, biological robots or organisms can be produced to swim toward an oil spill, degrade it into harmless byproducts, and replicate as needed. Although this may seem like the stuff of science fiction, many scientists and researchers believe that some or all of these ideas could become a reality in the near-future.

The realization of biological machines and their sub-components will require the development of enabling technologies. These technologies will be critical in studying the building blocks of the biological machinery. An intelligent and instructive micro-environment is critical in our efforts to understand and design cellular systems. The cells have to thrive, communicate, and proliferate in such a micro-environment while performing their designated functions. These 'instructive' and 'designer' 2D and 3D micro-environments should form the scaffolding of biological machines, and have spatially controlled mechanical and chemical properties to control their functionalities. Advancements in enabling technologies that can fabricate the desired intelligent scaffold will greatly expedite our progress in developing biological machines. Our central hypothesis is that by integrating 3D printing technology with appropriate biomaterials, we will have the capability to create spatially controlled 2D and 3D micro-environments that have the desired permeability, mechanical stiffness, chemical properties, and number of cell adhesion sites. With this technology, we will be able to build simple biological machines with prescribed tasks. In particular, we propose building two simple biological machines with the following functionalities: (i) a microvascular stamp that can pattern new blood vessels, and (ii) a locomotive bio-robot that can walk in fluid. These modules can potentially interact as sub-components for more complex biological machines. Please refer to the posters for detailed information and accomplishments of these two biological machines.

The idea of building biological machines with living cells is an innovative approach that is being developed as a new scientific discipline by the NSF Science and Technology Center (STC) entitled Emerging Behaviors of Integrated Cellular Systems (EBICS). New technological platforms are essential

to bridge molecular scale interactions with macroscale behavior of complex multi-cellular systems. Our work to introduce 3D printing technology as one of these platforms will not only advance our long-term goal of creating complex biological machines, but also significantly enhance our understanding of emergent biological behaviors under integrated biochemical and physical cues at the cellular, cell network, and cell population levels.

To my family

ACKNOWLEDGMENTS

With my deepest gratitude, I thank the many, many wonderful and inspirational people that I have had the fortune to cross paths with during my graduate studies at Purdue University and the University of Illinois at Urbana-Champaign. No matter how big or small, many of you have had a positive impact in my life. I am truly grateful. Please forgive me if I did not mention you by name.

Thank you, Prof. Rashid Bashir, for your strong leadership, grand visions, and relentless support. It has been a great pleasure to work for you. You have left many indelible marks on me over the years, among them: "*How do we quantify this?*", "*Stop trying to be too perfect!*", and of course, "*How do we take this to a publishable end?*" I am stronger because of it.

Thank you, Prof. Hyunjoon Kong, Prof. Taher Saif, and Prof. Larry Schook, for serving on my dissertation committee. Your contributions extend far beyond that, and I am grateful that each of you has given so much of your time to offer me your expertise, insights, and collaborative efforts that have ultimately led to published papers together.

Thank you, Dr. Jae Hyun Jeong. You have been a great mentor and friend. I still remember our first meeting outside the Union sketching out our plans for patterning blood vessels with the 3D printer – still can't believe it worked! My only regret is that we weren't more successful on the soccer field. Thank you, Mitchell Collens, for your unbelievable work ethic and late night conversations in the lab. It made those tough times so much more bearable. You will always be a good friend – even if we never get to start a company together. Thank you, Li-yen Wong, Matthew Alonso, Caroline Cvetkovic, and Ritu Raman, for working so closely with me. I wish you all the best and I hope our paths will cross again (and I'm sure they will!).

Thank you to so many of my talented and hard-working collaborators, I would not be where I am today without you: Dr. Basanta Bhaduri and Dr. Zhou Wang in the *Popescu Lab*, Dr. (!!) Erich Lidstone in the *Cunningham Lab*, Dr. (!!) Cathy Chu in the *Kong Lab*, Dr. Kidong Park and Dr. Larry Millet in the *Bashir Lab*, Dr. Shiv Mayandi at the *Microscopy Suite in IGB*, Dr. Tor Wolf Jensen, Dr. Laurie Rund, and Molly Melham in the *Schook Lab*, Dr. Emerson de Souza, Wylie Ahmed, and Brian Williams in the *Saif Lab*, Mike Poellmann in the *Wagoner-Johnson Lab*, Mary Rhoads and Dr. Jackie Shepard in the *Griffith Lab*, and Dr. Selman Sakar and Devin Neal in the *Asada Lab*. Thank you, Janet Sinn-Hanlon, for all the pretty covers and graphic images that make our research look so much cooler! Thank you, to my funding sources

at the National Science Foundation and U.S. Army Research Office, for the resources, equipment, and, most importantly, the many people that I have met and networked with through these grants.

Thank you, Ron Watkins, Avi Kopparthi, and Parmesh Venkateswaren at *Illinois Business Consulting (IBC)*, and Dr. Bruce Litchfield and Valeri Werpetinski at *Learning in Community (LINC)* for being incredible teachers and mentors. I've learned so much from all of you and enjoyed my time managing interdisciplinary student teams. It was a truly amazing experience to work on both client-based and community-based projects. Thank you, Feifan Wang, Mack McConnell, Chris Tsoukalas, and Varun Karkhanis, for being great IBC project managers and making my life that much easier. Thank you, Avery Bang and Mike Paddock, for preparing the LINC team and being so instrumental in sending us to Guatemala to build a suspended bridge. Simply incredible!

Thank you, Miri Kim, Nick Watkins, Abdullah Alhazzani, Dong Woo Kim, Nick Snead, and Joe Gangestad, for being my roommates during graduate school. Thank you, Kyra Lee, Isabel Neacato, Abe Qavi, Helen Hwang, Nicole Tsang, Sarah Holton, Max Rich, Brian Dorvel, Eric Salm, Elise Corbin, Cal Rabang, Heyjin Park, Khanh Nguyen, Lester Smith, Mike Pargett, Trisha Eustaquio, Lilly Meng, Aki Uchida, Naomi Diaz, and to all my friends, colleagues, and acquaintances at Purdue University and the University of Illinois at Urbana-Champaign. You guys have seen (and put up with) me at my best and worst times.

Finally, I cannot thank my family enough for their undying love and support, no matter what I do in life. I love you, Mom, for always asking me, "*When are you going to graduate?*" I love you for making a copy of my apartment key without my knowledge, for stocking my fridge with two weeks' worth of food, and for hiding a bag of rice in my car trunk even though I didn't want it. I love you, Dad, for being the best father, coach, teacher, counselor, friend, and man of God. You will always be my role model and someone that I aspire to be like. I love you, Beatrice and Dustin, for being the best sister and brother-in-law that I could ever ask for. You guys have the type of loving relationship that I want for myself someday. Thank you, thank you, *thank you*! I love you all unconditionally.

TABLE OF CONTENTS

LIST OF TABLES AND FIGURES

CHAPTER 1: INTRODUCTION

1.1 MOTIVATION

A cell-based biological machine, dubbed 'cellular system', is a set of sub-components consisting of living cells and cell-instructive micro-environments that interact to perform a prescribed task. Cell types such as neurons, muscle cells, and endothelial cells can be programmed for sensing, information processing, actuation, protein expression, or transport. By combining clusters of these different cell types, complex multi-cellular systems can be created for specific applications in health, security, and the environment. The central hypothesis in this dissertation is that 3D printing technology can be integrated with appropriate biomaterials to create spatially-controlled 2D and 3D micro-environments that have the desired permeability, mechanical stiffness, chemical properties, and number of cell adhesion sites. With this technology, we will be able to build cellular systems with prescribed tasks. In particular, we propose the development of miniaturized, walking bio-bots with biological actuators.

1.2 OVERVIEW

We summarized each chapter of the dissertation below with work achieved to date toward a locomotive bio-bot. Chapters 3, 4, 5, and 6 describe key developmental components in the creation of locomotive bio-bots, and Chapters 7 and 8 describe current work towards external control and scaling-up of these bio-bots.

In Chapter 3 ("*3D stereolithographic printing*"), we developed a 3D printing technology, called stereolithography, for cell-based hydrogel applications. We examined the mechanical properties of the hydrogels that were fabricated, and evaluated the survival of encapsulated cells (fibroblasts) exposed during the fabrication process. Furthermore, we attempted to control both the spatial distribution of cells and bioactive molecules in distinct 3D layers by exploiting the capabilities of our modified 'bottom-up' approach in the printer.

In Chapter 4 ("*Biological actuators*"), we utilized the 3D printer to fabricate 'soft' hydrogel cantilevers with tunable elastic properties. In particular, we cultured a cell sheet of cardiomyocytes on the backsides of the cantilevers to measure their contractile forces at varying stiffnesses. In addition, we evaluated how changes in cantilever stiffness affected the

contractility of the cardiomyocytes. The intent of these studies was to aid in the design of cell-based biohybrid actuators for locomotion.

In Chapter 5 ("*Cell alignment on bioactuators*"), we developed a simple method to align cells on the hydrogel cantilevers fabricated in the previous chapter. Cell organization and alignment has been demonstrated to increase the contractile force of cardiomyocytes. This was accomplished by stamping polydimethylsiloxane (PDMS) line patterns of acryl-fibronectin using micro-contact printing (μCP) and transferring the patterns to the surface of the hydrogels with the 3D printer. We evaluated pattern integrity and efficacy of fibronectin transfer from stamped glass to fabricated hydrogels.

In Chapter 6 ("*Locomotive bio-bots with 2D cell sheets*"), we built on our earlier work of cell-based biohybrid actuators by incorporating it into the design of autonomous bio-bots for locomotion. We showed that the initial shape and degree of curvature of the bio-bot cantilever could be precisely defined by adjusting its thickness during fabrication. The tension generated by self-organizing cardiomyocytes into cell sheets on the cantilever resulted in the final curvature. By harnessing an asymmetric design and synchronous contraction of the cardiac cell sheet, we demonstrated a walking motion of the bio-bot. We then examined how altering the cantilever curvatures changed the surface area of contact, and hence, the friction between the bio-bot 'legs' to affect net forward movement.

In Chapter 7 ("*3D muscle strips for bio-bots*"), we modified our locomotive bio-bots to incorporate clusters of light-activated skeletal muscle cells (C2C12-ChR2 myoblasts). To do this, we fabricated two-legged hydrogel constructs in a pillar/beam configuration with the 3D printer. The C2C12-ChR2 myoblasts were embedded in natural 3D scaffolding and cast around the pillars of the hydrogel constructs to form 3D muscle strips. The strips were optimized by evaluating a number of biological and mechanical parameters. We then assessed the differentiation and contractility of myotubes in these 3D muscle strips.

In Chapter 8 ("*Blood vessel patterning*"), we focused on angiogenesis (new blood vessel formation) either for future therapeutic applications carried out by our bio-bots, or to support the scaling-up of 3D muscle strips, which are limited by oxygen and nutrient diffusion. We created a 'microvascular stamp' with the 3D printer that released multiple angiogenic factors for new blood vessel growth and patterning. The stamp consisted of living cells that secreted angiogenic factors, an engineered hydrogel matrix that promoted cellular expression of angiogenic factors,

and a three-dimensional (3D) geometry that localized the angiogenic factors within the pattern. When the stamp was implanted on a target tissue, it created the desired pattern of new blood vessels based on the 3D geometry of the stamp.

CHAPTER 2: LITERATURE REVIEW ON BIOACTUATORS

> *Nature, in order to carry out the marvelous operations in animals and plants, has been pleased to construct their organized bodies with a very large number of machines, which are of necessity made up of extremely minute parts so shaped and situated, such as to form a marvelous organ, the composition of which are usually invisible to the naked eye, without the aid of the microscope.*
>
> -- Marcello Malpighi

2.1 INTRODUCTION

Nature has long been a source of wonderment and inspiration in producing complex yet elegant functional systems and life forms across a multitude of length scales.[1] Marcello Malpighi, one of the greatest seventeenth-century life scientists, was one of the first to attribute body function to an organized series of minute 'organic', or biological, machines.[2] The length scales of these biological machines span from the tiny machinery in cells that participate in replication (mitotic cell division) and locomotion (actin and myosin systems) to cell cluster interactions and formation of tissues having higher-order functionalities (or so-called 'emergent properties'). In fact, the human body is a large and complex functional system – the ultimate biological machine.[3] Traditionally, the study of these systems has been the domain of biology, while technological advances have been used by biologists as new tools to advance these studies. This has resulted in a one-way relationship between biology and engineering. However, recent advances in cellular and molecular biology, combined with new technologies to measure and manipulate cell behavior, have laid the foundation for the next frontier in biology, that of creating our own engineered biological machines.[4] The potential benefits of a technology that can harness and control nature's unique capabilities (*e.g.* self-organization, self-repair, and self-replication) to either improve on it or utilize it for other purposes are enormous.

Functional units of biological machines include sensing, information processing, actuation, protein expression, and transportation. These units can be combined into assemblages that work together seamlessly to significantly enhance or even transform our ability to accomplish certain tasks. Kamm *et al*. lists a few exemplary applications in the areas of health, security, and the environment that biological machines can have a significant impact.[5] In health, cellular systems can enhance tissues and organs by engineering a collection of cells to sense drug levels in the bloodstream, process it, and instruct secretory cells to counteract it. In security,

'noses' can be grown that are comparable or even more sensitive than that of dogs to identify explosives or toxic substances during airport screenings. In the environment, biological robots or organisms can be produced to swim toward an oil spill, degrade it into harmless byproducts, and replicate as needed. Although this may seem like the stuff of science fiction, many scientists and researchers believe that some or all of these ideas could become a reality in the near future.

Extensive research has been conducted in the past few years in an effort to exploit one of these functional units, the biological actuator (or 'bioactuator'), at a multitude of length scales. While bioactuators do not surpass artificial actuators in any one aspect, there are a number of attractive design features that could be emulated to great advantage.[6] In biomolecules, individual motor proteins can be combined to form multi-molecular assemblies that expand its utility to larger actuators compared to nanodevices. In cells and tissues, such as muscle, force can be graded by controlling the number of fibers that are activated in parallel, a process known as recruitment. This grading of force enables efficiency to be optimized over a wide range of loads and contraction velocities to control acceleration and force.[7] A further advantage of muscle is its ability to convert chemical energy to mechanical work. The 'combustion' of sugars and fats using freely available oxygen provides a fuel energy density that is two orders of magnitude greater than that of batteries.[8] Many of muscle's advantages relative to artificial actuator technologies stem from nature's ability to fabricate and control on length scales ranging from the molecular to the macroscopic. As fabrication technology improves and nature's mechanisms are better understood, a number of muscle's properties, including regeneration, nanostructuring, and direct chemical actuation, will likely become common in artificial actuators.

This review summarizes the recent developments in the emerging field of bioactuators across a multitude of length scales. First, we discuss the use of biomolecules as nano-scale actuators, from their *ex vivo* assembly to their various functional uses, such as for cargo selection and transport. Second, we discuss the use of single and small clusters of cells to power micro-scale devices. We will focus on both microorganisms, including bacteria, protozoa, and algae, and on mammalian cells, such as cardiomyocytes. Finally, we discuss the utilization of natural and synthetic 2D- and 3D-assembled tissues and other complex hierarchies. We are not aware of another review to date that catalogs the assembly, utilization, and external control of bioactuators across a multitude of length scales and in the context of driving new technologies.

2.2 BIOMOLECULAR ACTUATORS

Biomolecular motors are considered promising materials for constructing biological actuators.[9] In general, biomolecular actuators are driven by the conversion of adenosine triphosphate (ATP) to drive their movement. These actuators can be used in nanoscale mechanical devices to pump fluids, open and close valves, and provide translational movement of cargo.[10] The difficulty lies in how to integrate these sophisticated functions to do specific tasks. In the following section, we take a look at the current state of the field, from the *ex vivo* assembly of motor proteins, such as DNA, kinesin/microtubules, actin/myosin, and F_1-ATPases, to the transport and external control of these nanoscale engineered systems for carrying out distinct functions.

2.2.1 DNA AS A MOLECULAR MOTOR

DNA is an attractive nanodevice because of its self-assembly properties. It has been shown previously that branched motifs of DNA can provide components for the assembly of nanoscale objects, links, and arrays.[11,12] However, switchable biomolecular machines can also be assembled with DNA. The basic concept of DNA as a biomolecular actuator is based on the fact that DNA can switch between two stable conformational states. These states can be controlled based on the ionic composition of the medium or the presence of complementary single-stranded molecules. There have been several successful demonstrations that harness this ability for the construction of biomolecular actuators. Here, we describe several different types of motion with DNA machines: (1) rotation, (2) extension and folding, and (3) walking.

To achieve a rotational motion, Seeman and colleagues assembled a switchable molecular machine from synthetic DNA molecules.[13] The construct consisted of two rigid 'arms' of DNA that were rotated between fixed positions. The DNA arms consisted of 'double-crossover' (DX) molecules that linked to the long central DNA strand of 4.5 double-helical turns. The central strand had a base-paired sequence $d(CG)_{10}$, called a 'proto-Z' sequence that switched between the right-handed helical B-conformation and the left-handed Z-state at high ionic strength. When this conformational change occurred, the two DX-stabilized strands rotated around their longitudinal axes and twisted about 200^o relative to each other. This event was able to induce atomic displacements of 20-60 Å.

To achieve a 'scissor-like' extension and folding motion, Neumann and colleagues exploited the ability of DNA hybridization as an energy source to power a pair of 'nano-tweezers' constructed from three DNA molecules.[14] The DNA molecules were constructed with a rigid, double-stranded region and two flexible, single-stranded dangling ends. When single-stranded DNA 'fuel' was added, they hybridized with the dangling ends to pull the tweezers closed. The mechanism of movement was a change in flexural persistence length upon hybridization, which altered the bending stiffness.[15] Complementary strands that compete for hybridization of the DNA fuel were then added to allow the tweezers to open. In similar fashion, Yurke and colleagues constructed a 'nano-actuator' with two strands of DNA that hybridized together to form a loop-like structure.[16] The structure had two rigid double-stranded arms held together by one short and one long single-stranded region. Upon hybridization, the DNA fuel pushed the arms apart into a straightened configuration. The nano-actuator was relaxed by adding complementary strands of the DNA fuel.

To achieve a walking motion, Shin and Pierce developed a very simple DNA walker based on hybridization and branch migration.[17] The walker consisted of a DNA duplex with two single-stranded feet. The track also consisted of a DNA duplex with branched single-stranded extensions as binding sites for the walker. The feet of the walker were attached to the track by linker molecules in the solution. One of the linker molecules was then removed by competitive binding to free the foot for the next binding site. This was repeated several times to move the walker to arbitrary locations on the track. The downsides to these DNA walkers were that they simply detached from the track and that their next binding sites were found diffusively. Other DNA walkers used gears[18] or enzymes[19] to facilitate unidirectional movement, but the overall mechanisms were similar.

2.2.2 MICROTUBULE-DEPENDENT MOTOR PROTEINS

Microtubules are intracellular filaments involved in many cell processes.[20] They are involved in forming the mitotic spindle during cell division, maintaining cell structure, providing platforms for transport, and locomotion. The main building blocks of microtubules are α- and β-tubulin, which spontaneously bind together to form heterodimers. These tubulin heterodimers assemble into linear protofilaments that make up the structure of microtubules. Microtubules are hollow tubes of 25 nm in diameter and consist of 13 protofilaments *in vivo*. They have polarity

with the plus-end at the side that the β-tubulins point towards and the minus-end at the side that the α-tubulins point towards. Microtubules provide linear substrates that motor proteins, such as kinesin, can move along.

Kinesins are one class of motor proteins that use microtubules as a transport system for nanoscale cargo. Kinesins consist of two motor 'head' domains that are connected to an α-helical neck by short, highly flexible neck linkers. The neck is connected to a linear stalk that has cargo binding sites at its 'tail'. Each head has two separate binding sites: one for the microtubule and the other for ATP. Hydrolysis of ATP and subsequent ADP/P_i release changes the conformation of the microtubule-binding domain and the orientation of the neck linker that results in the walking motion of the kinesin. The walking motion proceeds in 8 nm steps using a 'hand-over-hand' mechanism that puts one motor domain before the other. The short neck linker is important for guiding the direction of movement of cargo. The linear stalk is important not only for binding cargo, but also for regulating motor activity. Without cargo, kinesin is turned off by self-inhibition.

It is not a trivial task to engineer microtubule transport systems *ex vivo*, particularly in versatile geometries with intersections and complex shapes. Murphy and colleagues developed a microtubule motility assay by fixing microtubules onto glass substrates with glutaraldehyde, which also served to stabilize the polar arrangements of the microtubules.[21] However, the movement of kinesin on the microtubules is only one dimensional, and the cargo drops off once the end of the filament is reached. Furthermore, kinesin only makes a few hundred steps before dissociating from the microtubule. Vale and colleagues demonstrated an inverted microtubule motility assay *in vitro* by immobilizing a bed of kinesin molecules on glass surfaces (Fig. 2.1A).[22] Microtubules were then perfused into the chamber and exhibited motility. Pivots around a single nodal point represented interaction of a microtubule with a single kinesin molecule. A number of track designs based on these inverted motility assays were fabricated to guide filaments efficiently. Tracks of kinesin were laid down on microscopic stripes of chemical adhesive surrounded by non-adhesive areas.[23] Microtubules that crossed the chemical edge would ultimately fall off as they did not find kinesins on the non-adhesive areas. Microchannel walls were also constructed to keep microtubules on the desired path as they were forced to bend.[24] Finally, the most efficient design that guided microtubules along a track was the construction of overhanging walls.[25] Since microtubules can still travel in opposite directions,

unidirectional motion was achieved by sorting microtubules with asymmetric channel features, such as dead-ends[26] or arrow-heads[27]. Microtubules that wandered into these channels were forced to turn around.

For cargo selection, the molecular recognition sites of microtubules have been engineered to allow desired cargo to be bonded and transported. This is typically done by tagging the cargo with antibodies or biotinylating microtubules and coating cargo with avidin or streptavidin (Fig. 2.1B). Polymeric and magnetic beads,[28,29] gold nanoparticles,[30,31] DNA,[32,33] and viruses,[34,35] have all been coupled to microtubules through these linkages. Furthermore, cargo loading zones have been built for large-scale transport applications.[31] Passing microtubules collide with cargo, pick them up, and transport them into cargo-free areas (Fig. 2.1C).

2.2.3 Actin-dependent motor proteins

Actin is another type of cytoskeletal filament and is important in cell motility, cytokinesis, and cell attachment to substrates by focal adhesions.[36] In many ways, they resemble microtubules. Actin filaments have polarity because their monomers orient with their cleft toward the same end of the filament (plus-to-minus). Their monomers also spiral around the axis of the filament with a structure similar to a double helix. They are highly dynamic and can polymerize and depolymerize rapidly. Like kinesin, myosin molecules are a class of motor proteins that bind to actin, hydrolyze ATP, and move along the filaments. They also tend to move toward the barbed end of actin.

The technologically-motivated development of classical motility assays into devices for controlled microscale transport has not been as rapid in actomyosin systems as in the case of microtubule/kinesin. There are several reasons for this. The most widely available myosin is myosin II, which is not 'processive'.[37,38] This means that after one step (ATP hydrolysis that leads to a conformational change), the myosin detaches from the actin. This makes it almost impossible to transport cargo along actin filaments. However, there does exist variants of myosin that are processive (myosin V and VI),[39,40] but there have not been many reports of its use as a biological machine. Furthermore, the stiffness of actin is much less than the stiffness of microtubules. As a result, the filaments are 'floppy' and can maneuver around microfabricated structures easily.[41] Because of the helical structure of actin, myosin will follow a helical path

when actin is attached to the substrate, or actin filaments gliding along a bed of myosin will rotate and eventually the cargo will inhibit its movement.

2.2.4 F_1-ATPase, a rotary motor

To date, F_1-ATPase is probably the best understood biomolecular motor. Coupled with the membrane-embedded proton-conducting unit F_0, it forms the H^+-ATP synthase that reversibly couples transmembrane proton flow to ATP synthesis/hydrolysis in respiring and photosynthetic cells. F_1-ATPase consists of a hexamer stator of alternating α and β subunits. In the central cavity of the hexamer is a stalk rotor made up of γ, δ, and ε subunits. This γδε-subunit rotates within the αβ-subunit.

Kinosita and colleagues first isolated and immobilized the F_1 complex on a glass surface by linking its histidine tags with Ni^{2+}-nitrilotriacetic acid (Ni-NTA).[42] Fluorescently-labeled actin filaments were attached to the γδε-subunits to visualize its rotation directly. In the presence of ATP, the filaments rotated for more than 100 revolutions in an anticlockwise direction, and the rotary torque produced more than 40 pN nm^{-1} under high load. Montemagno and colleagues combined inorganic and biological materials in a hybrid system by fabricating nickel nanopropellers (length 750 to 1400 nm, diameter 150 nm) that were attached to the γδε-subunit of F_1-ATPase through biotin-streptavidin linkages.[43] The torque on the motors were 20 and 19 pN nm^{-1} with a rotational velocity of 8.0 and 1.1 rps for the 750 and 1400 nm propeller, respectively. The F_1-ATPase motors were mounted on nickel-capped SiO_2 posts (height 200 nm) to prevent drag on the propellers due to proximity interactions with the substrate.

A reversible on/off 'switch' was added to the F_1-ATPase motor to control its function and the nanopropeller rotation. The same research group introduced a zinc-binding site to the αβ-subunit of the motor by site-directed mutagenesis. Rotation of the nanopropeller could then be inhibited in the presence of zinc because it interfered with the cyclic conformation changes that occurred during ATP hydrolysis. Removal of zinc by chelation restored both ATP hydrolysis and nanopropeller rotation.[44]

2.3 Biological actuators with single cells or cell clusters

Unlike biomolecules, single cells and microorganisms can self-replicate and perform multiple functions at once, such as synthesizing organic and inorganic materials, sensing,

communicating, converting energy, and generating mechanical motion. They are also larger in size and can be used to power microdevices in ways that would exceed the limits of conventional microfabrication technologies. Here, we discuss a number of cell-based biological actuators, including bacteria, protozoa, algae, and cardiomyocytes, and describe current efforts to control their movements externally.

2.3.1 BACTERIAL MICROORGANISMS

Several research groups have exploited the motility of bacteria for bioactuation because of the unique advantages of flagellar motors.[45] First, they offer a degree of miniaturization of a fully-powered actuator that has not been achieved to date. Second, the culture of bacteria is rapid and inexpensive. Third, bacteria draw chemical energy directly from the environment and are able to survive in a wide range of temperatures and pH. Finally, they are controllable *en masse* through different sensory mechanisms.

The flagellar motors can potentially be used as pumps to control fluid flow. Berg and colleagues absorbed the cell bodies of *Serratia marcescens* swarmer cells onto flat polydimethylsiloxane (PDMS) surfaces to form bacterial "carpets" with freely rotating flagellar filaments.[46] Tracer beads (1 μm diameter) near the surface of the carpet were displaced, revealing linear and rotational flow patterns. They also made simple "auto-mobile" chips and beads by similarly absorbing the swarmer cells to polystyrene beads (10 μm diameter) and various PDMS geometries to demonstrate translation and rotation. Breuer and colleagues used these bacterial carpets in microfluidic channels to pump and mix two fluid streams. Tung and Kim also demonstrated this with *Escherichia coli*.[47]

In addition, bacteria can be used to translate or rotate a microdevice. Uyeda and colleagues fabricated silicon dioxide micro-rotors and coated them with streptavidin.[48] The micro-rotors were released and attached to a silicon circular track functionalized with the sialic protein, fetuin. Biotinylated *Mycoplasma mobile* bacteria were introduced, binding to the micro-rotor and gliding unidirectionally along the track. As a result, rotation of the micro-rotor was achieved at a rate of 2 rpm. Similarly, Aranson and colleagues harnessed the collective swimming of randomly moving *Bacillus subtilis* bacteria to directionally rotate asymmetric gears at 1-2 rpm.[49]

The transport of synthetic cargo can be achieved by selectively attaching the cell bodies of bacteria to it. Park and colleagues fabricated poly(ethylene glycol) (PEG) microbeads that were selectively-coated on one half of the microbeads with poly-L-lysine (PLL).[50] This was meant to enhance the velocity and directionality of the microbeads as opposed to coating the entire PEG microbead. *Salmonella typhimurium* bacteria were mixed with the PEG microbeads and allowed to attach selectively to PLL-coated regions. The microbeads traveled at an average velocity of 0.37 μm s^{-1}.

Finally, bacteria can be controlled externally to enhance desired functionalities. Pappas and colleagues controlled a monolayer of *Serratia marcescens* swarmer cells with galvanotaxis using direct current (DC) electric fields.[51] The swarmer cells were blotted on the surface of SU-8 rectangular microstructures (100*L* x 50*W* x 5*T*) to form MicroBioRobots (MBRs). A star-shaped trajectory with 5 destination points was fed to a feedback control algorithm that used the real-time location of the MBR and the position of the next destination to control the applied voltage at a frequency of 8 Hz. Kim and colleagues used phototaxis as a switch to control a 50 μm triangular microstructure blotted with the swarmer cells.[52] After exposure of the cells with ultraviolet (UV) light, motility temporarily stopped until the light was removed.

2.3.2 PROTOZOAN MICROORGANISMS

In parallel to the bacteria work, some research groups are using complex eukaryotic microorganisms for bioactuation. Itoh controlled the motion of *Paramecium caudatum*, a unicellular microorganism, by changing the electrical potential gradient of the culture medium.[53] The paramedium exhibited negative galvanotaxis, and when a DC electric field was applied, the paramecium aligned to the electric field and started to swim toward the cathode at an applied electric potential grade of 0.3 V mm^{-1}. Using an automatic motion control program, the paramecium was guided along a figure 8 and star-shaped course, and it was used to rotate a 1 mm micro-impeller.

Kim and colleagues used 'artificial' magnetotaxis to control the movement of *Tetrahymena pyriformis*, a ciliate protozoan, with ferromagnetic nanoparticles and an external time-varying magnetic field.[54] Spherical iron oxide particles (50 nm diameter) were internalized by the protozoa and magnetized. When an electromagnet with magnetic field strength of 2 mT was applied, the protozoa aligned (or anti-aligned depending on the dipole) to the field. A

tracking algorithm was then used to guide a single protozoan through a sequence of five destination points.

2.3.3 Algal microorganisms

Whitesides and colleagues took it a step further by attaching cargo loads to biflagellated algae, *Chlamydomonas reinhardtii*, steering the swimming cells to a targeted location with phototaxis, and releasing those loads with photochemistry (Fig. 2.2).[55] Specially-modified polystyrene beads (1 to 6 μm diameter) attached to the cells on contact. As long as the beads did not interfere with the flagella, the cells continued to travel at velocities between 100-200 μm s^{-1}. The loaded cells were placed in a microfluidic channel with low intensity LEDs (λ = 505 nm) embedded at both ends. Alternating LEDs were illuminated and the loaded cells swam back and forth with rapid phototactic responses (<1 sec). The cells could be unloaded by photochemical cleavage of the modified polystyrene beads. UV irradiation (λ = 365 nm) of the cells released the loads within 18 seconds without damaging the cells.

2.3.4 Single and clustered cardiomyocytes

Cardiomyocytes are very promising as bioactuators because they are: (1) synchronous, (2) spontaneously contracting, and (3) powered by glucose as its only energy source without applied electrical power or stimulus.[56] A single cardiomyocyte can generate at least 1 μN of force. The concept of bioactuators using cultured cardiomyocytes is to couple them to polymer-based microstructures to convert chemical energy into mechanical energy to move the structures.

Kitamori and colleagues fabricated arrays of PDMS micropillars using a replica molding process and coated them with fibronectin to promote cardiomyocyte attachment.[57] Isolated from primary neonatal rat hearts, cardiomyocytes were cultured over the micropillars. About 80% of the pillars were coupled with cardiomyocytes that spontaneously beat at 1.4 Hz after the third day in culture. Contraction of the cardiomyocytes displaced the micropillars at a calculated force of 3.5 μN.

Lee and colleagues fabricated arrays of PDMS microcantilevers using a sandwich molding process and coated them with a fibronectin/gelatin mixture.[58] Cardiomyocytes were seeded on the microcantilevers and contractile forces caused them to deflect. Using analytical and numerical analysis, the contractile force of the cardiomyocytes on the microcantilevers was

2-5 nN μm^{-2}. This was improved to 7-10 nN μm^{-2} by fabricating grooves on the microcantilevers. Hickman and colleagues also did this with silicon microcantilevers.

Kim and colleagues developed a PDMS microgear using a sandwich molding process.[59] Poly(ethylene glycol) PEG microwells were patterned onto a glass substrate and the microwells were coated with collagen. The collagen selectively absorbed to the exposed glass. Small aggregates of cardiomyocytes were seeded on the microwells and had an estimated contractile force of 9.06 mN mm^{-2} (about 6 cells). The PDMS microgears were gently attached to these cell aggregates. However, the authors did not show directional movement of the gears by contraction of the cardiomyocyte aggregates.

2.4 Biological actuators with natural and synthetic tissues

While biomolecules and unicellular microorganisms are being extensively studied as bioactuators, there is surprisingly little effort directed towards the creation of bioactuators with tissues and other complex hierarchies. Although single or small clusters of cells can drive micro-scale structures, it is difficult to do this for higher-ordered structures. Nature provides an elegant solution by forming complex hierarchies of tissues using cells as building blocks. This hierarchy of increasing complexity is tied to an increase in functionalities. Based on active and passive self-organization principles, it has been demonstrated that more complex hierarchical structures can work as bioactuators for improved functional performance. In this last section, we focus on research related to mammalian-derived cardiac- and skeletal-based tissues and also the early development of insect-derived dorsal vessel-based tissue as bioactuators.

2.4.1 Cardiac muscle-based tissues

The assembly of cell sheets of cardiomyocytes can be harnessed to generate larger forces and be used to drive more complicated structures or fluids. One method that garnered a lot of attention was the use of temperature-responsive polymers functionalized with cell-adhesive ligands to culture cell sheets of cardiomyocytes. Okano and colleagues uniformly grafted poly(N-isopropylacrylamide) (PIPAAm) on polystyrene culture dishes by irradiation with an electron beam.[60] PIPAAm is a thermo-responsive polymer that shows remarkable changes in swelling by changing its temperature. Above 32 ^{o}C, PIPAAm was compact and hydrophobic. Cells were able to adhere, grow, and form sheets on these surfaces. When the temperature was

lowered, PIPAAm became hydrophilic and swollen. As a result, the cell sheets detached from the surface of the polymer (Fig. 2.3A). The cell attachment and adherence were prevented by the difficulty of displacing adsorbed water molecules on highly hydrated hydrophilic surfaces. The advantage of this technique was that only the connection between cell adhesive proteins and the PIPAAm surface was broken, and the cells remain connected together as a cell sheet. Cell sheets of cardiomyocytes grown using this method kept their cell-cell junctions, remained synchronous, and could be overlaid for increased contractility.[61]

While microdevices are usually powered by external energy sources, cell sheets of cardiomyocytes can be used to create self-actuated, wireless, and mechanochemical transducers that require no externally coupled energy source or stimuli. Kitamori and colleagues developed the first demonstration of a micropump powered by a cell sheet of cardiomyocytes.[62] A square microchip (2 x 2 cm) consisted of four PDMS-based elements: a push-bar, a chamber layer, a diaphragm membrane, and a microchannel layer with two holes for fluid transfer. A cell sheet of cardiomyocytes was layered on top of the push-bar and diaphragm. Spherical polystyrene tracking particles (1 μm diameter) were dispersed in the medium, and spontaneous, oscillating fluid motion was observed by their movement with optical microscopy. The fluid oscillating frequency was 0.7 Hz with 150 μm maximum linear displacement of tracking particles. Directional fluid flow was demonstrated with check valves, but only flow rates of 2 nL min^{-1} were achieved. The same group recently improved on their method by wrapping a sheet of functional primary cardiomyocytes around a hollow PDMS sphere with inlet and outlet capillary tubes to engineer a bio-artificial hybrid pump (Fig. 2.3B).[63] The sphere is strained by the collective contractile motions of the attached cardiomyocyte sheet, and the fluid volume inside the hollow sphere chamber is reduced, producing flow into the capillary. The chamber diameter is millimeter-order (5 mm diameter); the capillaries are micrometer-order (200 μm inside diameter); the PDMS elastomer membrane is micrometer-order (250 μm thick). Oscillating fluid motion in the capillary was monitored by polystyrene tracking particles. The fluid oscillating frequency measured at 37 ^{o}C was 0.4 Hz and the maximum observed linear displacement of tracking particles was 70 μm. The expected flow rate was 47 nL min^{-1}, which was an improvement to the previous design.

Besides bioactuators that act like pumps to direct fluid flow, there has also been growing interest in creating structures that swim or walk with a sheet of cardiomyocytes. Montemagno

and colleagues developed a microdevice using a silicon backbone with self-assembled cardiomyocytes grown on a chromium/gold layer.[64] They used photolithographic techniques to fabricate a micron-sized, self-assembled, and self-actuated walking bio-microactuator powered by cardiomyocyte muscular tissue. Cardiomyocytes were aligned on a patterned film of Cr/Au, which was attached to a thin Si beam. After the microdevice was released from the PIPAAm coating, muscle contractions caused the beam to break from the rest of the device. This allowed the structure to "walk" freely. The leg dimensions were 138 μm long, 40 μm wide, and 20 nm/300 nm (Cr/Au) thick; the average step frequency was 1.8 Hz and its average maximum step size was 25 μm; the maximum speed was 38 μm/s. Park and colleagues established a swimming microrobot by micromolding PDMS.[65] Using cardiomyocytes, cells were seeded on top of four conjoined cantilever beams that were grooved to influence the alignment and enhance their contractility relative to flat beams. An increase in force (88%) and bending (40%) was recorded, with an average swimming speed of 140 μm s^{-1}.

Parker and colleagues assembled cardiomyocytes on various PDMS thin films with proteins to create muscular thin films (MTFs).[66] When released from thermoresponsive polymers, the thin films curled or twisted into 3D conformations that purportedly performed gripping, pumping, walking (133 μm s^{-1}), and swimming functions (400 μm s^{-1}). The MTFs generated specific forces as high as 4 mN mm^{-2}. Recently, MTFs were used to reverse-engineer jellyfish-like constructs, dubbed "medusoids", by studying the structural design, stroke kinematics, and fluid-solid interactions of the *Aurelia aurita* moon jellyfish (Fig. 2.3C).[67] The artificial jellyfish, dubbed "medusoids", were composed of a bilayer of living muscle tissue and synthetic elastomer arranged in freely moveable lobes around a central disc. Medusoid propulsion, like that of jellyfish, was externally-driven by electrically-paced power and recovery strokes that alternately contracted the body into a quasi-closed "bell" and then relaxed into the open lobed form. The muscle layer, comprised of anisotropic rat cardiac tissue that intrinsically enables spatiotemporally synchronous contraction, replicated the power stroke of the jellyfish. The recovery stroke, which is a consequence of elastic recoil in the jellyfish compliant matrix, was replicated by tuning the stiffness of the synthetic elastomer substrate. The geometry was further refined to allow the formation of overlapping boundary layers between lobes, thereby resisting flow across the lobe gaps. Qualitative and quantitative comparisons of jellyfish and

medusoid propulsion showed that the engineered system was able to replicate the momentum transport and body lengths traveled per swimming stroke of the natural system.

2.4.2 SKELETAL MUSCLE-BASED TISSUES

There is considerable interest in using skeletal muscle as a cell source for the bio-bots because of the favorable attributes not available in cardiac muscle.[68] In the body, skeletal muscle facilitates movement by applying forces against bones and joints. The organization of the muscle is modular, having many longitudinally-aligned, multinucleated muscle fibers assembled together by connective tissue to form a densely-packed structure.[69] Recruitment of these fibers can be finely controlled by the nervous system, which innervates individual muscle fibers at localized regions.[7] By adjusting the number of contractile muscle fibers and the tension developed collectively, the nervous system can regulate graded muscle response for controlled movement.

There are two current methods for engineering artificial skeletal muscle in 3D: (1) 2D-to-3D, and (2) 3D-to-3D. The first method was developed by Dennis and Kosnik.[70,71] It consisted of myotubes, fibroblasts, cell-secreted ECM, and synthetic tendons. The beauty of this approach was that it did not require a pre-existing scaffold. Briefly, PDMS was set in a culture dish, and absorbed with a thin layer of laminin. Synthetic tendons were fixed at opposite ends and at a desired distance apart. Cells of myoblasts and fibroblasts were seeded, and upon reaching confluence, the medium was switched from growth to differentiation. After 2-3 weeks, the monolayer of myotubes would detach and self-organize to form a 3D muscle strip, dubbed 'myooids'. Baar and colleagues later modified the method to improve the speed of myooid formation.[72] Takayama and colleagues used wavy PDMS substrates to align the myotubes in the myooids.[73] The second method was developed by Karlisch and colleagues,[74] although many variations exist.[75-77] It typically consisted of a pre-existing scaffold in 3D, either derived naturally (most common) or synthetically. Myoblasts with or without fibroblasts were embedded in the 3D scaffold and casted in molds. The molds were there for 3D scaffolds compacted by cells to retain certain shapes, such as strips and rings.

Herr and Dennis demonstrated a swimming robot actuated by living skeletal muscle (Fig. 2.4A).[78] It was actuated by two explanted frog semitendinosus muscles and controlled by an embedded microcontroller with muscle stimulators. Using open loop stimulation protocols, the

robot performed basic swimming maneuvers such as starting, stopping, turning (400 mm radius), and straight-line swimming (>1/3 body lengths per second). The robot swam for a total of 4 hour over a 42 hour lifespan before its velocity degraded below 75% of its max. The length of the robot is nearly 80 cm long.

Consequently, skeletal muscle can be used in bio-bot designs to switch locomotion on and off by neural signals, to regulate step stroke and pacing by altering the combined contractile force, and to generate a wide range of motion by localized innervation of muscle fibers. Recently, optical methods have been developed to depolarize or hyperpolarize neurons using specific wavelengths of light.[79-81] This method, known as 'optogenetics,' combines the temporal and spatial precision of light pulses with cellular specificity of genetic targeting. The general strategy of optogenetics involves introducing a light-sensitive protein, such as channelrhodopsin-2 (ChR2, discovered in green algae) to a specific cell type, illuminating the cells with defined spatiotemporal parameters, and obtaining reliable readout of the cellular behavior.[82] This past year, the method was applied to cardiac[83,84] and skeletal[85,86] muscle cells to rhythmically control their contractions. It was also used to locally innervate specific regions of muscle tissue to generate movement in multiple degrees of freedom (multi-DOF). Overall, the advantage of optogenetics is its fast, precise, and local stimulation of cells and tissues, relative to electrical stimulation. Moreover, it does not require complex heterotypic cell-cell interactions that are need for neuromuscular (neuron-to-muscle) junctions.[87,88]

2.4.3 Insect dorsal vessel-based tissues

Research groups are also beginning to take advantage of the muscular power from the dorsal vessels of insects to power actuators because of their robustness between 5 and 40 ^{o}C. The dorsal vessel of insects is the major structural component of an insect's circulatory system. It is a tube that runs longitudinally through the thorax and abdomen, along the inside of the dorsal body wall. In the abdomen, the dorsal vessel is called the heart, and it has valves and musculature that contract autonomously. Morishima and colleagues removed the dorsal vessel tissue (DVT) from the larvae of Lepidopteran inchworms (*Ctenoplusia agnate*) and fixed them between micropillars of a "polypod microrobot" (PMR) made out of micromolded PDMS (12.5*L* x 1.35*W* x 0.2*T* mm dimensions) (Fig. 2.4B).[89] The PMR moved at 3.5 ± 0.7 μm s^{-1} with a contractile force of 20 μN. Electrical stimulation could be applied at 10 V with 20 ms durations and 50 ms delays to regulate

contractility and force output. In a separate study, dorsal vessel tissue of *Drosophila melanogaster* larvae were also excised and demonstrated to contract on their micropillars at 1.6 Hz with a contractile force of 197 nN.[90]

2.5 CONCLUSION

This review highlights the recent advancements in the emerging field of bioactuators across a multitude of length scales, including biomolecules, cells and microorganisms, and tissues. Clearly, there is an emphasis on closing the feedback loop between the biological and engineering worlds, and to use biological systems to improve engineering ones. However, despite the significant progress in the last few years, there are still plenty of opportunities to explore and challenges to overcome. In addition, this review is limited to one functional element, that of actuation. There are a number of other elements to be developed, such as sensing, information processing, protein expression, and transport. It is the realization and utility of all of these functional elements, either alone or combined, that will have significant impact in health, security, and the environment. These bioactuators represent one key component in this grand vision, and future developments will depend on an integrated approach to combine them in an effort to perform prescribed tasks.

2.6 REFERENCES

1. McMahon, T. & Bonner, J. T. *On size and life*. (Scientific American: 1983).
2. Piccolino, M. Biological machines: from mills to molecules. *Nat. Rev. Mol. Cell Biol.* 1, 149–152 (2000).
3. Sherwood, L. *Human physiology: from cells to systems*. (Brooks Cole: 2012).
4. Xiong, X., Lidstrom, M. E. & Parviz, B. A. Microorganisms for MEMS. *J. Microelectromech. Syst.* 16, 429 –444 (2007).
5. Kamm, R. D., Nerem, R. & Hsia, K. J. *Cells into systems*. Mechanical Engineering Magazine 132, (2010).
6. King, A. M., Loiselle, D. S. & Kohl, P. Force generation for locomotion of vertebrates: skeletal muscle overview. *IEEE J. Oceanic Eng.* 29, 684 – 691 (2004).
7. Berne, R. M., Levy, M. N., Koeppen, B. M. & Stanton, B. A. *Physiology*. (Mosby: 2003).
8. Lieber, R. L. *Skeletal muscle structure, function, and plasticity*. (Lippincott Williams & Wilkins: 2009).
9. Knoblauch, M. & Peters, W. S. Biomimetic actuators: where technology and cell biology merge. *Cell. Mol. Life Sci.* 61, 2497–2509 (2004).

10. Kabir, A. M. R., Kakugo, A., Gong, J. P. & Osada, Y. How to integrate biological motors towards bio-actuators fueled by ATP. *Macromol. Biosci.* 11, 1314–1324 (2011).

11. Seeman, N. C. *et al*. New motifs in DNA nanotechnology. *Nanotechnology* 9, 257–273 (1998).

12. Rothemund, P. W. K. Folding DNA to create nanoscale shapes and patterns. *Nature* 440, 297–302 (2006).

13. Mao, C., Sun, W., Shen, Z. & Seeman, N. C. A nanomechanical device based on the B–Z transition of DNA. *Nature* 397, 144–146 (1999).

14. Yurke, B., Turberfield, A. J., Mills, A. P., Simmel, F. C. & Neumann, J. L. A DNA-fuelled molecular machine made of DNA. *Nature* 406, 605–608 (2000).

15. Bustamante, C., Bryant, Z. & Smith, S. B. Ten years of tension: single-molecule DNA mechanics. *Nature* 421, 423–427 (2003).

16. Simmel, F. C. & Yurke, B. Using DNA to construct and power a nanoactuator. *Phys. Rev. E* 63, 041913 (2001).

17. Shin, J.-S. & Pierce, N. A. A Synthetic DNA walker for molecular transport. *J. Am. Chem. Soc.* 126, 10834–10835 (2004).

18. Tian, Y. & Mao, C. Molecular Gears: A pair of DNA circles continuously rolls against each other. *J. Am. Chem. Soc*. 126, 11410–11411 (2004).

19. Yin, P., Yan, H., Daniell, X. G., Turberfield, A. J. & Reif, J. H. A Unidirectional DNA walker that moves autonomously along a track. *Angew. Chem. Int. Ed. Engl.* 43, 4906–4911 (2004).

20. Nogales, E. Structural insights into microtubule function. *Annu. Rev. Biochem.* 69, 277–302 (2000).

21. Turner, D. C., Chang, C., Fang, K., Brandow, S. L. & Murphy, D. B. Selective adhesion of functional microtubules to patterned silane surfaces. *Biophys. J.* 69, 2782–2789 (1995).

22. Howard, J., Hudspeth, A. J. & Vale, R. D. Movement of microtubules by single kinesin molecules. *Nature* 342, 154–158 (1989).

23. Clemmens, J., Hess, H., Howard, J. & Vogel, V. Analysis of microtubule guidance in open microfabricated channels coated with the motor protein kinesin. *Langmuir* 19, 1738–1744 (2003).

24. Clemmens, J. *et al*. Mechanisms of microtubule guiding on microfabricated kinesin-coated surfaces: chemical and topographic surface patterns. *Langmuir* 19, 10967–10974 (2003).

25. Hess, H. *et al*. Molecular Shuttles Operating Undercover: A new photolithographic approach for the fabrication of structured surfaces supporting directed motility. *Nano Lett*. 3, 1651–1655 (2003).

26. Clemmens, J. *et al*. Motor-protein 'roundabouts': microtubules moving on kinesin-coated tracks through engineered networks. *Lab Chip* 4, 83 (2004).

27. Hiratsuka, Y., Tada, T., Oiwa, K., Kanayama, T. & Uyeda, T. Q. Controlling the direction of kinesin-driven microtubule movements along microlithographic tracks. *Biophys. J.* 81, 1555–1561 (2001).

28. Hess, H., Clemmens, J., Qin, D., Howard, J. & Vogel, V. Light-controlled molecular shuttles made from motor proteins carrying cargo on engineered surfaces. *Nano Lett*. 1, 235–239 (2001).

29. Hess, H., Howard, J. & Vogel, V. A piconewton forcemeter assembled from microtubules and kinesins. *Nano Lett*. 2, 1113–1115 (2002).

30. Boal, A. K., Bachand, G. D., Rivera, S. B. & Bunker, B. C. Interactions between cargo-carrying biomolecular shuttles. *Nanotechnology* 17, 349–354 (2006).

31. Brunner, C., Wahnes, C. & Vogel, V. Cargo pick-up from engineered loading stations by kinesin driven molecular shuttles. *Lab Chip* 7, 1263–1271 (2007).

32. Diez, S. *et al*. Stretching and transporting DNA molecules using motor proteins. *Nano Lett*. 3, 1251–1254 (2003).

33. Dinu, C. Z. *et al*. Parallel Manipulation of Bifunctional DNA Molecules on structured surfaces using kinesin-driven microtubules. *Small* 2, 1090–1098 (2006).

34. Bachand, G. D., Rivera, S. B., Carroll-Portillo, A., Hess, H. & Bachand, M. Active capture and transport of virus particles using a biomolecular motor-driven, nanoscale antibody sandwich assay. *Small* 2, 381–385 (2006).

35. Martin, B. D. *et al*. An engineered virus as a bright fluorescent tag and scaffold for cargo proteins – capture and transport by gliding microtubules. *J. Nanosci. Nanotechnol.* 6, 2451–2460 (2006).

36. Bray, D. *Cell movements: from molecules to motility*. (Garland Science: 2000).

37. Spudich, J. A. The myosin swinging cross-bridge model. *Nat. Rev. Mol. Cell Biol.* 2, 387–392 (2001).

38. Huxley, A. F. Mechanics and models of the myosin motor. *Philos. Trans. R. Soc. Lond. B Biol. Sci.* 355, 433–440 (2000).

39. Vale, R. D. & Milligan, R. A. The way things move: looking under the hood of molecular motor proteins. *Science* 288, 88–95 (2000).

40. Tyska, M. J. & Mooseker, M. S. Myosin-V motility: these levers were made for walking. *Trends Cell Biol.* 13, 447–451 (2003).

41. Gittes, F., Mickey, B., Nettleton, J. & Howard, J. Flexural rigidity of microtubules and actin filaments measured from thermal fluctuations in shape. *J. Cell Biol.* 120, 923–934 (1993).

42. Noji, H., Yasuda, R., Yoshida, M. & Kinosita, K. Direct observation of the rotation of F1-ATPase. *Nature* 386, 299–302 (1997).

43. Soong, R. K. *et al*. Powering an inorganic nanodevice with a biomolecular motor. *Science* 290, 1555–1558 (2000).

44. Liu, H. *et al*. Control of a biomolecular motor-powered nanodevice with an engineered chemical switch. *Nat. Mater.* 1, 173–177 (2002).

45. Steager, E. B. *et al*. Chapter 10 - Bacteria-powered microrobots. *Microbiorobotics* 249–275 (2012)

46. Darnton, N., Turner, L., Breuer, K. & Berg, H. C. Moving fluid with bacterial carpets. *Biophys. J.* 86, 1863–1870 (2004).

47. Kim, M. J. & Breuer, K. S. Use of bacterial carpets to enhance mixing in microfluidic systems. *J. Fluids Eng.* 129, 319–324 (2007).

48. Hiratsuka, Y., Miyata, M., Tada, T. & Uyeda, T. Q. P. A microrotary motor powered by bacteria. *Proc. Natl. Acad. Sci. U S A* 103, 13618–13623 (2006).

49. Sokolov, A., Apodaca, M. M., Grzybowski, B. A. & Aranson, I. S. Swimming bacteria power microscopic gears. *Proc. Natl. Acad. Sci. U S A* 107, 969–974 (2010).

50. Cho, S., Park, S. J., Ko, S. Y., Park, J.-O. & Park, S. Development of bacteria-based microrobot using biocompatible poly(ethylene glycol). *Biomed. Microdevices* (2012): DOI:10.1007/s10544-012-9704-1.

51. Sakar, M. S. *et al*. Modeling, control and experimental characterization of microbiorobots. *Int. J. Rob. Res.* 30, 647–658 (2011).

52. Steager, E. *et al*. Control of microfabricated structures powered by flagellated bacteria using phototaxis. *Appl. Phys. Lett.* 90, 263901 (2007).

53. Itoh, A. Motion control of protozoa for bio MEMS. *IEEE/ASME International Conference on Advanced Intelligent Mechatronics* 27–32 (1999)

54. Kim, D. H., Cheang, U. K., Kőhidai, L., Byun, D. & Kim, M. J. Artificial magnetotactic motion control of Tetrahymena pyriformis using ferromagnetic nanoparticles: A tool for fabrication of microbiorobots. *Appl. Phys. Lett.* 97, 173702 (2010).

55. Weibel, D. B. *et al*. Microoxen: microorganisms to move microscale loads. *Proc. Natl. Acad. Sci. U S A* 102, 11963–11967 (2005).

56. Tanaka, Y. *et al*. Biological cells on microchips: New technologies and applications. *Biosens. Bioelectron.* 23, 449–458 (2007).

57. Tanaka, Y. *et al*. Demonstration of a PDMS-based bio-microactuator using cultured cardiomyocytes to drive polymer micropillars. *Lab Chip* 6, 230–235 (2006).

58. Park, J. *et al*. Real-Time measurement of the contractile forces of self-organized cardiomyocytes on hybrid biopolymer microcantilevers. *Anal. Chem*. 77, 6571–6580 (2005).

59. Kim, D. H. *et al*. Fabrication of patterned micromuscles with high activity for powering biohybrid microdevices. *Sens. Actuators B Chem.* 117, 391–400 (2006).

60. Shimizu, T., Yamato, M., Kikuchi, A. & Okano, T. Cell sheet engineering for myocardial tissue reconstruction. *Biomaterials* 24, 2309–2316 (2003).

61. Shimizu, T. *et al*. Fabrication of Pulsatile Cardiac Tissue Grafts Using a Novel 3-Dimensional Cell Sheet Manipulation Technique and Temperature-Responsive Cell Culture Surfaces. *Circ. Res.* 90, e40–e48 (2002).

62. Tanaka, Y. *et al*. An actuated pump on-chip powered by cultured cardiomyocytes. *Lab Chip* 6, 362–368 (2006).

63. Tanaka, Y. *et al*. A micro-spherical heart pump powered by cultured cardiomyocytes. L*ab Chip* 7, 207–212 (2007).

64. Xi, J., Schmidt, J. J. & Montemagno, C. D. Self-assembled microdevices driven by muscle. *Nat. Mater.* 4, 180–184 (2005).

65. Kim, J. *et al*. Establishment of a fabrication method for a long-term actuated hybrid cell robot. *Lab Chip* 7, 1504 (2007).

66. Feinberg, A. W. *et al*. Muscular thin films for building actuators and powering devices. *Science* 317, 1366–1370 (2007).

67. Nawroth, J. C. *et al*. A tissue-engineered jellyfish with biomimetic propulsion. *Nat. Biotech.* 30, 792–797 (2012).

68. King, A. M., Loiselle, D. S., & Kohl, P. Force generation for locomotion of vertebrates: skeletal muscle overview, *IEEE J. Oceanic Eng*. 29, 684-691 (2004).

69. Lieber, R. L., *Skeletal muscle structure, function, and plasticity: the physiological basis of rehabilitation* Lippincott Williams & Wilkins, Baltimore, MD (2010).

70. Dennis, R. G., & Kosnik, P. E. Excitability and isometric contractile properties of mammalian skeletal muscle constructs engineered in vitro. *In Vitro Cell. Dev. Biol. Anim.* 36, 327-335 (2000).

71. Dennis, R. G., Kosnik, P. E., Gilbert, M. E., & Faulkner, J. A. Excitability and contractility of skeletal muscle engineered from primary cultures and cell lines. *Am J. Physiol. Cell Physiol.* 280, 288-295 (2001).

72. Huang, Y. C., Dennis, R. G., & Baar, K. Cultured slow vs. fast skeletal muscle cells differ in physiology and responsiveness to stimulation. *Am. J. Physiol. Cell Physiol.* 291, C11-17.

73. Lam, M. T., Huang, Y. C., Birla, R. K., & Takayama, S. Microfeature guided skeletal muscle tissue engineering for highly organized 3-dimensional free-standing constructs. *Biomaterials* 30, 1150-1155 (2009).

74. Vandenburgh, H., Swasdison, S., & Karlisch, P. Computer-aided mechanogenesis of skeletal muscle organs from single cells in vitro, *FASEB J.* 5, 2860-2867 (1991).

75. Zimmermann, W. H., *et al*. Tissue engineering of a differentiated cardiac muscle construct. *Circ. Res.* 90, 223-230 (2002).

76. Bian, W., Liau, B., Badie, N., & Bursac, N. Mesoscopic hydrogel molding to control the 3D geometry of bioartificial muscle tissues. *Nat. Protoc.* 4, 1522-1534 (2009).

77. Boudou, T., *et al*. A microfabricated platform to measure and manipulate the mechanics of engineered cardiac microtissues. *Tissue Eng. Part A* 18, 910-919 (2012).

78. Herr, H. & Dennis, R. G. A swimming robot actuated by living muscle tissue. *J. Neuroengineering Rehabil.* 1, 6 (2004).

79. Boyden, E. S., Zhang, F., Bamberg, E., Nagel, G., & Deisseroth, K. Millisecond-timescale, genetically targeted optical control of neural activity. *Nat. Neurosci.* 8, 1263-1268 (2005).

80. Arenkiel, B. R., *et al*. In vivo light-induced activation of neural circuitry in transgenic mice expressing channelrhodopsin-2. *Neuron* 54, 205-218 (2007).

81. Wang, H., *et al*. High-speed mapping of synaptic connectivity using photostimulation in channelrhodopsin-2 transgenic mice. *Proc. Natl. Acad. Sci. U S A* 104, 8143-8148 (2007).

82. Deisseroth, K. Optogenetics. *Nat. Methods* 8, 26-29 (2011).

83. Bruegmann, T., *et al.* Optogenetic control of heart muscle in vitro and in vivo. *Nat. Methods* 7, 897-900 (2010).

84. Arrenberg, B., Stainier, D. Y., Baier, H., & Huisken, J. Optogenetic control of cardiac function. *Science* 330, 971-974 (2010).

85. Asano, T., Ishizua, T., & Yawo, H. Optically controlled contraction of photosensitive skeletal muscle cells. *Biotechnol. Bioeng.* 109, 199-204 (2012).

86. Sakar, M. S., *et al*. Formation and optogenetic control of engineered 3D skeletal muscle bioactuators. *Lab Chip* 12, 4976-4985 (2012).

87. Umbach, J. A., Adams, K. L., Gundersen, C. B., & Novitch, B. G. Functional neuromuscular junctions formed by embryonic stem cell-derived motor neurons. *PLoS One* 7, e36049 (2012).

88. Kubo, T., Randolph, M. A., Gröger, A., & Winograd, J. M. Embryonic stem cell-derived motor neurons form neuromuscular junctions in vitro and enhance motor functional recovery in vivo. *Plast. Reconstr. Surg.* 123, 139S-148S (2009).

89. Akiyama, Y., Iwabuchi, K., Furukawa, Y. & Morishima, K. Electrical stimulation of cultured lepidopteran dorsal vessel tissue: an experiment for development of bioactuators. *In Vitro Cell Dev. Biol. Anim.* 46, 411–415 (2010).

90. Akiyama, Y., Hoshino, T., Iwabuchi, K. & Morishima, K. Room temperature operable autonomously moving bio-microrobot powered by insect dorsal vessel tissue. *PLoS ONE* 7, e38274 (2012).

2.7 FIGURES AND CAPTIONS

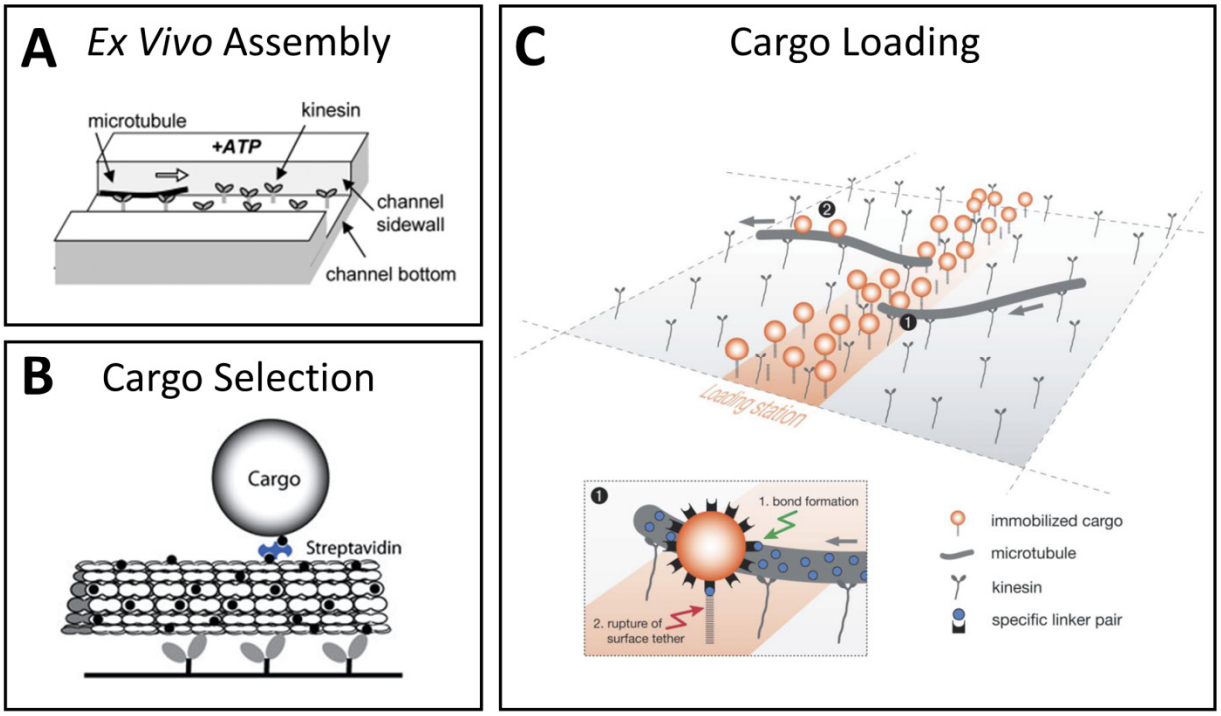

Fig. 2.1 | Molecular-level biological machines. (**A**) A bed of kinesin molecules coated on to glass substrates can be used to guide microtubules along patterned tracks or microchannels [Reprinted from (26)]. (**B**) Molecular recognition sites of microtubules have been engineered to allow desired cargo to be attached and transported. This is typically done by tagging the cargo with antibodies or biotinylating microtubules and coating cargo with avidin or streptavidin. (**C**) Cargo loading zones have been built for large-scale transport applications. Passing microtubules collide with cargo, pick them up, and transport them into cargo-free areas [Reprinted from (31)].

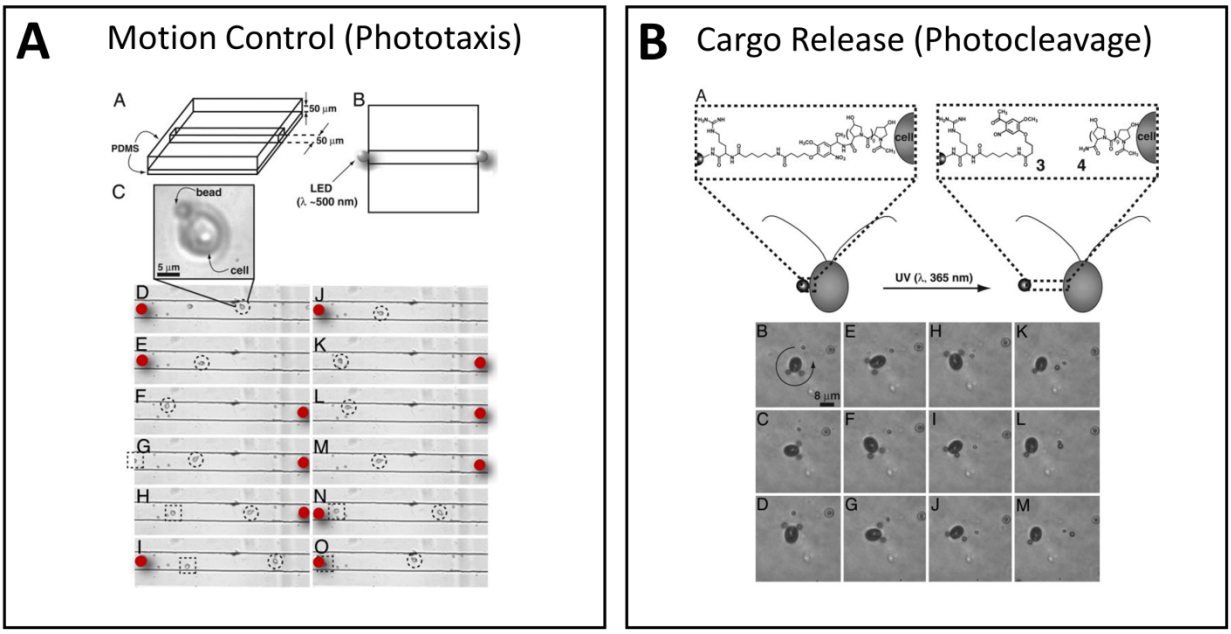

Fig. 2.2 | Cellular-level biological machines. (**A**) Specially-modified polystyrene beads (1 to 6 μm diameter) were attached to biflagellated algae on contact. The cells were able to transport the beads at velocities of 100-200 μm s^{-1} and could be controlled through phototactic responses using low intensity LEDs (λ = 505 nm). (**B**) The cells could be unloaded by photochemical cleavage of the modified polystyrene beads. UV irradiation (λ = 365 nm) of the cells released the loads within 18 seconds without damaging the cells [Reprinted from (55)].

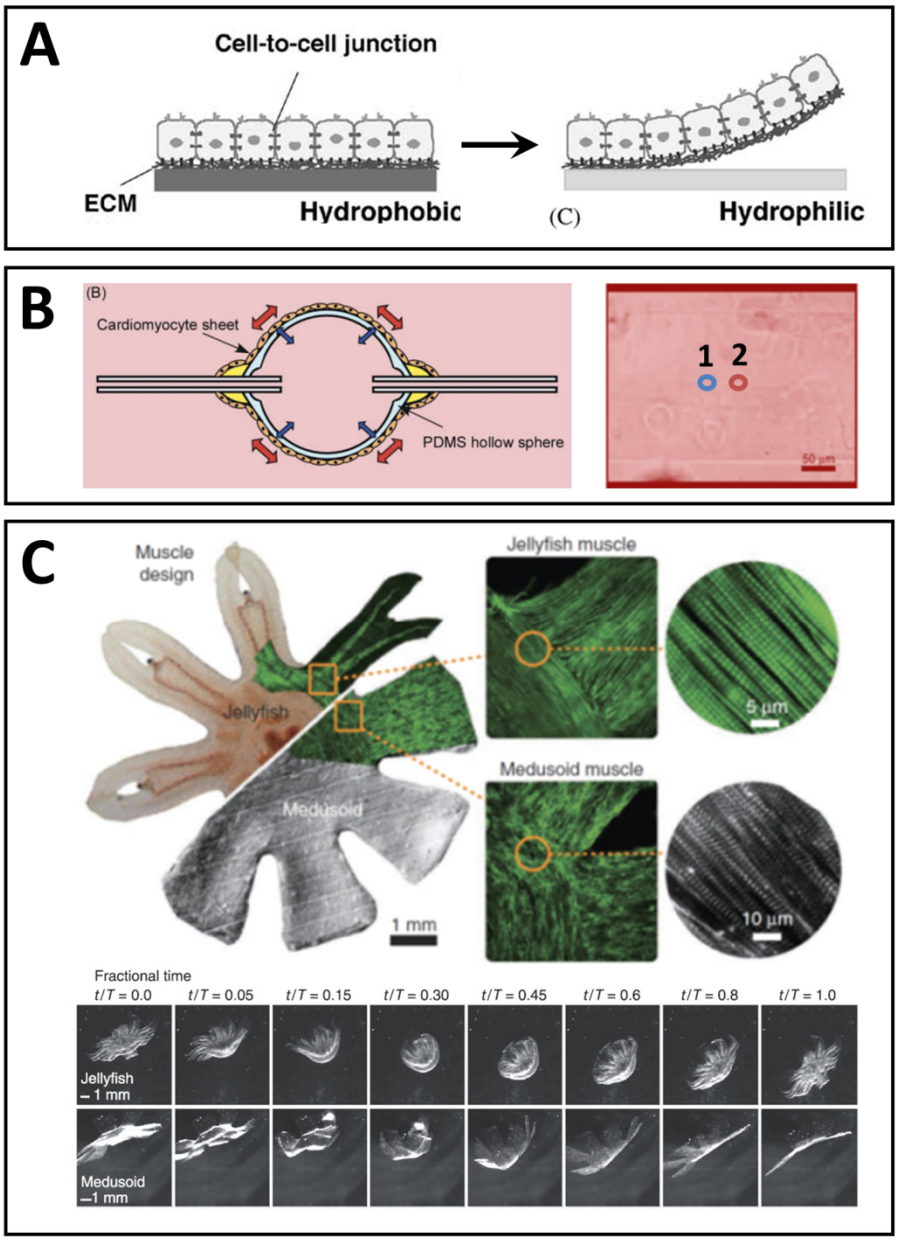

Fig. 2.3 | Tissue-level (synthetic) biological machines. (**A**) Cardiomyocytes can be grown on thermo-responsive polymers called poly(N-isopropylacrylamide) (PIPAAm) to form a 2D cell sheet. These sheets can be detached intact by lowering the temperature below 32 ^{o}C [Reprinted from (60)]. (**B**) The cell sheet of cardiomyocytes can be wrapped around a hollow PDMS sphere with inlet and outlet capillary tubes to engineer a bio-artificial hybrid pump. Oscillating fluid motion in the capillary was monitored by polystyrene tracking particles. The maximum observed linear displacement of tracking particles was 70 μm (**1** to **2**) [Reprinted from (63)]. (**C**) These cell sheets can also be grafted on PDMS thin films with carefully designed geometry and organized cardiomyocytes to mimic the swimming motion of jellyfish [Reprinted from (67)].

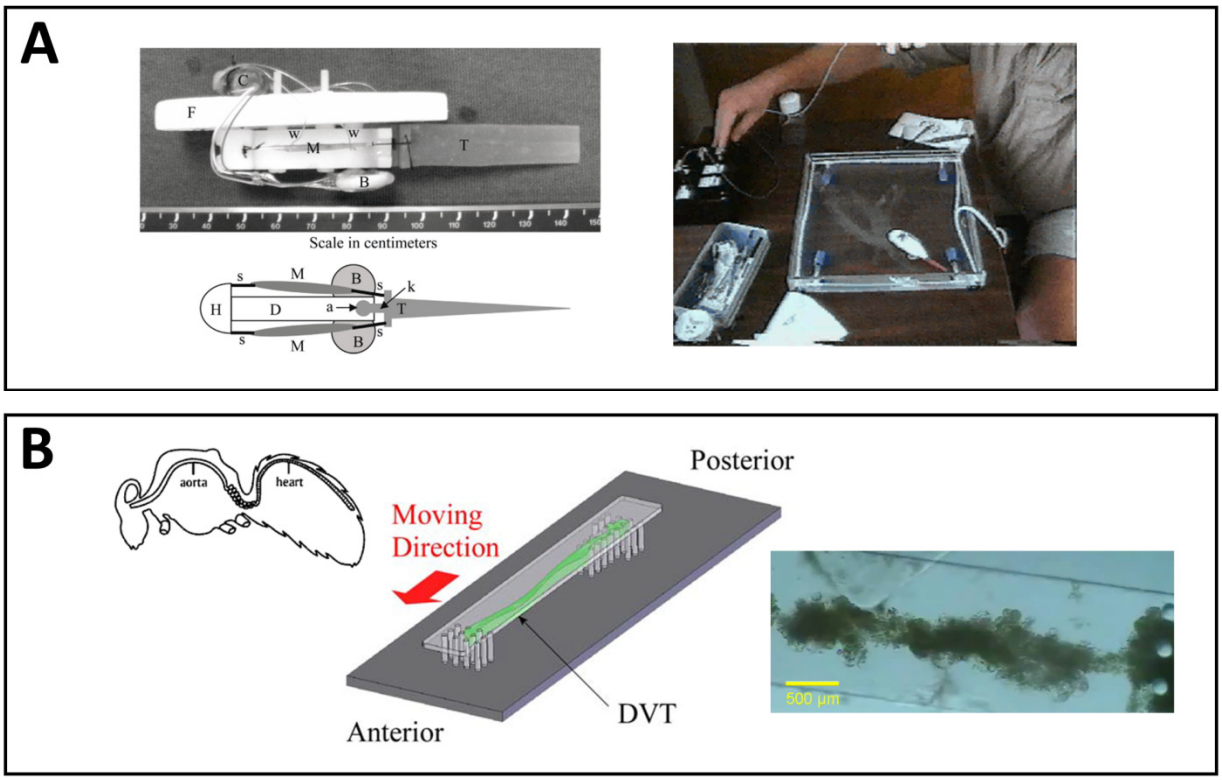

Fig. 2.4 | Tissue-level (natural) biological machines. (**A**) Two explanted frog semitendinosus muscles (M) were attached by sutures (s) to a swimming robot for actuation. The robot was controlled by an embedded microcontroller with muscle stimulators. Basic swimming maneuvers such as starting, stopping, turning (400 mm radius), and straight-line swimming (>1/3 body lengths per second) were demonstrated [Reprinted from (78)]. (**B**) The muscular power from dorsal vessel tissues (DVTs) of insects can also be used as actuators and are robust between 5 - 40 ^{o}C. DVTs from the larvae of Lepidopteran inchworms (*Ctenoplusia agnate*) were fixed between micropillars of a "polypod microrobot" (PMR) made out of micromolded PDMS, which moved at 3.5 ± 0.7 µm s^{-1} with a contractile force of 20 µN. Electrical stimulation could be applied at 10 V with 20 ms durations and 50 ms delays to regulate contractility and force output [Reprinted from (90)].

CHAPTER 3: 3D STEREOLITHOGRAPHIC PRINTING

3.1 INTRODUCTION

The need for in vitro 3D model systems that can substitute for specific tissues is becoming increasingly prevalent in applications ranging from fundamental scientific studies, cancer metastases, stem cell biology, drug discovery, and the replacement of organs.[1] Native tissues are composed of heterogeneous mixtures of cell types and extracellular matrix (ECM) molecules that are arranged in complex 3D hierarchies and supported by an intricate network of blood vessels. Mimicking the spatial organization of these cells and ECM molecules is one of the major challenges toward developing tissue equivalents.

Hydrogels have been of particular interest as biomaterial scaffolds in these systems because of their close resemblance to native tissues. They are crosslinked polymer networks that are highly hydrated and possess tissue-like elasticity.[2,3] In particular, poly(ethylene glycol) (PEG) is a synthetic hydrogel that has been widely used because of its hydrophilicity, biocompatibility, and ability to be chemically tailored.[4] Cell adhesion domains,[5,6] growth factors,[7] and hydrolytic[8] and proteolytic[9,10] sequences have also been incorporated into PEG hydrogels to guide cellular processes such as differentiation, proliferation, and migration. By modifying the ends with either acrylates or methacrylates, PEG hydrogels can be photocrosslinked in the presence of appropriate initiating agents.[11,12] This type of curing offers spatial control over polymerization that, while increasingly popular,[13–15] has not been fully exploited.

Computer-aided design (CAD)-based rapid prototyping technologies have recently been applied as enabling tools that provide excellent spatial control over scaffold architecture.[16,17] Rapid prototyping is the process of creating complex 3D structures by repetitive deposition and processing of individual layers using computer-controlled devices. Usually, a blueprint is developed first and translated into a 3D design in a format that can be used by the rapid prototyping system. The design is sliced into a collection of 2D cross-sectional layers that is then processed into a real 3D structure using layer-by-layer deposition. By controlling the micro- and macro-architecture of these scaffolds, rapid prototyping technologies can potentially be used to create artificial vasculature to facilitate the flow of oxygen and nutrients into the construct, thereby increasing the potential size of the tissue.[18,19] Additionally, angiogenic factors can be

added to the vasculature to induce the formation of new blood vessels.[20] Because of their excellent spatial control, it is possible to create 3D structures with multi-cellular components that are required for complex tissue function.[21–23] Furthermore, rapid prototyping technologies provide a means for large-scale production of reproducible tissue constructs that can be used in a variety of applications.

A common issue in the vast majority of rapid prototyping technologies is the acellular environment in which the scaffolds are fabricated in. Because cells cannot survive these processing conditions, they are normally seeded on top of the scaffolds and induced to migrate and populate into the inner regions. In this approach, however, it is often difficult to obtain scaffolds that are evenly seeded with cells.[24] An approach where it might be possible to entrap cells in the scaffolds during the fabrication process would be very advantageous because of their homogeneous distribution. One of the technologies that may be mild enough to encapsulate living cells during the fabrication process is stereolithography.

The conventional stereolithography apparatus (SLA) uses ultraviolet (UV) light to selectively solidify photosensitive polymers. There are two main approaches in the SLA: (1) masked-based writing and (2) direct or laser writing. Photopolymerizable PEG diacrylate (PEGDA) hydrogels have been used to encapsulate hepatocytes for up to 7 days in masked-based writing methods, which employ a flood lamp to shine UV light through the openings of a mask.[15] This method requires lots of masks to create a complex structure, and it is difficult to control the amount of energy that the cells are being exposed to in each layer. Direct-writing approaches, which employ a UV laser to selectively cure the liquid polymer in a predetermined manner, have also been explored with hydrogels recently.[25–28] However, long-term viability of cells encapsulated within these hydrogels has not yet been demonstrated.

In this study, a commercially available SLA was modified to accommodate for two fabrication methods: (1) the ‘top-down’ approach, which employs a process similar to the conventional SLA, and (2) the ‘bottom-up’ approach, which allows for multiple cell types and material compositions to be arranged in their own layers within a structure. Laser polymerization characteristics of PEGDA hydrogels were examined and optimized for their utilization in the SLA. The swelling and mechanical properties of these hydrogels were measured as a function of Mw. Long-term viability, proliferation, and spreading of encapsulated NIH/3T3 cells over 14 days were evaluated in single-layer and multi-layer 3D structures prepared from PEGDA

hydrogels with a range of Mw and RGDS peptide sequences. Furthermore, controlled spatial distribution of cells and bioactive molecules in distinct layers was achieved by exploiting the capabilities of the 'bottom-up' SLA approach.

3.2 MATERIALS AND METHODS

3.2.1 APPARATUS

A stereolithography apparatus (SLA, Model 250/50, 3D Systems, Rock Hill, SC, USA) was used for all experiments. Modifications were made to accommodate for two types of fabrication processes as shown in Fig. 3.1. In the 'top-down' approach, the standard vat and platform were removed to allow for low volume materials, including those containing living cells. A smaller custom-made mini-platform was fabricated and screwed into an aluminum shaft that was clamped to the elevator of the SLA. In the 'bottom-up' approach, the vat was removed and replaced with a 35 mm diameter culture dish. The dish was placed at the center of the platform with an 18 mm^2 cover glass bonded to the bottom to allow the cured hydrogel to temporarily attach to it during processing. This method was used for layering multiple cell types and material compositions in distinct regions of the structure.

3.2.2 CELL CULTURE

NIH/3T3 cells (ATCC, Manassas, VA, USA) were cultured in Dulbecco's modified Eagle's medium (DMEM, Sigma Aldrich, St Louis, MO, USA) containing 4.5 g L^{-1} glucose and supplemented with 10% fetal bovine serum (FBS, Sigma Aldrich, St Louis, MO, USA), 100 U mL^{-1} penicillin, and 100 µg mL^{-1} streptomycin (Gibco, Carlsbad, CA, USA). Cells were incubated in 175 cm^2 flasks (Fisher Scientific, Springfield, NJ, USA) at 37 °C and 5% CO2. Cells grown to pre-confluency were passaged no more than 10 times using 0.25% trypsin and 0.04% EDTA in HBSS (Gibco, Carlsbad, CA, USA). Prior to encapsulation in hydrogels, cells were added to the pre-polymer solution and mixed gently. For multi-cell type layering, cells were split into two separate suspensions and labeled with either CellTracker® CMFDA or CMTMR fluorescent dyes (Molecular Probes, Eugene, OR, USA).

3.2.3 PRE-POLYMER PREPARATION

Poly(ethylene glycol) diacrylates (PEGDAs) of Mw 700 (Sigma Aldrich, St Louis, MO, USA), 3,400, 5,000, and 10,000 Da (Laysan Bio, Arab, AL, USA) were dissolved in DMEM without phenol red (Gibco, Carlsbad, CA, USA) to form a 40% (w/v), or 2X, pre-polymer solution. The photoinitiator, 1-[4-(2-hydroxyethoxy)-phenyl]-2-hydroxy-2-methyl-1-propane-1-one (Irgacure 2959, Ciba, Tarrytown, NY, USA), was dissolved in dimethyl sulfoxide (DMSO, Fisher Scientific, Springfield, NJ, USA) at 50% (w/v) stock solution and added to the 2X pre-polymer solution to form 1.0% (w/v) of photoinitiator. Medium with or without cells and 20% fetal bovine serum (FBS, Sigma Aldrich, St Louis, MO, USA) were added to the pre-polymer solution in a 1:1 volumetric ratio prior to each SLA run. The final pre-polymer solution consisted of 20% (w/v) PEGDA, 0.5% (w/v) photoinitiator, and 10% FBS in DMEM without phenol red. For studies with bioactive groups, RGDS peptide sequences (Arg-Gly-Asp-Ser, Sigma Aldrich, St Louis, MO, USA) were conjugated to acrylate-PEG-NHS (Mw 3500, JenKem Technology, Allen, TX, USA).[15] Acryloyl-PEG-RGDS was added to the pre-polymer solution to make a final concentration of 5 mM RGDS.

3.2.4 Energy dose characterization

0.1% (w/v) fluorescent Nile Red microparticles (0.7-0.9 μm, Spherotech, Lake Forest, IL, USA) were incorporated into the pre-polymer solution at a 1:1000 dilution. The solution was then pipetted into a custom-made container with a thin cover glass on top, in contact with the solution. Samples were cured in the SLA by writing a cross-hatched pattern using a range of laser energy doses (E_{avg}). The energy doses were controlled by varying the laser beam writing speed in the SLA software. After polymerization, the cover glass was lifted off with the polymerized gel layer attached. The thickness of the cured gel (C_d) was then measured using an inverted fluorescent microscope (IX81, Olympus, Center Valley, PA, USA) and IPLab software (BD Biosciences, Rockville, MD, USA). The measured thicknesses were plotted on a semilogarithmic graph as a function of energy dose. Using the working curve equation,

$$C_d = D_p \ln\left(\frac{E_{avg}}{E_c}\right) \tag{3.1}$$

where D_p is the penetration depth and E_c is the critical exposure energy, D_p and E_c were calculated with linear regression analysis software (OriginPro 8.1, OriginLab, Northampton, MA, USA).

3.2.5 SEQUENTIAL LAYER-BY-LAYER HYDROGEL PHOTOPATTERNING

CAD models were generated using AutoCAD 2009 (Autodesk, San Rafael, CA, USA) and exported to stereolithography (STL) format. The SLA software, 3D Lightyear v1.4 (3D Systems, Rock Hill, SC, USA), was used to slice the 3D models into a series of 2D layers from a user-specified thickness. The penetration depth (D_p) and critical exposure energy (E_c) parameters, which are constants specific to a desired pre-polymer solution, were acquired from energy dose characterizations and entered into the SLA software. For the 'top-down' fabrication process, the platform was immersed just below the surface of the pre-polymer solution with or without cells. For the 'bottom-up' fabrication process, the pre-polymer solution with or without cells was pipetted into the culture dish at the correctly characterized volume. The laser was used to selectively crosslink the pre-polymer solution at a precisely calculated energy dose. The elevator controlled by the SLA was lowered by a specified distance, and the part was recoated. The process was repeated until completion of the complex 3D structure. The structure was rinsed several times in the appropriate medium to remove uncrosslinked polymer.

3.2.6 HYDROGEL CHARACTERIZATION

Gel disks fabricated in the SLA were subjected to compression using a mechanical testing system (Insight, MTS Systems, Eden Prairie, MN, USA). The elastic modulus (E) of the gel was measured by compressing at a constant deformation rate of 1.0 mm s^{-1} at 25 °C. From the strain limit to the first 10%, the elastic modulus was calculated using the slope of the stress (σ) vs. strain (λ) curve. Assuming that the gels follow an affined network model, the shear modulus (S) was calculated from the slope of the σ_{vs}. $-(\lambda - \lambda - 2)$ curve, where λ is the ratio of the deformed length to the undeformed length of the hydrogel.[10,29]

The swelling ratios of the gels at equilibrium were determined by measuring the weight of the swollen gels after 24 hours in pH 7.4 buffer solutions at 37 °C and the weight of the dried gels. The degree of swelling (Q), defined as the reciprocal of the volume fraction of a polymer in a hydrogel (v_2), was calculated from the following equation,

$$Q = v_2^{-1} = \rho_P \left(\frac{Q_m}{\rho_S} + \frac{1}{\rho_P} \right) \tag{3.2}$$

where ρ_S was the density of water, ρ_P was the density of polymer , and Q_m was the swelling ratio, the mass ratio of swelled gel to dried gel.

The average pore size (ξ) was calculated from the polymer volume fraction ($v_{2,s}$) and the unperturbed mean-square end-to-end distance of the monomer unit (r_o^{-2}) using Equations (3.3) and (3.4):

$$\xi = \left(v_{2,s}^{-1/3}\right)\left(r_o^{-2}\right)^{1/2} \tag{3.3}$$

$$\left(r_o^{-2}\right) = l\left(2\frac{\overline{M_c}}{M_r}\right)^{1/2} C^{1/2} = l\left(2n\right)^{1/2} C^{1/2} \tag{3.4}$$

where l is the average value of the bond length between C–C and C–O bonds in the repeatable unit of PEG [–O–CH_2–CH_2–], which is taken as 1.46 Å; M_c is the average molecular mass between crosslinks in the network; M_r is the molecular mass of the PEG repeating unit (44 g mol^{-1}); C is the characteristic ratio for PEG, which is taken here as 4.

3.2.7 Cell viability

Cell viability was quantitatively measured using MTS (3-(4,5-dimethylthiazol-2-yl)-5-(3-carboxymethoxyphenyl)-2-(4-sulfophenyl)-2H-tetrazolium, Promega, Madison, WI, USA), a tetrazolium compound which, in the presence of phenazine methosulfate (PMS, Sigma Aldrich, St Louis, MO, USA), is reduced by living cells to yield a water-soluble formazan product. MTS (333 µg mL^{-1}) and PMS (25 µM) were added to the cell-laden hydrogels in DMEM without phenol red in an incubator at 37 °C and 5% CO_2. After incubating for 4 hours, 20% SDS (Fisher Scientific, Springfield, NJ, USA) in sterilized $H2O^{dd}$ was added to stop the reaction. The hydrogels were incubated at 37 °C for 15 hours to allow diffusion of formazan into the medium. The absorbance was measured at 490 nm using a Synergy HT microplate reader (BioTek, Winooski, VT, USA). Viability was qualitatively evaluated in stereomicroscopy using an MTT assay (3-(4,5-dimethylthiazol-2-yl)-2,5-diphenyltetrazolium bromide, Sigma Aldrich, St Louis, MO, USA) by incubating the cell-laden hydrogels in a 10% solution of DMEM without phenol red at 37 °C and 5% CO_2 for 4 hours. Fluorescence microscopy using calcein AM and ethidium homodimer stains was also used for qualitative evaluation (Molecular Probes, Eugene, OR, USA).

3.2.8 Cell spreading

In order to visualize spreading, cell -laden hydrogels were examined every day by bright-field microscopy. After 14 days, cells were fixed using 4% formaldehyde solution (Fisher

Scientific, Springfield, NJ, USA) overnight at room temperature. After washing several times in PBS, the gels were incubated in Triton X-100 (Sigma Aldrich, St Louis, MO, USA) for 20 min and stained with rhodamine phalloidin (Molecular Probes, Eugene, OR, USA) and 4′,6-diamindino-2-phenylindole (DAPI, Sigma Aldrich, St Louis, MO, USA) for 30 minutes at 37 °C. The cells were imaged using an inverted fluorescent microscope (IX81, Olympus, Center Valley, PA, USA).

3.2.9 Statistical analysis

Error bars represent standard deviation, with n=3 for all experiments. Statistical significance was determined using one-way ANOVA followed by Tukey's Multiple Comparison Test ($P < 0.05$).

3.3 Results

3.3.1 Characterization of hydrogels for stereolithography

In order to build complex 3D hydrogels in the SLA with the highest levels of accuracy, two constants, D_p and E_c, need to be precisely determined. The SLA software utilizes these constants in Equation 3.1 to calculate the energy dose (E_{avg}) required to cure a layer of desired thickness (C_d) of that material. If the layer is not cured deeply enough, it will not attach to the layer below it, resulting in delamination. If the layer is cured too greatly, it will distort and reduce part accuracy.[30] In this experiment, the energy dose of the laser was varied to obtain a series of gels with different thicknesses. The thickness of each gel was measured by taking advantage of the transparent property of hydrogels and embedding fluorescent microbeads within each sample. These thicknesses were plotted as a function of energy dose on a semilogarithmic graph to obtain a linear working curve. By rearranging Equation 3.1 in linear form, it becomes apparent that D_p and E_c can be found by taking the slope and y-intercept of that curve, respectively.

The working curves for 20% (w/v) PEGDA with Mw 700, 3,400, and 5,000 Da are shown in Fig. 3.2(a). The R2 values, 0.973 for MW 700 Da, 0.999 for Mw 3,400 Da, and 0.999 for MW 5,000 Da, indicate that the measurements fit the linear regression model extremely well. The average standard deviation of all the layer thickness measurements was ± 11.9 μm. The D_p values, 0.346, 0.258, and 0.231 mm, and E_c values, 40.89, 11.10, 7.17 mJ cm^{-2}, for Mw 700,

3,400, and 5,000 Da, respectively, indicate a decreasing D_p and E_c trend with increasing Mw. To test whether these values were accurate, they were inputted into the SLA software, along with user-specified C_d, to make a new series of gels. As an example, the measured thicknesses for MW 700 Da were comparable to their specified thicknesses (Fig. 3.2(b)), showing very little deviation. As shown in Fig. 3.2(c) and 3.2(d), complex 3D structures prepared from these PEGDA hydrogels were successfully fabricated following the characterization process. For the bottom-up approach, a second characterization step was performed to determine the amount of volume required to cure a layer of specific thickness. This process is described in Fig. 3.3.

3.3.2 Swelling and mechanical properties of hydrogels

The degree of swelling and the mechanical properties of laser-polymerized PEGDA hydrogels were investigated as a function of Mw. At the time of the study, the laser power of the SLA was about 15 mW and the average energy dose used to photopolymerize the gel disks was 1600 mJ cm^{-2}. The swelling ratios (Q) and elastic moduli (E) for 20% (w/v) PEGDA hydrogels with Mw 700, 3,400, 5,000, and 10,000 Da were measured and calculated from these gel disks (Fig. 3.4). As expected, the Q increased and the E decreased with increasing PEG Mw. The swelling ratios were also used to calculate the average pore size of the gel disks as a function of Mw (Table 3.1). The elastic moduli obtained ranged from 4.73 ± 0.46 kPa for Mw 10,000 Da to 503 ± 57 kPa for Mw 700 Da, which covers quite an array of native tissues having similar moduli.[31] Stereomicroscopic images of PEG hydrogels after 24 hour incubation in cell culture medium showed an increase in swelling capacity with increasing Mw (Fig. 3.5).

3.3.3 Cell encapsulation

Cell encapsulation was initially accomplished by using the ‘top-down’ fabrication process, which held all the pre-polymer solution in a stationary container. A 2 mm thick complex 3D structure, which was composed of 20 layers (100 μm per layer), was fabricated using this approach (Fig. 3.6(a)). The distribution of cells embedded within these structures was examined using MTT stain and stereomicroscopy (Fig. 3.6(b)). The purple formazan crystals produced by the viable cells appeared to have an inhomogeneous distribution with more cells being embedded at the bottom of the structure than at the top of it. This was caused by cells that settled toward the bottom of the container due to gravity. To prevent this, the ‘top-down’ approach was altered, and the same complex 3D structure was fabricated using the ‘bottom-up’ fabrication process. In this

approach, the pre-polymer solution containing cells was pipetted into the container one layer at a time. The cells did not have time to settle to the bottom before the layer was cured. As a result, a uniform distribution of cells was achieved throughout the hydrogel, which was evident by the homogeneous distribution of purple formazan crystals (Fig. 3.6(c)). To quantitatively evaluate this, an intensity profile at different regions of the hydrogel was examined and confirmed to be uniform (Fig. 3.6(d)).

3.3.4 CELL VIABILITY

Two methods were used to evaluate long-term cell viability in the SLA: (1) encapsulation in single-layer 3D hydrogels (1 total layer, 1 mm thick per layer), and (2) encapsulation in multi-layer 3D hydrogels (10 total layers, 100 μm thick per layer).

In the first study, NIH/3T3 cells at a density of 2.0×10^6 cells mL^{-1} were encapsulated in 20% PEGDA hydrogels patterned in single-layer disks with dimensions of 1 mm thickness and 5 mm diameter. These disks were cultured over a period of 14 days. To achieve 1 mm thickness, the average energy dose of the laser during polymerization was 1,000 mJ cm^{-2}. Cell viability was quantitatively evaluated using MTS assays. The optical density (OD) measurements obtained from these assays on 1, 4, 7, and 14 days were converted to relative cell viability (%) by normalizing to 0 day (Fig. 3.7).

Cells encapsulated in PEGDA hydrogels with Mw 700 Da survived the initial processing conditions of the SLA , but died within 24 hours of culturing. This was seen with and without 5 mM RGDS functionalization. By increasing the Mw to 3,400 Da, cells survived both the processing and culturing conditions. Viability remained statistically constant through 4 days. Subsequently, there was a decrease in viability to 65.10 ± 9.81% after 7 days and to 47.46 ± 15.39% after 14 days. Adhesive RGDS peptide sequences at 5 mM concentration were chemically linked to PEGDA hydrogels with Mw 3,400 Da to test for any improvement in cell viability and proliferation. This resulted in a 1.6-fold increase in cell numbers after 24 hours, which was maintained over 7 days. The effect of an even greater Mw on cell viability was also evaluated. Cells encapsulated in PEGDA hydrogels with Mw 5,000 Da followed the same trend as that of Mw 3400 Da. Except for an unsustained rise in metabolic activity after 24 hours, the cell viability was relatively steady through 7 days, followed by a decrease in viability to 60.00 ± 0.2% viability after 14 days. This was an improvement over the 14 day viability of PEGDA

hydrogels with Mw 3,400 Da (47.46 ± 15.39%). When 5 mM RGDS was chemically linked to PEGDA hydrogels with Mw 5,000 Da, there was a 1.4-fold increase in cell numbers after 24 hours, which was maintained over 7 days. A significant increase in viability was seen after 14 days for Mw 3,400 and 5,000 Da with RGDS peptide sequences due to high cell spreading, proliferation, and network formation on the exterior of the gels. Cell viability was also related to average pore size in Fig. 3.8. The relative cell viability and proliferation generally increased with increasing average pore size.

Since cell viability in single-layer disks may not be truly representative of viability in complex 3D structures, the second study evaluated cells encapsulated in multi-layer 3D hydrogels over 14 days. RGDS peptide sequences at 5 mM concentration were chemically linked to PEGDA with Mw 5,000 Da for this study. According to Fig. 3.9(a), the cell numbers were increased 1.7-fold after 24 hours, which was maintained through 7 days. By the end of 14 days, 46.44 ± 19.56% of the cells were viable. Distribution of cells in single-layer and multi-layer PEGDA Mw 5,000 Da hydrogels can be seen from stereomicroscopic images of hydrogels subjected to MTT staining (Fig. 3.9(b) and (c)). Although there was a decrease in cell numbers after 14 days compared to 7 days, the distribution of the cells was homogeneous at both time points.

Qualitative LIVE/DEAD cell viability stain was performed during the same time points as the MTS assays. Representative images (Fig. 3.10) showed an increase in the dead cells over later time points, which supported the results of the more quantitative MTS assays. Nevertheless, in all cases except PEGDA Mw 700 Da, the number of live cells was much more abundant than the number of dead ones.

3.3.5 CELL SPREADING

NIH/3T3 cells encapsulated within multi-layer PEGDA hydrogels with Mw 5,000 Da were examined for cell spreading and attachment. Spreading, which involves the active processes of actin polymerization and myosin contraction,[32] is a sign of cell viability and function. Viable cells did not spread in hydrogels without adhesive RGDS peptide sequences. Cells in multi-layer PEGDA hydrogels with RGDS-linked groups (5 mM) were examined in bright-field microscopy and fluorescence microscopy after rhodamine phalloidin (cytoskeleton) and DAPI (nuclei) staining (Fig. 3.11). Cell spreading was clearly seen within hours of incubation and continued

through 14 days. Some of these cells formed 3D connections with other cells in different layers, suggesting network formation.

3.3.6 MULTI-CELL TYPE LAYERING

The concept of incorporating multiple cell types within hydrogels in a spatially predetermined manner was demonstrated by using NIH/3T3 cells. These cells were separated into two suspensions: one labeled with CellTracker® CMFDA (green) fluorescent dye, and the other labeled with CellTracker® CMTMR (red) fluorescent dye. Fig. 3.12 illustrates top- and side-view fluorescent images of a complex 3D structure with overhangs containing two differently labeled cell suspensions. The thickness of each set of layers was uniform and showed minimal mixing. Quantitative results confirmed the distribution of these cells in uniformly distinct layers.

3.4 DISCUSSION

Functional 3D tissues that are designed for individual patients using multi-cellular and multi-material compositions in an automated, high-throughput device will soon be the next generation in tissue engineering. The combination of process-optimized rapid prototyping technologies, such as stereolithography, with novel biomaterials may be one possible path toward this goal.

Cooke *et al*.[25] reported the use of stereolithography for tissue engineering applications by designing biodegradable scaffolds prepared from poly(propylene fumarate) (PPF) and diethyl fumarate (DEF). While this study demonstrated the capability of using photopolymerizable biomaterials in the SLA, cells were not seeded in or on any of these fabricated PPF/DEF structures. Subsequently, Dhariwala *et al*.[26] encapsulated Chinese hamster ovary (CHO) cells in poly(ethylene oxide) (PEO) and poly(ethylene glycol) dimethacrylate (PEGDM) hydrogels. A fluorescence-based LIVE/DEAD assay was used to evaluate cells immediately after polymerization in the SLA, but the results lacked any substantive evidence supporting sustained viability or proliferation. Moreover, the cells were only encapsulated within single layer structures. This study also reported hydrogel samples with an average elastic modulus of 1.116 ± 0.21 kPa, which limits its applications to very soft tissue types.[31] In contrast, our own studies using 20% PEGDA hydrogels with Mw from 700 to 10,000 Da had elastic moduli that varied

from 4.73 ± 0.46 kPa to 503 ± 57 kPa. These values are more suitable for a wider range of tissues.[31] Recently, Arcaute *et al*.[27] demonstrated complex 3D hydrogels in the SLA using low-swelling PEGDM hydrogels with Mw 1,000 Da. Their viability studies were performed with human dermal fibroblasts (HDFs) encapsulated in gel disks for up to 24 hours. Similar to the previous study, these results were short-term and made with single-layers.

In this study, we demonstrated that NIH/3T3 cells encapsulated in both single-layer and multi-layer 3D hydrogels retained long-term viability, proliferation, and spreading over 14 days using the SLA. This is a significant step toward the development of rapid prototyping technologies for cell encapsulation applications. The SLA is advantageous because it allows for precise internal pore structures and defined macroscopic shapes, as well as the potential to control the spatial organization of multi-cellular and material compositions within the complex 3D structure. Studies in literature have investigated the behavior of various multi-cellular cultures within hydrogels. Although the cultures were shown to enhance desired cellular functions and behaviors, there was no real control over the spatial distribution of these cells.[33,34] Other studies have shown more controlled distribution, but with micropatterned 2D surfaces.[35,36] Since native tissues are composed of more than one cell type, the 'bottom-up' SLA fabrication process described in our study can be used to study these multi-cellular cultures in defined 3D patterns.

The 'bottom-up' approach in the SLA also allowed us to use a variety of material compositions within the same structure for engineering the physical properties of the 3D matrix. It is now well-established that intrinsic mechanical properties of substrates have significant influences on the behavior of both somatic and stem cells in terms of development, differentiation, disease, and regeneration.[31,37] The promising results from these 2D experiments have given rise to new studies attempting to spatially control the physical properties in 3D. In a recent study, this was accomplished by sequential cross-linking of hyaluronic acid (HA) hydrogels using addition reactions and mask-based photoinitiated crosslinking. The result was a difference in mechanical properties stemming from variations in the crosslinking densities.[38] When a similar setup was used for stem cell encapsulation, cells with different morphologies on different regions of the hydrogel were obtained.[39] The fabrication process in our study may offer such control not only by varying the crosslinking density in different regions of the same material, but also by enabling the use of various types and concentrations of materials.

All PEGDA hydrogels tested in this study, except for Mw 700 Da, showed long-term viability for cells encapsulated over 14 days. The reason for poor viability in PEGDA with Mw 700 Da was most likely due to low degrees of swelling caused by small pore sizes. This restricted the diffusion of oxygen and nutrients into the inner core of the hydrogels. When PEGDA was functionalized with 5 mM RGDS at higher Mw, cells were not only viable, but they also spread and proliferated. Proliferation was observed through 7 days, followed by a decrease in the cell numbers after 14 days. A similar result was obtained when smooth muscle cells were encapsulated in RGDS-functionalized PEGDA hydrogels with Mw 3400 Da using bulk UV exposure.[40] Although there was a severe decrease in the initial cell viability after 24 hours, the same increasing trend in cell numbers were observed after 7 days. The initial decrease in their viability could have been due to cell damage caused by bulk polymerization conditions, such as the photoinitiator concentration, UV exposure time, and presence of organic solvents. The elastic modulus of the hydrogels produced from 20% PEGDA with Mw 3400 Da in the study by Peyton *et al*.[40] was approximately 400 kPa, while the modulus in our study was approximately 17 kPa. This discrepancy could be due to variations in the polymerization process or even the method of measurement. The advantage of the SLA process is its precise control over the average energy dose, which can limit the adverse effects to cells.

In general, PEG hydrogels have many attractive properties, including excellent biocompatibility and hydrophilicity. Even though PEG is an inert molecule, cell -surface recognition sites can be chemically tailored to it in a controllable manner.[40] During SLA fabrication of multi-layer 3D hydrogels, the first and last layers of the 10-layer structure were made without RGDS, while the middle layers were made with RGDS. While this was done to prevent cell growth at the exterior of the hydrogels, it also demonstrates the ability to spatially organize bioactive molecules in multi-layer 3D structures. The addition of these adhesive molecules or other types of molecules regulating cell function into distinct layers can easily be achieved by using the 'bottom-up' fabrication method in the SLA.

It should be noted that the PEG hydrogels used in this study were not biodegradable, which could have prevented further cell proliferation and extensive network formation. This may have been the reason for the decrease in cell viability after 14 days. Future studies can incorporate biodegradable matrix molecules or sequences within the hydrogels during the SLA process. Another reason for the decrease in cell viability after 14 days may have been the

constraints caused by low nutrient and waste transport in the hydrogels. Although PEG hydrogels used in our studies had high enough porosity for the diffusion of small molecules up to 22 kDa,[11] including oxygen and glucose, MTT staining after 14 days suggested problems caused by diffusion because there were more cells located at the periphery than at the middle of the hydrogels. This effect was only seen in long-term cultures. A possible explanation may be the diffusion restrictions caused by larger molecules like ECM components secreted by the cells building up around the cells that were secreting them, thereby causing a decrease in the diffusion of smaller Mw compounds. These issues can be overcome by providing degradable units in the PEG hydrogels. There are different methods reported in literature to render PEG degradable by including short peptides in its backbone for enzymatic cleavage by the encapsulated cells[41] or by making a copolymer with a hydrolytically degradable polymer like PLA[8]. A recent study supported this discussion by showing that SMCs and mesenchymal stem cells encapsulated in enzymatically degradable PEG possessed high cell spreading, network formation, and expression of matrix metalloproteinases for up to 21 days in culture.[41] Therefore, providing degradability in the hydrogels and combining that with our current technology could be the next step forward.

3.5 CONCLUSION

A custom-modified SLA was used to fabricate complex 3D structures from photopolymerizable PEG hydrogels to accommodate for two fabrication methods: (1) the 'top-down' approach, which employs a process similar to the conventional SLA, and (2) the 'bottom-up' approach, which allows for multiple types of cells and polymers to be arranged in their own layers within a structure. NIH/3T3 cells were successfully encapsulated within these structures, and by increasing the Mw of PEG and covalent linkage of bioactive RGDS groups, the cell viability, proliferation, and spreading were greatly improved over 14 days. The variation in PEG Mw also established the ability to tune the elasticity of the hydrogel to specific tissue types without sacrificing viability. The SLA is an enabling tool with excellent spatial control that can potentially be used to recapitulate the complex 3D hierarchy of the tissue microenvironment. This may have significant impact on driving the development of in vitro 3D models toward broader applications, including those in tissue engineering, cell mechanics, and bio-hybrid artificial devices and machines.

3.6 ACKNOWLEDGMENTS

This project was made possible by a cooperative agreement that was awarded and administered by the US Army Medical Research & Materiel Command (USAMRMC) and the Telemedicine & Advanced Technology Research Center (TATRC), under Contract #: W81XWH0810701.

3.7 REFERENCES

1. E. J. Suuronen, H. Sheardown, K. D. Newman, C. R. McLaughlin and M. Griffith, Building in vitro models of organs, *Int. Rev. Cytol.*, 2005, 244, 137–173.

2. J. L. Drury and D. J. Mooney, Hydrogels for tissue engineering: scaffold design variables and applications, *Biomaterials*, 2003, 24(24), 4337–4351.

3. B. V. Slaughter, S. S. Khurshid, O. Z. Fisher, A. Khademhosseini and N. A. Peppas, Hydrogels in regenerative medicine, *Adv. Mater.*, 2009, 21, 3307–3329.

4. C. C. Lin and K. S. Anseth, PEG hydrogels for the controlled release of biomolecules in regenerative medicine, *Pharm. Res.*, 2009, 26(3), 631–643.

5. D. L. Hern and J. A. Hubbell, Incorporation of adhesion peptides into nonadhesive hydrogels useful for tissue resurfacing, *J. Biomed. Mater. Res.*, 1998, 39, 266–276.

6. B. K. Mann, A. S. Gobin, A. T. Tsai, R. H. Schmedlen and J. L. West, Smooth muscle cell growth in photopolymerized hydrogels with cell adhesive and proteolytically degradable domains: synthetic ECM analogs for tissue engineering, *Biomaterials*, 2001, 22, 3045–3051.

7. E. A. Phelps, N. Landázur, P. M. Thule, R. Taylor and A. J. García, Bioartificial matrices for therapeutic vascularization, *Proc. Natl. Acad. Sci. U. S. A.*, 2010, 107(8), 3323–3328.

8. T. Metters, K. S. Anseth and C. N. Bowman, Fundamental studies of a novel, biodegradable PEG-b-PLA hydrogel, *Polymer*, 2000, 41, 3993–4004.

9. J. L. West and J. A. Hubbell, Polymeric biomaterials with degradation sites for proteases involved in cell migration, *Macromolecules*, 1999, 32, 241–244.

10. G. P. Raeber, M. P. Lutolf and J. A. Hubbell, Molecularly engineered PEG hydrogels: a novel model system for proteolytically mediated cell migration, *Biophys. J.*, 2005, 89, 1374–1388.

11. G. M. Cruise, D. S. Scharp and J. A. Hubbell, Characterization of permeability and network structure of interfacially photopolymerized poly(ethylene glycol) diacrylate hydrogels, *Biomaterials*, 1998, 19(14), 1287–1294.

12. J. L. Ifkovits and J. A. Burdick, Review: photopolymerizable and degradable biomaterials for tissue engineering applications, *Tissue Eng.*, 2007, 13(10), 2369–2385.

13. Y. Du, E. Lo, S. Ali and A. Khademhosseini, Directed assembly of cell-laden microgels for fabrication of 3D tissue constructs, *Proc. Natl. Acad. Sci. U. S. A*., 2008, 105(28), 9522–9527.

14. M. S. Hahn, J. S. Miller and J. L. West, Three-dimensional biochemical and biomechanical patterning of hydrogels for guiding cell behavior, *Adv. Mater*., 2006, 18, 2679–2684.

15. V. L. Tsang, A. A. Chen, L. M. Cho, K. D. Jadin, R. L. Sah and S. DeLong, *et al.*, Fabrication of 3D hepatic tissues by additive photopatterning of cellular hydrogels, *FASEB J*., 2007, 21(3), 790–801.

16. V. L. Tsang and S. N. Bhatia, Fabrication of three-dimensional tissues, *Adv. Biochem. Eng./Biotechnol*., 2006, 103, 189–205.

17. S. M. Peltola, F. P. Melchels, D. W. Grijpma and M. Kellomäki, A review of rapid prototyping techniques for tissue engineering purposes, *Ann. Med*., 2008, 40(4), 268–280.

18. J. J. Pancrazio, F. Wang and C. A. Kelley, Enabling tools for tissue engineering, *Biosens. Bioelectron*., 2007, 22(12), 2803–2811.

19. M. Rücker, M. W. Laschke, D. Junker, C. Carvalho, F. Tavassol and R. Mülhaupt, *et al.*, Vascularization and biocompatibility of scaffolds consisting of different calcium phosphate compounds, *J. Biomed. Mater. Res., Part A*, 2008, 86a(4), 1002–1011.

20. R. Yao, R. J. Zhang, Y. N. Yan and X. H. Wang, In vitro angiogenesis of 3D tissue engineered adipose tissue, *J. Bioact. Compat. Polym*., 2009, 24(1), 5–24.

21. P. Yang, C. Wang, Z. Shi, X. Huang, X. Dang and S. Xu, *et al*., Prefabrication of vascularized porous three-dimensional scaffold induced from rhVEGF(165): a preliminary study in rats, *Cells Tissues Organs*, 2009, 189(5), 327–337.

22. E. A. Silva and D. J. Mooney, Effects of VEGF temporal and spatial presentation on angiogenesis, *Biomaterials*, 2010, 31(6), 1235–1241.

23. K. Kyriakidou, G. Lucarini, A. Zizzi, E. Salvolini, M. M. Belmonte and F. Mollica, *et al*., Dynamic co-seeding of osteoblast and endothelial cells on 3D polycaprolactone scaffolds for enhanced bone tissue engineering, *J. Bioact. Compat. Polym*., 2008, 23(3), 227–243.

24. K. F. Leong, C. K. Chua, N. Sudarmadji and W. Y. Yeong, Engineering functionally graded tissue engineering scaffolds, *J. Mech. Behav. Biomed. Mater*., 2008, 1(2), 140–152.

25. M. N. Cooke, J. P. Fisher, D. Dean, C. Rimnac and A. G. Mikos, Use of stereolithography to manufacture critical-sized 3D biodegradable scaffolds for bone ingrowth, *J. Biomed. Mater. Res*., 2003, 64b(2), 65–69.

26. B. Dhariwala, E. Hunt and T. Boland, Rapid prototyping of tissue-engineering constructs, using photopolymerizable hydrogels and stereolithography, *Tissue Eng*., 2004, 10(9/10), 1316–1322.

27. K. Arcaute, B. K. Mann and R. B. Wicker, Stereolithography of three-dimensional bioactive poly(ethylene glycol) constructs with encapsulated cells, *Ann. Biomed. Eng.*, 2006, 34(9), 1429–1441.

28. G. Mapili, Y. Lu, S. Chen and K. Roy, Laser-layered microfabrication of spatially patterned functionalized tissue-engineering scaffolds, *J. Biomed. Mater. Res., Part B*, 2005, 75(2), 414–424.

29. C. Chu, B. W. Schaefer, R. J. DeVolder and H. J. Kong, Quantitative analysis of the cross-linked structure of microgels using fluorescent probes, *Polymer*, 2009, 50, 5288–5292.

30. D. E. Discher, P. Janmey and Y. L. Wang, Tissue cells feel and respond to the stiffness of their substrate, *Science*, 2005, 310(5751), 1139–1143.

31. H. Nguyen, J. Richter, P. F. Jacobs, On Windowpanes and Christmas Trees: Diagnostic Techniques for Improved Part Accuracy, in *Proc. 1st Eur. Conf. Rapid Prototyping*, ed. P. M. Dickens, University of Nottingham, Nottingham, 1992, pp. 133–161.

32. J. McGrath, Cell spreading: the power to simplify, *Curr. Biol.*, 2007, 17(10), R357–R358.

33. H. N. Yang, J. S. Park, K. Na, D. G. Woo, Y. D. Kwon and K. H. Park, The use of green fluorescence gene (GFP)-modified rabbit mesenchymal stem cells (rMSCs) co-cultured with chondrocytes in hydrogel constructs to reveal the chondrogenesis of MSCs, Biomaterials, 2009, 30(31), 6374–6385.

34. X. T. Mo, S. C. Guo, H. Q. Xie, L. Deng, W. Zhi and Z. Xiang, *et al.*, Variations in the ratios of co-cultured mesenchymal stem cells and chondrocytes regulate the expression of cartilaginous and osseous phenotype in alginate constructs, Bone, 2009, 45(1), 42–51.

35. S. A. Lee, S. E. Chung, W. Park, S. H. Lee and S. Kwon, Three-dimensional fabrication of heterogeneous microstructures using soft membrane deformation and optofluidic maskless lithography, Lab Chip, 2009, 9(12), 1670–1675.

36. J. Fukuda, A. Khademhosseini, Y. Yeo, X. Yang, J. Yeh and G. Eng, *et al.*, Micromolding of photocrosslinkable chitosan hydrogel for spheroid microarray and co-cultures, Biomaterials, 2006, 27(30), 5259–5267.

37. A. J. Engler, S. Sen, H. L. Sweeney and D. E. Discher, Matrix elasticity directs stem cell lineage specification, Cell, 2006, 126(4), 677–689.

38. S. Khetan, J. S. Katz and J. A. Burdick, Sequential crosslinking to control cellular spreading in 3-dimensional hydrogels, Soft Matter, 2009, 5, 1601–1606.

39. R. A. Marklein and J. A. Burdick, Spatially controlled hydrogel mechanics to modulate stem cell interactions, Soft Matter, 2010, 6, 136–143.

40. S. R. Peyton, C. B. Raub, V. P. Keschrumrus and A. J. Putnam, The use of poly(ethylene glycol) hydrogels to investigate the impact of ECM chemistry and mechanics on smooth muscle cells, Biomaterials, 2006, 27(28), 4881–4893.

41. C. Adelöw, T. Segura, J. A. Hubbell and P. Frey, The effect of enzymatically degradable poly(ethylene glycol) hydrogels on smooth muscle cell phenotype, Biomaterials, 2008, 29(3), 314–326.

3.8 FIGURES AND CAPTIONS

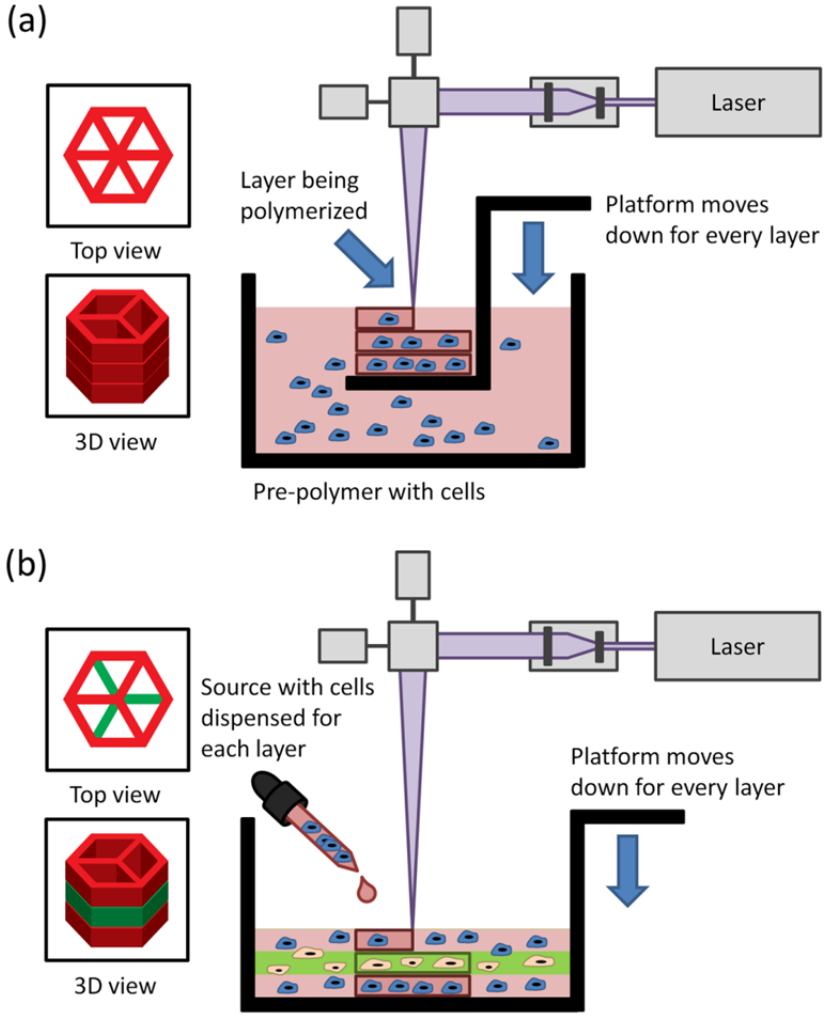

Fig. 3.1 | A schematic representation of the SLA modifications. (**a**) In the top-down approach, the layout consists of a platform immersed just below the surface of a large tank of pre-polymer solution. After the layer is photopolymerized, the platform is lowered a specified distance to recoat the part with a new layer. (**b**) In the bottoms-up approach, the pre-polymer solution is pipetted into the container one layer at a time from the bottom to the top. This setup was modified especially for cell encapsulation applications, which required: (1) reduction in total volume of photopolymer in use, and (2) removal of photopolymer from static conditions that cause cells to settle.

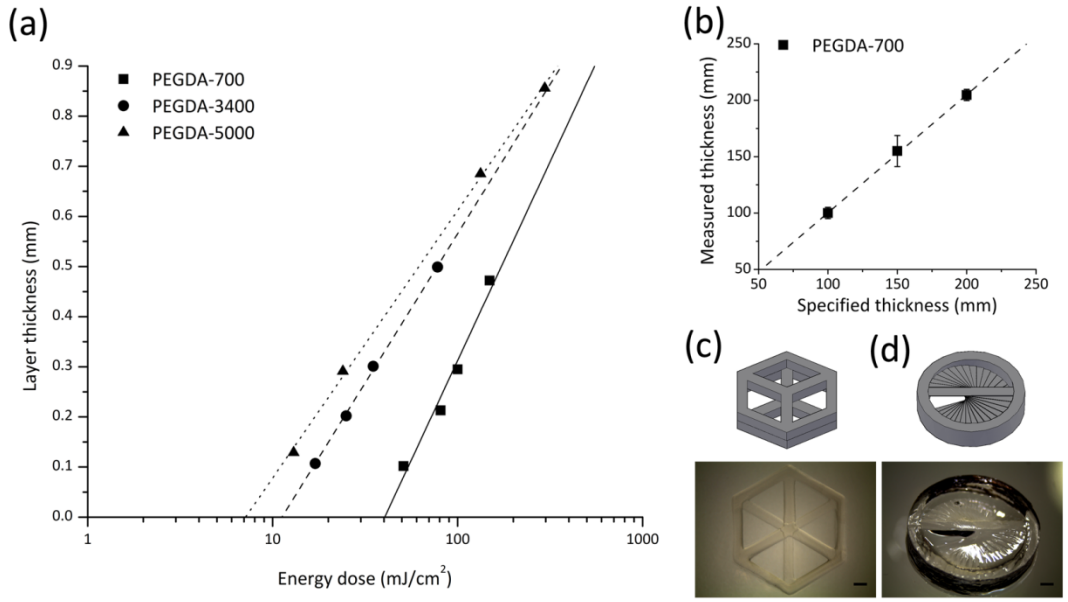

Fig. 3.2 | Fabrication of complex 3D hydrogels in the SLA. (**a**) Characterization of the laser energy dose required to cure 20% PEGDA hydrogels with M_W 700, 3,400, and 5,000 Da. (**b**) Example test of D_p and E_c parameters found in (a) for M_W 700 Da. (**c and d**) CAD drawings and actual images of complex 3D hydrogels prepared from M_W 700 Da and fabricated in the bottoms-up SLA modification. All experiments used 0.5% photoinitiator concentration. Scale bars are 1 mm.

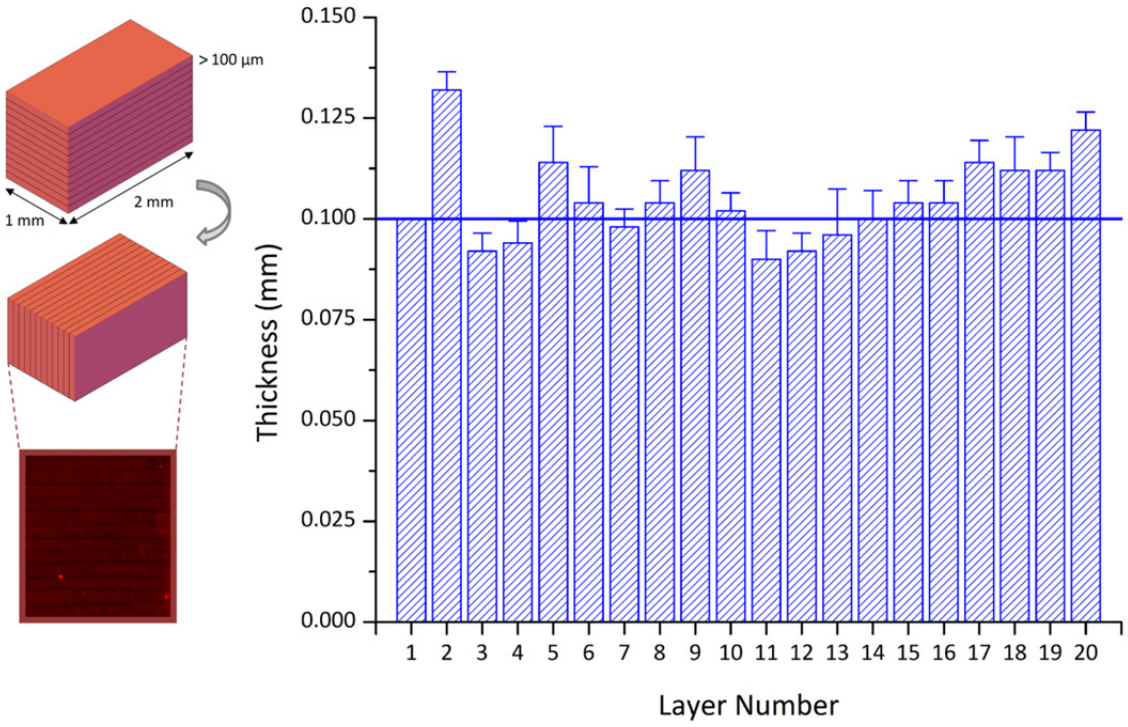

Fig. 3.3 | Volume deposition characterization. For all multi-layer experiments utilizing the bottoms-up approach, the thickness of each layer was, on average, 100 µm. In order to do this, the volume had to be calibrated precisely for each layer due to surface tension between the walls of the container and the pre-polymer solution. 1 X 2 mm blocks were built in the SLA with embedded fluorescent microbeads. Each block had up to 20 layers. The thickness of each layer was measured by tipping the block on its side and visualizing in fluorescence microscopy. ImageJ analysis software was used to determine the thickness. The volume was then adjusted until the average of all layers reached 100 µm. All values are mean ± standard deviation of n = 10.

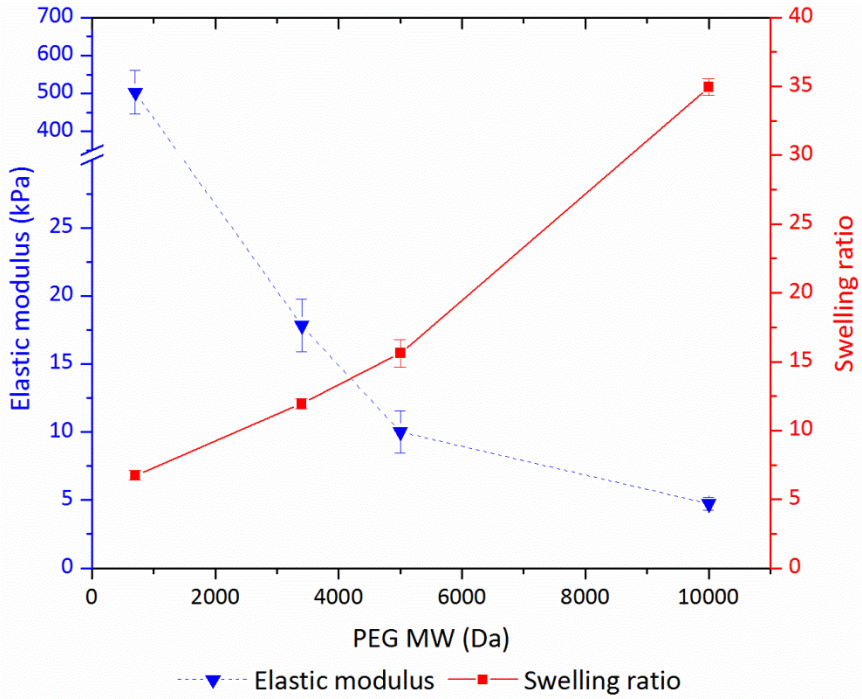

Fig. 3.4 | Mechanical properties and swelling of hydrogels. The elastic moduli (E, left axis) and swelling ratios (Q, right axis) were measured and calculated for 20% PEGDA hydrogels as a function of M_W (700, 3,400, 5,000, and 10,000 Da). All experiments used 0.5% photoinitiator concentration.

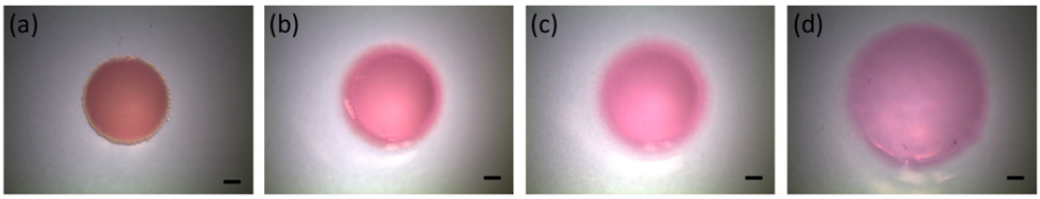

Fig. 3.5 | Swelling of hydrogels as a function of Mw. 20% PEGDA hydrogels with MW (**a**) 700, (**b**) 3,400, (**c**) 5,000, and (**d**) 10,000 Da were used to make disks with a diameter of 5 mm in the SLA. The gel disks were incubated in culture medium for 24 hours at 37^{o}C before imaging in the stereomicroscope. The diameter of the gel disks increased as a function of increasing M_W. Scale bars are 1 mm.

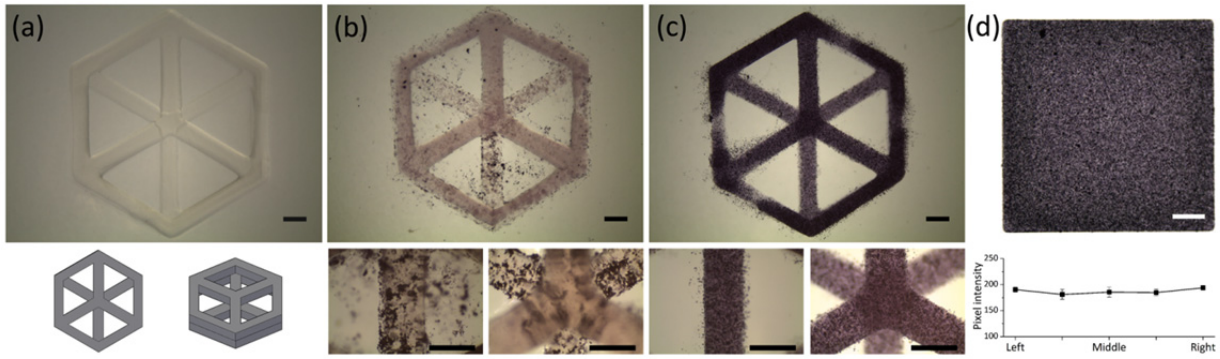

Fig. 3.6 | Encapsulation of NIH/3T3 cells in hydrogels. (**a**) Fabrication of a 2 mm thick complex 3D structure composed of 20 layers (with CAD images). Two approaches were used to encapsulate 10 x 10^6 cells/mL: (**b**) top-down and (**c**) bottoms-up SLA modifications. Cells were immediately stained with MTT (over 4 hours) for visualization. In the top-down approach, cells settled to the bottom of the container and did not encapsulate well. In the bottoms-up approach, cells and pre-polymer were added before polymerization of each layer, which led to homogeneous and high cell densities. (**d**) Intensity measurements of an MTT stain quantitatively showed homogeneity throughout the structure immediately after encapsulation. Scale bars are 1 mm.

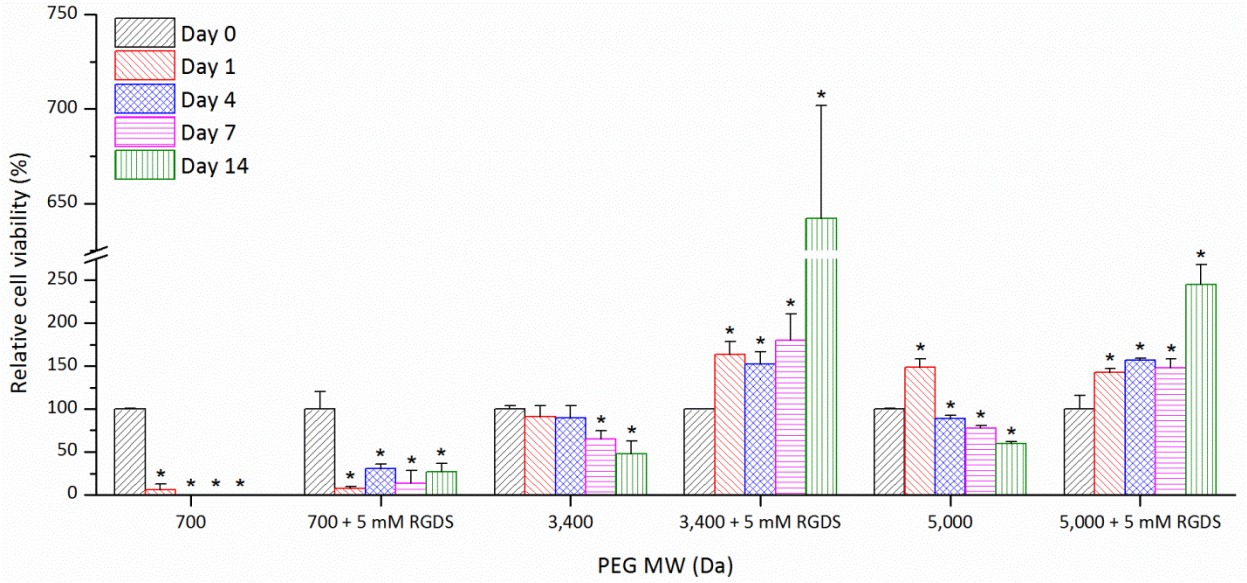

Fig. 3.7 | NIH/3T3 cell viability over 14 days in single-layer approach. The Mw of PEGDA hydrogels were varied using 700, 3,400, and 5,000 ± RGDS groups. OD (490 nm) values quantified by MTS assays were normalized to 0 day. All values are mean ± standard deviation of n = 3. (*) denotes statistical difference compared to 0 day of same M_W.

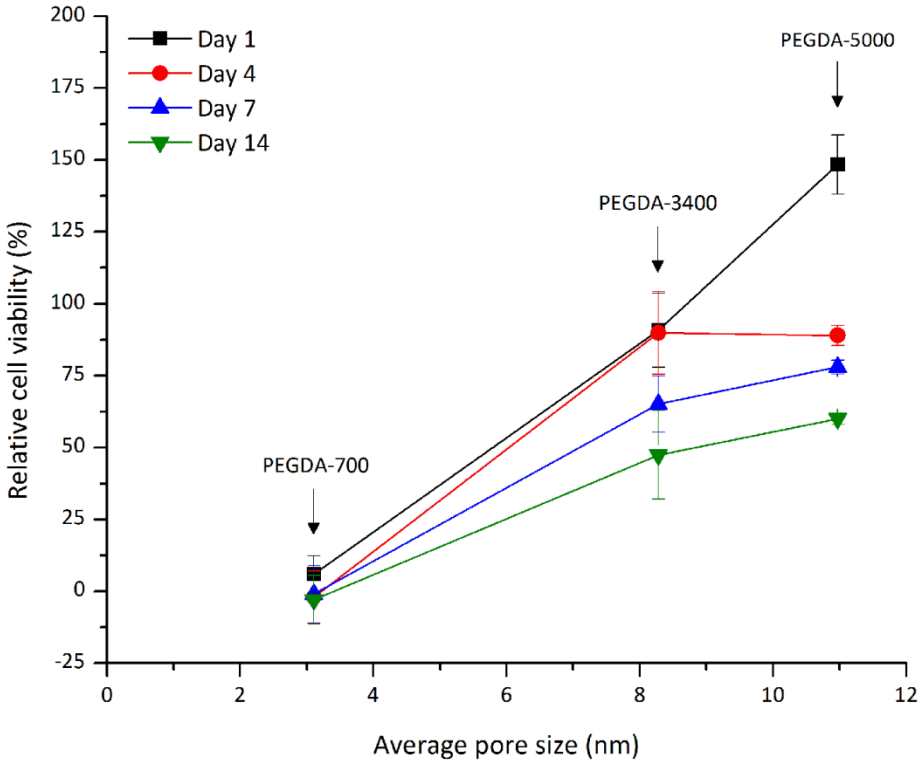

Fig. 3.8 | Effect of average pore size on cell viability. The relative cell viability and proliferation generally increased with increasing average pore size. It is well-known that larger pore sizes increase the diffusion of oxygen, nutrients, and waste into and out of the cell-embedded gels. Larger pore sizes also remove the photoinitiator compounds and its free radical by-products out of the gel quicker, thereby increasing initial cell viability. Additionally, cell spreading and protein synthesis/secretion is improved in higher chain length gels, even in the absence of adhesion peptides.

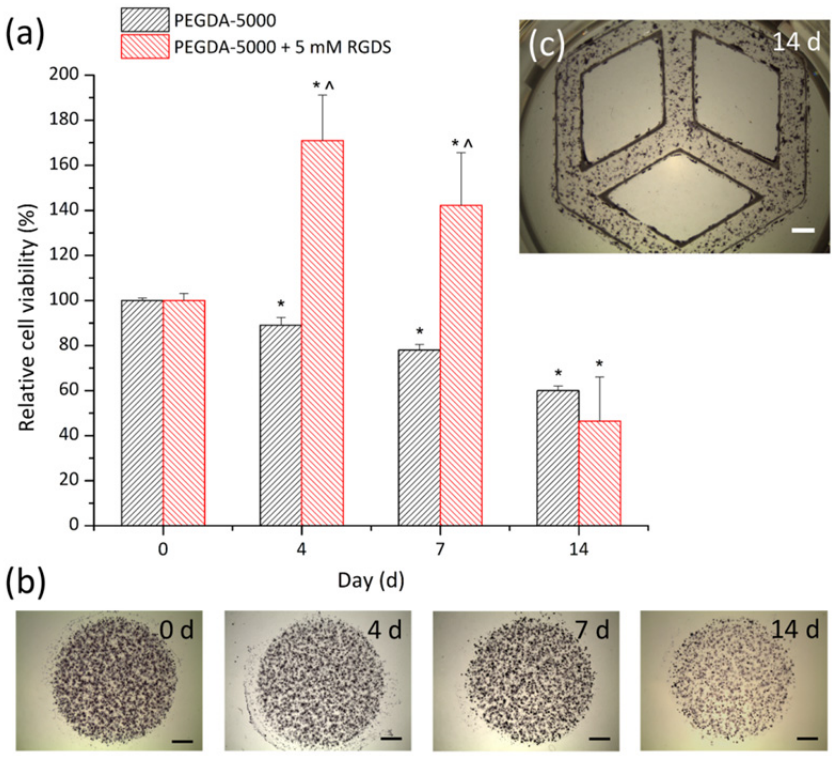

Fig. 3.9 | NIH/3T3 cell viability over 14 days in multi-layer approach. The Mw of PEGDA hydrogels were varied using Mw 5,000**.** (**a**) OD (490 nm) values quantified with MTS assay were normalized to Day 0. All values are mean ± standard deviation of n = 3. (*) denotes statistical difference compared to 0 day of same approach. (^) denotes statistical difference compared to different approach of same day. (**b**) MTT staining that shows living cells in a patterned multi-layer PEGDA hydrogel with M_W 5,000 Da after 14 days. (**c**) MTT staining that shows living cells in single-layer PEGDA hydrogel disks with M_W 5,000 Da after 0, 4, 7, and 14 days. There is a noticeable difference in intensity after 14 days. Scale bars are 1 mm.

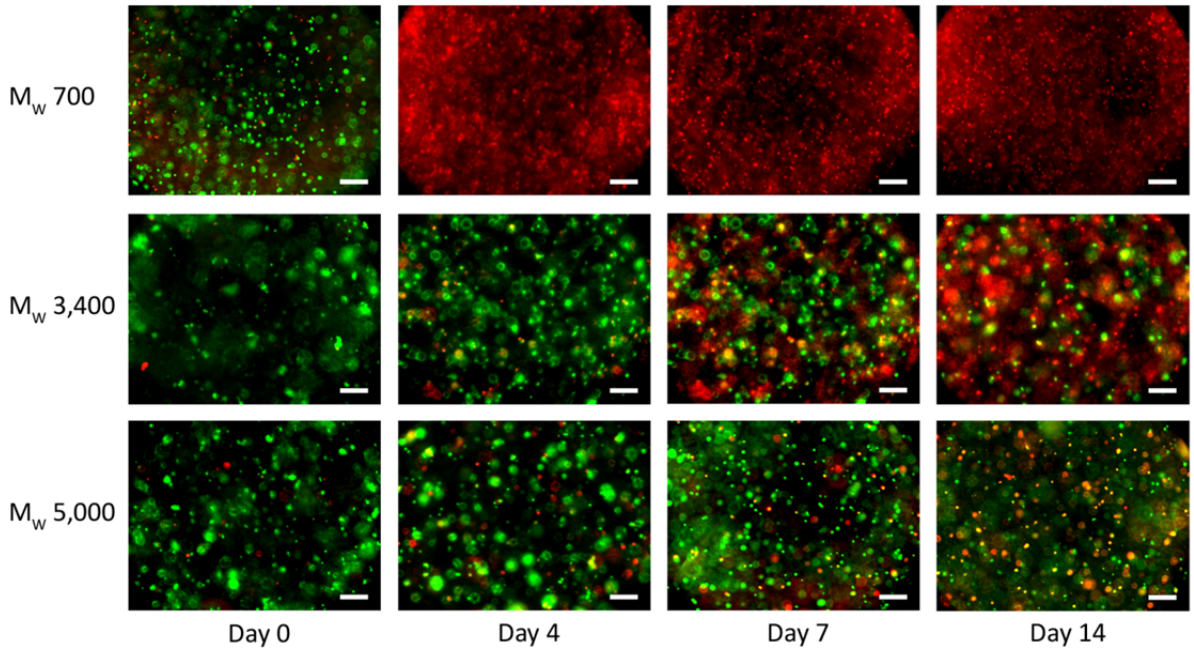

Fig. 3.10 | Qualitative LIVE/DEAD staining of PEGDA hydrogels. NIH/3T3 cells were encapsulated in laser-polymerized 20% PEGDA hydrogels at a density of 1 X 10^6 cells/mL and cultured over 14 days. Viability was evaluated at 0, 4, 7, and 14 days using calcein AM and ethidium homodimer in fluorescence microscopy. Green indicates live cells and red indicates dead cells. Scale bars are 200 μm.

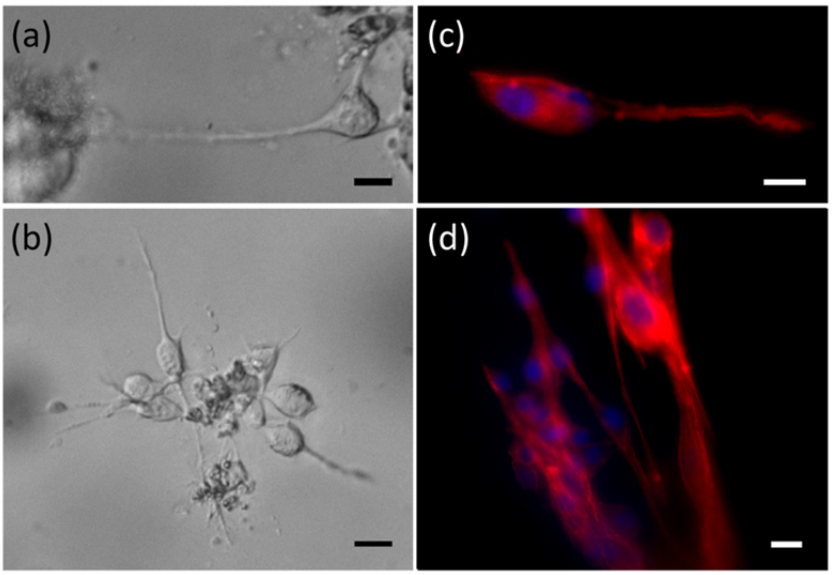

Fig. 3.11 | NIH/3T3 cells spreading in hydrogels containing bioactive RGDS groups. Single and clustered cells were clearly seen spreading in patterned multi-layer PEGDA hydrogels with M_W 5,000 Da. These hydrogels were tailored with bioactive RGDS groups at a concentration of 5 mM. (**a**) and (**b**) Bright-field and (**c**) and (**d**) fluorescence microscopy images of the cells were taken after 14 days. For fluorescence microscopy, cells were fixed and stained with rhodamine phalloidin (cytoskeleton) and DAPI (nuclei). Scale bars are 20 μm.

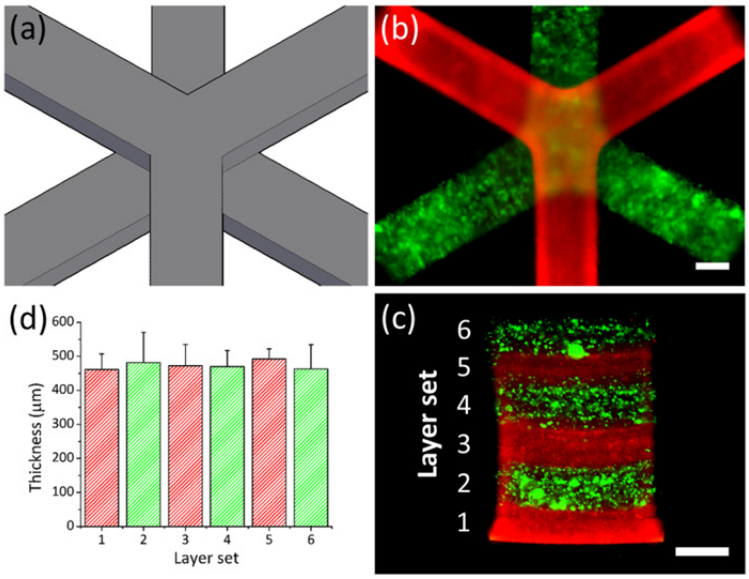

Fig. 3.12 | Spatial 3D layer-by-layer cell patterning of viable cells at distinct layers. (**a**) CAD rendering of cross-hatch pattern used for layer-by-layer spatial patterning. Each layer set was 1 mm thick (10 total layers, 100 μm each). (**b**) Fluorescence image of NIH/3T3 cells encapsulated on different layer sets stained with either CellTracker$^{(R)}$ CMFDA (green) dye or CMTMR (orange) dye. (**c**) Cross-sectional view of a block pattern consisting of alternating layer sets (5 total layers, 100 μm each). (**d**) Quantitative analysis of (c) showing layer sets comparable to the desired 500 μm thickness. All values are mean ± standard deviation of n = 4. Scale bars are 1 mm.

PEG M_W (Da)	Pore size (nm)
700	3.105
3,400	8.280
5,000	10.973
10,000	20.340

Table 3.1 | Calculated average pore size of PEGDA hydrogels as a function of Mw. The average pore size of 20% PEGDA hydrogels with M_W 700, 3,400, 5,000, and 10,000 Da were calculated from values obtained by measuring the swelling ratios of gel disks with a diameter of 5 mm. The pore size increased as a function of increasing M_W.

CHAPTER 4: BIOLOGICAL ACTUATORS

4.1 INTRODUCTION

Cell-based biohybrid actuators are integrated systems that employ elements of biology to power synthetic structures. The biological and synthetic components have a dependent relationship, which pass information in one or both directions; this direct interaction forms a 'biohybrid' system. For example, cells are able to sense the mechanical properties of the substrate they are grown on and respond through biological functions such as migration, differentiation, or proliferation.[1] Driven by cells, biohybrid actuators can be autonomous, or controlled chemically or electrically. Using glucose as a chemical energy source, cells can generate power by converting it to mechanical energy. These systems could be used to promote the design of more effective and intelligent bio-machines (*i.e.* bio-bots[2–4] and power generators[5]), help us understand the emergent behavior of cellular systems, and have applications in drug discovery.

Significant progress in developing cell-based biohybrid actuators has recently been reported. Contractile stresses and forces of single cells and cell sheets of cardiomyocytes and skeletal myotubes cultured on silicon[6] and PDMS[7] micro-cantilevers have been measured. Xi *et al.*[2] developed a microdevice using a silicon backbone with self-assembled cardiomyocytes grown on a chromium/gold layer. The collective and cooperative contraction of the cells caused the backbone to bend and stretch in a walking motion, which traveled at a maximum speed of 38 μm s^{-1}. Kim *et al.*[3] established a swimming microrobot by micromolding PDMS. Using cardiomyocytes, cells were seeded on top of four conjoined cantilever beams that were grooved to influence the alignment and enhance their contractility relative to flat beams. An increase in force (88%) and bending (40%) was recorded, with an average swimming speed of 140 μm s^{-1}. Feinberg *et al.*[4] assembled cardiomyocytes on various PDMS thin films with proteins to create muscular thin films. When released, these thin films curled or twisted into 3D conformations that purportedly performed gripping, pumping, walking (133 μm s^{-1}), and swimming functions (400 μm s^{-1}).

However, progress in developing cell-based biohybrid actuators has been limited to rigid materials, ranging in elastic moduli on the order of mega (10^6) to giga (10^9) Pascals. Recent reports in the literature have established a correlation between substrate rigidity and its influence

on the contractile behavior of cardiomyocytes.[8-11] These studies show that cardiomyocytes cultured on hard substrates overstrain themselves, lack striated myofibrils, and stop beating. Conversely, substrates showing a close correspondence to tissue elasticity (10 kPa) are optimal for transmitting contractile work to the substrate and for longer periods of time.[8] Therefore, it is worthwhile to explore and evaluate more compliant cantilevers with tissue-like elasticity on the order of kilo (10^3) Pascals, and subsequently measure the contractile stresses and forces of cardiomyocytes on these devices.

While its mechanical properties can easily be altered in the kilo (10^3) Pascal range[12–14] by changing the monomer-to-curing agent mixing ratio, functionalization of PDMS-based substrates for cell adhesion is challenging.[15] This can be attributed to its chemical inertness, hydrophobicity, and high chain mobility. In particular, chain mobility is probably the key limiting factor in modifying PDMS; surface treatments lead to unstable and short-lived oxidized layers.[16] Thus, physical adsorption is relatively inefficient and transient on PDMS. Furthermore, PDMS-based microfabrication requires master molds patterned by photolithography with SU-8 photoresist and silicon. This conventional photolithography process requires clean room facilities and costly equipment, which limits the complexity of multi-layer constructs and the ability to make changes quickly and cheaply.

In contrast, poly(ethylene glycol) (PEG) is a synthetic polymer that has tissue-like elasticity, which can be fine-tuned by changing its molecular weight or percent composition.[17] PEG-based hydrogels are hydrophilic and can be functionalized by activating with Sulfo-SANPAH and conjugating with full-length ECM molecules.[18] Cell adhesion domains,[19,20] growth factors,[21] and hydrolytic[22] and proteolytic sequences[23,24] can also be incorporated directly into the PEG backbone. Additionally, PEG is highly permeable to oxygen, nutrients, and other water-soluble metabolites. This is especially advantageous for cell-encapsulated, three-dimensional (3D) model systems. PEG-based hydrogels can be photopolymerized with a UV laser or lamp based on 3D CAD images; thus, complex 3D geometries can be formed through direct exposure.

This study uses a 3D stereolithographic printer to rapidly fabricate multi-material hydrogel cantilevers with varying stiffness. A stereolithography apparatus (SLA) is a rapid prototyping tool[25,26] used to produce three-dimensional (3D) models, prototypes, and patterns by repetitive deposition and processing of individual layers.[27,28] It uses a UV laser (325 nm) to directly write on and polymerize photosensitive liquid materials based on a CAD-designed

digital blueprint, sliced into a collection of two-dimensional (2D) cross-sectional layers, and processed into a real 3D part using layer-by-layer deposition. The automated, high-throughput process is particularly useful for biohybrid systems due to its multi-material capability, which can be used to change the synthetic material composition or insert cells or proteins at precise locations on the structure.[29] It has recently been adapted for use with photopolymerizable hydrogels,[30,31] which are highly hydrated and crosslinked polymer networks. The SLA is particularly useful for testing biohybrid actuator designs because of the ease in changing the dimension and shapes quickly and producing new ones to seed cardiomyocytes on. The aim of this paper is to incorporate acrylic-PEG-collagen into photopolymerizable PEGDA hydrogels (PEGDA-PC) to create cantilevers in the SLA that can be used to measure contractile forces at different stiffnesses and to see how those stiffnesses affect the contractility of cardiomyocytes for the design of cell -based biohybrid actuators.

4.2 Materials and Methods

4.2.1 Apparatus and preparation of pre-polymer solution

A commercial stereolithography apparatus (SLA, Model 250/50, 3D Systems, Rock Hill, SC, USA) was modified for the fabrication of biohybrid cantilevers. The modification employed an additive "bottom-up" method as previously described.[31] The laser wavelength was in the UV-A region (325 nm) with a 250 μm beam diameter at the set focal plane. The platform had a minimum Z-step of 50 μm. Acrylic-PEG-collagen was prepared by mixing a working solution of acrylic-PEG-NHS (50 mg mL^{-1} in ice cold HBSS) with collagen I (3.68 mg mL^{-1}, rat tail; BD Biosciences) at a 1:1 acryl-to-lysine molar ratio for 30 minutes at 4 °C. A 50% (v/v) acrylic-PEG-collagen solution was mixed with 20% poly(ethylene glycol) diacrylate (PEGDA) and 0.5% Irgacure 2959 photoinitiator in ice cold HBSS to form the pre-polymer solution. The PEGDA molecular weight (Mw) was varied to fabricate the base (Mw 700 Daltons) and beam (either Mw 700 or Mw 3,400 Daltons) of the cantilevers. PEGDA was purchased from Sigma-Aldrich (Mw 700 Daltons) and Laysan Bio (Mw 3,400 Daltons). A working solution of Irgacure 2959 photoinitiator (Ciba, Basel, Switzerland), which is only partially water-soluble, was prepared at 50% (w/v) by dissolution in DMSO.

4.2.2 Fabrication of multi-material biopolymer cantilevers

To prepare for use in the SLA, energy dose characterizations of the pre-polymer solutions were performed using a method described previously.[31] Briefly, the pre-polymer solutions were pipetted into small containers capped on top by thin cover glasses. The SLA laser was used to draw circles that were 1 cm in diameter through the cover glass. The energy dose was varied by changing the scan speeds of the laser, which produced cylindrical gels of different thicknesses attached to the cover glasses. The thicknesses of these gels were measured and a working curve was plotted to determine the penetration depth (D_p) and critical exposure energy (E_c) of the pre-polymer solution necessary to produce cantilever beams with precise thicknesses. It was also observed that a change in the energy dose affected the elastic modulus of the gels. As a result, a constant energy dose (150 mJ cm^{-2}) was used to polymerize both the PEGDA-PC 700 and 3400 cantilever beams so that only the Mw of the hydrogels would affect the elastic modulus.

The fabrication setup consisted of a 35 mm diameter Petri dish and an 18 × 18 mm cover glass that was bonded to the dish with double-sided tape. The dish was positioned at the center of the SLA platform, and a carefully characterized volume of pre-polymer solution was added into it. The beam of the cantilever was fabricated first, by selective laser crosslinking of the prepolymer solution, to ensure the precise thickness was not affected by the energy dose. The unpolymerized solution was then evacuated using a pipette and an equal volume of the pre-polymer solution for the cantilever base was added. The SLA then polymerized the first layer of the base (300 μm thick) according to the characterized energy dose for PEGDA-PC 700. The pre-polymer solution was added, and the elevator controlled by the SLA was lowered to a specified distance. After photopolymerization, the part was recoated, and the process was repeated until completion. In all, the fabrication of the cantilevers took not more than 15 minutes, although the processing time can be accelerated. The cantilevers were then transferred to a 0.02 N acetic acid solution to be washed. This step prevented the high collagen concentration in the unpolymerized pre-polymer solution from gelling around the cantilever; however, this step should only be done for less than a minute as acetic acid affects cardiomyocyte adhesion on the polymerized collagen from the cantilever beams. After washing out the pre-polymer solution, the cantilevers were moved to a physiological pH buffer solution to swell overnight. A total of 4 cantilevers were fabricated in one run, but the SLA process can easily be scaled up to accommodate many more.

4.2.3 CARDIOMYOCYTE ISOLATION AND CULTURE

The warm growth medium consisting of Dulbecco's modified Eagle's medium (DMEM) and 10% fetal bovine serum (FBS) was prepared for cell culture. Cardiomyocytes were obtained from 2 day old neonatal Sprague-Dawley rats (Harlan Laboratories) using an approved protocol by the Institutional Animal Care and Use Committee (IACUC; Protocol #08190). Briefly, whole hearts were excised from the rats as described by Maass and Buvoli,[32] and placed in an ice-cold HBSS buffer. Using small scissors, the left and right atria were removed and the remaining ventricles were minced into 1 mm^3 pieces. The minced ventricles were digested in 0.1% (w/v) purified trypsin (Worthington Biochemicals), while gently rocking at 4 °C overnight. After 18 hours, warm growth medium was added for 5 minutes at 37 °C to inhibit trypsin digestion. The supernatant was discarded, and 0.1% (w/v) purified type II collagenase (Worthington Biochemicals) was added for 45 minutes while gently rocking at 37 °C. The digested tissue was triturated to mechanically loosen the cells, and the suspension was filtered through a 75 μm cell strainer to remove undigested connective tissue. The suspension was removed after centrifugation at 150 × g for 5 minutes. The remaining cell pellet was re-suspended in warm growth medium and pre-plated for 1 hour to enrich the suspension for cardiomyocytes. The cardiomyocytes were then counted and seeded on the backside of the cantilevers. To do this, individual cantilevers were placed in a 24-well plate, turned upside down, and evacuated of all liquid. They were allowed to dry for 10 min so that the cantilevers would temporarily attach to the bottom of the dish. The cantilevers were then seeded at 2 million cells per well (1×10^6 cells cm^{-2}) and incubated for 12 hours. After cell attachment, the cantilevers were transferred to a new dish with fresh medium and cultured overnight.

4.2.4 HYDROGEL CHARACTERIZATION

The stiffness of a gel disk fabricated in the SLA was evaluated by measuring the elastic modulus (E) using a mechanical testing system (Insight, MTS Systems, Eden Prairie, MN, USA). The gel disk with a diameter of 5 mm was compressed at a constant deformation rate of 1.0 mm s^{-1} at 25 °C, and the resulting stress was recorded by MTS software (Testworks 4). From the strain limit to the first 10%, the elastic modulus was calculated using the slope of the stress (σ) vs. strain (λ) curve.

The swelling ratios of the gels at equilibrium were determined by measuring the weight of the swollen gels after 24 hours in pH 7.4 buffer solutions at 37 °C and the weight of the dried

gels. The degree of swelling (Q), defined as the reciprocal of the volume fraction of a polymer in a gel (v_2), was calculated from the following equation:

$$Q = v_2^{-1} = \rho_P \left(\frac{Q_m}{\rho_S} + \frac{1}{\rho_P} \right) \tag{4.1}$$

where ρ_S was the density of water, ρ_P was the density of polymer, and Q_m was the swelling ratio, the mass ratio of the swelled gel to the dried gel.

4.2.5 Experimental setup for measuring cantilever bending angles

Vertical motion and bending angles of the cantilevers due to cardiomyocyte cell sheet contraction were captured using a camcorder (HandyCam, Sony USA, New York, NY USA) with an advanced HAD CCD imager at 720 × 480 pixel video capture resolution. The camcorder recorded at 60 fps with a 60× optical zoom. It was fixed on a multi-axis stage (Thorlabs) and placed in a temperature- and CO_2-controlled culture chamber due to cardiomyocyte sensitivity to changes in the outside environment. The temperature and CO_2 were set to 37 °C and 5%, respectively. The bending angles, θ, and deflection values, δ, were measured using the Measure Tool in Adobe Photoshop software (Fig. 4.1). Still images were taken by the camcorder, and a line was fitted along the slope of the free end of the deformed cantilever. A second line was drawn along the horizontal axis of the undeformed cantilever, which created a protractor for measuring the angle. The vertical distance of the cantilever from the undeformed base to its deformed base was also measured to determine the deflection value. The smallest resolution that could be measured with this software platform was 0.1°.

4.2.6 Modeling and analysis methods

Modeling and analysis of the cell -based biohybrid cantilevers were carried out using an analytical solution based on finite element modeling (FEM) analysis and validated by classical beam equations. FEM is a powerful technique when used to find numerical solutions to problems with irregular geometries or nonlinear material behavior. This is especially the case for cantilevers in which the beam width cannot be ignored. The intrinsic stress calculations were validated using the following equation:[33]

$$\sigma_{beam} = \frac{2E_b \delta t_b}{L^2} \tag{4.2}$$

where σ_{beam} is the intrinsic stress (Pa), E_b is the elastic modulus of the beam, δ is the deflection of the beam (m), t_b is the thickness of the beam (m), and L is the length of the beam (m).

Cells seeded on the cantilevers formed sheets that were considered thin films, and the cantilevers were modeled as composite, two-component systems. The model was validated by simulating cantilevers with beam dimensions and comparing the stress calculations to Atkinson's approximation, a variant of Stoney's equation:[8]

$$\sigma_{film} \approx \frac{\delta E_b t_b^3}{4t_f (1-\nu_b)(t_f + t_b)L} \tag{4.3}$$

where σ_{film} is the cell sheet stress (Pa), t_f is the thickness of the cell sheet (m), and ν_b is Poisson's ratio of the beam.

The simulations were performed with measured elastic moduli of 503 kPa for PEGDA-PC 700 and 17.82 kPa for PEGDA-PC 3400. Poisson's ratio of PEGDA-PC was assumed to be 0.499. Based on the literature, the elastic modulus of a sheet of cardiomyocytes was assumed to be 10 kPa with a thickness of 10 μm.[34,35] The density of cardiomyocytes and the PEGDA-PC material was assumed to be 1.06 kg m^{-3} and 1.12 kg m^{-3}, respectively.

4.2.7 IMMUNOSTAINING

Cells seeded on cantilevers after 3 days were washed twice with HBSS and fixed in 4% (v/v) formaldehyde solution for 10 minutes at room temperature. The cantilever beams were physically detached from their bases with a sharp razor. The beams were permeabilized in 0.2% (v/v) Triton-X 100 in HBSS for 10 minutes at room temperature. The samples were washed twice with HBSS before a blocking agent, Signal FX (Invitrogen), was added for 30 minutes. After another wash step, the samples were incubated overnight at 4 °C with primary antibodies , mouse anti-α-actinin (sarcomeric) and rabbit anti-connexin-43. The tissues were washed twice before being incubated with Alexa Fluor 488 goat anti-mouse and Alexa Fluor 594 goat anti-rabbit secondary antibodies for 2 hours at 37 °C. The stained samples were washed with HBSS and subsequently stained with an antibody for DNA, 4′,6-diamindino-2-phenylindole (DAPI, Sigma Aldrich, St Louis, MO, USA) for 5 minutes. After a final wash step, the cells on the cantilevers were imaged using an inverted fluorescent microscope (IX81, Olympus, Center Valley, PA, USA).

4.3 RESULTS AND DISCUSSION

4.3.1 CANTILEVER FABRICATION

The cantilevers were fabricated using a PEGDA backbone that was chemically linked with acrylic-PEG-collagen (Fig. 4.2A). PEGDA is a tissue-like, synthetic hydrogel that can be crosslinked in the presence of a photoinitiator.[36,37] It is mechanically stable, and its properties can be tuned by varying the polymer molecular weight, percent composition, or laser energy dose. It was previously established that changing the molecular weight of 20% PEGDA from 700 to 10,000 Daltons and photopolymerizing it in the SLA could be used to modulate the elasticity from 503 ± 57 kPa to 4.73 ± 0.46 kPa, respectively.[31] Collagen was chemically linked to the PEGDA backbone by acrylating its lysines, making them photocrosslinkable. Because PEGDA is normally inert, the collagen served to promote cell adhesion to the cantilever beams. The addition of collagen to the PEGDA backbone did not noticeably affect the mechanical properties of the hydrogel. Both the elastic modulus (Fig. 4.2B) and swelling ratio (Fig. 4.2C) were conserved for PEGDA-PC 700 and 3,400. For 20% PEGDA-PC 700, the elastic modulus was 507 ± 110 kPa, and the swelling ratio was 6.25 ± 0.06. For 20% PEGDA-PC 3,400, the elastic modulus was 29.8 ± 17 kPa, and the swelling ratio was 13.6 ± 0.95. From a biological perspective, mechanical properties of these hydrogels are closer to the in vivo environment of cells than either silicon or PDMS. They are also optically transparent, and therefore force measurements and immunofluorescence imaging of specific biological markers can be made simultaneously under light microscopes.[38,39]

Eight cantilevers were built for every fabrication run, with two sharing a common base. The SLA setup (Fig. 4.3A) can be easily modified with a larger-sized container to scale up the number of cantilevers in each run. The original dimensions (length × width × thickness) for the cantilevers were specified in CAD-based software, with the bases being 2 × 2 × 4 mm and the cantilever beams being 2 × 4 × 0.45 mm (Fig. 4.3B). An inherent characteristic of PEGDA hydrogels, however, is its tendency to imbibe water and swell many times beyond its intended dimensions. The cantilever thickness had to be adjusted to account for this swelling. The actual dimensions of PEGDA-PC 700 and 3,400 cantilevers after 24 hours of equilibrium swelling were 4.1 × 2.1 × 0.45 mm and 4.3 × 2.3 × 0.45 mm, respectively. One major benefit of the SLA approach is that more than one biomaterial, growth factor, or cell type can be introduced and spatially defined in the same 3D construct.[40] This is especially useful for creating gradients of varying mechanical or bioactive properties. In particular, cantilevers were fabricated on a base

consisting of PEGDA 700. The beams themselves were exchanged for either PEGDA-PC 700 or 3,400, depending on the desired elasticity. As shown in the simplified process flow (Fig. 4.3C), the cantilever beams were fabricated first in the SLA to ensure the correct thickness, while maintaining the laser energy dose (150 mJ cm^{-2}) between PEGDA-PC 700 and 3,400 materials to preserve the same trend in elasticity. The resulting PEGDA-PC 700 (Fig. 4.4A) and PEGDA-PC 3,400 (Fig. 4.4B) cantilevers are shown with comparable dimensions after equilibrium swelling in HBSS.

4.3.2 Cantilever beam intrinsic stress

Following the fabrication phase, cantilevers were rinsed in 0.02 N acetic acid to remove unpolymerized material before soaking overnight in HBSS. The cantilever beams would initially bend downward due to the weight of the unpolymerized pre-polymer solution and begin to swell as water diffused into them. Over time, the cantilevers would reach an equilibrium swelling state and bending would resolve to a final angle. These angles were measured using ImageJ analysis software and converted to displacement values. It was found that as the average molecular weight of the PEG-based cantilevers increased, the bending angle would increase upward in the clockwise direction. Similarly, the bending angle of the cantilevers would increase as the thickness of the cantilever decreased (Fig. 4.5). PEGDA-PC 3,400 had a bending angle of 67.1 ± 7.9° (3,420 ± 560 μm deflection), whereas PEGDA-PC 700 did not bend (0° angle and 0 μm deflection).

Finite element analysis (COMSOL simulations) was used with the displacement values to calculate the intrinsic stress of the cantilever beams (Fig. 4.4C). The insets in Fig. 4.4C show the simulated displacement values, which were used to calculate the intrinsic stress for PEGDA-PC 700 and 3,400. The intrinsic stresses obtained were 0 ± 0 Pa and 4160 ± 910 Pa, respectively. One hypothesis for the cantilever bending due to non-uniform residual stress is that during the UV laser polymerization in the SLA, the highest concentration of energy is focused at the surface of the pre-polymer solution. As the laser penetrates into the solution, it is absorbed by the photoinitiator and monomers. By the time it reaches a penetration depth of 450 μm at the other end of the beam, the energy is decreased, which reduces the overall crosslinking density. A simple calculation using the Beer–Lambert law reveals a 79.1% decrease in light transmittance (λ = 325 nm) through the pre-polymer solution at a depth of 450 μm. This leads to a gradient in

microstructure of the polymerized gel across the thickness. Consequently, the properties of the gel, such as swelling due to water absorption and stiffness, also have a gradient. This gradient in swelling across the thickness causes bending of the cantilever.

4.3.3 Cantilever bending due to non-uniform stress gradient

The Beer-Lambert law was used to calculate the absorbance of the SLA laser (λ = 325 nm) through the pre-polymer solution:

$$A = \varepsilon l c \tag{4.4}$$

where A is the absorbance, ε is the molar extinction coefficient (L mol^{-1} cm^{-1}), l is the pathlength (cm), and c is the concentration of the solution (mol L^{-1}). The molar extinction coefficient, ε, at the laser wavelength of 325 nm was obtained experimentally for the photoinitiator, Irgacure 2959: 676.7 L mol^{-1} cm^{-1}, which was similar to results extrapolated from Fairbanks *et al*.[41]

Next, the absorbance was calculated through the pre-polymer solution using ε = 676.7 L mol^{-1} cm^{-1}, l = 450 μm (cantilever thickness), and c = 0.0223 mol L^{-1} (Irgacure 2959 concentration). The resulting absorbance, A, was 0.679. To be clear, this is the absorbance of the SLA laser at the bottom of the pre-polymer solution, or the back face of the cantilever hydrogel. The absorbance was converted to percent transmittance, %T, to better understand the significance of this value:

$$A = 2 - \log 10\ \%T \tag{4.5}$$

The resulting percent transmittance, T, was 20.9%. That means at the surface of the pre-polymer solution, or the incident face of the cantilever hydrogel, there was 100% transmittance. At the bottom or back face, the transmittance decreased to 20.9%, which was a difference of 79.1%, due to the absorbance of the laser by the photoinitiator. Therefore, there was a significant difference in the UV exposure dose at the incident face and back face of the cantilever hydrogel, which supports the hypothesis that a gradient in the swelling due to water absorption and stiffness caused the cantilever to bend due to non-uniform residual stress. Finally, there may be other factors that affect the stress gradient. For example, total energy dose may play a critical role during the photopolymerization process. As the crosslinking density reaches a maximum at the incident face, overexposure can continue to crosslink the back face of the cantilever and minimize or even eliminate the stress gradient.

4.3.4 Cardiomyocyte adhesion and spreading

PEGDA hydrogels are hydrophilic and well-known to resist cell adhesion. Many groups have chemically modified them with proteins and peptide sequences to make them more amenable to cell attachment.[19] One of the most frequently used sequences with PEGDA is RGD (arginine-glycine-aspartic acid), which is found in numerous extracellular matrix proteins. However, several reports have suggested that while RGD peptides promote cardiomyocyte adhesion, they are unable to promote the signaling required for normal FAK expression and complete sarcomere formation in cardiomyocytes.[42] Sarin *et al*.[43] went further to demonstrate that RGD depressed the rate of contractile force by altering the myofilament activation process. Based on these findings, we sought to improve cardiomyocyte function by chemically attaching collagen molecules to PEGDA hydrogels. This chemistry was performed by the reaction of lysine amines on collagen to acrylate-PEG-NHS, which is an N-hydroxysuccinimidyl ester reactive to amines. The acrylate-PEG-collagen was then combined in solution with PEGDA to form a PEG-based hydrogel linked with bioactive collagen for cell adhesion.

Cardiomyocytes extracted from neonatal rat ventricular myocytes were seeded on PEGDA, PEGDA-RGD, and PEGDA-collagen (PEGDA-PC) hydrogels. After 2 days, cells were qualitatively evaluated for cell adhesion and spreading. It was clear that cardiomyocytes spread much better on PEGDA-PC hydrogels than PEGDA and PEGDA-RGD (Fig. 4.6). The cells on PEGDA and PEGDA-RGD appeared to remain balled up in spheres and preferentially attached to each other rather than on the substrate. Many of the cells had washed off after a change of media indicating poor cell attachment. On the other hand, cardiomyocytes on PEGDA-PC spread greatly, formed gap junctions, and began to contract in synchrony. Because of that, we used PEGDA-PC hydrogels as our material choice for cantilever fabrication, which has the bioactivity for cell attachment and function, and ability to change its mechanical stiffness through its molecular weight.

4.3.5 Cantilever bending due to cell traction forces

As a result of the intrinsic stress, the curvature of the PEGDA-PC 3,400 cantilevers made it difficult to seed cells uniformly and at high densities on the beams. One solution was to turn the cantilevers on their back sides and evacuate the liquid they were immersed in. This created a surface tension that mechanically flattened the curved cantilever beams onto the bottom of the plate. Neonatal rat ventricular myocytes were then extracted and seeded on the flattened

cantilever beams at 1 million cells cm^{-2}. This backside seeding also prevented the cell sheets on the two cantilevers from linking together, so that they could be examined as two independent measurements. The cantilevers with seeded cells were centrifuged to distribute cells evenly on the cantilevers.

After seeding, cardiomyocytes were allowed to adhere for 24 hours. By then, the cantilevers had already started to bend downward due to cell traction forces as the cardiomyocytes began to spread and reorganize themselves. Cell traction forces are generated by actomyosin interactions and actin polymerization, and regulated by intracellular proteins such as α-smooth muscle actin and soluble factors such as TGF-β. Once transmitted to the extracellular matrix through stress fibers via focal adhesions, which are assemblies of ECM proteins, transmembrane receptors, and cytoplasmic structural and signaling proteins , cell traction forces direct many cellular functions, including cell migration, ECM organization, and mechanical signal generation. The stress induced by the cell sheet is clearly seen by the change in displacement over time on the cantilever beams (Fig. 4.7A). The cell sheet continued to apply traction forces on the cantilevers over 72 hours before it stabilized. The bending angle of the curved beams was measured and recorded every day for 4 days (Fig. 4.7B). Because of the cell traction forces, the bending angle for PEGDA-PC 3,400 cantilevers was decreased from its intrinsic value of 67.1 ± 7.9° to 44.2 ± 6.0° by the third day of culture. PEGDA-PC 700 cantilevers, having a high elastic modulus, did not bend at all during culture. The displacement values were also measured and used in FEM simulations to calculate the stress on the cantilever beams by the cell sheet. The simulated displacements and stresses for PEGDA-PC 700 and 3,400 are shown in Fig. 4.7C. For PEGDA-PC 3,400, the highest level of stress was seen at the fixed end of the beam. The maximum stress values were calculated every day (Fig. 4.7D), and the change in stress was plotted every 24 hours. The cell sheet reached a maximum stress of 2,040 Pa before it leveled off. The change in stress was highest after the first day and continually decreased before there was virtually no change between 72 and 96 hours.

4.3.6 Cantilever actuation and force

Although cardiomyocytes began to contract individually as early as 24 hours after seeding, the cells did not beat synchronously as a whole sheet until at least 48 hours. During this period, cardiomyocytes formed electrical connections between each other through gap junctions.

Membrane proteins known as connexins formed six-membered rings called connexons on the sarcolemma of cardiomyocytes. When gap junctions are open, they provide direct communication between the sarcoplasmic spaces of adjoining cells, creating a functional synctium or network of synchronized cells.[44,45] After 76 hours, when the majority of these connections were formed, cells were stained for sarcomeric α-actinin to qualitatively elucidate the morphology of cardiomyocytes on PEGDA-PC 700 and 3,400 cantilevers (Fig. 4.8A). In both cases, cardiomyocytes exhibited the expression of sarcomeric α-actinin, an actin-binding protein that plays a key role in the formation and maintenance of Z-lines, throughout the cytoskeleton . The localization of sarcomeric α-actinin in both PEGDA-PC 700 and 3,400 demonstrated a typical periodicity in the Z-lines of cardiomyocytes.

Actuation of the cantilevers is a consequence of the contraction and relaxation of the cardiomyocyte cell sheet through the sliding filament mechanism.[46] During contraction, cardiomyocyte filaments shorten by the sliding of actin and myosin filaments in sarcomeres, as triggered by action potentials and intracellular calcium signals.[47] Calcium is the critical part of the medium that allows the actin, myosin, and ATP to interact, causing crossbridge formation and muscle contraction. This process continues as long as calcium is available to the actin and myosin. During relaxation, cardiomyocyte filaments return to their original position as calcium is pumped back into the sarcoplasmic reticulum, preventing interaction of the actin and myosin. Cardiomyocyte cell sheets on PEGDA-PC 3,400 cantilevers had all started to actuate after 48 hours (100%), whereas only a quarter of the cardiomyocyte cell sheets on PEGDA-PC 700 cantilevers followed suit (25%) during the same time period (Fig. 4.8B). This percentage increased after 72 hours (83%), but the development of functional synctium was clearly slower. Furthermore, the beating frequency of the cardiomyocyte cell sheet was greater for PEGDA-PC 3,400 than 700. After 48 hours, cardiomyocytes on cantilever plates with Mw 3,400 reached a beating frequency of 1.12 ± 0.14 Hz, while those for Mw 700 reached 0.39 ± 0.05 Hz, respectively (Fig. 4.8C). The frequency increased slightly for both after 72 hours to 1.40 ± 0.16 Hz and 0.44 ± 0.06 Hz, respectively. These results seem to be in agreement with previous reports that claim that the substrate elasticity of the developing myocardial microenvironment are optimal for transmitting contractile work to the matrix and for promoting actomyosin striations.[1] In addition to the substrate elasticity, it is possible the hydrogels with higher molecular weight

have more cell adhesive sites exposed on the surface of the cantilever than hydrogels with lower molecular weight.

Finally, we measured the actuation amplitudes of the cantilevers over 96 hours (Fig. 4.9A). Similar to the beating frequency, the amplitudes reached a maximum on the third day post-seeding with values of 2 ± 8 μm and 390 ± 40 μm for PEGDA-PC 700 and 3400, respectively. The actuation amplitudes did not reach a maximum suddenly; rather, they increased linearly over time as more cardiomyocytes joined the synctium of cells. Using these amplitudes, we calculated the contractile forces of cardiomyocyte cell sheets on PEGDA-PC 700 and 3400 cantilevers by using the following equations (Fig. 4.9B):

$$F = k_c \delta \tag{3.6}$$

$$k_c = \frac{w}{4\left(E_f t_f + E_b t_b\right)L^3}\left(E_f^2 t_f^4 + E_b^2 t_b^4 + 4E_b t_b E_f t_f^3 + 6E_b t_b^2 E_f t_f^2 + 4E_b t_b^3 E_f t_f\right) \tag{3.7}$$

where F is the contractile force, k_c is the stiffness of the cantilever, w is the width of the beam, and E_f is the elastic modulus of the film. Stiffness, k_c, was derived for a composite, two-component system.[48] The stiffness values for PEGDA-PC 700 and 3,400 were calculated to be 0.36 N m^{-1} and 0.013 N m^{-1}, respectively. Using these values, and the peak deflection of actuated cantilevers (from its relaxation state to its contraction state), the total calculated forces were 0.89 ± 2.89 μN for PEGDA-PC 700 and 5.09 ± 0.48 μN for PEGDA-PC 3,400.

The mechanical forces generated with cardiomyocyte cell sheets on elastic substrates near that of the native myocardium can be used to model and design self-propelled bio-bots. There are several ways to improve the current output of force, such as aligning the cardiomyocytes by patterning proteins or grooves into the substrate.[49] The stiffness of the beam can be decreased by reducing the beam thickness or expanding its length. The density of cells can be increased by encapsulating them in 3D. Varying rigid (PEGDA-PC 700) and soft (PEGDA-PC 3,400) materials throughout the bio-bot design can also be beneficial for maximizing deflection in one direction and minimizing it in another. These designs can be used to form the basis of more complex cell systems. For example, cardiomyocytes can later be replaced with skeletal myoblasts and co-cultured with neurons to form neuromuscular junctions. The genetic machinery of the neurons can be reprogrammed to form simple functions of switching on and off chemical secretions, which in turn can be used to stimulate muscle cells to propel the bio-bot. The advantage of using this hydrogel system over silicon and PDMS is that

when we switch over to other cell types, which are sensitive to their environment, we can tune the elasticity of the substrate in accordance to them. As the stiffness is modulated for these specific cell types (*i.e.*, neurons and skeletal muscle cells), this may affect the curvature of the material due to cell traction forces, in which case more rigid materials can be used to maintain the structural integrity of the bio-bot. Thus, a true living, multi-cellular machine could be created using the capabilities of the SLA, which can perform multiple functions such as sensing, moving, and effecting.[50]

4.3.7 Effect of fibroblasts on cardiomyocyte culture

Cells isolated from neonatal rat hearts consist predominantly of matrix-depositing fibroblasts by number and striated cardiomyocytes by volume. It has been argued that a minimum number of fibroblasts (10-20%) are necessary to maintain a proper functioning cardiomyocyte culture.[51] There are at least three essential functions that fibroblasts play in the heart: (1) synthesis and deposition of ECM components, (2) synthesis and release of enzymes responsible for the degradation and turnover of the ECM, and (3) generation of mechanical tension on the epimysial collagen network.[52] The third point would imply that fibroblasts also contribute to the initial static bending of the cantilevers. Like cardiomyocytes, active tension in fibroblasts is developed through microtubules and actomyosin-based forces, though the structure, assembly, composition, and contractile profile of these differ. In culture, however, fibroblasts divide more rapidly than cardiomyocytes and pervade the entire free substrate surface. An overgrowth of fibroblasts can cause diminished contractile capacity and phenotype plasticity. As such, it is important to keep the number of fibroblasts to a minimum. The majority of non-muscle cells, including the fibroblasts, were eliminated using a simple method developed by Blondel *et al*.[53] that enriched for cardiomyocytes, purportedly as high as 97-99%. Therefore, the effect of fibroblasts on our cantilevers was minimized.

4.3.8 Control and longevity of cantilevers and actuators

The influence of various drug treatments has been evaluated on the contractile activity of cardiomyocytes.[54] For example, the addition of isoproterenol to the medium can cause an increase in the contraction frequency, whereas the addition of carbamylcholine chloride to the medium can cause a decrease in the contraction frequency. Gap junction blockers, such as heptanol, can completely stop synchronous contractility. These effects are reversible; after 10

min in the drug-free culture medium, the synchronous beating of the cardiomyocytes was restored to its original amplitude and frequency. Pulsatile electrical stimulation can also be used to pace the contractions of cardiomyocytes.[55] Recently, light-induced stimulation of genetically engineered cardiomyocytes that express the light-activated cation channels, halorhodopsin or channelrhodopsin, was demonstrated.[56,57]

Experimentally, these cantilevers have been verified to function optimally for at least 5 days post-seeding. After this period, the frequency and amplitude of the actuating cantilevers decrease significantly. The lifetime of these cantilevers can be extended by reducing the overgrowth of fibroblasts in low serum medium.[58] Other groups have demonstrated up to 16 days of functional components with cardiomyocytes.[6] Furthermore, previous reported results on cardioids show that periods up to 60 days are readily attainable in culture.[59] Lifetimes beyond this would require new technologies to support long-term survival in vitro.

4.4 Conclusion

Multi-material cantilevers were fabricated using a 3D stereolithographic printer with a PEGDA backbone that was incorporated with acrylic-PEG-collagen. The SLA allows us to quickly and easily change the material and its properties in the same 3D construct, which we show here with PEGDA-PC 700 and 3,400 cantilevers. Cardiomyocytes were extracted and seeded on the backside of the cantilevers and cultured to form cell sheets. Through its traction forces, the cardiomyocytes created a stress on the cantilever, causing it to bend. These stresses were modeled using finite element analysis by mimicking the displacement of the cantilevers. For PEGDA-PC 3,400, the maximum stress was 2040 Pa, while there was no stress on PEGDA-PC 700 because of its high stiffness. The cardiomyocytes then began to beat in synchrony after two days in culture, and the contractile forces were calculated. The peak contractile forces were 0.89 ± 2.89 μN for PEGDA-PC 700 and 5.09 ± 0.48 μN for PEGDA-PC 3,400. The stresses and forces calculated here can be used to design and optimize a cell -based biohybrid actuator that can generate net motion. The cantilevers can be used as an early prototype for the design and optimization of cell-based biohybrid actuators.

4.5 Acknowledgments

This project was funded by the National Science Foundation (NSF), Science and Technology Center (STC) and Emerging Behaviors in Integrated Cellular Systems (EBICS) Grant CBET-0939511 (R.B., T.S., and H.K.) and by a cooperative agreement that was awarded to UIUC and administered by the U.S. Army Medical Research & Materiel Command (USAMRMC) and the Telemedicine & Advanced Technology Research Center (TATRC), under Contract #: W81XWH0810701.

4.6 REFERENCES

1. Discher, D. E., Janmey, P., & Wang, Y., Tissue cells feel and respond to the stiffness of their substrate. *Science* 310, 1139–1143 (2005).

2. Xi, J., Schmidt, J. J., & Montemagno, C. D., Self-assembled microdevices driven by muscle, *Nat. Mater.* 4, 180–184 (2005).

3. Kim, J., *et al*., Establishment of a fabrication method for a long-term actuated hybrid cell robot. *Lab Chip* 7, 1504–1508 (2007).

4. Feinberg, A. W., Feigel, A., Shevkoplyas, S. S., Sheehy, S., Whitesides, G. M., & Parker, K. K., Muscular thin films for building actuators and powering devices. *Science* 317, 1366–1370 (2007).

5. Choi, E., Lee, S. Q., Kim, T. Y., Chang, H., Lee, K. J., & Park, J., MEMS-based power generation system using contractile force generated by self-organized cardiomyocytes. *Sens. Actuators B* 151, 291–296 (2010).

6. Wilson, K., Das, M., Wahl, K. J., Colton, R. J., & Hickman, J., Measurement of contractile stress generated by cultured rat muscle on silicon cantilevers for toxin detection and muscle performance enhancement. *PLoS One* 5, e11042 (2010).

7. Park, J., *et al*., Real-time measurement of the contractile forces of self-organized cardiomyocytes on hybrid biopolymer microcantilevers. *Anal. Chem*. 77, 6571–6580 (2005).

8. Engler, A. J., *et al*., Embryonic cardiomyocytes beat best on a matrix with heart-like elasticity: scar-like rigidity inhibits beating. *J. Cell Sci*. 121, 3794–3802 (2008).

9. Bajaj, P., Tang, X., Saif, T. A., & Bashir, R., Stiffness of the substrate influences the phenotype of embryonic chicken cardiomyocytes. *J. Biomed. Mater. Res. Part A* 95A, 1261–1269 (2010).

10. Jacot, J. G., McCulloch, A. D., & Omens, J. H., Substrate stiffness affects the functional maturation of neonatal rat ventricular myocytes. *Biophys. J*. 95, 3479–3487 (2008).

11. Tang, X., Bajaj, P., Bashir, R., & Saif, T. A., How far cardiac cells can see each other mechanically. *Soft Matter* 7, 6151–6158 (2011).

12. Ikeda, S., *et al*., In vitro Patient-tailored Anatomical Model of Cerebral Artery for Evaluating Medical Robots and Systems for Intravascular Neurosurgery. *2005 IEEE/RSJ International Conference on Intelligent Robots and Systems*, 1558–1563 (2005).

13. Armani, D., Liu, C., & Aluru, N., Re-configurable Fluid Circuits by PDMS Elastomer Micromachining. *12th IEEE International Conference on Micro Electro Mechanical Systems, MEMS '99*, 222–227 (1999).

14. Brown, X. Q., Ookawa, K., & Wong, J. Y., Evaluation of polydimethylsiloxane scaffolds with physiologically-relevant elastic moduli: interplay of substrate mechanics and surface chemistry effects on vascular smooth muscle cell response. *Biomaterials* 26, 3123–3129 (2005).

15. Khademhosseini, A., *Micro and Nanoengineering of the Cell Microenvironment: Technologies and Applications*, Artech House, Boston (2008).

16. Wong, J. Y., Leach, J. B., & Brown, X. Q., Balance of chemistry, topography, and mechanics at the cell-biomaterial interface: issues and challenges for assessing the role of substrate mechanics on cell response. *Surf. Sci*. 570, 119–133 (2004).

17. Ifkovits, J. L., & Burdick, J. A., Review: photopolymerizable and degradable biomaterials for tissue engineering applications. *Tissue Eng*. 13, 2369–2385 (2007).

18. Peyton, S. R., Raub, C. B., Keschrumrus, V. P., & Putnam, A. J., The use of poly(ethylene glycol) hydrogels to investigate the impact of ECM chemistry and mechanics on smooth muscle cells. *Biomaterials* 27, 4881–4893 (2006).

19. Hern, D. L., & Hubbell, J. A., Incorporation of adhesion peptides into nonadhesive hydrogels useful for tissue resurfacing. *J. Biomed. Mater. Res*. 39, 266–276 (1998).

20. Mann, B. K., Gobin, A. S., Tsai, A. T., Schmedlen, R. H., & West, J. L., Smooth muscle cell growth in photopolymerized hydrogels with cell adhesive and proteolytically degradable domains: synthetic ECM analogs for tissue engineering. *Biomaterials*, 22, 3045–3051 (2001).

21. Phelps, E. A., Landazur, N., Thule, P. M., Taylor, R., & Garcia, A. J., Bioartificial matrices for therapeutic vascularization. *Proc. Natl. Acad. Sci. U. S. A*. 107, 3323–3328 (2010).

22. Metters, A. T., Anseth, K. S., & Bowman, C. N., Fundamental studies of a novel, biodegradable PEG-b-PLA hydrogel. *Polymer* 41, 3993–4004 (2000).

23. West, J. L., & Hubbell, J. A., Polymeric biomaterials with degradation sites for proteases involved in cell migration. *Macromolecules* 32, 241–244 (1999).

24. Raeber, G. P., Lutolf, M. P., & Hubbell, J. A., Molecularly engineered PEG hydrogels: a novel model system for proteolytically mediated cell migration. *Biophys. J*. 89, 1374–1388 (2005).

25. Peltola, S. M., Melchels, F. P. W., Grijpma, D. W., & Kellomaki, M., A review of rapid prototyping techniques for tissue engineering purposes. *Ann. Med*., 40, 268–280 (2008).

26. Burg, T., Cass, C. A. P., Groff, R., Pepper, M., & Burg, K. J. L., Building off-the-shelf tissue-engineered composites. *Philos. Trans. R. Soc. London, Ser. A* 368, 1839–1862 (2010).

27. Mechels, F. P. W., Feijen, J., & Grijpma, D. W., A review on stereolithography and its applications in biomedical engineering. *Biomaterials* 31, 6121–6130 (2010).

28. Nguyen, H., Richter, J., & Jacobs, P. F., On Windowpanes and Christmas Trees: Diagnostic Techniques for Improved Part Accuracy, in *Proc. 1st Eur. Conf. Rapid Prototyping*, ed. P. M. Dickens, University of Nottingham, Nottingham, 133–161 (1992).

29. Arcaute, K., Mann, B. K., & Wicker, R. B., Stereolithography of spatially controlled multi-material bioactive poly(ethylene glycol) scaffolds. *Acta Biomater*. 6, 1047–1054 (2010).

30. Arcaute, K., Mann, B. K., & Wicker, R. B., Stereolithography of three-dimensional bioactive poly(ethylene glycol) constructs with encapsulated cells. *Ann. Biomed. Eng*. 34, 1429–1441 (2006).

31. Chan, V., Zorlutuna, P., Jeong, J. H., Kong, H., & Bashir R., Three-dimensional photopatterning of hydrogels using stereolithography for long-term cell encapsulation, *Lab Chip* 10, 2062–2070 (2010).

32. Maass, A. H., & Buvoli, M., Cardiomyocyte preparation, culture, and gene transfer. *Methods Mol. Biol*. 366, 321–330 (2007).

33. Sentura, S. D., *Microsystem Design*, Springer, New York (2000).

34. Shi, X., *et al*., Elasticity of cardiac cells on the polymer substrates with different stiffness: an atomic force microscopy study. *Phys. Chem. Chem. Phys*. 13, 7540–7545 (2011).

35. Berry, M. F., *et al*., Mesenchymal stem cell injection after myocardial infarction improves myocardial compliance. *Am. J. Physiol*. 290, H2196–H2203 (2006).

36. Fisher, J. P., Dean, D., Engel, P. S., & Mikos, A. G., Photoinitiated polymerization of biomaterials. *Annu. Rev. Mater. Res*. 31, 171–181 (2001).

37. Nguyen, K. T., & West, J. L., Photopolymerizable hydrogels for tissue engineering applications. *Biomaterials,* 23, 4307–4314 (2002).

38. Rajagopalan, J., & Saif, M. T. A., MEMS sensors and microsystems for cell mechanobiology. *J. Micromech. Microeng*. 21, 1–11 (2011).

39. Addae-Mensah, K. A., & Wikswo, J. P., Measurement techniques for cellular biomechanics in vitro. *Exp. Biol. Med*. 233, 792–809 (2008).

40. Zorlutuna, P., Jeong, J. H., Kong, H., & Bashir, R., Stereolithography-based hydrogel microenvironments to examine cellular interactions. *Adv. Funct. Mater*. 21, 3642–3651 (2011).

41. Fairbanks, B. D., Schwartz, M. P., Bowman, C. N., & Anseth, K. S., Photoinitiated polymerization of PEG-diacrylate with lithium phenyl-2,4,6-trimethylbenzoylphosphinate: polymerization rate and cytocompatibility. *Biomaterials* 30, 6702-6707 (2009).

42. Boateng, S. Y., Lateef, S. S., Mosley, W., Hartman, T. J., Hanley, L., & Russell, B., RGD and YIGSR synthetic peptides facilitate cellular adhesion identical to that of laminin and fibronectin but alter the physiology of neonatal cardiomyocytes. *Am. J. Physiol. Cell Physiol.* 288, C30–C38 (2005).

43. Sarin, V., Gaffin, R. D., Meininger, G. A., & Methuchamy, M., Arginine-glycine-aspartic acid (RGD)-containing peptides inhibit the force production of mouse papillary muscle bundles via alpha 5 beta 1 integrin. *J. Physiol*. 564, 603–617 (2005).

44. Severs, N. J., Bruce, A. F., Dupont, E., & Rothery, S., Remodeling of gap junctions and connexin expression in diseased myocardium. *Cardiovasc. Res.* 80, 9–19 (2008).

45. Noorman, M., *et al*., Cardiac cell–cell junctions in health and disease: electrical versus mechanical coupling. *J. Mol. Cell. Cardiol*. 47, 23–31 (2009).

46. Berne, M. D., Levy, M. N., & Koeppen, B. M., *Physiology*, Mosby, St Louis (2003).

47. Curtis, M. W., & Russell, B., Micromechanical regulation in cardiac myocytes and fibroblasts: implications for tissue remodeling. *Eur. J. Physiol*. 462, 105–117 (2011).

48. Shih, W. Y., Li, X., Gu, H., Shih, W., & Aksay, I. A., Simultaneous liquid viscosity and density determination with piezoelectric unimorph cantilevers. *J. Appl. Phys*. 89, 1497–1505 (2001).

49. Kim, J., *et al*., Quantitative evaluation of cardiomyocyte contractility in a 3D micro-environment. *J. Biomech*. 41, 2396–2401 (2008).

50. Kamm, R. D., Nerem, R. M., & Hsia, K. J., *Cells into systems*. Mech. Eng., 30–34 (Nov 2010).

51. Salameh, A. & Dhein, S., Culture of neonatal cardiomyocytes. *Practical Methods in Cardiovascular Research* 5, 568-576 (2005).

52. Kanekar, S., Hirozanne, T., Terracio, L., & Borg, T. K., Cardiac fibroblasts: form and function, *Cardiovasc. Pathol*. 7, 127-133 (1998).

53. Blondel, B., Roijem, I., & Cheneval, J. P., Heart cells in culture: a simple method for increasing the proportion of myoblasts. *Experientia* 27, 356-358 (1971).

54. Shapira-Schweitzer, K., Habib, M., Gepstein, L., & Seliktar, D., A photopolymerizable hydrogel for 3-D culture of human embryonic stem cell-derived cardiomyocytes and rat neonatal cardiac cells. *J. Mol. Cell. Cardiol*. 46, 213–224 (2009).

55. Berger, H. J., *et al*., Continual electric field stimulation preserves contractile function of adult ventricular myocytes in primary culture. *Am. J. Physiol*. 266, H341–H349 (1994).

56. Bruegmann, T., *et al.*, Optogenetic control of heart muscle in vitro and in vivo. *Nat. Methods*, 7, 897–900 (2010).

57. Arrenberg, A. B., Stainier, D. Y., Baier, H., & Huisken, J., Optogenetic control of cardiac function. *Science* 330, 971–974 (2010).

58. Chlopcikova, S., Psotova, J., & Miketova, P., Neonatal rat cardiomyocytes—a model for the study of morphological, biochemical and electrophysiological characteristics of the heart. *Biomed. Pap*. 145, 49–55 (2001).

59. Baar, K., Birla, R., Boluyt, M. O., Borschel, G. H., Arruda, E. M., & Dennis, R. G., Self-organization of rat cardiac cells into contractile 3-D cardiac tissue. *FASEB J*. 19, 275–277 (2005).

4.7 FIGURES AND CAPTIONS

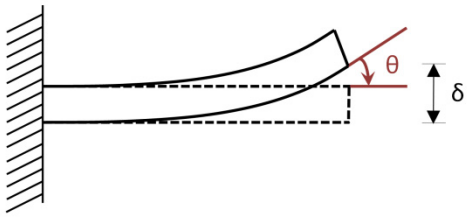

Fig. 4.1 | Schematic for measuring bending angles and deflection values. For bending angles, θ, a line was fitted along the slope of the free end of the deformed cantilever. A second line was drawn along the horizontal axis of the undeformed cantilever, which created a protractor for measuring the angle. For deflection values, δ, the vertical distance of the cantilever from the undeformed base to its deformed base was also measured to determine the deflection value.

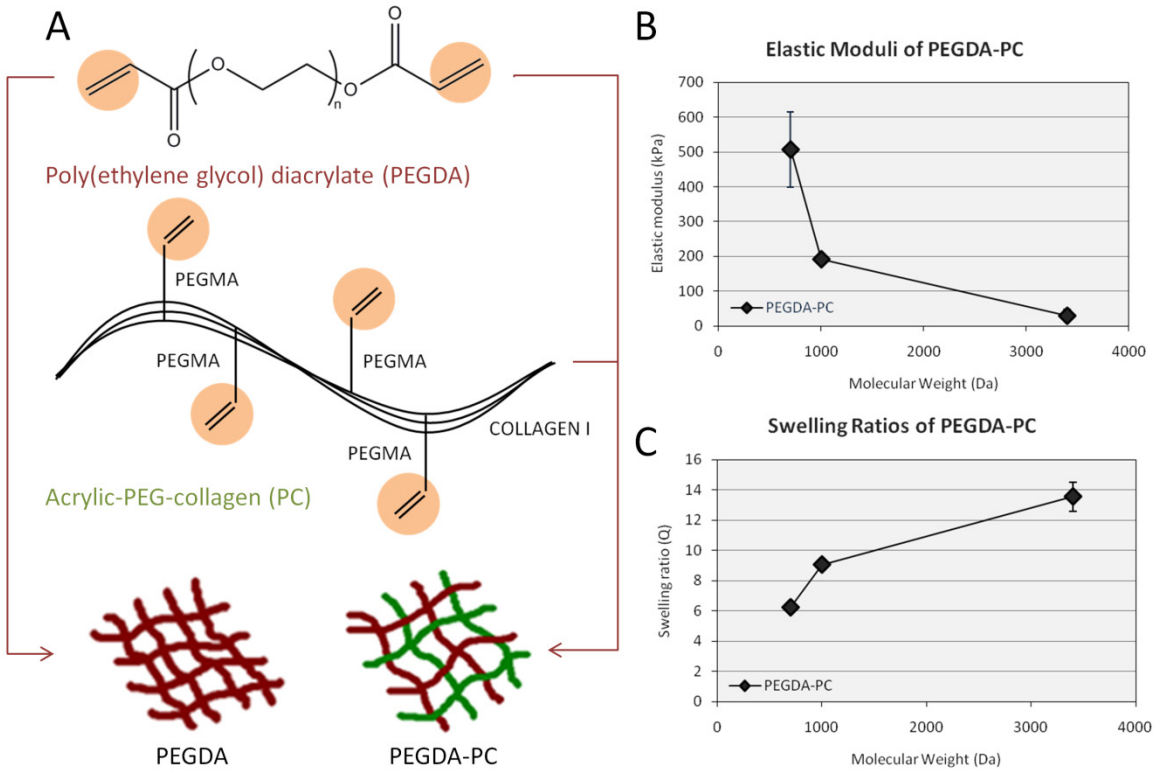

Fig. 4.2 | Biohybrid material. (A) A mixture consisting of poly(ethylene glycol) diacrylate (PEGDA) and acrylic-PEG-collagen (PC) was formulated as photopolymerizable material for fabricating cantilever beams. Collagen I, extracted from rat tail, was modified on their lysine groups with acrylic groups to UV cross-link to the PEG backbone in the presence of a photoinitiator. **(B and C)** The mechanical properties of PEGDA-PC hydrogels were measured using a compression test at increasing molecular weight, demonstrating that the cantilever beams can be tuned to a wide range of elastic moduli and swelling ratios. These values did not change from that of PEGDA-only hydrogels, which suggests that the incorporation of acrylic collagen did not affect bulk mechanical properties. For n = 3 and SD.

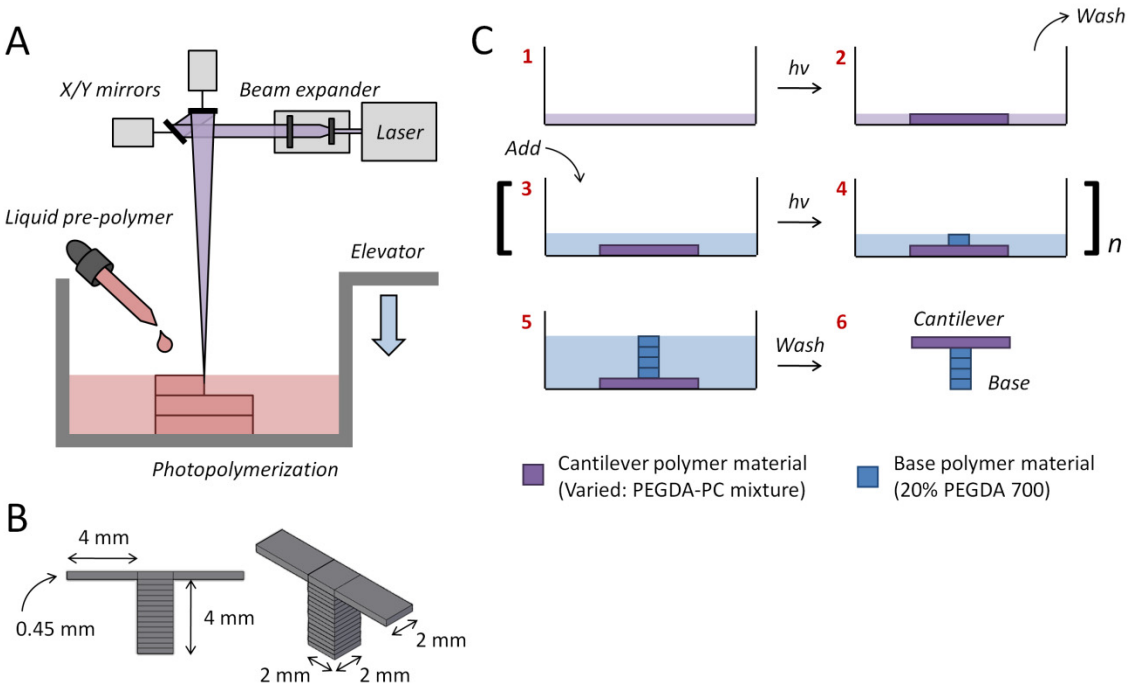

Fig. 4.3 | Multi-material cantilever fabrication. (A) The cantilevers were fabricated with a 3D stereolithographic printer, which uses a UV laser to construct layer-by-layer patterns. **(B)** Two separate cantilevers (2 mm wide X 4 mm long X 0.45 mm thick) were built on opposite ends of one base (2 mm wide X 2 mm long X 4 mm thick). The molecular weight of the PEGDA-PC cantilever beam was varied using either PEGDA-PC 700 or 3400, while the base was kept constant using PEGDA-PC 700. **(C)** A simplified fabrication process flow is shown, which begins with the formation of the cantilever beam before the base.

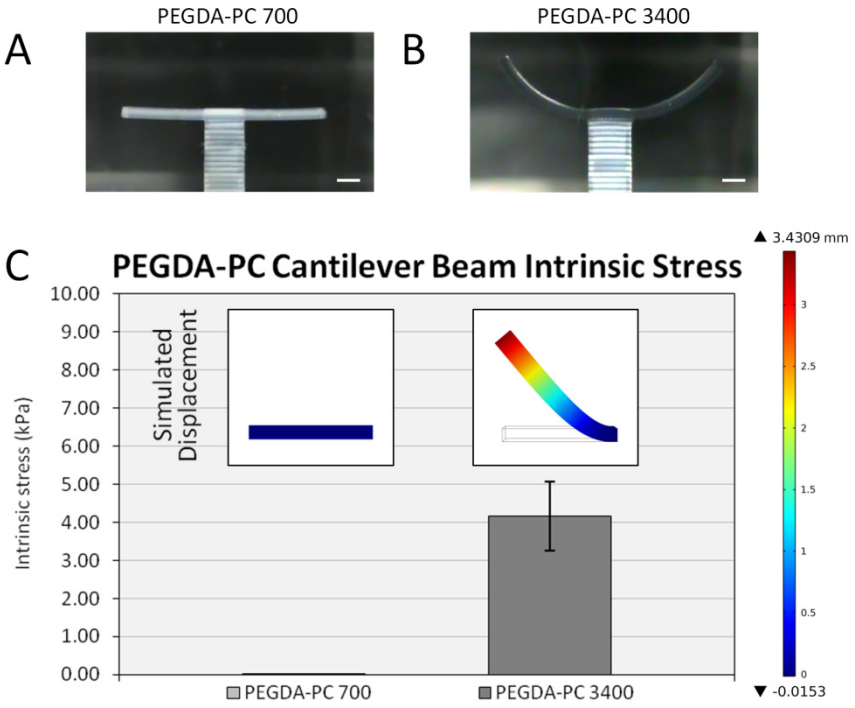

Fig. 4.4 | Intrinsic stress calculations. After the fabrication process, **(A)** PEGDA-PC 700 and **(B)** PEGDA-PC 3400 cantilevers were washed in HBSS to remove uncrosslinked pre-polymer solution. Due to an intrinsic stress, PEGDA-PC 3400 cantilevers would bend upward to relieve stress in the beams. **(C)** The peak stress was calculated by using finite element analysis to simulate the deflection of the cantilever beam ***(Inset)***. Scale bars are 1 mm. Statistics by one-way ANOVA, Tukey's test, *$p < 0.05$ for $n = 8$ and SD.

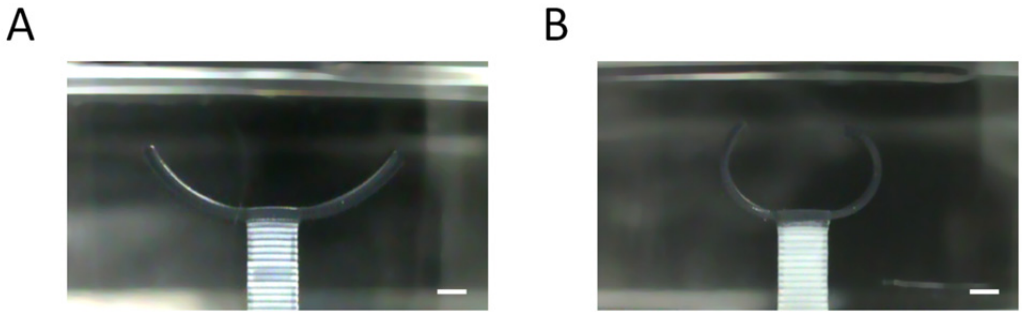

Fig. 4.5 | Intrinsic stress changes as the cantilever thickness varies. The thickness for PEGDA-PC 3400 cantilevers was decreased from **(A)** 450 μm to **(B)** 300 μm. Consequently, the beam curved upward sharply, decreasing its radius of curvature and increasing its intrinsic stress. This implied that stiffness has a role in determining the intrinsic stress of the beam. The PEGDA-PC 700 cantilever (450 μm) did not bend supported this line of reasoning.

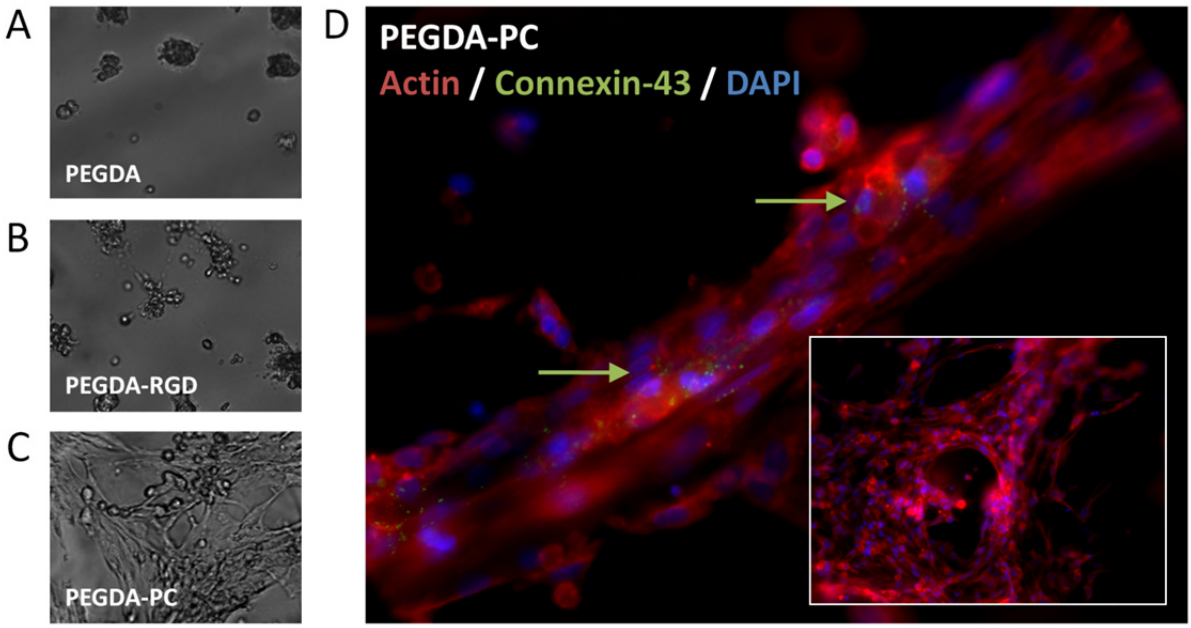

Fig. 4.6 | Cardiomyocytes on PEGDA-based substrates. Cardiomyocytes were seeded and cultured on **(A)** PEGDA, **(B)** PEGDA-RGD (20 mM), and **(C)** PEGDA-PC (1.84 mg/mL) for 72 hours before imaging. Compared to PEGDA and PEGDA-RGD, PEGDA-PC was a better substrate for cardiomyocyte attachment and spreading. **(D)** The cells on PEGDA-PC substrates were fixed and stained for α-actinin, connexin-43, and nuclei. Arrows indicate high density areas of connexin-43.

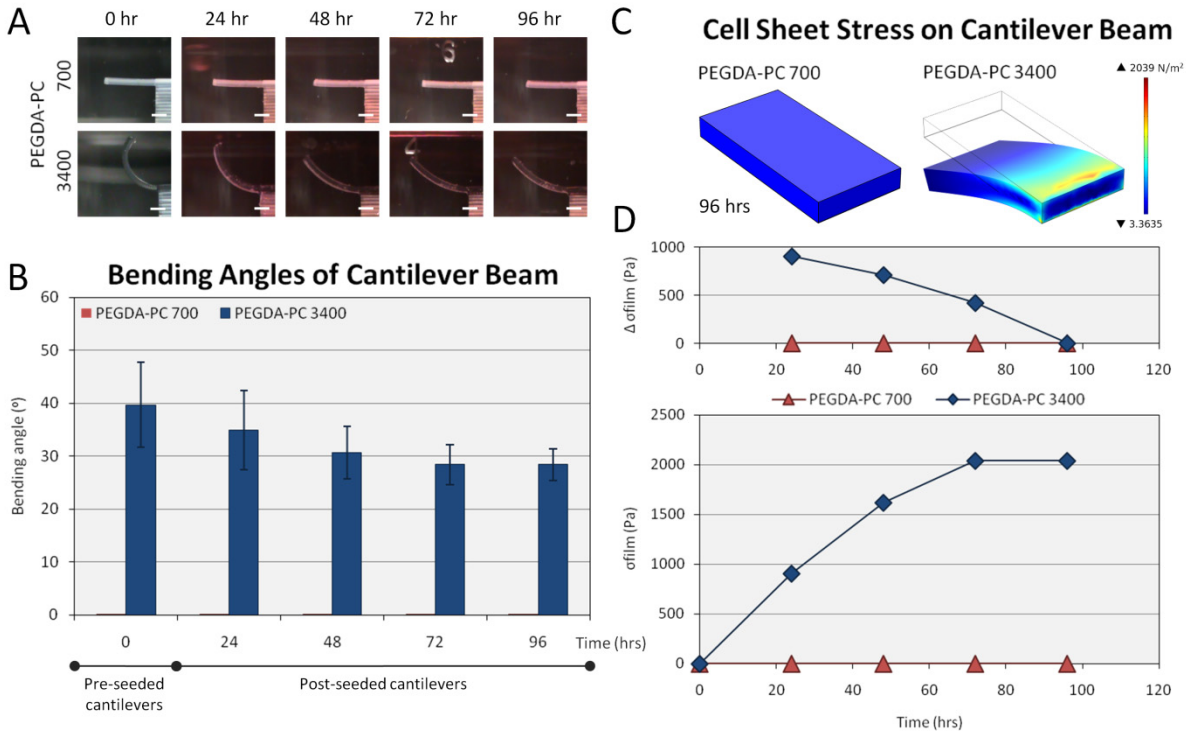

Fig. 4.7 | Cell sheet stress calculations. Cells from the ventricles of neonatal rat hearts were seeded on the backside of the cantilever beams. **(A)** The traction forces of these cells, which are responsible for migration, proliferation, and differentiation, caused the PEGDA-PC 3400 cantilever beams to deflect downward in the Z-direction over time. **(B)** The average bending angles of the cantilevers were measured over a 96 hour period, which was used to calculate the deflection at the tip of the beams. **(C)** These deflections were simulated using finite element analysis to calculate the stresses exerted by the cell sheets due to traction forces. **(D)** These stresses exerted by the cell sheet and modeled as a thin film were plotted over time. The change in stress over 24 hour time points decreased and reached 0 by 96 hours. Scale bars are 1 mm. Statistics by one-way ANOVA, Tukey's test, *$p < 0.05$ for $n = 8$ and SD.

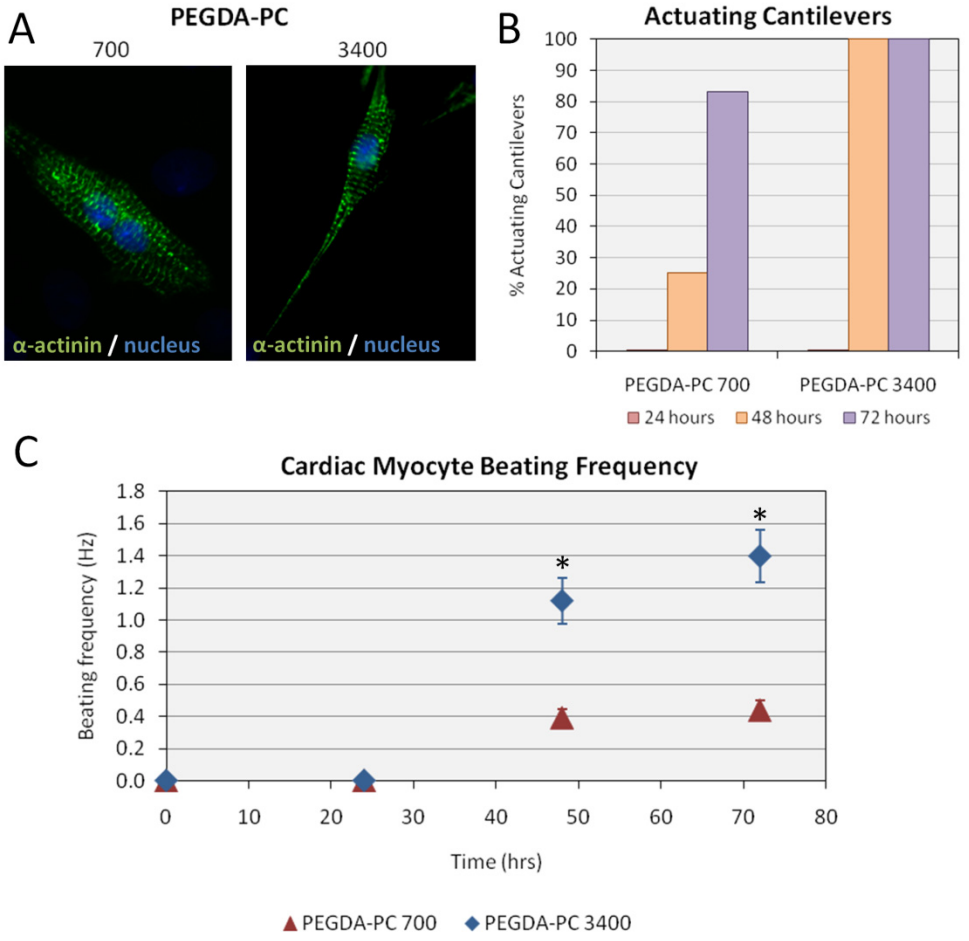

Fig. 4.8 | Cardiomyocytes on PEGDA-PC substrates. (A) Cells on the cantilevers were fluorescently-labeled with anti-sarcomeric α-actinin and anti-DNA. Qualitatively, cardiomyocytes on PEGDA-PC 3400 and PEGDA-PC 700 both expressed actomyosin complexes (striations), but those on PEGDA-PC 3400 appeared to be more elongated and spindle-shaped. **(B)** None of the PEGDA-PC cantilevers actuated until at least the second day in culture, but the number of actuating cantilevers on this day was much greater for PEGDA-PC 3400 than PEGDA-PC 700. **(C)** The beating frequency of the cardiomyocytes was also much greater for PEGDA-PC 3400 than PEGDA-PC 700, indicating a preference for the softer material. Statistics by one-way ANOVA, Tukey's test, *$p < 0.05$ for $n = 8$ and SD.

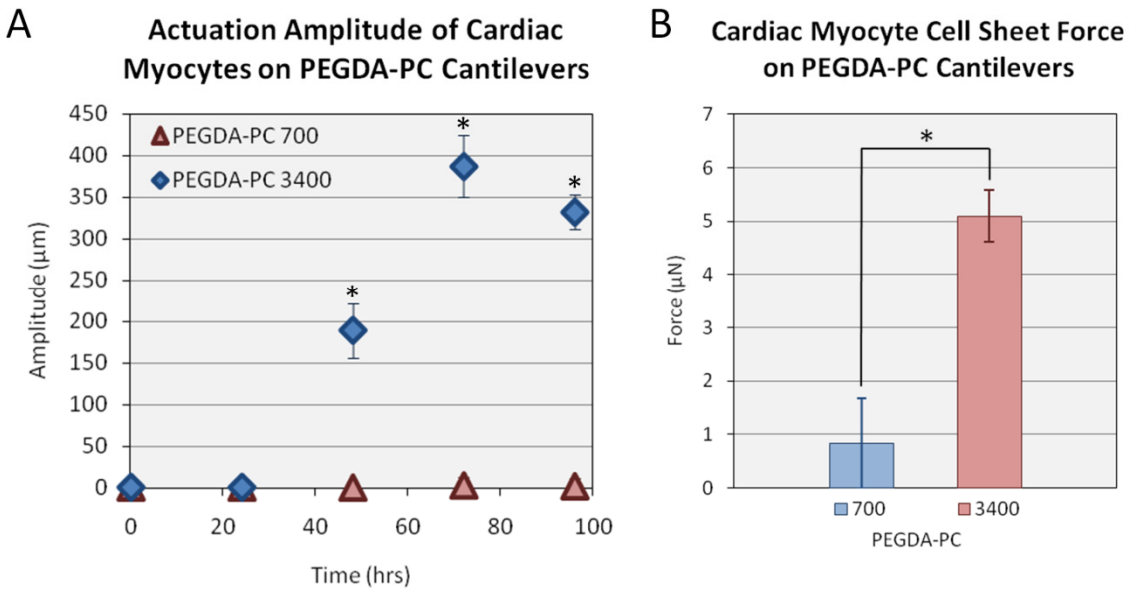

Fig. 4.9 | Force of contraction. Using an equation for cantilever beam stiffness, the force of contraction was calculated by multiplying the stiffness by the deflection of the cantilever after contraction. Statistics by one-way ANOVA, Tukey's test, *$p < 0.05$ for $n = 8$ and SD.

CHAPTER 5: CELL ALIGNMENT ON BIOACTUATORS

5.1 INTRODUCTION

The stereolithography apparatus (SLA) is a computer-assisted, three-dimensional (3D) printing system used for creating complex structures from photopolymerizable resins.[1] Traditionally, it is a manufacturing technique intended to produce 3D models and prototypes, but practitioners in the medical field have embraced it as a way to develop custom end-use parts and preoperative surgical plan.[2,3] The SLA and other 3D printing platforms have greatly improved the performance and fit of prosthetics and implants in combination with computed tomography (CT) or magnetic resonance imaging (MRI) technologies.[4] Fabricated parts from the SLA have been implanted as scaffolding for bone ingrowth,[5,6] molds for breast reconstruction,[7] replicas for aortic heart valves,[8] and shells for 'in-the-ear' hearing aids.

In the past few years, photopolymerizable hydrogels have been explored in the SLA as a potential class of implantable, soft materials.[9] Hydrogels, which are networks of cross-linked polymers that imbibe large amounts of water, can be used directly with living cells as a synthetic extracellular matrix (ECM) analog for providing a variety of physical, chemical, and biological cues.[10-13] In contrast to stiff 2D substrates made of polystyrene and glass, hydrogels possess 3D architecture and have tunable elasticity similar to tissues and organs. Cell attachment,[12,14,15] spreading,[16-18] communication,[19-21] and differentiation of stem cells[16,22,23] are a few of the physical effects of matrix elasticity.

Poly(ethylene glycol) diacrylate (PEGDA) is the most commonly used photopolymerizable hydrogel in the SLA. Using the working curve equation,[1] PEGDA with varying molecular weights was characterized for building complex 3D structures.[24] Living cells encapsulated in PEGDA ($\geq M_W$ 1,000) survived the stereolithographic process and remained viable within the hydrogel for up to two weeks.[25] Integrating living cells with PEGDA hydrogels patterned in the SLA offers exciting new possibilities for tissue engineering and the development of cellular systems. For example, the SLA was used to examine cell interactions of co-cultures, such as neurons and muscle cells, encapsulated in discrete spatial locales in the same 3D construct.[26] In another example, geometric patterns of hydrogels defined in the SLA were used to localize gradients of angiogenic growth factors secreted by encapsulated fibroblasts. When implanted *in vivo* on a vascular membrane, new blood vessels sprouted on the membrane in the

same pattern as the hydrogel.[27] Furthermore, the SLA was modified for applications using multiple materials, such as hydrogel cantilevers and actuators that mimic the elasticity of the native myocardium for contractile muscle cells.[28]

Despite recent progress, the SLA is limited to minimum feature sizes that are dependent on the diameter of the laser beam. Commercial SLA systems utilize gas or solid-state lasers that have a spot size between 75 and 250 μm. This limits the ability of researchers interested in creating patterns that control cell growth and alignment to imitate the *in vivo* tissue architecture. Distinct patterns are seen throughout the body, such as complex neural networks in the brain and linear arrangement of muscle cells around the myocardium.[29] Protein immobilization for patterning has been shown on and in hydrogels[30] using thiol chemistry and two-photon irradiation,[31,32] and photolithography. Additionally, cell patterning has been shown mechanically by creating grooves,[33-36] microchannels,[37] and geometric restrictions;[33,38] however, these methods can alter material properties and mechanics which are important to maintain for specific applications.

In this current study, we exploited the cells' dependence on ECM molecules to control their growth, organization, and distribution. Specifically, we have developed a simple method to align cells on structures fabricated using the SLA by first stamping polydimethylsiloxane (PDMS) patterns of acryl-fibronectin with micro-contact printing (μCP) and transferring the patterns to hydrogels fabricated in the SLA. This technique can then be used to align living cells on 3D hydrogel geometries, including neurons, muscle cells, and endothelial cells. From a biological perspective, the elastic properties of hydrogels combined with the ability to align cells allows for realistic *in vitro* models for understanding the biology of cell development, organization, and disease. From an engineering perspective, using the SLA to create geometrically-defined, biohybrid constructs generates exemplary new applications in tissue engineering, regenerative medicine, synthetic biology, and cellular machines.

5.2 Materials and Methods

5.2.1 Preparation of PDMS stamp

Master molds for the PDMS stamps were fabricated on a silicon wafer with SU-8 negative photoresist following a standard procedure.[39,40] The master molds contained patterns of 10, 50, and 100 μm wide lines with equal spacing. The height of each pattern was 5 um. The

patterned master molds were silanized with (tridecafluoro-1,1,2,2-tetrahydrooctyl)-1-trichlorosilane in vacuum for 1 hour. PDMS (Dow Corning Sylgard 184 Silicone Elastomer Kit) was weighed out at a 10:1 ratio of polymer-to-curing agent (heat activated). The materials were thoroughly mixed for 3 minutes to ensure even distribution of the curing agent and poured onto the patterned master molds. Samples were placed in a desiccator, pulled under vacuum, and baked at 80 ^{o}C overnight.

5.2.2 Preparation of fibronectin and acryl-fibronectin ink

Fibronectin from bovine plasma solution (Sigma Aldrich, St. Louis, MO, USA) was diluted in PBS to a concentration of 50 μg mL^{-1}. For acryl-fibronectin ink, monoacrylated poly(ethylene glycol)-N-hydroxysuccinimide (acryl-PEG-NHS, M_W 3500, JenKem Technology, Allen, TX, USA) was dissolved in PBS at a concentration of 30 mg mL^{-1}. A working solution of acryl-fibronectin ink was prepared by mixing acryl-PEG-NHS with fibronectin at a 2:1 molar ratio of acrylate-to-lysine. The reaction was allowed to proceed for 30 minutes at 4 ^{o}C.

5.2.3 Micro-contact printing ink on glass coverslips

Glass coverslips were patterned by μCP[39,40] using clean PDMS stamps. Fibronectin and acryl-fibronectin ink (50 μg mL^{-1}) were coated onto PDMS stamps for one hour at 37 ^{o}C. After incubation, excess ink was aspirated and dried under a stream of N_2. Stamps were placed pattern-side down onto 18 mm^2 glass coverslips. Pressure was applied for 30 s to allow adsorption of ink to the glass, and the coverslips were incubated for 45 minutes. Stamps were removed, and the coverslips were used within one hour.

5.2.4 Preparation of hydrogel pre-polymer solution

Hydrogel pre-polymer solutions were prepared by dissolving 20% poly(ethylene glycol) diacrylate (PEGDA, M_W 3400, Laysan Bio, Arab, AL USA) in PBS. The photoinitiator, 1-[4-(2-hydroxyethoxy)-phenyl]-2-hydroxy-2-methyl-1-propane-1-one (Irgacure 2959, Ciba, Basel, Switzerland), was diluted to a 50% (w/v) stock solution in dimethyl sulfoxide (DMSO, Fisher Scientific). A final concentration of 0.5% (w/v) was added to the pre-polymer solution. All materials were prepared immediately before photopolymerization in the SLA.

5.2.5 Fabrication of photopolymerizable hydrogels

Hydrogel constructs were fabricated with a modified stereolithography apparatus (SLA 250/50, 3D Systems, Rock Hill, SC).[25] Cylindrical disks (5 mm radius) were designed in AutoCAD 2012 (Autodesk, San Rafael, CA USA) and prepared in 3D Lightyear v1.4 software (3D Systems, Rock Hill, SC) for cross-sectional slicing into 2D layers. Parameters were specified based on desired layer thickness. An 18 mm^2 glass coverslip with unpatterned and patterned lines of fibronectin or acryl-fibronectin ink 10, 50, or 100 μm wide was fixed to a 35 mm polystyrene dish with double-sided tape. Surfaces with no patterns were always used as controls. The dish was coated with hydrogel pre-polymer solution at a characterized volume determined by desired layer thickness. It was positioned at the center of the SLA platform and photopolymerized with a characterized energy dose of 150 mJ cm^{-2}. After photopolymerization, disks were rinsed in PBS and allowed to swell overnight before cell seeding.

5.2.6 Cell culture

NIH/3T3 mouse embryonic fibroblasts (ATCC, Manassas, VA USA) were cultured at 37 ^oC and 5% CO_2 in Dulbecco's modified Eagle medium (DMEM, Cellgro, Manassas, VA USA) supplemented with 10% fetal bovine serum (FBS, Sigma-Aldrich, St. Louis, MO USA), 100 U ml^{-1} penicillin, and 100 μg ml^{-1} streptomycin (Gibco, Carlsbad, CA USA). Cells were passaged no more than 10 times using 0.25% trypsin and 0.04% EDTA in HBSS (Gibco, Carlsbad, CA USA). Prior to cell seeding, hydrogel constructs were positioned in 12-well plates with fibronectin and acryl-fibronectin patterns facing up. Cells were then seeded at a density of 90,000 cells cm^{-2} over the hydrogels.

5.2.7 Fluorescence immunostaining

To verify fibronectin transfer from patterned glass slides to hydrogels, monoclonal anti-fibronectin produced in mouse (Sigma-Aldrich, St. Louis, MO USA) was diluted at 1:300 in PBS and added to the samples overnight at 4 ^oC. The solution was then aspirated and rinsed there times with PBS. Alexa Fluor 488 goat anti-mouse IgG (Life Technologies, Grand Island, NY USA) was diluted at 1:1000 in PBS and added for 2 hours at 37 ^oC. After rinsing three times with PBS, the samples were imaged with an inverted fluorescence microscope (IX81, Olympus, Center Valley, PA USA).

To visualize the morphology of fibroblasts on hydrogel constructs, the cells were fixed and labeled at different time points. For fixation, samples were rinsed with PBS and incubated in

4% paraformaldehyde (PFA, Sigma-Aldrich, St. Louis, MO USA) for 30 minutes. After rinsing three times with PBS, a solution of 3,3′-dihexyloxacarbocyanine iodide ($DiOC_6$, Life Technologies) was added at 1:1000 dilution in PBS to stain for a cell's endoplasmic reticulum, vesicle membranes, and mitochondria. Samples were then permeabilized with 0.1% Triton X-100 (Sigma Aldrich) for 10 minutes and blocked with 2.5% bovine serum albumin (BSA) in PBS to prevent non-specific binding. Cell nuclei were stained with a 1:1,000 dilution of 2-(4-amidinophenyl)-1H-indole-6-carboxamidine (DAPI, Life Technologies), and actin was stained with a 1:1,000 dilution of rhodamine phalloidin (BD Biosciences). Fluorescent images were taken with the inverted fluorescence microscope.

5.2.8 Fibronectin and acryl-fibronectin transfer to hydrogels

ImageJ software[41] was used for analysis of fibronectin, acryl-fibronectin, and cell alignment patterns. Transfer of fibronectin and acryl-fibronectin from glass coverslips to hydrogels were confirmed quantitatively by measuring the pixel intensity of fluorescent images. To calculate pixel intensity values, a line profile was drawn across the image and grey values were extracted at each point on the line. To determine the integrity and resolution of patterns, line width measurements of μCP glass coverslips and patterned hydrogels were taken. The line profile tool was used to draw horizontal lines perpendicular to patterned lines on 40x images, and the measured line widths were recorded.

5.2.9 Fast Fourier transform analysis

Fast Fourier transform (FFT) image processing analysis was previously demonstrated for cell patterning on hydrogels.[42] Briefly, ImageJ software was used to enhance image contrast, subtract the background, and filter noise from the image. Images were converted to the frequency domain by FFT transformation and rotated 90^o to account for the inherent rotation that occurs during transformation. A circle was drawn over the FFT image, and the oval profile plugin was used to radially sum pixel intensities around the circle. A power spectrum was generated based on radially summated values, with 0^o correlating to frequencies at 3 o'clock, 90^o at 12 o'clock, 180^o at 9 o'clock, and 270^o at 6 o'clock.

5.2.10 Cell morphometrics analysis

The effect of patterning at the cellular level was analyzed by observing changes in cell

shape, direction of cell elongation, and orientation of nuclei. Post-image processing, a threshold was applied to make a binary image and individual cells were identified. Image J software object tools were used to measure and compare the cell circularity and nuclear orientation. Ten circularity bins of 0.1 intervals were set up, and circularity values between 0 and 1 were placed in each bin (0 being a line and 1 being a circle). Significance was verified with a Student's t-test statistical analysis. Nuclear orientation was measured by using the 'analyze particles' tool to fit an ellipse to threshold images of DAPI-stained nuclei and measuring the angle of the ellipse. Direction and length of cell elongation was determined by measuring the angle and distance from the nucleus to the furthest edge of the actin stained cell.

5.3 RESULTS

5.3.1 FIBRONECTIN TRANSFER AND PATTERN RETENTION

To create patterns of proteins on 3D hydrogel constructs, we modified fibronectin molecules with chemically linkable acrylate groups for crosslinking to the backbone of PEGDA hydrogels during photo-polymerization. This simple concept allowed us to utilize the μCP technique to pattern acryl-fibronectin onto hydrogels prepared with the SLA (Fig. 5.1). We confirmed the transfer of acryl-fibronectin from glass coverslips to hydrogels by quantitative analysis of immunofluorescence imaging. Comparison of hydrogels built on glass coverslips with fibronectin (Fig. 5.2A) and acryl-fibronectin (Fig. 5.2B) showed that acryl-fibronectin successfully transferred from the glass coverslip to PEGDA (M_W 3,400) hydrogels. The average pixel intensity of acryl-fibronectin on hydrogels was measured at 129 ± 10.9, while fibronectin on hydrogels had an average pixel intensity of 2.6 ± 0.5 (Fig. 5.2C).

Patterned line widths of 10, 50, and 100 μm on glass coverslips and hydrogels were measured to verify pattern integrity after acryl-fibronectin transfer. Fig. 5.3 shows fluorescent images of patterned lines on glass coverslips and hydrogels. The actual line widths were 11.5 ± 0.4 μm, 49.1 ± 1.8 μm, and 98.7 ± 0.60 μm, respectively, after PDMS stamping on glass coverslips (Fig. 5.3A), and 13.4 ± 0.5 μm, 57.3 ± 0.6 μm, 110.5 ± 5.8 μm, respectively, after acryl-fibronectin transfer to the 3D hydrogel constructs (Fig. 5.3B). Fibronectin transfer did not occur without acrylate groups (Fig. 5.3C**)**. It is well-known that PEGDA (M_W 3,400) swells after photopolymerization and subsequent washing in PBS. This phenomenon caused the measured line widths on the hydrogels to be greater than those on the glass coverslip (Fig. 5.3D). However,

the average pixel intensity of fluorescently-labeled acryl-fibronectin patterns on hydrogels did not appear to decrease significantly to the extent that it would affect cell alignment.

5.3.2 Cell growth and alignment on hydrogels

NIH/3T3 mouse embryonic fibroblasts were cultured on 3D hydrogel constructs with acryl-fibronectin patterns of unpatterned, 10, 50, and 100 μm wide lines to demonstrate feasibility of cell alignment. The cells rapidly adhered to and began to spread on the line patterns after one hour in culture. Within 24 hours, the cells were activated to proliferate along the line patterns. Fig. 5.4A shows that the cells recognized the acryl-fibronectin patterns and aligned parallel to the lines. As the line spacing decreased from 100 to 10 μm, number of cells that bridged patterned lines increased. Regardless of cell bridging, the cells continued to align parallel to the lines.

It was evident from the fluorescent images that as the line patterns decreased from 100 to 10 μm, alignment of individual cells increased. At 100 μm line patterns, the cells were generally not spatially-confined, and they could spread in any direction that was not restricted by a neighboring cell. This was confirmed quantitatively with fast Fourier transform analysis (Fig. 5.4B). Conversion of images to the frequency domain revealed directed fibroblast growth and linear pattern formation. Distinct peaks were seen in the power spectrum of fibroblasts grown on patterned lines of all widths at 0^o and 180^o. Fibroblasts grown on unpatterned hydrogels lacked these peaks and had more uniformly-scattered spectrums. Furthermore, as the line widths increased, the peaks also decreased, and the spectrums were more scattered.

Cell morphometrics were used to examine the individual shape of cells on patterned and unpatterned 3D hydrogel constructs. Growth of cells along the patterned lines altered their shape, making them more linear. Fig. 5.4C shows the decreasing shift of cell circularity measurements between patterned and unpatterned cells. Average circularity was significantly different (Student's t-test, p-values = $1.97E^{-25}$ and $4.83E^{-25}$ for 10 and 50 μm lines, respectively) between unpatterned fibroblasts (0.41 ± 0.22) and fibroblasts restricted to growth on 10 μm (0.15 ± 0.10) and 50 μm (0.15 ± 0.11) lines. Cell shape was altered on 100 μm lines but was not statistically significant.

Fig. 5.5 shows further analysis of the effect of acryl-fibronectin patterns on cell shape and growth. Fibroblast elongation, which was measured from the furthest edge of stained actin on

each side of the cell to the nucleus, was parallel to line direction. Average angles were 90.86, 88.85, and 89.92^{o} for 10, 50, and 100 μm lines respectively. Unpatterned fibroblasts had an average angle of 95.35^{o} which was significantly different than patterned fibroblasts (Student's t-test, p-values = $4.6E^{-2}$, $4.9E^{-3}$, and $8.6E^{-4}$, respectively). Length of elongation caused by patterning showed a significantly greater difference. The average length of extended actin in the cell was 44.33 μm for unpatterned fibroblasts. Patterned cells had average lengths of 78.8, 54.9, and 40.6 μm for 10, 50, and 100 μm lines, respectively (Student's t-test, p-values = $9.16E^{-18}$, $6.78E^{-08}$, and $2.05E^{-4}$). Nuclear alignment proved to be insignificant (Student's t-test, p = 0.42, 0.90, 0.52 for 10, 50, and 100 μm) on patterned and unpatterned lines, although there was a trend seen that nuclei aligned parallel to patterns (average orientation = 79.97, 89.98, 93.43, and 93.13^{o} for unpatterned, 10, 50, and 100 μm). The scatter plots in Fig. 5.5A and B show the clustering of cell elongation around 90^{o} for cells grown on patterns and the distribution of nuclear alignment, respectively.

5.4 DISCUSSION

Applications for the SLA and other 3D printing platforms using living cells and cell-instructive 3D microenvironments are expanding rapidly. However, none of these enabling technologies are without their drawbacks, and continual development is needed to accommodate for the growing number of applications. One of the current limitations of commercial laser-based stereolithographic systems is the minimum feature size required to imitate cell growth and alignment patterns in complex tissue architecture. While photopolymerizable hydrogels can be functionalized with proteins and peptides to enhance cell attachment, it is difficult to pattern them with the SLA at length scales comparable to the cell size. Grooves, microchannels, and other geometrically-restrictive techniques that affect the topology of the hydrogels can alter mechanical properties, which are important in many of these applications.

Micro-contact printing (μCP) is a well-established technique that does not affect the mechanical properties of hydrogels. It was chosen to pattern acryl-fibronectin in combination with the SLA based on its ease of use, compatible setup, and unrestricted variation in shapes and sizes. Modification of fibronectin with acrylate groups (acryl-fibronectin) was the key component to this method. Without tethered ECM proteins or peptides, PEGDA hydrogels are intrinsically resistant to protein adsorption and cell adhesion. Based on low measured fluorescent

intensity, unmodified fibronectin did not transfer to the PEGDA hydrogels (Fig. 5.2A). In contrast, acryl-fibronectin had uniform and high fluorescent intensity throughout the surface of the hydrogels (Fig. 5.2B). This method is not restricted to fibronectin; other proteins or peptides with free lysine ($-NH_3$) groups, such as laminin, collagen, and gelatin, can also be modified with acrylate groups using the same method described. The amino acid sequence for fibronectin was collected from a protein database (NCBI) to calculate the number of free lysine groups.

PEGDA was chosen as the hydrogel material based on its tunable swelling ratio, elastic modulus, and pore size. It can also be modified for cell-specific adhesion, enzyme-sensitive or hydrolytic degradation, and growth factor-binding signals.[43] The swelling ratio and pore size should be large enough to allow for an adequate supply of oxygen and nutrients, while the elastic modulus and patterning resolution should be high enough for the specific application. Fig. 5.3, which compared the measured line widths on glass coverslips and hydrogels, shows a decrease in the patterning resolution on the PEGDA (M_W 3,400) hydrogels. By decreasing the M_W of PEGDA, the patterning resolution can be improved because of the reduced swelling, but this can also affect the organization and function of cells on the hydrogels.

Although a variety of other configurations are possible, we used line patterns to demonstrate directed cell growth and alignment on the hydrogels. The widths of those line patterns were varied to determine the length scale at which cells would align on the hydrogels. If widths are too thin, cell bodies may be larger than the lines, preventing appropriate cell attachment; if widths are too wide, cells may not recognize the patterns and align to them.[44] Previous findings show that individual cells can recognize lines measuring 5-100 μm wide.[45] Trends in our data support these findings, with single cells patterning to 10-50 μm wide lines and multiple cells patterning to 100 μm wide lines. In addition, a reduction in circularity can be seen, length of cell elongation, and angle of cell elongation differs between cells grown on patterned lines opposed to unpatterned cells.

Line spacing was also varied to determine length scales at which 'bridging' of cells between patterns occurred. This could prove useful for applications that require cell-cell connections between patterns or formation of cell sheets, without disturbing their alignment. For example, it is known that the complex organization of cardiac muscle cells and fibroblasts is critical to electrical and mechanical properties in the heart. Because of this, biological cantilevers and actuators cultured with aligned sheets of contractile muscle cells could generate more force

than unaligned sheets. Cell bridging would synchronize contraction of the aligned muscle cells and increase density of cells on the devices. However, an optimum line width and spacing would need to be characterized to maximize the performance of the muscle cell sheet. If line spacing was too small, cells may not be restricted to the acryl-fibronectin patterns and align properly on the hydrogels.

Other biological applications that study co-cultures and emerging behaviors of cells can benefit from this method. Motor neurons can be directed to align and interact with contractile muscle cells to form functional neuromuscular junctions (NMJ).[46] These motor neuron and muscle co-cultures can be used as *in vitro* models to understand NMJ-related pathogenesis, drug discovery, and even creation of cellular machines that utilize the sensing and actuation capabilities of the two cell types. This method can also be directly employed to study stem cell niches based on various physical properties, such as cellular organization and matrix elasticity.[47] Organized cell alignment is critical to controlling tissue architecture and biological function. Overall, there are numerous future experiments and applications that can be explored with the ability to design 3D hydrogel substrates that can support, pattern, and harness the outputs of multiple cell types.

5.5 CONCLUSION

We have demonstrated a simple method for patterning and aligning living cells on hydrogel substrates by combining the micro-contact printing (μCP) technique with the stereolithographic process. The key component of this method was acryl-fibronectin, which could be patterned onto glass surfaces and transferred to photopolymerizable PEGDA hydrogels. NIH/3T3 mouse embryonic fibroblasts were cultured on hydrogels patterned with acryl-fibronectin of various line widths. While resolution of the line widths depended on swelling ratios of the hydrogels, it did not visibly affect cell attachment or alignment on the patterns. Analysis of cells cultured on the hydrogels showed cells spreading and growing parallel to the direction of the lines. Cell 'bridging' occurred between patterns and increased as line spacing decreased. Overall, μCP can be used to enhance cell-based applications with the SLA by patterning proteins of various shapes and size on photopolymerizable hydrogels for directed cell growth and alignment. It can be used to increase hierarchical organization of cells in engineered

biohybrid systems, or to expand our understanding of developmental biology and mechanism of diseases.

5.6 Acknowledgments

This project was funded by the National Science Foundation (NSF), Science and Technology Center (STC) and Emerging Behaviors in Integrated Cellular Systems (EBICS) Grant CBET-0939511 (R.B. and H.K.) and by a cooperative agreement that was awarded to UIUC and administered by the U.S. Army Medical Research & Materiel Command (USAMRMC) and the Telemedicine & Advanced Technology Research Center (TATRC), under Contract #: W81XWH0810701.

5.7 References

1. Jacobs, P. F., *Rapid Prototyping and Manufacturing: Fundamentals of Stereolithography*, Dearborn, MI: Society of Manufacturing Engineers (1992).
2. Barker, T. M., Earwaker, W. J., & Lisle, D. A., Accuracy of stereolithographic models of human anatomy. *Australas. Radiol.* 38, 106-111 (1994).
3. Winder, J., & Bibb, R., Medical rapid prototyping technologies: state of the art and current limitations for application in oral and maxillofacial surgery. *J. Oral Maxillofac. Surg.* 63, 1006-1015 (2005).
4. Melchels, F., *et al*., Additive manufacturing of tissues and organs. *Prog. Polym. Sci.* 37, 1079-1104 (2012).
5. Cooke, M. N., *et al*., Use of stereolithography to manufacture critical-sized 3D biodegradable scaffolds for bone ingrowth. *J. Biomed. Mater. Res. B Appl. Biomater.* 64, 65-69 (2003).
6. Seitz, H., *et al*., Three-dimensional printing of porous ceramic scaffolds for bone tissue engineering. *J. Biomed. Mater. Res. B Appl. Biomater.* 74, 782-788 (2005).
7. Melchels, F., *et al*., CAD/CAM-assisted breast reconstruction. *Biofabrication* 3, 034114 (2011).
8. Sodian, R., *et al*., Application of stereolithography for scaffold fabrication for tissue engineered heart valves. *ASAIO J.,* 48, 12-16 (2002).
9. Melchels, F., Feijen, J., & Grijpma, D. W., A review on stereolithography and its applications in biomedical engineering. *Biomaterials* 31, 6121-6130 (2010).
10. Tibbitt, M. W., & Anseth, K. S., Hydrogels as extracellular matrix mimics for 3D cell culture. *Biotechnol. Bioeng.* 103, 655-663 (2009).

11. Jabbari, E., Bioconjugation of hydrogels for tissue engineering. *Curr. Opin. Biotechnol.* 22, 655-660 (2011).

12. Nguyen, K. T., & West, J. L., Photopolymerizable hydrogels for tissue engineering applications. *Biomaterials* 23, 4307-4314 (2002).

13. Ifkovits, J. L., & Burdick, J. A., Review: photopolymerizable and degradable biomaterials for tissue engineering applications. *Tissue Eng.* 13, 2369-2385 (2007).

14. Hadjipanayi, E., Mudera, V., & Brown, R. A., Guiding cell migration in 3D: a collagen matrix with graded directional stiffness. *Cell Motil. Cytoskeleton* 66, 121-128 (2009).

15. Guillame-Gentil, O., *et al*., Engineering the extracellular environment: Strategies for building 2D and 3D cellular structures. *Adv. Mater.* 22, 5443-5462 (2010).

16. Discher, D. E., Janmey, P., & Wang, Y. L., Tissue cells feel and respond to the stiffness of their substrate. *Science* 310, 1139-1143 (2005).

17. Bott, K., *et al*., The effect of matrix characteristics on fibroblast proliferation in 3D gels. *Biomaterials* 31, 8454-8464 (2010).

18. Wong, J. Y., Leach, J. B., & Brown, X. Q., Balance of chemistry, topography, and mechanics at the cell–biomaterial interface: Issues and challenges for assessing the role of substrate mechanics on cell response. *Surf. Sci.* 570, 119-133 (2004).

19. Geiger, B., Spatz, J. P., & Bershadsky, A. D., Environmental sensing through focal adhesions. *Nat. Rev. Mol. Cell Biol.* 10, 21-33 (2009).

20. Buxboim, A., Ivanovska, I. L., & Discher, D. E., Matrix elasticity, cytoskeletal forces and physics of the nucleus: how deeply do cells "feel" outside and in? *J. Cell Sci.* 123, 297-308 (2010).

21. Reinhart-King, C. A, Dembo, M., & Hammer, D. A., Cell-cell mechanical communication through compliant substrates. *Biophys. J.* 95, 6044-6051 (2008).

22. Engler, A. J., *et al*., Matrix elasticity directs stem cell lineage specification. *Cell* 126, 677-689 (2006).

23. Vogel, V., & Sheetz, M., Local force and geometry sensing regulate cell functions. *Nat. Rev. Mol. Cell Biol.* **7**, 265-275 (2006).

24. Arcaute, K., Mann, B. K., & Wicker, R. B., Stereolithography of three-dimensional bioactive poly(ethylene glycol) constructs with encapsulated cells. *Ann. Biomed. Eng.* 34, 1429-1441 (2006).

25. Chan, V., *et al*., Three-dimensional photopatterning of hydrogels using stereolithography for long-term cell encapsulation. *Lab Chip* 10, 2062-70 (2010).

26. Zorlutuna, P., *et al*., Stereolithography-based hydrogel microenvironments to examine cellular interactions. *Adv. Func. Mater.* 21, 3642-3651 (2011).

27. Jeong, J. H., *et al*., "Living" microvascular stamp for patterning of functional neovessels; orchestrated control of matrix property and geometry. *Adv. Mater.* 24, 58-63 (2012).

28. Chan, V. *et al*., Multi-material bio-fabrication of hydrogel cantilevers and actuators with stereolithography. *Lab Chip* 12, 88-98 (2012).

29. McDevitt, T., Angello, J., & Whitney, M., In vitro generation of differentiated cardiac myofibers on micropatterned laminin surfaces. *J. Biomed. Mater. Res.*, 60, 472-479 (2002).

30. Khetan, S., & Burdick, J. A., Patterning hydrogels in three dimensions towards controlling cellular interactions. *Soft Matter* **7**, 830-838 (2011).

31. Lee, S.-H., Moon, J. J., & West, J. L., Three-dimensional micropatterning of bioactive hydrogels via two-photon laser scanning photolithography for guided 3D cell migration. *Biomaterials* 29, 2962-2968 (2008).

32. West, J. L., Protein-patterned hydrogels: customized cell microenvironments. *Nature Mater.* 10, 727-729 (2011).

33. Aubin, H., *et al*., Directed 3D cell alignment and elongation in microengineered hydrogels. *Biomaterials* 31, 6941-6951 (2010).

34. Park, J., *et al*., Fabrication of complex 3D polymer structures for cell–polymer hybrid systems. *J. Micromech. Microeng.* 16, 1614-1619 (2006).

35. Kim, J., *et al*., Establishment of a fabrication method for a long-term actuated hybrid cell robot. *Lab Chip* **7**, 1504-1508 (2007).

36. Charest, J. L., *et al*., Combined microscale mechanical topography and chemical patterns on polymer cell culture substrates. *Biomaterials* 27, 2487-2494 (2006).

37. Sarig-Nadir, O., *et al*., Laser photoablation of guidance microchannels into hydrogels directs cell growth in three dimensions. *Biophys. J.* 96, 4743-4752 (2009).

38. Parker, K. K., *et al*., Directional control of lamellipodia extension by constraining cell shape and orienting cell tractional forces. *FASEB J.* 16, 1195-1204 (2002).

39. Chen, C. S., *et al*., Micropatterned surfaces for control of cell shape, position, and function. *Biotechnol. Prog.* 14, 356-363 (1998).

40. Kane, R. S., *et al*., Patterning proteins and cells using soft lithography. *Biomaterials* 20, 2363-2376 (1999).

41. Abramoff, M. D., Magalhaes, P. J., & Ram, S. J., Image processing with ImageJ. *Biophotonics Int.* 11, 36-42 (2004).

42. Millet, L. J., *et al*., Pattern analysis and spatial distribution of neurons in culture. *Integr. Biol.* 3, 1167-1178 (2011).

43. Zhu, J., Bioactive modification of poly (ethylene glycol) hydrogels for tissue engineering. *Biomaterials* 31, 4639-4656 (2010).

44. Dike, L. E., *et al*., Geometric control of switching between growth, apoptosis, and differentiation during angiogenesis using micropatterned substrates. *In Vitro Cell Dev. Biol. Anim.* 35, 441-448 (1999).

45. Kaji, H., *et al*., Intracellular Ca2+ imaging for micropatterned cardiac myocytes. *Biotechnol. Bioeng.* 81, 748-751 (2003).

46. Paik, I., *et al*., Rapid micropatterning of cell lines and human pluripotent stem cells on elastomeric membranes. *Biotechnol. Bioeng.* 109, 2630-2641 (2012).

47. Guo, X., *et al*., Neuromuscular junction formation between human stem cell-derived motoneurons and human skeletal muscle in a defined system. *Biomaterials* 32, 9602-9611 (2011).

5.8 FIGURES AND CAPTIONS

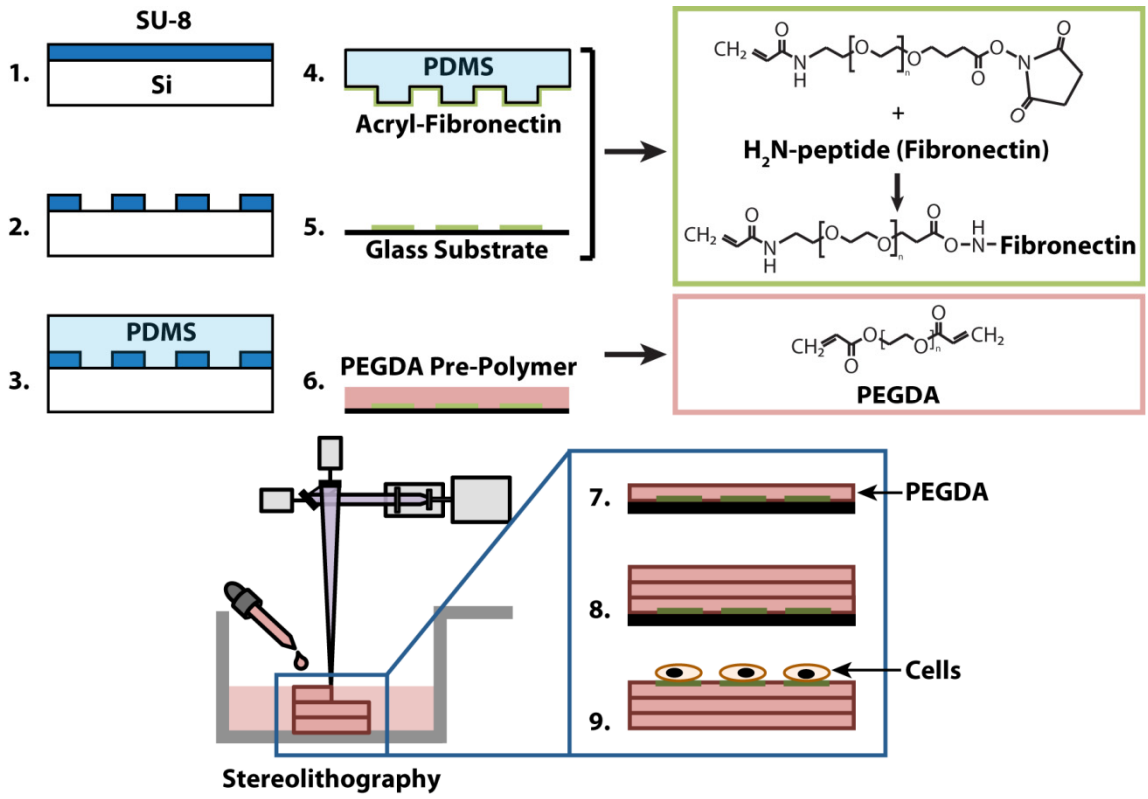

Fig. 5.1 | Patterning acryl-fibronectin hydrogels. (1) Silicon wafers were coated with 5 μm of SU-8 photoresist. (2) Line patterns were formed after exposure of photoresist and silicon with UV light through a chrome mask. (3) PDMS was poured over the silicon master and polymerized by baking. A negative of the pattern from the silicon master was imprinted on the surface of the PDMS making a stamp. (4) An ink solution containing acryl-fibronectin was pipetted onto the PDMS stamp. Acrylic fibronectin was made by mixing acryl-PEG-NHS and fibronectin in PBS and allowing the PEGDA cross-linker to attach to free lysine groups in fibronectin. (5) After stamps were incubated with ink, line patterns were transferred to glass slides by stamping. (6) Pre-polymer solution of PEGDA (M_W 3,400) and a photoactivator is poured into a dish over patterned glass slides. (7) The dish containing pre-polymer and patterned glass is put into the stereolithography apparatus (SLA) and polymerized to form a hydrogel. (8) 3D structures were built layer-by-layer adding additional pre-polymer before crosslinking. (9) Hydrogels were inverted and seeded with cells. During building of the first layer, acryl-fibronectin was transferred to the surface of the hydrogel allowing for cell attachment.

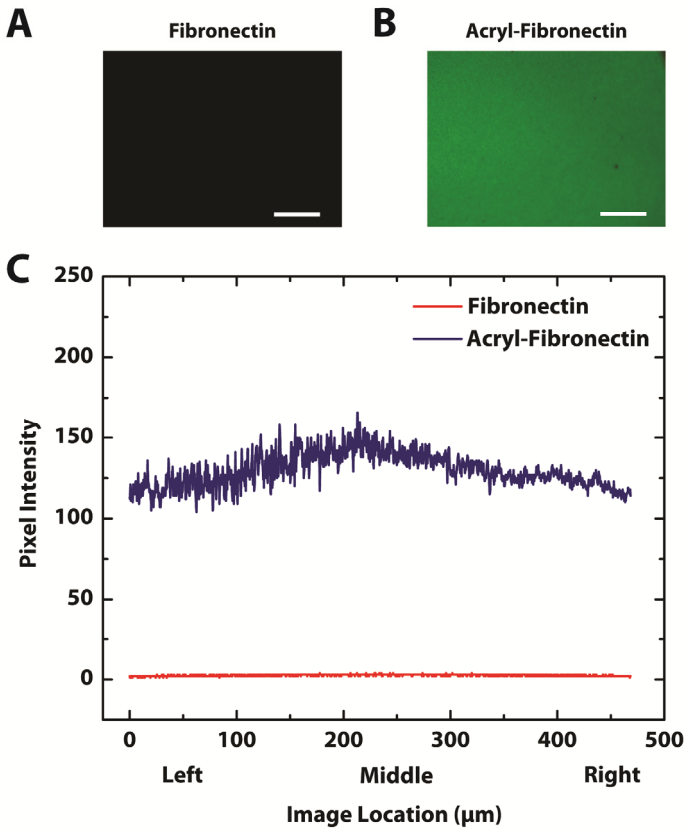

Fig. 5.2 | Measuring the transfer of fibronectin and acryl-fibronectin on hydrogels. Hydrogels were fabricated on glass slides with fluorescently-labeled fibronectin and acryl-fibronectin. (**A**) Fluorescent image of a hydrogel fabricated on a glass slide with fibronectin. (**B**) Fluorescent image of a hydrogel built on a slide with acryl-fibronectin. (**C**) Using Image J software, fluorescent intensity of fibronectin and acryl-fibronectin images were extracted and compared. Hydrogels with fibronectin had an average intensity of 2.6, while those with acryl-fibronectin had an average intensity of 129.9. This confirmed that acryl-fibronectin chemically cross-linked fibronectin to the hydrogels.

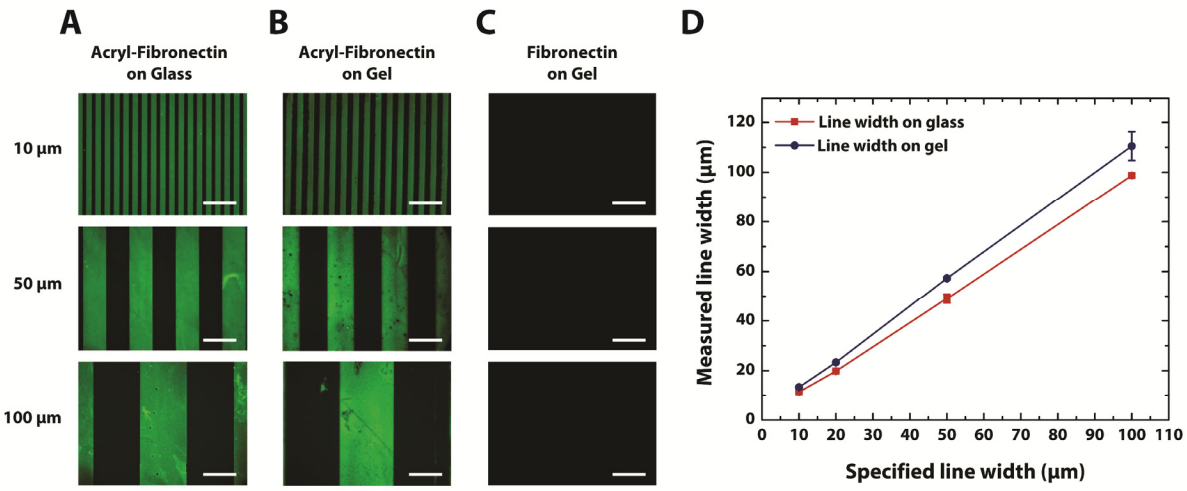

Fig. 5.3 | Transferring fibronectin patterns from glass coverslips to hydrogels. (**A**) Glass coverslips with fluorescently-labeled acryl-fibronectin lines 10, 50, and 100 µm wide. (**B**) Hydrogels with fluorescently-labeled acryl-fibronectin lines 10, 50, and 100 µm wide transferred from glass coverslips. (**C**) Hydrogels with fluorescently-labeled fibronectin lines 10, 50, and 100 µm wide (control). (**D**) Comparison of measured line widths on glass coverslips and hydrogels. Scale bars represent 50 µm wide.

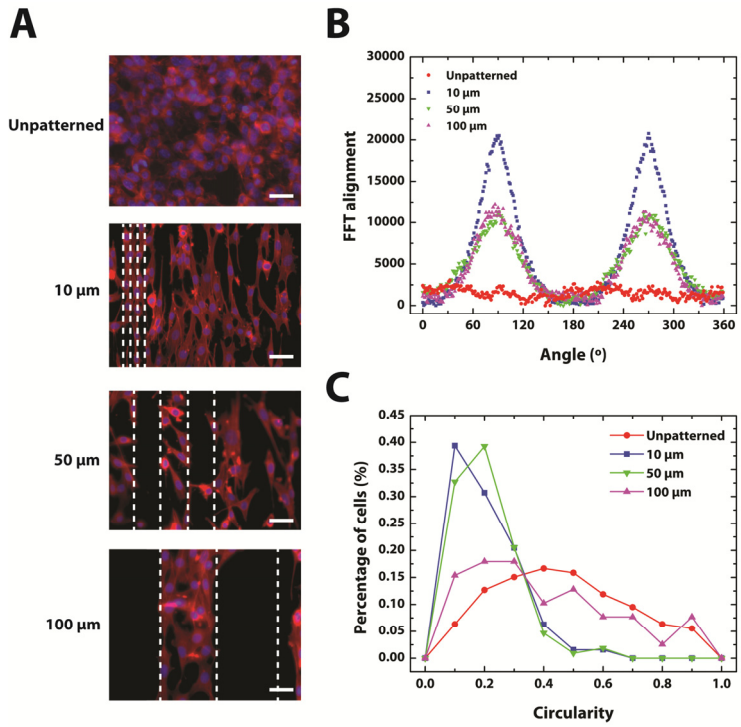

Fig. 5.4 | Aligning fibroblasts on unpatterned and patterned hydrogels. (**A**) Fibroblasts with fluorescent nuclear (DAPI) and actin (rhodamine-phalloidin) stains were cultured on hydrogels with unpatterned and patterned acryl-fibronectin with lines 10, 50, and 100 µm wide. (**B**) Power spectrum generated by radially summating frequencies from fast Fourier (FFT) converted images. Peaks at 90^{o} and 180^{o} correspond to vertical alignment in images and can be seen for fibroblasts patterned on lines. (**C**) Analysis of fibroblasts at the cellular level shows a significant decrease in circularity for cells grown on 10 and 50 µm lines. A small but insignificant shift can be seen on 100 µm lines. A decrease in circularity can be attributed to a constriction of cellular growth area. Scale bars represent 50 µm wide.

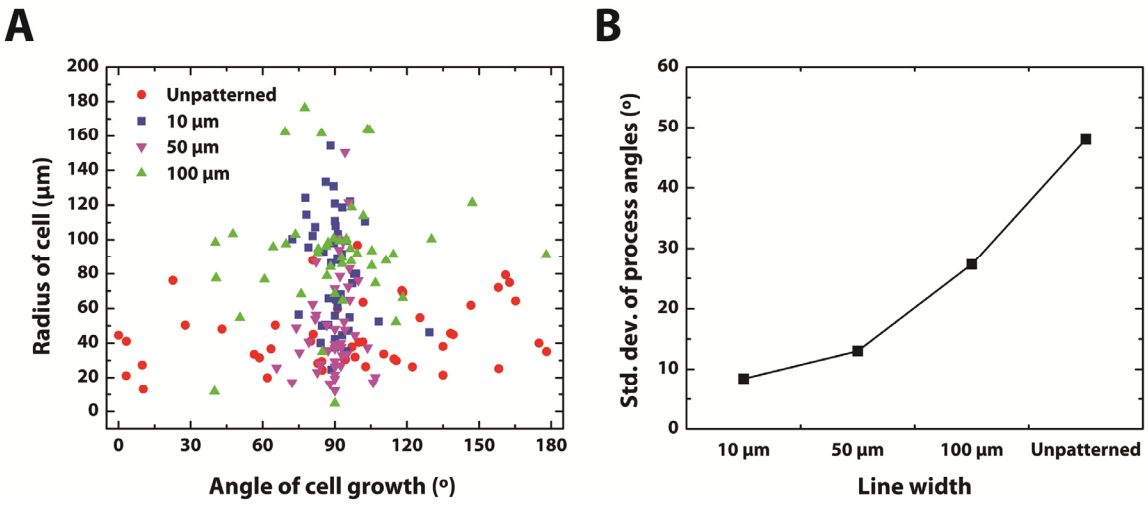

Fig. 5.5 | Measuring direction of cell elongation and nuclear alignment of fibroblasts. (**A**) Cell elongation and direction was measured by drawing a line from the nucleus to the furthest extended edge of the cell. Scatter distribution shows clustering of cell elongation near 90° for fibroblasts grown on 10 and 50 µm lines. Unpatterned cells were significantly different in both elongation and uniform distribution of edge direction. (**B**) Nuclear alignment was measure by fitting an ellipse to images of cell nuclei labeled with DAPI. There was no significant difference in the elongation or alignment of cell nuclei, but a trend in clustering near 90° for patterned cells was seen.

CHAPTER 6: LOCOMOTIVE BIO-BOTS WITH 2D CELL SHEETS

6.1 INTRODUCTION

A 'biological machine' or cellular system can be defined as a set of sub-components consisting of living cells and cell-instructive micro-environments that interact to perform a range of prescribed tasks.[1] Examples of prescribed tasks include sensing, information processing, transport, protein expression, and actuation. By combining clusters of different cell types, such as neurons, muscle cells, and endothelial cells, complex biological machines can possibly be created for specific applications in health, security, and the environment. Exemplary biological machines include organ mimics for drug testing, biological robots for replication and repair, and implantable systems for drug sensing, synthesis, and release.[2] An intelligent and instructive micro-environment is critical in these efforts to understand and design biological machines. The cells have to thrive, communicate, and proliferate in such a micro-environment while performing their designated functions. These engineered 2D and 3D micro-environments should form the scaffolding of biological machines, and should have spatially controlled mechanical and chemical properties to control their functionalities.[3] The development of enabling technologies that can fabricate the desired intelligent scaffold will greatly expedite the development of biological machines.[4-8]

Progress in developing biological actuators powered by mammalian cells has been limited to just a few reports. Carlo Montemagno and colleagues[9] cultured cardiomyocytes on a patterned film of chromium and gold attached to a thin silicon beam. After releasing the microdevice, muscle contractions caused the beam to break from the rest of the structure and bend/stretch in a walking motion, traveling at a maximum speed of 38 $\mu m \cdot s^{-1}$. Sukho Park and colleagues[10] created a microrobot with grooved cantilever beams by micromolding PDMS and aligning primary cardiac cells on the grooves to enhance their contractility. Relative to flat beams, an increase in force (88%) and bending (40%) was recorded, with an average walking speed of 140 $\mu m \cdot s^{-1}$. Finally, Kevin Kit Parker and colleagues[11] seeded cardiomyocytes on 2D thin films of PDMS, which were cut into various shapes. When released, the thin films curled or twisted into 3D conformations that performed customized functionalities of gripping, pumping, walking (133 $\mu m \cdot s^{-1}$), and swimming functions (400 $\mu m \cdot s^{-1}$). Recently, these thin film devices

were used to reverse engineer jellyfish-like constructs with comparable functional performance.[12]

In this study, we built a biological machine with an actuation module for locomotion, which we refer to as an autonomous "bio-bot". Actuation produced by a cluster of muscle cells when appropriately designed can be used to power the bio-bot. Our central hypothesis is that by integrating 3D lithographic technology with appropriate biomaterials, we can 'forward-engineer' spatially organize contractile cardiac cells on a bio-bot with desired geometry, mechanics, and cell adhesion molecules for optimal and robust locomotion. A stereo-lithographic apparatus (SLA) is a rapid prototyping tool[13,14] used to produce 3D models, prototypes, and patterns by repetitive deposition and processing of individual layers.[15,16] It uses an ultraviolet laser (325 nm) to directly write on and polymerize photosensitive liquid materials based on a computer-aided design (CAD)-based digital blueprint, sliced into a collection of 2D cross-sectional layers, and processed into a real 3D part using layer-by-layer polymerization. The automated, high-throughput process can be particularly useful for the development of cellular systems due to its multi-material capability,[17-19] which has been used with photopolymerizable hydrogels[20,21] to pattern cells or proteins at precise locations on the structure.[22,23] Cell adhesion domains, growth factors, and hydrolytic and proteolytic sequences can be incorporated into the backbone. With this technology, we expect to build biological machines with a number of prescribed tasks.

Here, we build on our earlier work of developing cell-based biohybrid actuators[19] by incorporating it into the design of our autonomous bio-bots for locomotion. We show that the initial shape and degree of curvature of the bio-bot cantilever can be precisely defined by adjusting its thickness during fabrication. The tension generated by self-organizing cardiomyocytes into cell sheets on the cantilever results in the final curvature. Based on its radii of curvature, the residual stress and cell-induced surface stresses on the cantilevers can be simulated and used in future designs. By harnessing an asymmetric design and the synchronous contraction of the cardiac cell sheet, we demonstrated a walking motion of the bio-bot. Locomotion was predicated on varying friction between the bio-bot legs and the substrate during the course of contraction. We examined how altering the cantilever curvatures can change the surface area of contact, and hence, the friction, and its effect on net forward movement of the bio-bot. Together, these studies demonstrate a unique approach to the design and fabrication of a

walking, autonomous bio-bot with hydrogels and cardiomyocytes, and explain the mechanisms underlying the directional actuation.

6.2 Materials and methods

6.2.1 Preparation of 3D printer and pre-polymer solution

The 3D printer, SLA 250/50 (3D Systems), was modified as described previously.[23] Briefly, an 18 x 18mm square No. 1 cover glass (0.13-0.17 mm thick, Corning) was attached to the center of a 35 mm culture dish (Corning) using two 1 x 1mm squares of double-sided tape. The dish was positioned at the center of the printing platform. Poly(ethylene glycol) diacrylate (PEGDA) of Mw 700 (Sigma-Aldrich) or 3400 (Laysan Bio) was dissolved in sterilized distilled water (dH_2O) to form a 20% (w/v) pre-polymer solution. The photoinitiator, 1-[4-(2-hydroxyethoxy)-phenyl]-2-hydroxy-2-methyl-1-propane-1-one (Irgacure 2959, Ciba), was dissolved in dimethyl sulfoxide (DMSO, Fisher Scientific) at 50% (w/v) stock solution and added to the pre-polymer solution to form 0.5% (w/v) of photoinitiator.

6.2.2 Bio-bot fabrication

CAD models of bio-bot arrays were generated using AutoCAD 2012 (Autodesk) and exported to 3D Lightyear v1.4 (3D Systems) in .stl format. The models were sliced into thin 2D cross-sectional layers. PEGDA M_W 3400 pre-polymer solution was pipetted into the culture dish at carefully characterized volumes. An ultraviolet laser beam was used to selectively crosslink the bio-bot cantilever structures at 150 mJ/cm^2. The elevator controlled by the SLA 250/50 was lowered by a distance equal to the thickness of the layer. Uncrosslinked PEGDA M_W 3400 was removed, and replaced with PEGDA M_W 700 to begin building the bio-bot bases. PEGDA M_W 700 was pipetted into the culture dish at the same volume that PEGDA M_W 3,400 was removed. The laser was used to selectively crosslink the bio-bot base. The part was recoated with 250 μL of PEGDA M_W 700, and the process was repeated until completion of the bio-bot base structures. The bio-bot arrays were rinsed with dH_2O in a shaker to remove uncrosslinked pre-polymer solution.

6.2.3 Surface functionalization with collagen

The bio-bot constructs invariably swelled and lifted-off the glass coverslips because of their hydrogel material. Each construct was transferred using a small spatula onto individual 12 mm circular glass coverslips (Fisher Scientific) with cantilevers down (as fabricated). Sufosuccinimidyl-6-(4'-azido-2'-nitrophenylamino)-hexanoate (Sulfo-SANPAH; Pierce Biotechnology) was prepared at 0.5 mg/mL in sterilized 50 mM HEPES, pH 8.5 immediately before use. Approximately 100 μL volume of Sulfo-SANPAH solution was added to cover the bio-bot cantilever structures. The solution was exposed to a 302 nm ultraviolet lamp (UVP Blak-Ray) at a distance of 3 inches for 5 min. The solution was aspirated out and the bio-bots were rinsed with HEPES solution to eliminate excess solution. Collagen was prepared at a concentration of 0.10 mg/mL in 0.1 N acetic acid. It was added to cover the bio-bot cantilever structures and incubated overnight at 37 ^{o}C. The solution was then aspirated and rinsed with sterilized water and PBS, pH 7.4.

6.2.4 RAT HEART DISSECTION AND CELL SHEET FORMATION

Complete growth medium consisted of Dulbecco's modified Eagle's medium (DMEM, Corning cellgro), 10% horse serum (HS, Lonza), 2.5% fetal bovine serum (FBS, Atlanta Biologicals), 100 U mL^{-1} penicillin, and 100 μg mL^{-1} streptomycin (Gibco). Neonatal hearts obtained from 0-5 day old Sprague-Dawley rats were dissected according to the Institutional Animal Care and Use Committee (IACUC) at the University of Illinois, Urbana-Champaign, under an approved protocol #11160. Briefly, whole hearts were excised from the rats and immediately placed in ice-cold HBSS buffer. Ventricles were separated from the hearts and minced into 1 mm^3 pieces with small scissors in ice-cold HBSS. The minced ventricles were gently rocked in sterilized 0.1% (w/v) purified trypsin (Worthington Biochemical) in ice-cold HBSS for 18 hours at 4 ^{o}C. Complete growth medium was added to inhibit trypsin digestion and warmed in the water bath at 37 ^{o}C for 5 min. The tissue was then digested in warm 0.1% (w/v) purified type II collagenase (Worthington Biochemical) in HBSS on a rocker for 45 min at 37 ^{o}C. The tissue was gently triturated to mechanical loosen cells and passed through a 75 μm cell strainer to filter undigested connective tissue. Cells were pelleted by centrifugation at 150 x *g* for 5 minutes to remove the supernatant with trypsin and type II collagenase. After re-suspension in warm complete growth medium, the cells were pre-plated twice for 30 minutes each to enrich for cardiac myocytes. The cells were counted and seeded on the bio-bot cantilever structures at

1,800 cells mm^{-2}. The cell-laden bio-bots were incubated overnight at 37 ^{o}C and 5% CO_2 before changing the medium.

6.2.5 Experimental setup and analysis

Side-view images and movies of the bio-bots were taken with a Sony Handycam DCR-SR68 camcorder at 30 frames per second (fps). The camcorder was fixed on a custom-made multi-axis stage (Thorlabs). Top-view images and movies of the bio-bots were taken with digital microscope cameras (Flex and RT3, SPOT) and software on either an inverted microscope (IX81, Olympus) or stereomicroscope (MZ FL III, Leica). Movies were recorded at approximately 11 fps. Net displacement of bio-bot forward motion was measured using the Measure Tool in Photoshop software (CS5.1, Adobe) by superimposing consecutive frames. Frames (3 ms) were extracted in Movie Maker (Windows) software. Contact area of the bio-bot legs to the substrate was also measured with side-view movies in Movie Maker and Photoshop, with the assumption that the contact was uniform into the frame.

6.2.6 Characterization of cantilever thickness

Thicknesses were characterized by embedding 0.1% (w/v) fluorescent polystyrene beads (500 nm, Spherotech) at 1:500 dilution in the cantilevers during photopolymerization. To change the cantilever thickness, the volume of the pre-polymer solution was varied. After photopolymerization, the cantilevers were allowed to swell in PBS on a shaker overnight at room temperature. An inverted fluorescent microscope (IX81, Olympus) with IPLab (Becton Dickenson) software was used to optically measure the vertical position of the microscope stage by manually adjusting the focus on the topmost layer of beads in the gel, z_1. The vertical position was then readjusted to the bottommost layer of beads in the gel, z_2. The cantilever thickness was then calculated using: $d = z_2 - z_1$.

6.2.7 Determination of the radii of curvature

To minimize manual error in measuring the radius of curvature (ROC), we used the average of the three ROCs obtained by three independent methods. First, we used the ThreePointCircularROI plugin in ImageJ software (NIH), which automatically calculates the center of circle and the radius of curvature from the three manually-specified points on the cantilever image. Secondly, we used the arc angle of the bent cantilever, θ to calculate ROC. The

center of the circle calculated with previous method was used to measure the arc angle. Since the length of the cantilever, L_c is fixed to be 4 mm, the ROC can be readily obtained with a simple equation $L_c = \theta$ *ROC. Lastly, the fitting circle was manually superimposed on the cantilever images and the radius of the circle was used.

6.2.8 Finite element simulation of cantilever surface stresses

The residual and cell-induced surface stresses were extracted with finite element analysis software (ANSYS). The radius of curvature (ROC) of the cantilever with varying surface stress (0~0.5N/m) on its bottom side was simulated and the residual surface stress was interpolated from the simulation results with the measured ROC from the experimental images. The cell-induced surface stress was obtained in similar manner. The ROC of the cantilever with the previously obtained residual surface stress on the bottom side and varying surface stress (0~0.5N/m) on the top side, as simulated and the cell-induced stress was interpolated with the experimentally measured ROC.

6.3 Results

6.3.1 Bio-bot fabrication

A 3D stereo-lithographic printer was used to build an array of multi-material bio-bots (Fig. 6.1*A*). Each bio-bot consisted of 'biological bimorph' cantilever structures and a base structure as its main components. The cantilevers were fabricated first; a pattern of the cantilevers was traced onto the surface of a thin layer of PEGDA (Mw 3,400) hydrogel precursor solution with an ultraviolet (UV, 325 nm) laser beam. The part was then recoated with a thin layer of PEGDA (Mw 700) hydrogel precursor solution, and the laser traced a pattern of the bases. This layer-by-layer process was repeated until the base structures were complete (Fig. 6.1*B*). The cantilever material was chosen to mimic the elasticity of the rat heart muscle (22-50 kPa),[24] while the base material was chosen to be rigid (~500 kPa) and to retain its shape.[19] A top down image of an array of bio-bots with cantilevers (7 x 2 mm) attached to their corresponding bases (2 x 2 mm) is shown (Fig. 6.1*C*). Since PEG is relatively inert, it requires surface modification with extracellular matrix proteins to enable subsequent cell attachment. We coated type I collagen onto the surface of the cantilever through addition reactions of light-activated Sulfo-SANPAH. Cardiomyocytes derived from neonatal rat hearts were extracted and seeded

onto the cantilevers (Fig. 6.1*D*). The cardiomyocytes attached to the cantilevers, increased in size, and exhibited spontaneous contractile activity. Over several days, they produced a confluent culture and formed a cardiac cell sheet that contracted in synchrony.

6.3.2 Design considerations for locomotion

Our primary experimental approach was to use the 3D printer to generate precise and iterative designs of a bio-bot that would demonstrate and help understand the basic mechanical principles for simple locomotion. The first condition was to design a bio-bot that could produce asymmetric actuation. Actuation was a result of the contractile forces of a cardiac cell sheet to retract a cantilever structure (a power stroke). A bio-bot with appropriate asymmetry would maximize the use of a power stroke for net forward movement. To support this argument, we created a symmetric bio-bot in which the base was positioned at the center of the cantilever. While the bio-bot actuated with each power stroke, it did not generate any net forward movement. Consequently, we re-positioned the base away from the center of the cantilever to establish an asymmetric structure. To accomplish this, the length of the cantilever was shortened on one side of the base. Cross-sectional images showing several iterations of the bio-bot were taken after rotating it onto its base (Fig. 6.1*E*). The last iteration was used as the final bio-bot design, as illustrated by a schematic image with attached cardiac cell sheet (Fig. 6.1*F*).

The second condition was to optimize the shape of the bio-bot, which was determined by the curvature of the cantilever, in order to regulate the friction between bio-bot "legs" and substrate. Friction is necessary to generate propulsive forces for locomotion. As it relates to the surface area of contact, friction can be optimized by using a cantilever with proper curvature. The residual surface stress generated during photopolymerization was employed to introduce a well-controlled curvature on the hydrogel cantilever following hydrogel swelling. The final curvature of the cantilever was a combined effect of the residual surface stress in the hydrogel fabrication process and a cell-induced surface stress originated from the cardiac cell sheet. By varying the thickness of the cantilever, we were able to control the initial and final curvature of the cantilever as well as the locomotive mechanism of the bio-bots. The thickness of the cantilever can be easily controlled by adjusting the volume of PEGDA (M_W 3400) hydrogel precursor solution that was added during fabrication (Fig. 6.2).

6.3.3 Extraction of residual and cell-induced surface stresses

For quantitative analysis of the bending mechanism of the cantilever, bio-bots with five different cantilever thicknesses were fabricated and imaged before seeding the cardiomyocytes (Fig. 6.3*A*) and after formation of the cardiac cell sheet (Fig. 6.3*B*). The cantilevers before cell seeding were bent upward by the residual surface stress on the top side of the cantilever and the curvature of the cantilever increased with decreasing cantilever thickness. After the formation of the cardiac cell sheet, it was clearly shown that the cell-induced surface stress on the bottom side of the cantilever decreased the curvature of the cantilever or even bent the cantilever downward.

The radii of curvature (ROC) of the cantilevers were measured from the cross-sectional images and presented as the inverse of the measured ROC (Fig. 6.3*C*). From the measured ROC of the cantilevers, the intrinsic residual surface stress and the cell-induced surface stress were extracted using finite element analysis (Fig. 6.3*D* and 6.4). The intrinsic residual surface stress was 200 ± 62 $mN \cdot m^{-1}$, and decreased with decreasing cantilever thickness. The origin of the residual surface stress can be attributed to the changes of laser intensity through the thickness of the cantilever during photopolymerization. As the laser penetrates the hydrogel precursor solution, its intensity decreases exponentially as described by the Beer-Lambert law. It is speculated that varying the intensity of the laser affected the mechanical properties of the hydrogel during photopolymerization, and that the variation in the swelling properties would lead to the generation of the surface stress.[19] The dependence of the residual surface stress on the cantilever thickness can be explained in a similar manner. As the cantilever becomes thicker, the difference in laser intensity increases and the cantilever experiences a larger variation in hydrogel swelling, resulting in higher residual surface stress. The final curvature of the cantilever was also affected by the surface stress induced by cytoskeletal tension of the cardiac cell sheet on the bottom side of the cantilever. As the cardiac cells adhered to the cantilever surface and formed a sheet, cell traction forces[25] from that sheet generated a compressive surface stress on the bottom side of cantilever surface and forced the cantilever to bend downward. This cell-induced surface stress was found to be 155 ± 30 $mN \cdot m^{-1}$.

6.3.4 Demonstration of locomotion

By varying the thickness and the curvature of the cantilever, three distinctive locomotive mechanisms were demonstrated (Fig. 6.5). Bio-bot 1 with 229~326 μm thick cantilever exhibited the first locomotive mechanism, in which the bio-bot was turned upside-down with an up-facing

base so that the actuating leg would be in contact with the substrate. The 182 μm thick cantilever would result in the bio-bot 2. When relaxed, the actuating leg of bio-bot 2 was not in contact with the substrate, but the leg retracted against the substrate during its power stroke. Bio-bot 3 was implemented with the 155 μm thick cantilever. The locomotive mechanism of bio-bot 3 was similar to that of bio-bot 2, except that the actuating leg was always in contact with the substrate. The movements of the bio-bots with the following cantilever thicknesses, 326 ± 17 (bio-bot 1), 182 ± 31 (bio-bot 2), and 155 ± 9 (bio-bot 3) μm, were further evaluated by quantitative characterization.

Time course images show net displacement of the bio-bots (Fig. 6.5 *A*-*C*). The cumulative net displacement over 30 seconds was 0, 7.15, and 1.95 mm, with an average velocity of 0, 236, and 71 $\mu m \cdot s^{-1}$ for bio-bots 1, 2, and 3, respectively (Fig. 6.5*D*). We also measured the net displacement of the bio-bots over 10 power strokes. The cumulative net displacement over 10 power strokes was 0, 3.37, and 1.82 mm, with an average displacement per power stroke of 0, 337, and 182 μm for bio-bot 1, 2, and 3, respectively. High R-squared values (above 0.999) shows that the locomotive mechanism produces a stable and identical movement of the bio-bots for each power stroke. The average beating frequencies of the cardiac cell sheets were found to be 1.14, 1.50, and 0.39 Hz for bio-bots 1, 2, and 3, respectively, at the time of recording (Fig. 6.6*A*). The beating frequencies showed fluctuations during different measurement periods (Fig. 6.6*B*).

6.3.5 Evaluation of the locomotive mechanisms

The driving force for locomotion of our bio-bot is the 'biological bimorph' cantilever consisting of a cardiac cell sheet and a variably-thick hydrogel layer. Spontaneous contraction of the cell sheet causes the cantilever to actuate and produce a power stroke. We will refer to the cantilever as the actuating leg. The power stroke of the actuating leg must exceed all opposing forces which are dominant at these length scales, including drag force and friction in an aqueous medium. Friction between the actuating leg and substrate must be present. If it is too low, the actuating leg will slide; if it is too high, it will prevent the bio-bot from moving forward. Friction between the supporting leg and substrate is also needed to balance the relaxation force of the actuating leg; otherwise, the bio-bot will slide back to its original position. Therefore, friction

between the legs and substrate need to be adjusted to maximize the power stroke for net forward movement.

Friction (F) is proportional to the actual area of contact (A): $F = \mu N = \mu N(A)$, where μ is the coefficient of friction and N is the normal force.[26] There are two forms of friction to consider here: kinetic and static. The applied force needed to overcome static friction of a stationary bio-bot is greater than that to keep it sliding, or kinetic friction. The angle of repose method was used to determine the coefficients of static (μ_s) and kinetic (μ_k) friction by raising and lowering the incline plane until the bio-bot started and stopped sliding, respectively. The measured angles, θ_s = 39.7 º for static friction and θ_k = 18.9 º for kinetic friction, were used to calculate their coefficients of friction: $\mu_x = \tan\theta_x$, which were μ_s = 0.83 and μ_k = 0.34. Relative friction forces were generated for each of the legs against the substrate by multiplying the area of contact by the normalized ratio of μ_x/μ_k depending on the motion state, as assessed through video capture (Fig. 6.7).

By changing the ROC of the cantilevers, we were able to generate three different iterations of bio-bots with distinct locomotive mechanisms. To evaluate how these bio-bots moved, we analyzed their representative power strokes using a digital camcorder at 30 frames per second (fps). A single power stroke spanned a total of 39, 27, and 30 ms each for bio-bots 1, 2, and 3, respectively. Bio-bot 2 produced power strokes with the shortest time and farthest distance of all three bio-bot designs. The sequence of a single power stroke for each bio-bot was revealed in several characteristic steps (Fig. 6.8). We examined each of these power strokes as it relates to the aforementioned principles to evaluate the efficiency of their locomotive mechanisms:

Bio-bot 1 – Generally, there was no net forward movement from bio-bot 1. The actuating leg slid back and forth between power strokes and subsequent relaxation periods (Fig. 6.8 *A* and *B*). This would indicate that there was not enough friction between the actuating leg and substrate to generate enough propulsion force to overcome the friction between the supporting legs and substrate (Fig. 6.8*C*). Without displacement of the supporting leg, the actuating leg returned to its original position. As it relates to friction, similar surface areas of contact between both legs and the substrate seem to support this argument. Without a dominant power stroke, bio-bot 1 would not able to overcome the opposing friction of the supporting leg to produce net

forward movement. However, there was the rare case that bio-bot 1 moved very slowly (27 $\mu m \cdot s^{-1}$).

Bio-bot 2 – The mechanism of locomotion for bio-bot 2 was the most efficient and produced the largest net displacement. During the power stroke, the actuating leg bent against the substrate, which caused a conformational change in its shape (Fig. 6.8 *D* and *E*). As a result, there was an increase in contact area of the actuating leg. The supporting leg tilted upward, causing a decrease in its area of contact. During relaxation, the bio-bot reverted back to its original conformation. Because the friction of the actuating leg was greater than the friction of the supporting leg, it resulted in net forward motion (Fig. 6.8*F*). After returning to its original conformation, the contact area (and thus, the friction) of the supporting leg increased, which prevented the bio-bot from moving backwards.

Bio-bot 3 – The mechanism of movement for bio-bot 3 worked similarly, but less efficiently. The actuating leg was already in contact with the substrate. During the power stroke, it retracted, causing a similar forward tilt of the supporting leg (Fig. 6.8 *G* and *H*). However, the friction of the actuating leg was smaller and did not change much. The supporting leg friction decreased as a result of the tilt, causing net forward movement during relaxation. However, during relaxation, the friction of the supporting leg was not high enough to withstand the momentum from relaxation of the actuating leg, which caused the bio-bot to slide back slightly. Therefore, the net displacement of bio-bot 3 was smaller than that of bio-bot 2 (Fig. 6.8*I*).

6.4 DISCUSSION

While various non-biological mechanical devices have been reported for locomotion on surfaces[27,28] and in aquatic environments[29], locomotion using biological elements has remained a major challenge. Inspired from biological micromachines, we have developed precise and repeatable methodologies for realizing autonomous, walking biological machines using a 3D stereo-lithographic printer. This technology enables convenient design and fabrication of bio-bots for actuation and locomotion. The 3D printer is particularly useful for testing numerous iterations of designs because of the reduction in cycle time for fabricating new constructs and the ease with which to do so by simply editing a CAD model. In contrast, micro-fabrication techniques require master molds patterned by photolithography. This conventional process requires clean room facilities and equipment, which limits the complexity of multi-layer

constructs and the ability to make changes rapidly. Furthermore, a multi-material component can be added to the 3D printer for changing the synthetic material composition or inserting cells or proteins at precise locations in the structure. Thus, material properties, such as substrate elasticity or cell adhesiveness, can be specified depending on the desired structure and function of the bio-bot to maximize force output. Hydrogels also have the unique capability of being used simultaneously as sensors, actuators, and delivery systems for therapeutic agents. Kong and colleagues demonstrated that reservoirs of living 'cell factories' can be embedded in a numerically-designed, 3D-printed hydrogel to produce and deliver growth factors in a sustained and targeted manner. These cell factories were used to actively stimulate and pattern new blood vessels.[30] Shinohara and colleagues demonstrated that glucose oxidase can be combined with pH-sensitive hydrogels to sense glucose and regulate insulin release. The presence of glucose and its subsequent conversion to gluconic acid by glucose oxidase enhanced insulin permeability through the hydrogel because of the lower pH.[31] These and other intelligent hydrogels, which respond to stimuli such as pH, temperature, enzyme, antigen, glucose, and electrical stimulation, can eventually be integrated into the bio-bots to add new tasks and functionalities.[32]

It will be necessary to further improve net displacement and longevity of the bio-bots, as well as to implement control mechanisms for developing more complex biological machines. Improved net displacement will be dependent on an optimized bio-bot design and proper formation of the cardiac cell sheet to include alignment and appropriate ratios of cardiomyocytes-to-fibroblasts. Increased longevity is important for long-term function of complex biological machines. The 'biological bimorph' cantilevers of our bio-bots perform optimally for 3-5 days before the contraction force of the power stroke decreases significantly. This is also seen in other cell-based biohybrid actuators.[9,10] A decrease in performance can be attributed to enzymatically-isolated cardiac myocytes reverting to a less differentiated phenotype by losing many of their myofibrils and other ultrastructural properties when cultured in monolayers. Furthermore, while a heterogeneous cell composition is necessary for the alignment, elongation, and network formation of cardiac myocytes and the secretion and degradation of ECM components,[34] high fractions of proliferative noncardiac cell populations can be detrimental to the performance by forming high resistance junctions with cardiac myocytes that act as passive current sinks.[35] It has also been found that the ultrastructure closely resembles the adult ultrastructure if the culture cells are placed into media containing low serum concentrations

which inhibits cell division and favors differentiation. By optimizing factors such as plating density, embryonic/neonatal age of the hearts, composition of the culture medium, and period in culture while minimizing damage during cell isolation, we can improve its long-term performance. Cultivation of cardiac myocytes in 3D biomaterial scaffolds along with electrically-induced stimulation rather than relying on spontaneous contraction may also promote more differentiated cellular phenotype and function.[36]

Future work to control when the bio-bot starts and stops or changes speed or direction can be implemented for more complex locomotion. For example, influence of various drug treatments and other control mechanisms are available.[37] The addition of isoproterenol (β-agonist) or carbamylcholine chloride (cholinergic agonist) will increase or decrease contraction frequency of the cardiac cell sheet, respectively. Heptanol is a gap junction blocker that will reversibly stop synchronous contraction. Pulsatile electrical stimulation can also be used to induce and pace the muscle cells.[38] Recently, light-induced stimulation of genetically-engineered muscle cells that express the light-activated cation channels, halorhodopsin or channelrhodopsin-2 was demonstrated.[39-42] Integration of these engineered muscle cells to optically drive the bio-bots offers another exciting future possibility. Furthermore, we envision that neural networks can be integrated into our bio-bots to regulate muscle contraction through neuromuscular junctions.[43,44] Clusters of sensory neurons can be engineered to sense and monitor the concentration of a particular species, drive the synthesis of a neurotransmitter, and communicate it to the processing neurons. The processing neurons can then initiate locomotion by translating these sensory events into action potentials that activate muscle contraction. One particular task that the bio-bots could be instructed to perform is to sense and move toward a chemical toxin and subsequently release chemicals to neutralize the toxin. Many challenges would still need to be addressed, including the development of *in vitro* neuromuscular junctions, neuronal circuitry to control the actuation of the muscle strips, coordination of the biological actuators for net movement, sensing of the target neurotoxins, and release of the neutralization agents by cell factories embedded in the hydrogels. Overall, the potential applications for these bio-bots can be truly transformative in the areas of biosensing, drug delivery, energy production, environmental remediation, and the development of artificial immune systems. In summary, we believe that our work provides a path to design and produce intelligent multi-cellular bio-bots for applications in health, security, and the environment.

6.5 ACKNOWLEDGMENTS

We thank Brian Williams and Wylie Ahmed at the University of Illinois at Urbana-Champaign (UIUC) for their help with the angle of repose measurements. We thank Elise Corbin, Larry Millet, and Professor K. J. Hsia at UIUC, and Professors H. Harry Asada, Ron Weiss, and Roger D. Kamm at the Massachusetts Institute of Technology (MIT) for their helpful discussions. This project was funded by the National Science Foundation (NSF), Science and Technology Center (STC), and Emergent Behaviors in Integrated Cellular Systems (EBICS) Grant CBET-0939511 and by a cooperative agreement that was awarded to UIUC and administered by the U.S. Army Medical Research & Materiel Command (USAMRMC) and the Telemedicine & Advanced Technology Research Center (TATRC), under Contract #: W81XWH0810701.

6.6 REFERENCES

1. Basu, S., Gerchman, Y., Collins, C. H., Arnold, F. H., & Weiss, R. A synthetic multicellular system for programmed pattern formation. *Nature* 434, 1130-1134 (2005).
2. Kamm, R. D., Nerem, R. M., & Hsia, K. J. Cells into systems. *Mech. Eng.* 30-34 (2010).
3. Lutolf, M. P. & Hubbell, J. A. Synthetic biomaterials as instructive extracellular microenvironments for morphogenesis in tissue engineering. *Nat. Biotechnol.* 23, 47-55 (2005).
4. Chung, S., Lee, J. H., Moon, M. W., Han, J., & Kamm, R. D. Non-lithographic wrinkle nanochannels for protein preconcentration. *Adv.Mater.* 20, 3011-3016 (2008).
5. Grzybowski, B. A., & Bishop, K. J. Micro- and nanoprinting into solids using reaction diffusion etching and hydrogel stamps. *Small* 5, 22-27 (2009).
6. Lee, S. J., Kang, T., Rhie, J. W., & Cho, D. W. Development of three-dimensional hybrid scaffold using chondrocyte-encapsulated alginate hydrogel. *Sens. Mater.* 19, 445-451 (2007).
7. Ling, Y., *et al.* A cell-laden microfluidic hydrogel. *Lab Chip* 7, 756-762 (2007).
8. Park, K., *et al*. 'Living cantilever arrays' for characterization of mass of single live cells in fluids. *Lab Chip* 8, 1034-1041 (2008).
9. Xi, J., Schmidt, J. J., & Montemagno, C. D. Self-assembled microdevices driven by muscle. *Nat. Mater.*, 4, 180-184 (2005).
10. Kim, J., *et al*. Establishment of a fabrication method for a long-term actuated hybrid cell robot. *Lab Chip* 7, 1504-1508 (2007).

11. Feinberg, A. W., *et al*. Muscular thin films for building actuators and powering devices. *Science* 317, 1366-1370 (2007).

12. Nawroth, J. C., *et al.* A tissue-engineered jellyfish with biomimetic propulsion. *Nat. Biotech.* 30, 792-797 (2012).

13. Peltola, S. M., Melchels, F. P. W., Grijpma, D. W., & Kellomaki, M. A review of rapid prototyping techniques for tissue engineering purposes. *Ann. Med.* 40, 268-280 (2008).

14. Burg, T., Cass, C. A. P., Groff, R., Pepper, M., & Burg, K. J. L. Building off-the-shelf tissue-engineered composites. *Philos. Transact. A Math Phys. Eng. Sci.* 368, 1839-1862 (2010).

15. Mechels, F. P. W., Feijen, J., & Grijpma, D. W. A review on stereolithography and its applications in biomedical engineering. *Biomaterials* 31, 6121-6130 (2010).

16. Jacobs, P. F. *Rapid prototyping and manufacturing: Fundamentals of StereoLithography* (Society of Manufacturing Engineers, Dearborn, 1992).

17. Arcaute, K., Mann, B. K., & Wicker, R. B. Stereolithography of spatially controlled multi-material bioactive poly(ethylene glycol) scaffolds. *Acta Biomater.* 6, 1047-1054 (2010).

18. Zorlutuna, P., Jeong, J.H., Kong, H., & Bashir, R. Stereolithography-based hydrogel microenvironments to examine cellular interactions. *Adv. Func. Mater.* 21, 3642-3651 (2011).

19. Chan, V., *et al.* Multi-material bio-fabrication of hydrogel cantilevers and actuators with stereolithography. *Lab Chip* 10, 2062-2070 (2012).

20. Drury, J. L. & Mooney, D. J. Hydrogels for tissue engineering: scaffold design variables and applications. *Biomaterials* 24, 4337-4351 (2003).

21. Slaughter, B. V., Khurshid, S. S., Fisher, O. Z., Khademhosseini, A., & Peppas, N. A. Hydrogels in regenerative medicine. *Adv. Mater.* 21, 3307-3329 (2009).

22. Arcaute, K., Mann, B. K., & Wicker, R. B. Stereolithography of three-dimensional bioactive poly(ethylene glycol) constructs with encapsulated cells. *Ann. Biomed. Eng.* 34, 1429-1441 (2006).

23. Chan, V., Zorlutuna, P., Jeong, J. H., Kong, H., & Bashir, R. Three-dimensional photopatterning of hydrogels using stereolithography for long-term cell encapsulation. *Lab Chip* 10, 2062-2070 (2010).

24. Wang, J. H. C. & Lin, J. S. Cell traction force and measurement methods. *Biomechan. Model Mechanobiol.* 6, 361-371 (2007).

25. Bhana, B., *et al.* Influence of substrate stiffness on the phenotype of heart cells. *Biotechnol. Bioeng.* 105, 1148-1160 (2010).

26. Krim, J. Friction at the atomic scale. *Sci. Am.* 275, 74-80 (1996).

27. Shepherd, R. F., *et al.* Multigait soft robot. *Proc. Natl. Acad. Sci. USA* 108, 20400-20403 (2011).

28. Chan, B., Ji, S., Kovea, C., & Hosoi, A. E. Mechanical devices for snail-like locomotion. *J. Int. Mater. Sys. Struct.* 18, 111-116 (2007).

29. Sfakiotakis, M., Lane, D. M., & Davies, J. B. C. Review of fish swimming modes for aquatic locomotion. *IEEE J. Oceanic Eng.* 24, 237-252 (1999).

30. Jeong, J. H., *et al*. 'Living' microvascular stamp for patterning of functional neovessels; orchestrated control of matrix property and geometry. *Adv. Mater.* 24, 58-63 (2012).

31. Ishihara, K., Kobayashi, M., Ishimaru, N., & Shinohara, I. Glucose induced permeation control of insulin through a complex membrane consisting of immobilized glucose oxidase and a poly(amine). *Polymer J.* 16, 625-631 (1984).

32. Ravichandran, R., Subramanian, S., Jayarama, R. V., Shayanti, M., & Seeram, R. Advances in polymeric systems for tissue engineering and biomedical applications. *Macromol. Biosci.* 12, 286-311 (2012).

33. Chan, V., *et al*. Directed cell growth and alignment on protein-patterned 3D hydrogels with stereolithography. *Virtual Phys. Prototyp.* 7, 219-228 (2012).

34. Luna, J. I., *et al*. Multiscale biomimetic topography for the alignment of neonatal and embryonic stem cell-derived heart cells. *Tissue Eng. Part C Methods* 17, 579-588 (2011).

35. Bursac, N., *et al*. Cardiac muscle tissue engineering: toward an in vitro model for electrophysiological studies. *Am. J. Physiol. Heart Circ. Physiol.* 277, H433–H444 (1999).

36. Sperelakis, N. Cultured heart cell reaggregate model for studying cardiac toxicology. *Environ. Health Perspect*. 26 243-267 (1978).

37. Shapira-Schweitzer, K., Habib, M., Gepstein, L., & Seliktar, D. A photopolymerizable hydrogel for 3-D culture of human embryonic stem cell-derived cardiomyocytes and rat neonatal cardiac cells. *J. Mol. Cell Cardiol.* 46, 213-224 (2009).

38. Berger, H. J., *et al.* Continual electric field stimulation preserves contractile function of adult ventricular myocytes in primary culture. *Am. J. Physiol.* 266, H341-H349 (1994).

39. Bruegmann, T., *et al.* Optogenetic control of heart muscle in vitro and in vivo. *Nat. Methods* 7, 897-900 (2010).

40. Arrenberg, B., Stainier, D. Y., Baier, H., & Huisken, J. Optogenetic control of cardiac function. *Science* 330, 971-974 (2010).

41. Asano, T., Ishizua, T., & Yawo, H. Optically controlled contraction of photosensitive skeletal muscle cells. *Biotechnol. Bioeng.* 109, 199-204 (2012).

42. Sakar, M. S., *et al*. Formation and optogenetic control of engineered 3D skeletal muscle bioactuators. *Lab Chip* 12, 4976-4985 (2012).

43. Umbach, J. A., Adams, K. L., Gundersen, C. B., & Novitch, B. G. Functional neuromuscular junctions formed by embryonic stem cell-derived motor neurons. *PLoS One* 7, e36049 (2012).

44. Kubo, T., Randolph, M. A., Gröger, A., & Winograd, J. M. Embryonic stem cell-derived motor neurons form neuromuscular junctions in vitro and enhance motor functional recovery in vivo. *Plast. Reconstr. Surg.* 123, 139S-148S (2009).

6.7 FIGURES AND CAPTIONS

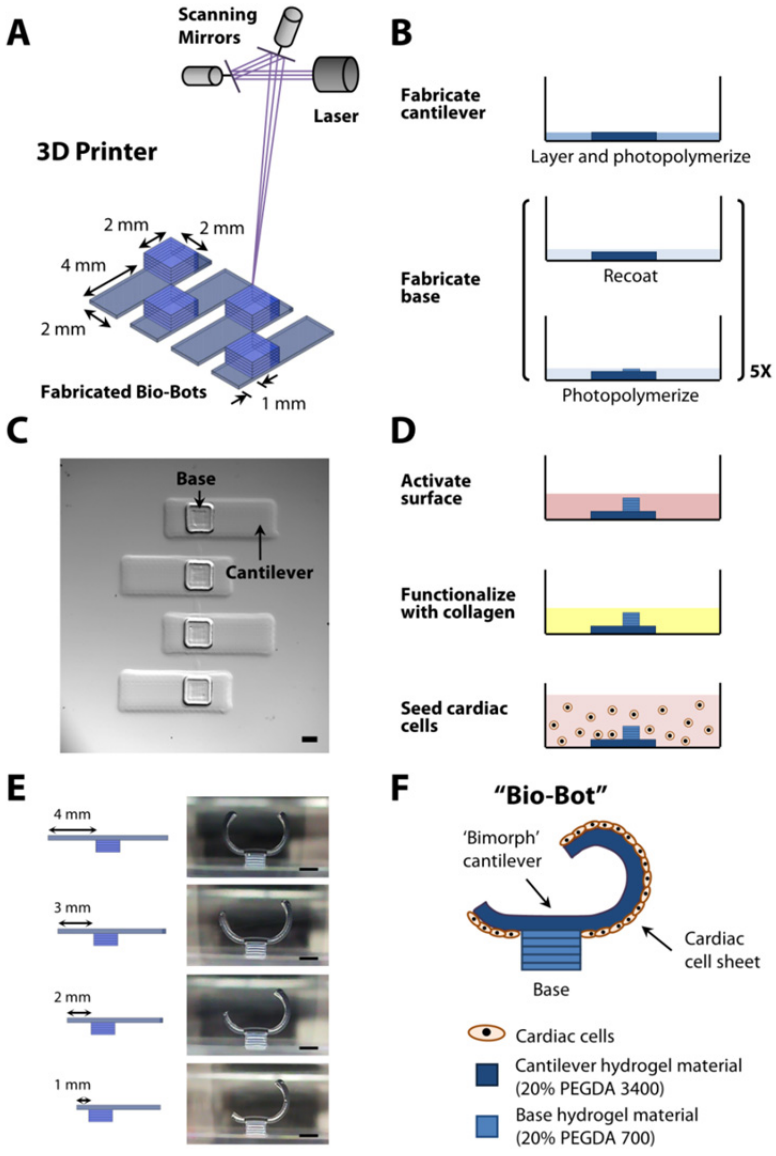

Fig. 6.1 | Fabrication and cell seeding methods. (**A**) Diagram of 3D stereo-lithographic printer consisting of a HeCd laser at 325 nm and galvanometer scanning mirrors. The mirrors are computer-controlled, and a stage lowers the part a specified distance after each layer. (**B**) Process flow diagram for high-throughput array of bio-bots. (**C**) Representative top-down images depicting an array of fabricated bio-bots with cantilever and base structures. (**D**) Process flow diagram for functionalization of the cantilevers with collagen and seeding of cardiac cells. (**E**) Representative cross-sectional images depicting iterative bio-bot designs from symmetry-to-asymmetry. (**F**) Diagram of final bio-bot design consisting of biological bimorph cantilever with seeded cardiac cell sheet. All scale bars are 1 mm

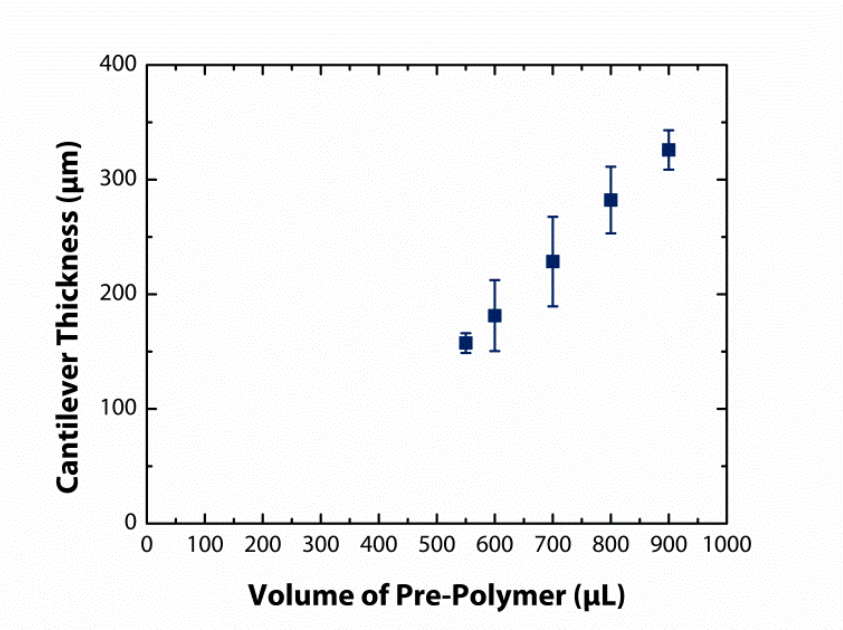

Fig. 6.2 | Characterization of cantilever thickness. Plot of cantilever thickness vs. volume of pre-polymer solution in experimental set-up. Volumes below 550 µL did not cover build area for uniformly-thick polymerization.

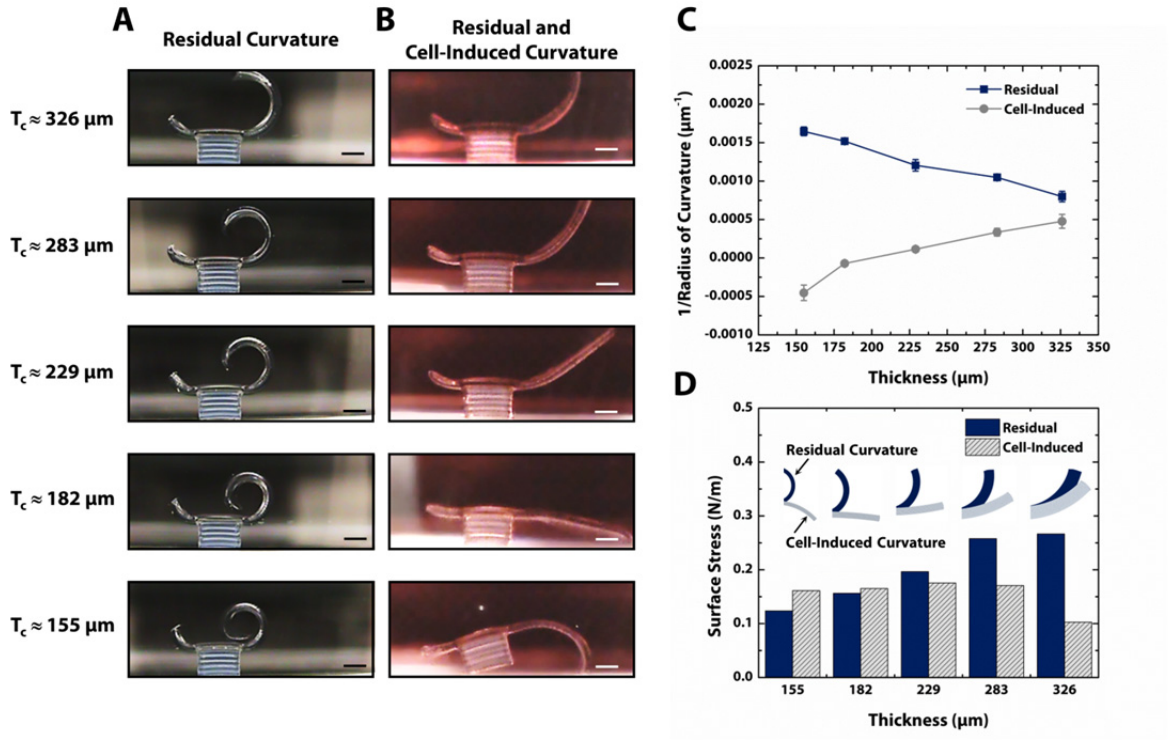

Fig. 6.3 | Design of bio-bots through residual and cell-induced surface stresses. (**A**) Representative cross-sectional images of bio-bots with varying cantilever thicknesses. After overnight swelling, the residual stresses cause the cantilevers to curl upward, depending on the thickness of the cantilever. (**B**) Representative cross-sectional images of bio-bots three days after cardiac cell seeding on the cantilever side facing the base. Cytoskeletal tension from the cells causes the cantilever to curl downward to a final bio-bot shape. (**C**) Plot of inverse radius of curvature vs. cantilever thickness for residual (pre-seeded) and residual + cell-induced curvature (post-seeded). (**D**) Plot of surface stress vs. cantilever thickness for residual and residual + cell-induced curvature. All scale bars are 1 mm.

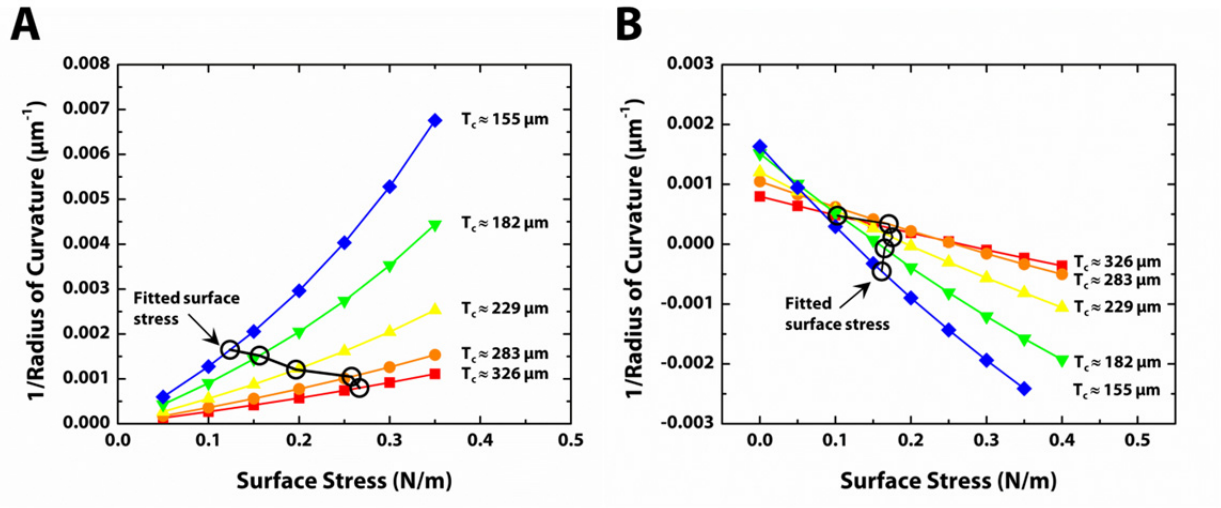

Fig. 6.4 | Extraction of residual and cell-induced surface stresses. (**A**) Plot of inverse radius of curvature vs. surface stress for residual curvature (pre-seed). (**B**) Plot of inverse radius of curvature vs. surface stress for residual + cell-induced curvature (post-seed). The measured radius of curvature was used to interpolate residual and cell-induced surface stresses from these plots.

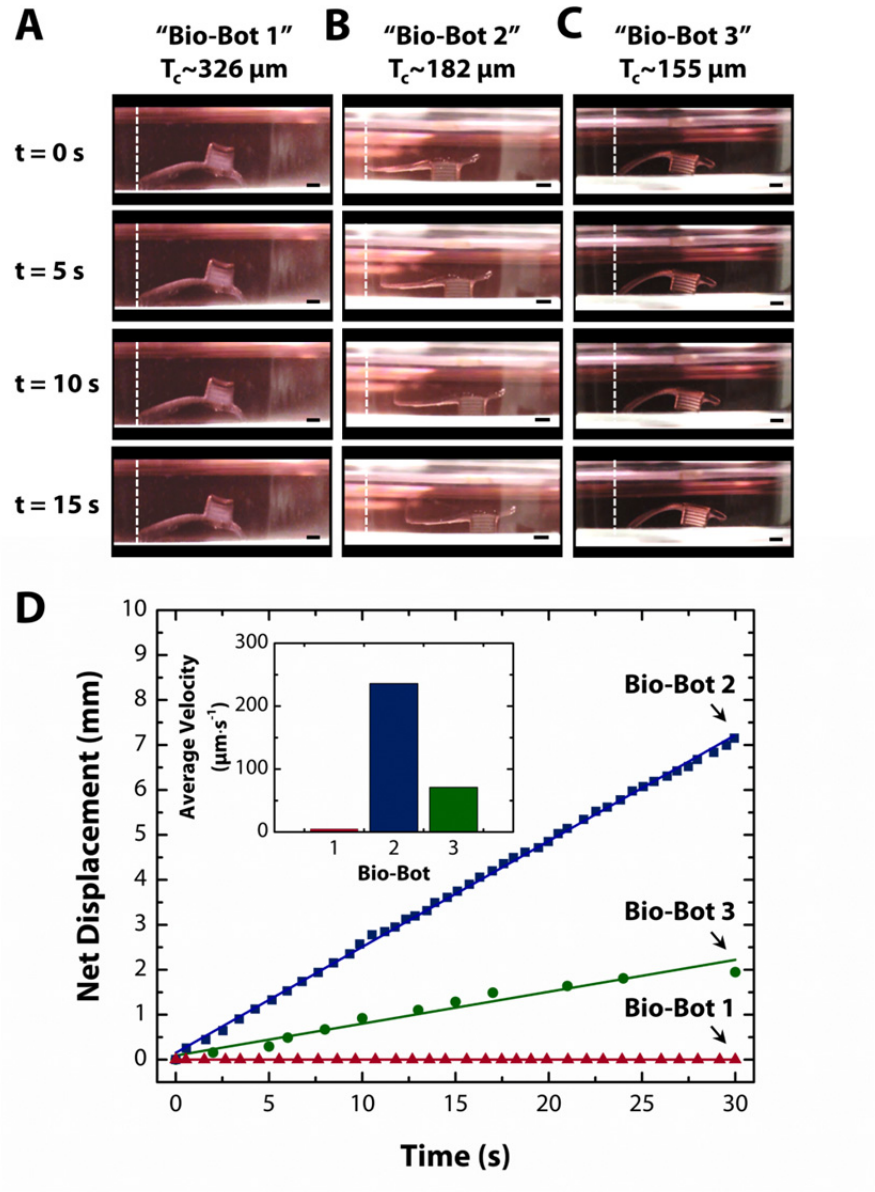

Fig. 6.5 | Demonstrations of bio-bot locomotion. (**A-C**) Time course of net forward motion for "bio-bot 1" (326 µm thick), "bio-bot 2" (182 µm thick), and "bio-bot 3" (155 µm thick) over 5 second intervals for a period of 15 seconds. (**D**) Plot of net displacement vs. time for all three bio-bot designs. The inset is a plot of average velocity vs. bio-bot design, which is extracted from the plot of net displacement vs. time. All scale bars are 1 mm.

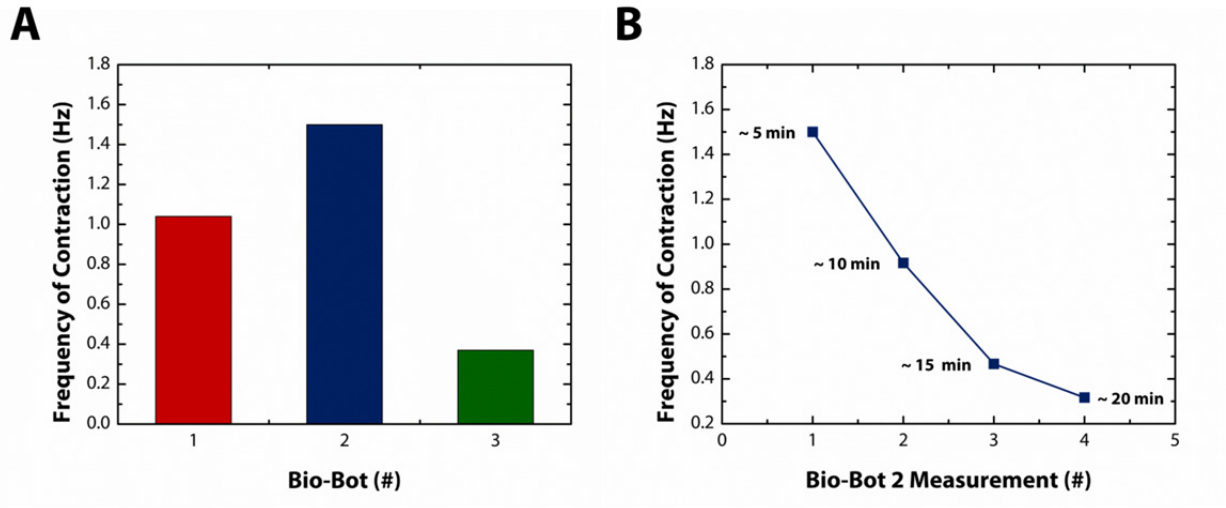

Fig. 6.6 | Measured frequency of contraction for bio-bots. (**A**) Plot of frequency of contraction vs. bio-bot. (**B**) Plot of frequency of contraction vs. number of measurement for bio-bot 2. Each measurement took approximately 5 minutes each.

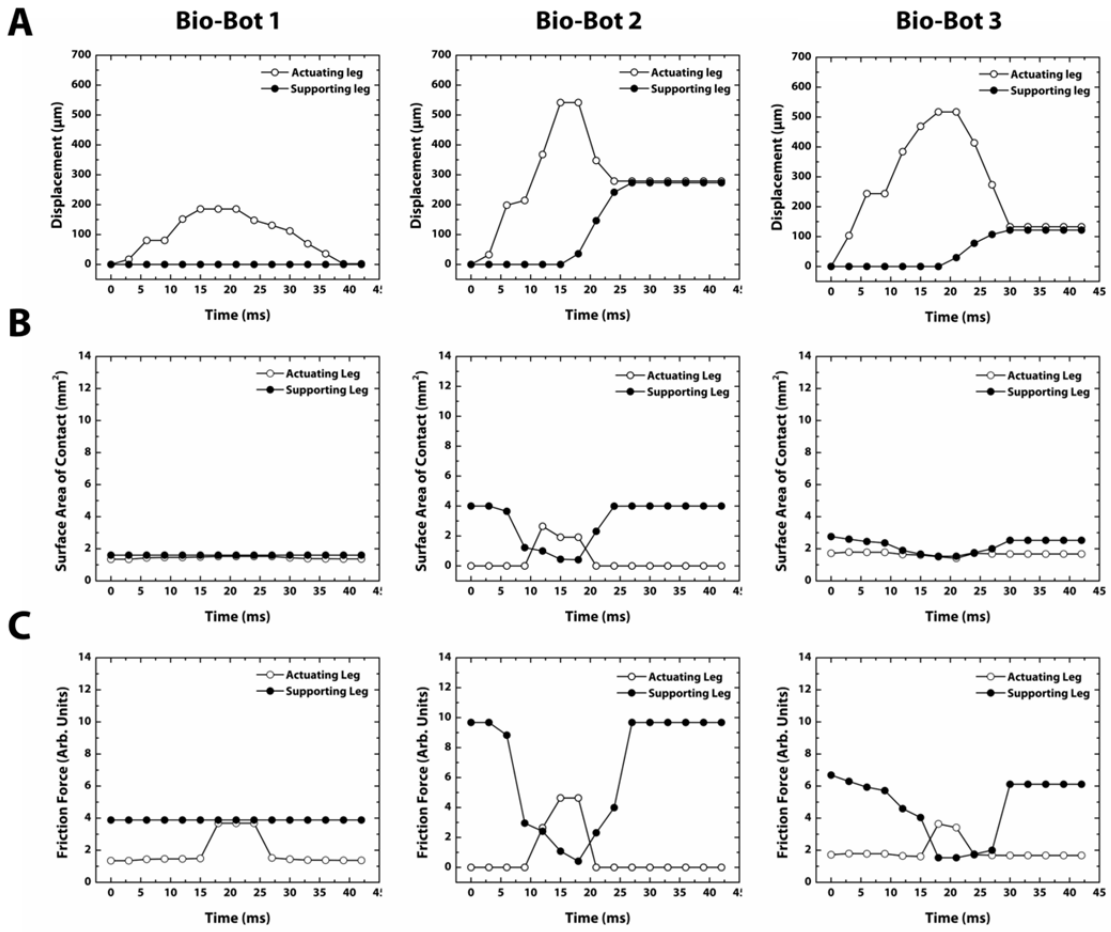

Fig. 6.7 | Derivation of relative friction force: F = μ·N(A), where μ is the coefficient of friction and N(A) is the normal force as a function of the surface area of contact. (**A**) Plot of displacement vs. time for the actuating and supporting legs during a single power stroke to determine their motion state. (**B**) Plot of the surface area of contact vs. time between the legs and substrate during a single power stroke. (**C**) Plot of relative friction force vs. time by multiplying the surface area of contact by the normalized ratio of static and kinetic friction depending on the motion state of each leg.

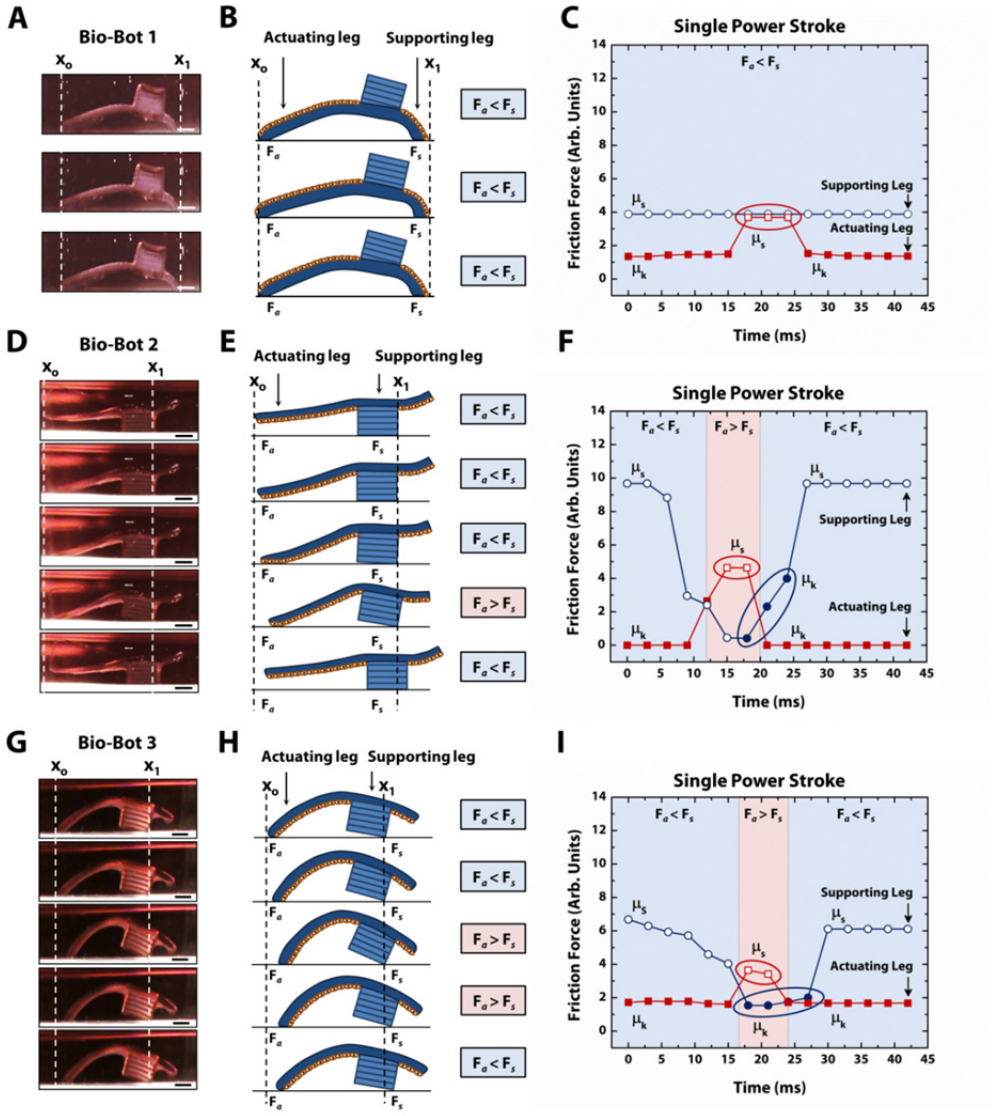

Fig. 6.8 | Mechanisms of bio-bot locomotion. (**A**) Representative cross-sectional images of a bio-bot 1 power stroke. (**B**) Step-by-step diagram of bio-bot 1 power stroke depicting no change between the friction forces of the actuating (F_a) and supporting legs (F_s), which results in no net forward motion. (**C**) Plot of friction force vs. time for a single power stroke of bio-bot 1 showing the change between the coefficients of static friction (μ_s, open fill) and kinetic friction (μ_k, solid fill). (**D**) Representative cross-sectional images of a bio-bot 2 power stroke. (**E**) Step-by-step diagram of bio-bot 2 power stroke depicting changes between F_a and F_s, which results in net forward motion. (**F**) Plot of friction force vs. time for a single power stroke of bio-bot 2 showing changes in μ_s (open fill) and μ_k (solid fill). (**G**) Representative cross-sectional images of a bio-bot 3 power stroke. (**H**) Step-by-step diagram of bio-bot 3 power stroke depicting changes between F_a and F_s, which results in net forward motion. (**I**) Plot of friction force vs. time for a single power stroke of bio-bot 3 showing changes in μ_s (open fill) and μ_k (solid fill). All scale bars are 1 mm.

CHAPTER 7: 3D MUSCLE STRIPS FOR BIO-BOTS

7.1 INTRODUCTION

The development of locomotive biological machines, or 'bio-bots', is beginning to make significant progress in the last few years. To date, locomotive bio-bots have been commonly (1) powered by cardiac myocytes, and (2) assembled on 2D substrates.[1-5] Xi *et al*. (2005)[1] cultured cardiac myocytes on a hard substrate (a thin film of chromium and gold on silicon) that would bend and stretch during contraction in a walking motion (38 $\mu m \cdot s^{-1}$). Kim *et al*. (2007)[2] fabricated grooved cantilever beams on PDMS in order to align cardiac myocytes for enhanced force (88%) and bending (40%) relative to flat beams during its walking motion (140 $\mu m \cdot s^{-1}$). Feinberg *et al*. (2007)[3] cultured cardiac myocytes on geometrically-defined 2D thin films of PDMS, which curled or twisted into 3D conformations, and demonstrated gripping, pumping, walking (133 $\mu m \cdot s^{-1}$), and swimming (400 $\mu m \cdot s^{-1}$) motions. Nawroth *et al*. (2012)[4] used this same technology to reverse engineer jellyfish-like constructs dubbed 'medusoids'. Chan *et al*. (2012)[5] cultured cardiac myocytes on 3D printed hydrogels with a long, thin leg supported by a stout supporting leg. When the cardiac myocytes contracted, the long leg pulsed, propelling the bio-bot forward.

There is considerable interest now in using skeletal muscle as a cell source for the bio-bots because of favorable attributes not available in cardiac muscle.[6] In the body, skeletal muscle facilitates movement by applying forces against bones and joints. The organization of the muscle is modular, having many longitudinally-aligned, multinucleated muscle fibers assembled together by connective tissue to form a densely-packed structure.[7] Recruitment of these fibers can be finely controlled by the nervous system, which innervates individual muscle fibers at localized regions.[8] By adjusting the number of contractile muscle fibers and the tension developed collectively, the nervous system can regulate graded muscle response for controlled movement. Consequently, skeletal muscle can be used in bio-bot designs to switch locomotion on and off by neural signals, to regulate step stroke and pacing by altering the combined contractile force, and to generate a wide range of motion by localized innervation of muscle fibers.

Recently, optical methods have been developed to depolarize or hyperpolarize neurons using specific wavelengths of light.[9-11] This method, known as 'optogenetics,' combines the

temporal and spatial precision of light pulses with cellular specificity of genetic targeting. The general strategy of optogenetics involves introducing a light-sensitive protein, such as channelrhodopsin-2 (ChR2, discovered in green algae) to a specific cell type, illuminating the cells with defined spatiotemporal parameters, and obtaining reliable readout of the cellular behavior.[12] This past year, the method was applied to cardiac[13,14] and skeletal[15,16] muscle cells to rhythmically control their contractions. It was also used to locally innervate specific regions of muscle tissue to generate movement in multiple degrees of freedom (multi-DOF). Overall, the advantage of optogenetics is its fast, precise, and local stimulation of cells and tissues, relative to electrical stimulation. Moreover, it does not require complex heterotypic cell-cell interactions that are needed for neuromuscular (neuron-to-muscle) junctions.[17,18]

The other area of improvement in locomotive bio-bots is the culture of skeletal muscle cells in 3D, rather than 2D. 3D culture is more conducive to growth and differentiation because they support a high density and 3D spreading of muscle cells, unidirectional cell alignment through the application of geometric constraints, and macroscope tissue contractions.[19] There are two current methods for engineering artificial skeletal muscle in 3D: (1) 2D-to-3D, and (2) 3D-to-3D. The first method was developed by Dennis and Kosnik (2000).[20,21] It consisted of myotubes, fibroblasts, cell-secreted ECM, and synthetic tendons. The beauty of this approach is that it does not require a pre-existing scaffold. Briefly, PDMS was set in a culture dish, and absorbed with a thin layer of laminin. Synthetic tendons were fixed at opposite ends and at a desired distance apart. Cells of myoblasts and fibroblasts were seeded, and upon reaching confluence, the medium was switched from growth to differentiation. After 2-3 weeks, the monolayer of myotubes would detach and self-organize to form a 3D muscle strip, dubbed 'myooids'. Huang *et al*. (2006) later modified the method to improve the speed of myooid formation.[22] Lam *et al.* (2009) used wavy PDMS substrates to align the myotubes in the myooids.[23] The second method was developed by Vandenburgh *et al*.,[24] although many variations exist.[25-27] It typically consisted of a pre-existing scaffold in 3D, either derived naturally (most common) or synthetically. Myoblasts with or without fibroblasts were embedded in the 3D scaffold and casted in molds. The molds were there for 3D scaffolds compacted by cells to retain certain shapes, such as strips and rings.

Here, we built on our previous work by integrating our locomotive bio-bots with a cluster of light-activated skeletal muscle cells (C2C12-ChR2 myoblasts) in 3D-to-3D scaffolding. These

skeletal muscle cells were transfected with channelrhodpsin-2, a directly light-gated cation-selective membrane channel. First, we fabricated two-legged hydrogel constructs in a pillar/beam configuration using a 3D stereo-lithographic apparatus (SLA). The SLA is a rapid prototyping tool that is used to produce 3D models, prototypes, and patterns by repetitive deposition and processing of individual layers.[28,29] The C2C12-ChR2 myoblasts were embedded in type I collagen and Matrigel™ extracellular matrix (ECM) proteins and cast around the pillars of the hydrogel constructs to form the 3D muscle strips. A number of parameters, such as the cell concentration, ECM composition, and protease inhibitors were evaluated to determine their importance in muscle formation and contractile function. Beam stiffness was also adjusted through exposure energy during fabrication to accommodate for the passive tension of the 3D muscle strips. Finally, we qualitatively assessed the differentiation and contractility of myotubes in our 3D muscle strips by fluorescently staining and visualization.

7.2 Materials and methods

7.2.1 Fabrication of hydrogel construct

The bio-bots were constructed with two capped posts as the 'legs' connected by a thin beam. A CAD model of these bio-bots was generated using AutoCAD 2012 (Autodesk) and exported to 3D Lightyear v1.4 (3D Systems) in .stl format. The models were sliced into thin 2D cross-sectional layers of specified thickness (100 μm). A pre-polymer solution of 20% (w/v) poly(ethylene glycol) diacrylate (PEGDA Mw 700) was prepared with 0.5% (w/v) Irgacure 2959 photoinitiator in distilled water to form the pre-polymer solution. PEGDA M_W 700 solution was pipetted into the culture dish at carefully characterized volumes. An ultraviolet laser beam was used to selectively crosslink the hydrogel structures. The energy dose of the laser was varied by controlling the scan speed. The elevator operated by the SLA 250/50 computer was lowered by a distance equal to the thickness of the layer. The process was then repeated until completion of the 3D part. Overnight, the bio-bots were sterilized in 100% ethanol and rinsed in PBS before interaction with cells and growth medium.

7.2.2 Cell culture

C2C12-ChR2 cells were a gift from H. Harry Asada (MIT). Briefly, C2C12 myoblasts were purchased from American Type Culture Collection (ATCC). For the generation of the

transgenic cell line, C2C12-ChR2, the cells were transfected with pAAV-Cag-Chr2-GFP-2A-Puro with Lipofectamine 2000 (Invitrogen, Carlsbad, CA) and were grown under puromycin (2.5 μg ml^{-1}) selection for 2 weeks. More than 98% of the population expressed ChR2 after selection. C2C12-ChR2 cells were cultured in growth medium containing Dulbecco's modified Eagle's medium (DMEM) supplemented with 10% fetal bovine serum (FBS, Atlanta Biologicals) and 100 U ml^{-1} penicillin, and 100 μg ml^{-1} streptomycin (Gibco). C2C12-ChR2 cells were not grown over confluence of 70% and passaged over 10 times in culture.

7.2.3 Mechanical properties of hydrogel beam

Hydrogel constructs in the form of dumbbells were fabricated with stereolithography (3D Systems). A pair of 1.2 mm diameter bent stainless steel rods (McMaster Carr) was super-glued to the ends of the dumbbells. The rods were placed into a custom-made fixture fabricated from VeroWhite polymer with an Eden 350 3D printing system (Objet). The fixture was designed to fit within an Electroforce Biodynamic test frame (Bose). The Electroforce system was fitted with a 1000 g load cell and sealed sample chamber for submerged testing. Testing was conducted within a 37 ^{o}C incubator. Once the hydrogel construct was placed in the fixture, the distance between the rods was measured with calipers and the fluid chamber was filled with 37 ^{o}C phosphate buffered saline (Lonza). The test was conducted in displacement control using WinTest control software (Bose). The samples were stretched under uniaxial tension in a Bose Electroforce Biodynamic tester at 0.05 mm/s. A video extensometer was used to track the displacement of four dots placed on the sample with a permanent marker. Load, displacement, and strain data were collected at 10 Hz using the Wintest software. The cross-sectional area of each sample was measured with calipers following the test.

7.2.4 Formation of 3D muscle strips

A cooled suspension of liquid type I collagen from rat tail (0.8, 1.4, or 2.0 mg ml^{-1}, BD Biosciences) was mixed with equal parts ice-cold growth medium and neutralized with 0.01 N NaOH. Pelleted cells (1.0, 2.5, or 5.0 x 10^{6} cells ml^{-1}) were resuspended in ice-cold growth medium and mixed with Matrigel™ (30% v/v, BD Biosciences). Liquid neutralized type I collagen was combined and mixed thoroughly with cells and Matrigel™. The mixture was then added to the post/beam assembly and incubated at 37 ^{o}C to induce collagen polymerization. Growth medium was added to each assembly upon gelation. Time-lapsed compaction was

captured with a stereomicroscope (MZ FL III, Leica). Growth medium was changed every other day. After 7 days, the myoblasts were induced to differentiate by switching to high-glucose DMEM supplemented with 10% horse serum (Lonza) and 50 ng ml^{-1} insulin-like growth factor-1 (IGF-1, Sigma). A protease inhibitor, ε-aminocaproic acid (EAC, 1 mg ml^{-1}, Sigma) was added to the growth and differentiation medium to prevent degradation of the extracellular matrix (ECM) proteins by the cells.

7.2.5 Optical stimulation of myotubes

Contractile myotubes in the muscle strips were stimulated with blue light using a fluorescent light (Xeon) that is passed through a FITC filter (460-490 nm) and focused through a 20X objective lens. The light was switched on and off at 5 second intervals using this setup. For pulsed light, a blue LED light was connected to a waveform generator (Agilent) and pulsed at different periods (250, 500, and 1000 ms) with a pulse width of 100 ms. Actuation of the bio-bot legs were imaged with an inverted microscope (IX81, Olympus).

7.2.6 Confocal fluorescence imaging

Muscle strips were washed with PBS containing calcium and magnesium and fixed in 4% (v/v) formaldehyde solution for 10 minutes at room temperature. The strips were permeabilized in 0.2% (v/v) Triton-X 100 in HBSS for 10 minutes at room temperature. The samples were washed twice with PBS before a blocking agent, Signal FX (Invitrogen), was added for 30 minutes. After another wash step, the samples were incubated overnight at 4 °C with primary antibodies, rabbit anti-α-actinin (sarcomeric) and mouse MF-20. The tissues were washed twice before being incubated with Alexa Fluor 594 goat anti-rabbit and Alexa Fluor 488 goat anti-mouse secondary antibodies for 2 hours at 37 °C. The stained samples were washed with PBS and subsequently stained with an antibody for DNA, 4′,6-diamindino-2-phenylindole (DAPI, Sigma Aldrich) for 5 minutes. After a final wash step, the cells on the cantilevers were imaged using an inverted fluorescent microscope (IX81, Olympus). The samples were also imaged with a multi-photon confocal microscope (710, Zeiss) and Mai Tai eHP Ti:sapphire laser. Images were tiled and stitched together to get a full view of the muscle strips.

7.3 Results and discussion

7.3.1 Fabrication of hydrogel constructs

The cantilevers previously developed were modified with a design for two capped posts or 'legs' to accommodate for the cell-embedded 3D collagen gels (Fig. 7.1). Without this design, the cell-embedded 3D collagen gels detached from the beam and aggregated into the shape of a ball due to cell traction forces. The capped posts acted like synthetic tendons that kept the collagen gels from shrinking and provided uniaxial tension that aligned the cells. The stiffness of the beam that connected the two legs could be modulated by the laser exposure energy. The dimensions (length x width x thickness) of the beams were 4 x 2 x 0.5 mm. These posts can later be re-designed with asymmetry for net movement (locomotion). In addition, the PEGDA backbone was not chemically-linked with cell attachment proteins because it hindered compaction of the muscle strips. Four post/beam assemblies were built for every fabrication run, and PEGDA 'holders' were built separately to confine the hydrogel constructs for 3D muscle strip formation.

7.3.2 Characterization of hydrogel constructs

While our previous cantilevers and actuators were constructed with two different Mw (700 and 3,400 g mol^{-1}), the post/beam assembly was constructed with only one Mw (700 g mol^{-1}). Instead of tuning the elastic modulus of the beam by changing its Mw, we realized that this could be done simply by varying the laser exposure energy. To measure the bulk elastic modulus of the beams, we fabricated dumbbell-shaped hydrogels with four different laser exposure energies: 100, 150, 250, and 550 mJ cm^{-1}. The dumbbells were fit to a tensile tester and stretched under uniaxial tension in liquid (Fig. 7.1A). The extracted elastic moduli were 155, 402, 551, and 757 kPa, respectively (Fig. 7.2B). This wide range in values demonstrates the utility of laser exposure energy in tuning the elastic modulus of the beam without having to change materials. It is a unique advantage of the SLA that would otherwise be difficult to do with other UV light sources.

Furthermore, we previously demonstrated that hydrogels with Mw 3,400 g mol^{-1} have an inherent residual surface stress that causes them to curl. The radius of curvature depended on the thickness of the cantilever. We have found this to be true of hydrogels with Mw 700 g mol^{-1} as well, despite their higher elastic modulus values. Additionally, the laser exposure energy was a contributing factor to the radius of curvature, independent of thickness. At low energy doses, the

cantilevers were straight, yet flexible; at higher energy doses, the cantilevers are rigid, yet curved.

7.3.3 Formation of 3D muscle strips

3D muscle strips were formed by embedding cells in extracellular matrix (ECM) proteins. In this particular case, the ECM was a mixture of type I collagen and Matrigel™, a composition of laminin, entactin, and type IV collagen. We chose collagen because naturally-derived hydrogels undergo macro-scale compaction when mixed with cells. This leads to a much higher cell density and unidirectional cell alignment between the posts. After pH neutralization, the ECM proteins gelled, and the cells were immobilized inside. The mixture was incubated in growth medium, allowing the cells to attach and generate traction forces on the fibers. Spontaneous compaction (or 'shrinkage') of the gels occurred as a result over time.

After several days, the gels compacted around the two posts, which served to restrict compaction and act as synthetic tendons, to create passive, or static, tension on the muscle strips (Fig. 7.3A). Caps at the end of the posts prevented the muscle strips from sliding off and kept them anchored in one position. As a control, the muscle strips were treated with blebbistatin (50 $\mu g\ ml^{-1}$) to confirm that gel compaction was caused by traction forces from the cells (Fig. 7.3B). Blebbistatin blocks myosin II activity in the cells, which prevents inward translation of the traction forces. Dissipation of compressive strain and lack of compaction on the ECM proteins followed. Separately, we treated cells with insulin-like growth factor 1 (IGF-1, 50 $ng\ ml^{-1}$), which is strongly mitogenic but also known to enhance differentiation in C2C12 cells. The muscle strips compacted rapidly but snapped near the posts within 24 hours (Fig. 7.3C). As a result, we showed that the formation of 3D muscle strips was cell-induced through passive tension around the two posts. However, it will be critical to adjust the passive tension accordingly on the muscle strips to prevent them from snapping.

7.3.4 Optimization of passive tension

There are several methods that we can use to adjust or control the passive tension exerted by the cells on the muscle strips. In this study, we focused on the cell concentration, collagen concentration, protease inhibitors, and beam stiffness. As we saw with the IGF-1 results, a high cell concentration, either initially or through proliferation during culture, produced higher traction forces that ultimately led to snapping of the muscle strips (normally at its weakest point,

near the posts). We systematically varied cell concentration at 1.0 (Fig. 7.4A), 2.5 (Fig. 7.4B), and 5 x 10^6 (Fig. 7.4C) cells ml^{-1}. All three conditions snapped before the 5^{th} day (120 hours). We also varied the collagen concentration at 0.8 (Fig. 7.4A), 1.4 (Fig. 7.4D), and 2.0 (Fig. 7.4E) mg ml^{-1}, which increased the stiffness of the muscle strip due to higher crosslinking densities. Again, all the conditions snapped before the 5^{th} day. However, when we added a protease inhibitor known as ε-aminocaproic acid (1 mg ml^{-1}) to the medium, the muscle strips remained intact (Fig. 7.4F). Proteases, which are either secreted by cells or presented in the serum of growth medium, break down the structural integrity of the muscle strip, leading to eventual rupture. Supplementing the medium with ε-aminocaproic acid inhibited the proteases and prevented the muscle strips from breaking down. Aprotinin is another known protease inhibitor.

7.3.5 Differentiation of 3D muscle strips

The C_2C_{12}-ChR2 muscle strips were incubated in growth medium for 7 days, followed by a switch to differentiation medium for an additional 7 days. After two weeks in culture, the muscle strips stained for heavy myosin chain and sarcomeric α-actinin. Multiple myotubes were aligned within each muscle strip (Fig. 7.6A). Because of the size of the muscle strip, it was apparent that the majority of the myotubes had formed around the exterior. This may be a result of the lack of oxygen and nutrient transport to the core of the muscle strip. A closer look at the myotubes did not reveal the well-developed parallel cross-striations (Fig. 7.6B). Curiously, the muscle strip did start to twitch spontaneously. Each time the muscle strip twitched, the posts displaced inward and returned to their original position upon relaxation. When the muscle strips were exposed to blue light, either continuously or pulsed at 500 ms intervals, there were several cases that the frequency of the twitching had increased. However, there was no evidence that pulsed blue light was controlling the actuation of the muscle strips.

7.4 Conclusion

We have demonstrated that skeletal muscle can be integrated into our locomotive bio-bot designs. We have also demonstrated that formation of muscle strips in 3D-to-3D scaffolding on our locomotive bio-bot designs is possible simply by adding a second leg to anchor and retain the bundled shape of matrix. To produce muscle strips that twitch against the legs, the optimal conditions were (1) cell concentration: 2.5 – 5.0 x 10^6 cells ml^{-1}; (2) matrix concentration: 1.4

mg ml^{-1} type 1 collagen and 30% v/v Matrigel™; (3) beam parameters: ~500 μm thick with an elastic modulus of ~400 kPa.

7.5 ACKNOWLEDGMENTS

We thank Dr. Sivaguru Mayandi at the Institute of Genomic Biology (IGB), University of Illinois at Urbana-Champaign (UIUC) for his multi-photon confocal imaging expertise and Mike Poellmann at IGB, UIUC for his ElectroForce tensile testing expertise. This project was funded by the National Science Foundation (NSF), Science and Technology Center (STC), and Emergent Behaviors in Integrated Cellular Systems (EBICS) Grant CBET-0939511.

7.6 REFERENCES

1. Xi, J., Schmidt, J. J., & Montemagno, C. D. Self-assembled microdevices driven by muscle. *Nat. Mater.* 4, 180-184 (2005).
2. Kim, J., *et al*. Establishment of a fabrication method for a long-term actuated hybrid cell robot. *Lab Chip* 7, 1504-1508 (2007).
3. Feinberg, A. W., *et al*. Muscular thin films for building actuators and powering devices. *Science* 317, 1366-1370 (2007).
4. Nawroth, J. C., *et al.* A tissue-engineered jellyfish with biomimetic propulsion. *Nat. Biotech.* 30, 792-797 (2012).
5. Chan, V., *et al*. Development of miniaturized walking biological machines. *Sci. Rep.* 2, 857 (2012).
6. King, A. M., Loiselle, D. S., & Kohl, P. Force generation for locomotion of vertebrates: skeletal muscle overview, *IEEE J. Oceanic Eng*. 29, 684-691 (2004).
7. Lieber, R. L., *Skeletal muscle structure, function, and plasticity: the physiological basis of rehabilitation* Lippincott Williams & Wilkins, Baltimore, MD (2010).
8. Berne, M. D., Levy, M. N., & Koeppen, B. M., *Physiology* Mosby, St Louis, MO (2003).
9. Boyden, E. S., Zhang, F., Bamberg, E., Nagel, G., & Deisseroth, K. Millisecond-timescale, genetically targeted optical control of neural activity. *Nat. Neurosci.* 8, 1263-1268 (2005).
10. Arenkiel, B. R., *et al*. In vivo light-induced activation of neural circuitry in transgenic mice expressing channelrhodopsin-2. *Neuron* 54, 205-218 (2007).
11. Wang, H., *et al*. High-speed mapping of synaptic connectivity using photostimulation in channelrhodopsin-2 transgenic mice. *Proc. Natl. Acad. Sci. U S A* 104, 8143-8148 (2007).
12. Deisseroth, K. Optogenetics. *Nat. Methods* 8, 26-29 (2011).

13. Bruegmann, T., *et al.* Optogenetic control of heart muscle in vitro and in vivo. *Nat. Methods* 7, 897-900 (2010).

14. Arrenberg, B., Stainier, D. Y., Baier, H., & Huisken, J. Optogenetic control of cardiac function. *Science* 330, 971-974 (2010).

15. Asano, T., Ishizua, T., & Yawo, H. Optically controlled contraction of photosensitive skeletal muscle cells. *Biotechnol. Bioeng.* 109, 199-204 (2012).

16. Sakar, M. S., *et al*. Formation and optogenetic control of engineered 3D skeletal muscle bioactuators. *Lab Chip* 12, 4976-4985 (2012).

17. Umbach, J. A., Adams, K. L., Gundersen, C. B., & Novitch, B. G. Functional neuromuscular junctions formed by embryonic stem cell-derived motor neurons. *PLoS One* 7, e36049 (2012).

18. Kubo, T., Randolph, M. A., Gröger, A., & Winograd, J. M. Embryonic stem cell-derived motor neurons form neuromuscular junctions in vitro and enhance motor functional recovery in vivo. *Plast. Reconstr. Surg.* 123, 139S-148S (2009).

19. Hinds, S., Bian, W., Dennis, R. G., & Bursac, N. The role of extracellular matrix composition in structure and function of bioengineered skeletal muscle. *Biomaterials* 32, 3575-3583 (2011).

20. Dennis, R. G., & Kosnik, P. E. Excitability and isometric contractile properties of mammalian skeletal muscle constructs engineered in vitro. *In Vitro Cell. Dev. Biol. Anim.* 36, 327-335 (2000).

21. Dennis, R. G., Kosnik, P. E., Gilbert, M. E., & Faulkner, J. A. Excitability and contractility of skeletal muscle engineered from primary cultures and cell lines. *Am J. Physiol. Cell Physiol.* 280, 288-295 (2001).

22. Huang, Y. C., Dennis, R. G., & Baar, K. Cultured slow vs. fast skeletal muscle cells differ in physiology and responsiveness to stimulation. *Am. J. Physiol. Cell Physiol.* 291, C11-17.

23. Lam, M. T., Huang, Y. C., Birla, R. K., & Takayama, S. Microfeature guided skeletal muscle tissue engineering for highly organized 3-dimensional free-standing constructs. *Biomaterials* 30, 1150-1155 (2009).

24. Vandenburgh, H., Swasdison, S., & Karlisch, P. Computer-aided mechanogenesis of skeletal muscle organs from single cells in vitro, *FASEB J.* 5, 2860-2867 (1991).

25. Zimmermann, W. H., *et al*. Tissue engineering of a differentiated cardiac muscle construct. *Circ. Res.* 90, 223-230 (2002).

26. Bian, W., Liau, B., Badie, N., & Bursac, N. Mesoscopic hydrogel molding to control the 3D geometry of bioartificial muscle tissues. *Nat. Protoc.* 4, 1522-1534 (2009).

27. Boudou, T., *et al*. A microfabricated platform to measure and manipulate the mechanics of engineered cardiac microtissues. *Tissue Eng. Part A* 18, 910-919 (2012).

28. Chan, V., *et al*., Three-dimensional photopatterning of hydrogels using stereolithography for long-term cell encapsulation. *Lab Chip* 10, 2062-70 (2010).

29. Chan, V. *et al*., Multi-material bio-fabrication of hydrogel cantilevers and actuators with stereolithography. *Lab Chip* 12, 88-98 (2012).

7.7 FIGURES AND CAPTIONS

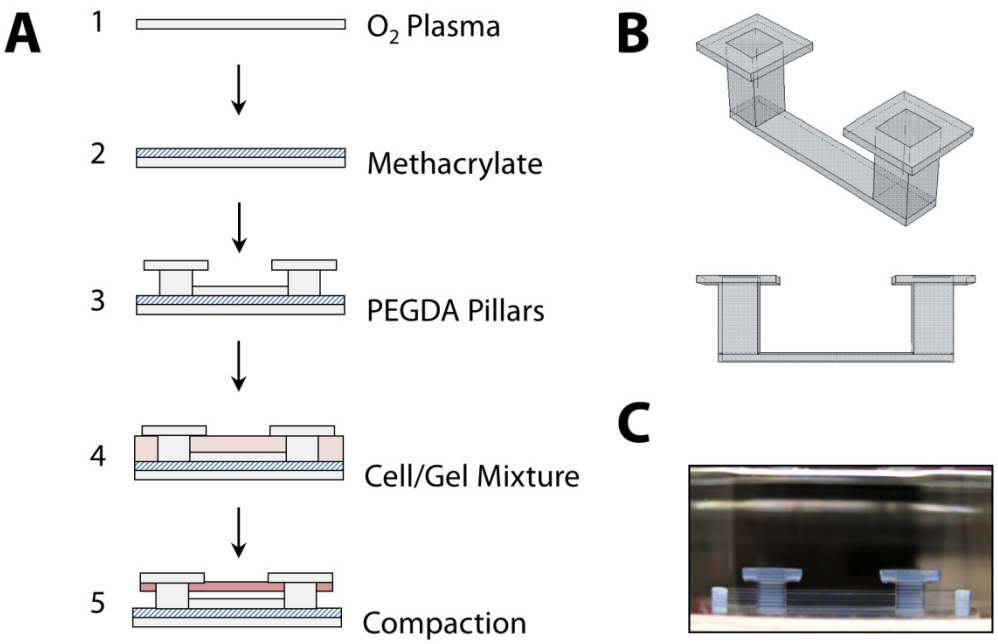

Fig. 7.1 | Fabrication of hydrogel constructs. (**A**) Fabrication process flow of hydrogel constructs and formation of 3D muscle strips: (1) Glass substrates were cleaned with oxygen-plasma treatment, (2) Dilute 3-(trimethoxysilyl)propyl methacrylate (TPM, 2% v/v) in 100% ethanol was added to methacrylate the glass substrate, (3) Poly(ethylene glycol) diacrylate (PEGDA, 20% v/v Mw 700) was layered and photopolymerized with the SLA to fabricate pillar/beam hydrogel constructs, (4) Mixtures of cell-embedded type I collagen and Matrigel™ were casted around the pillars and set in the incubator, (5) Cell attachment and traction forces pulled on and compacted the gels to form 3D muscle strip. (**B**) AutoCAD drawing (3D views) of PEG pillar/beam. Fabrication can be scaled-up to generate high-throughput, multiple arrays. (**C**) Actual image (side view) of PEG pillar/beam positioned in a PEG 'holder' for casting of a cell/gel mixture.

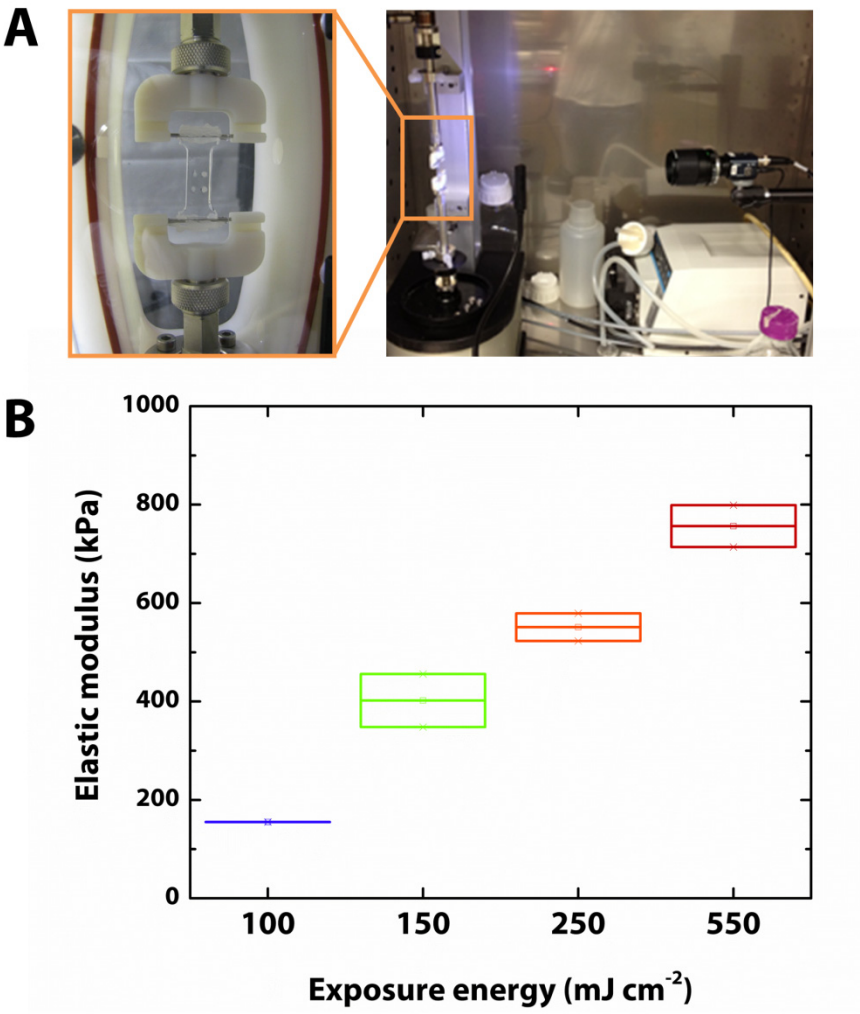

Fig. 7.2 | Mechanical testing of hydrogel beam properties. (**A**) ElectroForce (Bose) tensile tests were performed on dumbbell-shaped hydrogel samples fabricated in the SLA at various exposure energies (100, 150, 250, and 500 mJ cm^{-2}) to extract elastic modulus values. The shoulder region of the samples were glued to steel rods and inserted on clamps connected to the load frame systems. Four glued dots were added to the gauge region of the samples to track the load displacements (Inset). (**B**) Boxplot of the calculated elastic modulus values.

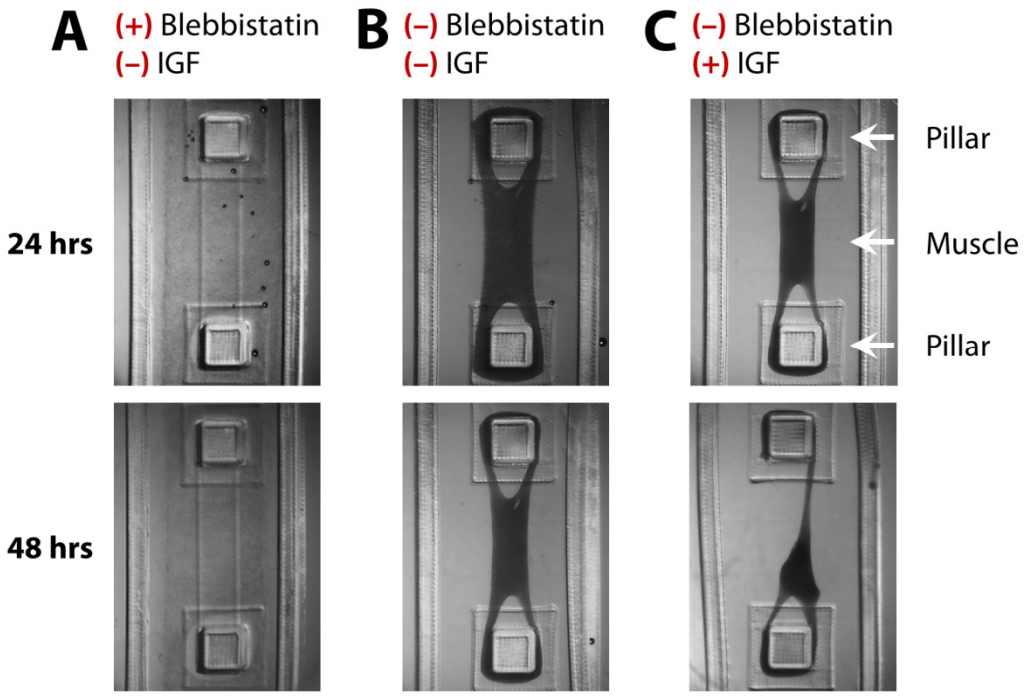

Fig. 7.3 | Formation of 3D skeletal muscle strips. (**A**) The traction forces of skeletal myoblasts (C_2C_{12}) embedded in and attached to type I collagen and Matrigel™ caused compaction of the solidified gels around pillar/beam hydrogel constructs. This was verified by independently adding (**B**) insulin-like growth factor 1 (IGF-1, 50 ng ml^{-1}) and (**C**) blebbistatin (50 μM) to the medium. Since IGF-1 is a potent mitogen, there were increased traction forces on the muscle strip, which caused it to break within 48 hours of culture. In contrast, blebbistatin is a myosin ATPase inhibitor that reduced cell contraction on the muscle strip and prevented its compaction after 48 hours of culture.

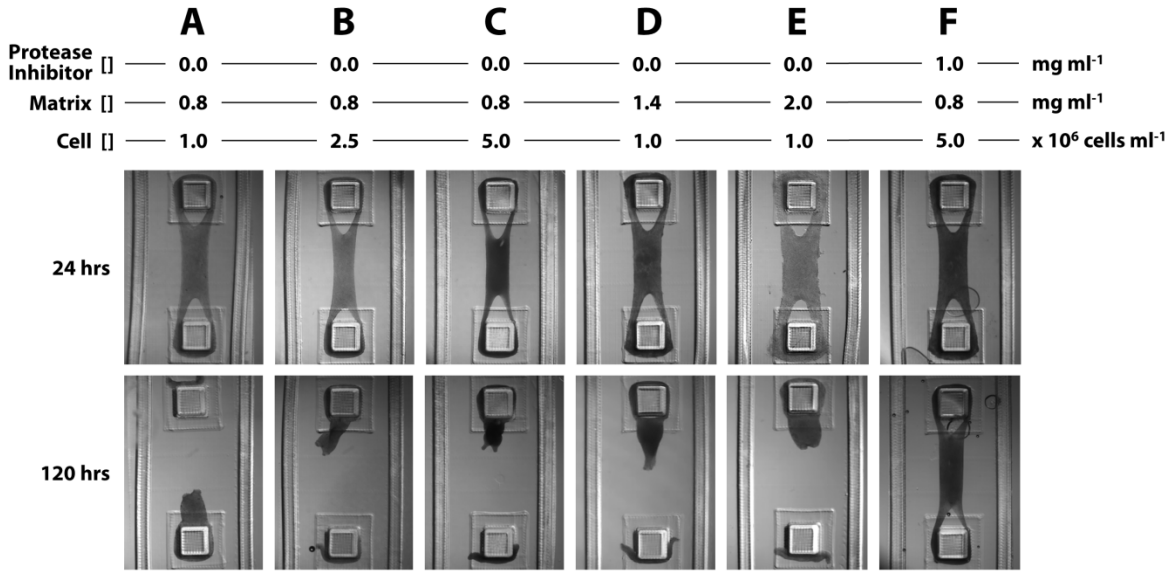

Fig. 7.4 | Optimization of passive tension parameters. 3D skeletal muscle strips consistently snapped after 5 days in culture, which led us to vary a number of parameters, such as cell (C_2C_{12} myoblast) concentration, matrix (type I collagen) concentration, and the presence of protease inhibitors (ε-aminocaproic acid). Despite variation of cell concentrations at (**A**) 1.0, (**B**) 2.5, and (**C**) 5.0 cells ml^{-1} in 0.8 mg ml^{-1} type I collagen, all the muscle strips continued to snap within 5 days. This was the also the case with increasing the matrix concentration at 0.8, (**D**) 1.4, and (**E**) 2.0 mg ml^{-1}. It is noteworthy to mention that the area of the muscle strips decreases with cell concentration, but increases with matrix concentration. (**F**) Finally, ε-aminocaproic acid (EAC) inhibits protease activity that degrades proteins, such as collagen. Addition of EAC (1 mg ml^{-1}) prevented the muscle strip from snapping (stable even after 14 days).

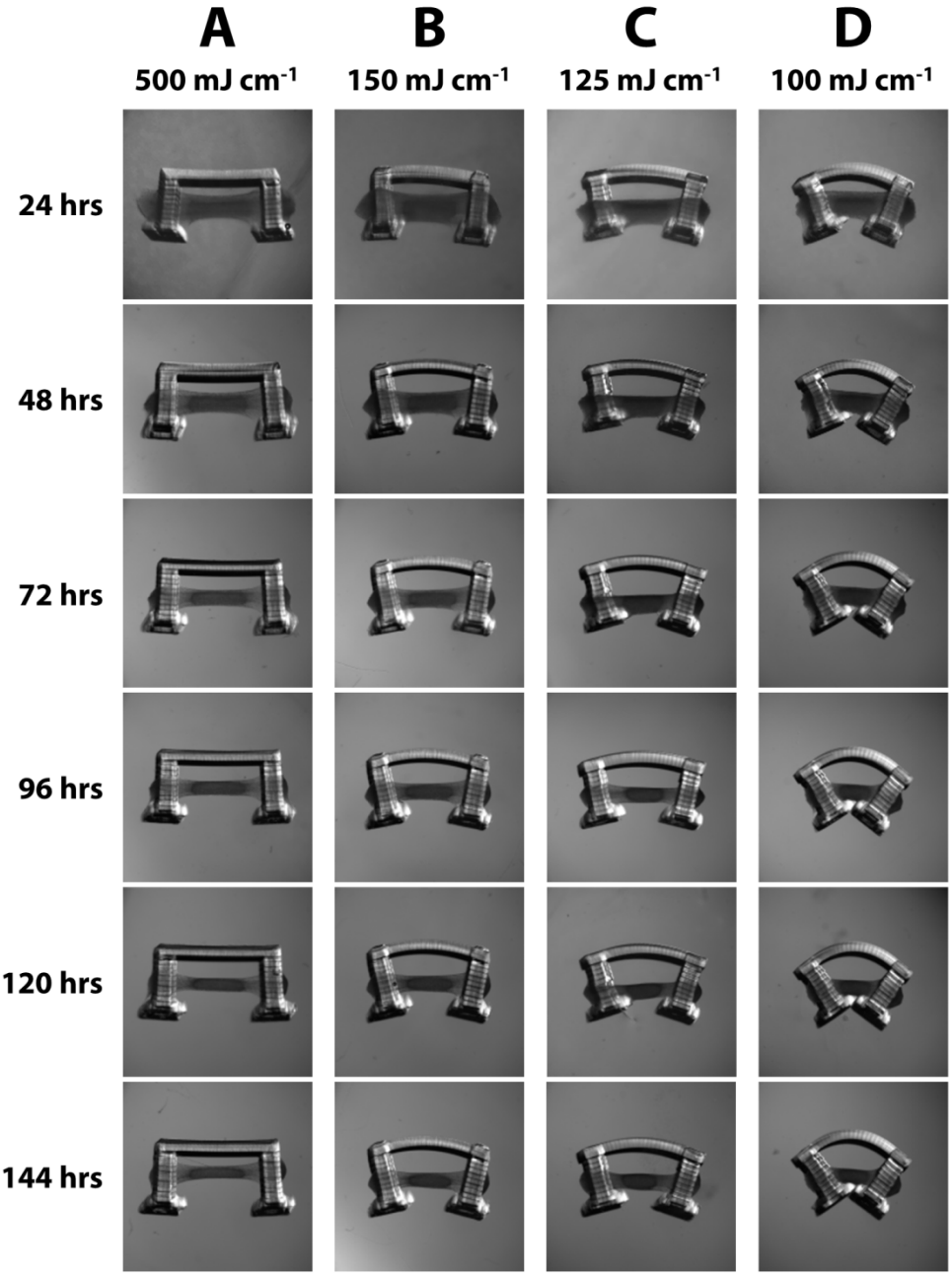

Fig. 7.5 | Optimization of beam stiffness with passive tension parameters. The beam stiffness between the pillars was varied as a function of exposure energy for (**A**) 500, (**B**) 150, (**C**) 125, and (**D**) 100 mJ cm^{-1}. The passive tensions generated by the muscle strips were applied to the beam, causing it to flex. The degree of flexure was dependent on the stiffness of the beam.

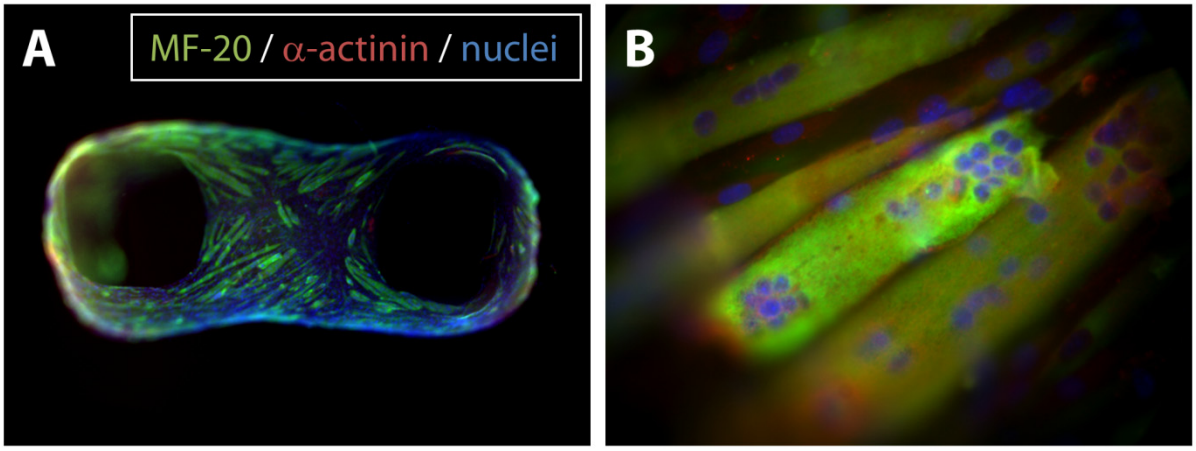

Fig. 7.6 | Differentiation of myotubes in 3D muscle strips. After 7 days in growth medium (10% fetal bovine serum) and another 7 days in differentiation medium (10% horse serum), the 3D muscle strips were stained and visualized with epifluorescence. (**A**) A view of the entire muscle strip shows dense clusters of differentiated myotubes (*green*). (**B**) However, a closer look at the organization of sarcomeres in individual myotubes did not display the characteristic striations found in contractile muscle fibers (*red*).

CHAPTER 8: BLOOD VESSEL PATTERNING

8.1 INTRODUCTION

Neovessels play a critical role in homeostasis, regeneration, and pathogenesis of tissues and organs, and their spatial organization is a major factor in influencing vascular function.[1,2] Therefore, successful treatments of wounds, ischemic tissue, and tissue defects greatly rely on the ability to control the number, size, spacing, and maturity of blood vessels regenerated within a target tissue.[3,4] However, technologies to control the spatial organization of mature neovessels in vivo over physiologically relevant length scales are still lacking. Here, we present a study of a "living" microvascular stamp that releases multiple angiogenic factors and subsequently creates neovessels with the same pattern as that engraved in the stamp. The stamp consists of live cells that secrete angiogenic factors, an engineered hydrogel matrix that promotes cellular expression of angiogenic factors, and a three-dimensional (3D) geometry that localizes the angiogenic factors within the pattern. When the stamp was implanted on a target tissue, it created the desired pattern of neovessels based on 3D geometry of the stamp, allowing the control of the density and spacing of blood vessels (Fig. 8.1). Analytical modeling and numerical simulations validated the experimental observations that the desired blood vessel patterns were formed under specific physical 3D designs of the stamp. The microvascular stamp developed in this study would serve to direct the emergent cellular behavior towards vascularization, improve the quality of revascularization therapies, and allow the vascularization of biological machines in vitro.

Prior studies have demonstrated that spatiotemporal distributions of multiple angiogenic growth factors can control growth direction and macro-scale spacing of neovessels. For example, polymeric scaffolds were developed by chemically attaching a growth factor-releasing layer with a growth factor-free layer, while varying layer thickness at millimeter scales.[4,5] In addition, certain membranes prepared with polytetrafluoroethylene have been clinically used to guide the growth of capillaries into tissue defects.[6] These results have advanced the state of the art, but many challenges remain unaddressed for precise patterning of functional blood vessels at the physiologically relevant sub-micrometer scale. Recently, various micropatterning, ink-jet printing, and microfluidic techniques have been reported to pattern molecules or cells on surfaces and in microfluidic environments.[7–9] These techniques have created patterned cell adhesion substrates, microfluidic devices or microfiber patches with chemotactic protein concentration

gradients,[10] and cell-laden microporous tissue engineering scaffolds. However, these microfabricated devices still have to advance to regulate the desired spatial organization of mature and functional neovessels.

In response to the above challenges, we hypothesized that a construct assembled to sustainably release multiple angiogenic factors along a pre-defined micrometer-sized pattern would generate mature and functional neovessels with a desired pattern at an implant site. Therefore, the construct would allow us to control the area density and spacing of neovessels generated at the implant site. We examined this hypothesis by encapsulating cells that endogenously express multiple angiogenic growth factors into a rigid but permeable hydrogel of poly(ethylene glycol) (PEGDA) and methacrylic alginate (MA). Vertical microchannels with tuned diameter and spacing were incorporated into the cell-encapsulating hydrogel using a stereolithographic assembly (SLA) unit, in order to attain the local increase of angiogenic factors within the circularly patterned areas. The resulting living microvascular stamp was implanted onto a chick embryo chorioallantoic membrane (CAM) to confirm its ability to create the patterned neovessels within tissue covered by the stamp.

8.2 Materials and methods

8.2.1 Synthesis of MA and PEGDA

Gel-forming polymers, poly(ethylene glycol) diacrylate (PEGDA) and methacrylic alginate (MA), were synthesized in our previous work.[11] For the synthesis of MA, 2-aminoethyl methacrylate was conjugated to the carboxylate group of alginate via EDC chemistry. The alginate used in this experiment (molecular weight (Mw) ~ 50,000 g/mol) was obtained by irradiating alginate rich in gluronic acid residues, (LF20/40, FMC Technologies, Mw ~ 250,000 g/mol) with a dose of 2 Mrad for 4 hours from a 60Co source. The irradiated alginate was dissolved in the 0.1 M MES ((2-(N-morpholino) ethanesulfonic acid) buffer (pH 6.4, Sigma-Aldrich) at the concentration of 1.0 % (w/v). Then, 1-hydroxybenzotriazole (HOBt, Fluka), 1-ethyl-3-(3-dimethylaminopropyl) carbodiimide (EDC, Thermo Scientific) and 2-aminoethyl methacrylate (AEMA, Sigma Aldrich) were dissolved in the alginate solution and stirred for 18 hours. Both the molar ratio of HOBt to AEMA and the molar ratio of EDC to AEMA were kept constant at 2:1. The mixture was dialyzed extensively against deionized (DI) water for three days, while exchanging the DI water every 12 hours. The dialyzed alginate solution was lyophilized,

and reconstituted to a 3 wt % stock solution. The conjugation of methacrylate groups onto the alginate was confirmed by ^{1}H-NMR (300MHz, QE300, General Electric), as previously reported. In this study, the number of methacrylates linked to a single alginate with molecular weight (Mw) of 50,000 g/mol was kept constant at 60.

In parallel, PEGDA was synthesized via chemical reaction between poly(ethylene glycol) (PEG, Sigma Aldrich) and acryloyl chloride (Sigma Aldrich). First, PEG was dissolved in dichloromethane at the concentration of 10 wt %. Next, acryloyl chloride and triethylamine (Fisher Chemical) were dissolved in the PEG solution and stirred overnight under dry N2 gas. The molar ratio of PEG, acryloyl chloride and triethylamine was 1:4:4. Finally, the insoluble salt (triethylamine-HCl) was filtered, and the product was precipitated by adding ice-cold ether. The crude product was dissolved into DI water and dialyzed for one day to remove unreacted starting materials and the salt, a byproduct. Then, the product was frozen at -20 ºC and lyophilized. The conjugation of acrylate groups onto PEG was confirmed by ^{1}H-NMR (300 MHz, QE300, General Electric).

8.2.2 HYDROGEL PREPARATION

The PEGDA and MA dissolved in Dulbecco's modified Eagle's medium (DMEM, Sigma Aldrich) were mixed at varied mass ratios, while keeping the total polymer concentrations constant. The pre-gel solution was subsequently placed into the dish at the center of the platform in SLA.[12] The SLA process was repeated until completion of the 3D assembly of the hydrogel. For cell encapsulation, the mixture of NIH/3T3 cells (ATCC) (5.0×10^{6} cells/mL) and pre-gel solution was exposed to the laser of SLA to activate hydrogel formation.

8.2.3 HYDROGEL CHARACTERIZATION

The hydrogel stiffness was evaluated with measurement of the elastic modulus of a hydrogel using a mechanical testing system (MTS Insight). The hydrogel swelling ratio at equilibrium was determined by measuring the weight of the hydrated gel after 24 hours in neutral buffered solution at 37 °C and that of the dried gel. The hydrogel permeability was also evaluated by monitoring water uptake into a hydrogel at non-equilibrium state with the magnetic resonance imaging (600 MHz Varian Unity/Inova nuclear magnetic resonance (NMR) spectrometer (14.1 T Magnet).

8.2.4 MAGNETIC RESONANCE IMAGING (MRI)

Spin echo multi-slice (SEMS) pulse sequence for MR imaging of the hydrogel was used to acquire resonance data, which were then converted into water density map using VNMR 6.1C software. For SEMS pulse sequence, the repetition time (TR) of 2.5 s and the echo time (TE) of 5 ms were used. The field of view (FOV) was 1.6 x 1.6 cm, and the image matrix was 128 x 64 pixels. The resulting water density images were processed to present the density spectrum for comparison using MATLAB (Mathworks). For visualization, pseudo-color was added to the images using the ImageJ software (free image analysis software from National Institutes of Health). For counting water intensity peaks, the rectangular gel picture from the image was selected, and the histogram of the image (count vs. color intensity) was taken using the ImageJ software.

$$\frac{W_t}{W_\infty} = \frac{4}{\sqrt{\pi}} \times \left(\frac{D \times t}{L^2} \right)^{1/2} \tag{8.1}$$

8.2.5 NUMERICAL ANALYSIS

An axisymmetric finite element model was created using Abaqus/CAE version 6.8 - 4. It was assumed that the diffusional flow effects of each microchannel had a negligible impact on the neighboring microchannels and therefore the modeling focused on an individual microchannel of varying diameter. Only the radius of the hole and the corresponding area of the tissue would be changed from one model to the next. The size of hydrogel stamp used in the model was held constant at 250 μm in width and 200 μm in height to correspond with the experimental stamp height and spacing between channels. A mesh was created with microchannel with diameters of 300, 500, 750, and 1,000 μm using 3 node axisymmetric triangles. The top surface of the model was assumed to have no diffusional flow or loss through the top of the gel and microchannel as was dictated by the experimental setup. The outer vertical surface was also assumed to have no diffusional flow in the horizontal direction outside of the control volume. The CAM membrane was modeled as being 400 μm thick with a constant concentration of zero at the lower boundary of the model. This constant concentration acted as a sink, thereby consuming the VEGF once it reached the bottom surface of the model. The diffusion calculations were governed by Fick's law of diffusion with diffusion coefficients of 200 $\mu m^2/s$, 1.0 $\mu m^2/s$, and 0.1 $\mu m^2/s$ for the media, CAM, and hydrogel stamp, respectively

(Equation 8.1). The diffusion across the boundaries between different materials was assumed to be unobstructed. The diffusion coefficient for each of the boundaries was subsequently set as the average of the two materials involved. The stamp had a constant body flux of 3.1×10^{-14} pg/μm^3·s which represented the constant production of VEGF by the fibroblasts. All simulations were in micrometers, seconds, and picograms. Each of the diameters was modeled to simulate a period of 7 days.

8.2.6 CELL ENCAPSULATION

NIH/3T3 cells (ATCC) were expanded and passaged at 37 °C with 5 % CO_2 in Dulbecco's modified Eagle's medium (DMEM, ATCC) supplemented by 10 % fetal bovine serum (FBS, ATCC), and 1 % penicillin/streptomycin (ATCC). All the cells before the passage number of 10 were used in this study. Prior to encapsulation in hydrogels, cells were mixed with the pre-gel polymer solution. The cell density was kept constant at 2.0×10^6 cells/ml. The mixture of cell and pre-gel solution was exposed to the laser of SLA to activate hydrogel formation. The cell-hydrogels were incubated in DMEM supplemented by 10 % fetal bovine serum (FBS), while changing the media every two days. On days 0, 1, 3, 5, and 7, viability of cells encapsulated into the hydrogel was quantitatively evaluated using a MTT ((3-(4,5-dimethylthiazol-2-yl)-2,5-diphenyltetrazolium bromide) reagent (ATCC)) assay kit. The encapsulated cells were stimulated to secrete growth factors by adding 0.2 mL of DMEM and 100 ng/ml of 12-O-tetradecanoylphorbol-13-acetate (TPA, ATCC) reagent into a well of a 96-well plate which contains each cell-encapsulating gel. After incubating the cell-hydrogel construct for 24 hours, 100 μl of cell culture media was mixed with a cocktail of biotinylated detection antibodies, and incubated overnight with the proteome profiler mouse angiogenesis array (R&D Systems). The array membrane was washed to remove unbound material and streptavidin-Fluor® (430) conjugates (Invitrogen) and positively stained spots were imaged using a Phosphor Imager (Bio-Rad). In addition, on days 1, 3, and 5, the amount of VEGF secreted by cells was quantitatively evaluated by the sandwich enzyme immunoassay technique using the mouse VEGF Immunoassay kit (R&D Systems). The sample containing VEGF was pipetted into a well where a polyclonal antibody specific for mouse VEGF has been pre-coated and incubated for 2 hours. After washing away any unbound substances, an enzyme-linked polyclonal antibody specific for mouse VEGF was added to the well. The enzyme reaction yielded a blue-colored product, and

the color intensity was measured using a microplate absorbance reader (Synergy HT, Biotek). The measured value was converted to the amount of VEGF using a calibration curve. The amount of VEGF was further normalized by the number density of cells initially encapsulated into each hydrogel.

8.2.7 Chorioallontoic membrane (CAM)-based angiogenesis assay

The function of microvascular stamp to engineering neovessels pattern was examined by implanting the cell-hydrogel construct onto chicken chorioallontoic membrane (CAM) according to a previously developed method.[13] Fertilized chicken eggs (Hy-Line W-36) were obtained from the University of Illinois Poultry Farm (Urbana, IL). Following the initial incubation, a small window (1.0 × 1.0 cm) was created on top of each egg shell. Then, a freshly fabricated fibroblasts-encapsulating hydrogel disk (5×10^6 cells/ml) was implanted on top of the CAM of individual embryos. At days 0, 2, 4 and 7 after implantation, CAM images were captured using a S6E stereomicroscope (Leica) linked with D-Lux E Camera (Leica). In parallel, the fixed membrane was also embedded in paraffin and the cross-section was stained for α-smooth muscle actin (α-SMA Immunohistology Kit, Sigma-Aldrich) to count the number of mature blood vessels.

8.2.8 Statistical analysis

Error bars represent standard deviation, with n = 4 for all experiments. Statistical significance was determined using one-way ANOVA followed by Tukey's Multiple Comparison Test ($p < 0.05$).

8.3 Results

8.3.1 Tuning cellular viability and angiogenic factor expression

First, the elastic modulus and swelling ratio of the PEGDA hydrogel were tuned to prepare a rigid and permeable hydrogel, so that the cell-encapsulated hydrogel would not only remain structurally stable at the implanted site but also support cellular activities. Increasing the total polymer concentration of the PEGDA hydrogel showed an increase in elastic modulus and a decrease in swelling ratio, which is the typical inverse relationship between stiffness and bulk permeability of conventional hydrogel systems. In contrast, the hydrogel consisting of PEGDA

and MA, which has multivalent methacrylic groups and hydrophilic hydroxyl groups,[11] showed an increase in both elastic modulus and swelling ratio with increasing mass fraction of MA (Fig. 8.2A). The role of MA in increasing the swelling ratio of the hydrogel was further examined by monitoring water uptake into a hydrogel at non-equilibrium state using magnetic resonance imaging (MRI). Despite the higher stiffness of the PEGDA-MA hydrogel compared to the PEGDA hydrogel, water diffused into the PEGDA-MA hydrogel more rapidly (Fig. 8.2B).

Subsequently, cells were encapsulated into the PEGDA and PEGDA-MA hydrogels via in situ photo cross-linking reaction with SLA unit.[12] Fibroblasts encapsulated into the PEGDA-MA hydrogel exhibited higher viability than those encapsulated into the PEGDA hydrogel, as confirmed with the larger intracellular cleavage of yellow tetrazolium salt (MTT) into a purple formazan product (Fig. 8.3A). Human mesenchymal stem cells (hMSCs) also exhibited similar viability in PEGDA-MA to those of the fibroblasts (Fig. 8.3B). While hMSCs naturally secrete angiogenic growth factors, fibroblasts were stimulated to express multiple angiogenic factors by exposing them to a 12-O-tetradecanoylphorbol-13-acetate, protein kinase C (PKC) activator.[14] Nevertheless, hMSCs naturally secreted higher amounts of VEGF per day than the fibroblasts (Fig. 8.4A). The cellular expression levels of VEGF for both cell types in the PEGDA-MA hydrogel were higher and more sustained than those encapsulated in the pure PEGDA hydrogel. The multitude of angiogenic growth factors expressed by these cells was demonstrated by performing an angiogenesis assay of over 55 known growth factors (Fig. 8.4B).

8.3.2 STEREOLITHOGRAPHIC ASSEMBLY OF 'LIVING' MICROVASCULAR STAMP

Next, we introduced cylindrical microchannels (pores) into the PEGDA-MA hydrogels to localize cell-secreted angiogenic factors within the circular patterns (Fig. 8.5A and 8.5B). To determine the appropriate microchannel geometry, we estimated the dependency of the amount of angiogenic factors released through the channels on the microchannel diameter as follows. Assuming that the molar flux of angiogenic factors into the microchannel is J (depicted by the horizontal arrows in the side view of Fig. 8.5C), and that there is no consumption of angiogenic factors in the channel, the average molar flux to be delivered to the tissue through the bottom of the channel, $J_{channel}$, would be:

$$J_{channel} = \frac{\pi d H}{\pi d^2 / 4} \times J \tag{8.2}$$

where d is the diameter of the channel, and H is the height of the stamp. Therefore, the flux of angiogenic factors enhanced with the microchannels is:

$$\frac{J_{channel}}{J} = \frac{4H}{d} \tag{8.3}$$

Hence, for a stamp with a thickness of 200 μm, this simple scaling law predicts that the enhancement of flux increases as the diameter of the microchannels decreases. A microchannel of 800 μm diameter would be enhancement-neutral, i.e., would neither increase nor decrease the average amount of angiogenic factors delivered to the tissue through the channels. This critical microchannel diameter increases with thickness of the stamp (Fig. 8.5D).

8.3.3 Numerical analysis

To validate the scaling law, a finite element model was created to simulate the molar flux of cell-secreted growth factors from the hydrogel with microchannels. The boundary conditions of the model are the constant production of VEGF molecules per unit volume in the hydrogel, with no diffusional flow or loss through the top of the gel. The diffusional flows in the hydrogel, microchannels, and within the tissue were presumed to be governed by the diffusion coefficients following Fick's law of diffusion. The diffusion across the hydrogel-channel, channel-tissue, and hydrogel-tissue interfaces were estimated by taking the average values of the diffusion coefficients of the two neighboring materials.

AutoCAD blueprints were shown for three different microchannel diameters (Fig. 8.6A). The simulation results clearly show that the concentration of VEGF below the smaller-diameter microchannel is much greater than that below the larger-diameter microchannel (Fig. 8.6B and 8.6C). The concentration of VEGF directly below the stamp is lower than that below the channel, regardless of the difference of the microchannel diameter. This is due to the very slow diffusional rate in the hydrogel stamp compared to that in the media inside the microchannels. The media acts as a route for the VEGF to move along the entire inner surface of the channel, with a much higher diffusion rate at the surface of the tissue. In addition, there is an increased mass flow rate at the circumference of the microchannels (Fig. 8.6D).

8.3.4 Patterning of functional neovessels using the 'living' microvascular stamp

Finally, the hydrogel-based vascular stamps with controlled microchannels were implanted onto chick chorioallantoic membrane (CAM) (Fig. 8.7A). Prior to their implantation,

all hydrogels with fibroblasts were incubated in media supplemented with the PKC activator for 24 hours, in order to stimulate cellular expression of angiogenic factors. Implantation of the PEGDA hydrogel with cells onto the CAM stimulated inflammation within two days, most likely because of the low cell viability and extravasation of the debris from the dead cells. In contrast, the PEGDA-MA hydrogel minimally stimulated host inflammation, most likely because of its ability to increase the viability of encapsulated cells. Implantation of the PEGDA-MA hydrogel containing microchannels of diameter smaller than 800 μm stimulated the growth of neovessels with blood flow along its circular pattern (Fig. 8.7B). The spacing between the circular neovessels was 500 or 1000 μm which was the same as the spacing of the microchannels introduced into the hydrogel. The cells encapsulated in the stamps remained viable at the implant sites. In addition, the circularly patterned neovessels were interconnected to each other, which suggested that sprouting of new capillaries from the neovessels stimulated formation of neighboring patterned neovessels. The reproducibility of patterning neovessels was maintained with all of the samples (100%). None of the neovessels replicated the circular pattern of microchannels when the diameter of the microchannels was increased to 1,000 μm. Furthermore, other blood vessel patterning geometries, such as circles, lines, and text ('uiuc'), were demonstrated using the microvascular stamp (Fig. 8.7C). Compared to the microchannel-free control conditions and the hydrogel containing microchannels with diameter of 1000 μm, the vascular stamp containing microchannels with diameter of 500 μm resulted in a significant increase in the number and size of mature neovessels at the implantation site. Furthermore, images of neovessels formed near 300 μm microchannels were straight and directed (Fig. 8.8A), while those formed near 1000 μm microchannels were winding and tortuous (Fig. 8.8B). The vascular stamp resulted in the 2.5-fold increase of the thickness of CAM, as compared with CAM implanted with other controls. The size analysis of the blood vessels exhibited that the microchannels with diameter of 500 μm significantly stimulated formation of arterioles with vessel area of over 1000 μm^2 (*i.e.*, 40% of total blood vessels in CAM).

8.4 DISCUSSION

Overall, our results demonstrate that the microvascular stamp created mature and functional neovessels with desired patterns in live tissue. Ultimately, the microvascular stamp could increase the vascular size and density at an implant site. To our knowledge, such refined

patterning of blood vessels through which blood flows has not been reported to date. One interesting feature of the vascular stamp is the capability to enable cells to retain their viability and growth factor production in a PEGDA-MA hydrogel system. We propose that MA in the PEGDA-MA hydrogel is a key factor because hydrophilic MA enhances the transport of oxygen and nutrients into the hydrogel.[15,16] Therefore, the resulting PEGDA-MA hydrogel would greatly overcome the challenges encountered with current hydrogel design, which is often plagued by the inverse dependency between stiffness and permeability. This enhanced transport property can be further modulated by controlling size distribution of nanometer-sized pores in hydrogels with the molecular weights of PEGDA or MA.[17]

Another highlight of the vascular stamp was its ability to localize angiogenic factors in a pre-defined pattern using microchannels incorporated into the gel. According to the diffusion-based scaling law and the numerical analysis, the molar flow rate of angiogenic factors into the tissue beneath the circumference of the microchannel wall was increased with the use of the appropriate microchannel dimension. We propose that the local increase of the mass flow rate of angiogenic factors at the edge of the microchannel wall may be a key factor to determine whether blood vessels are able to grow in the circular pattern. As a newly formed blood vessel actively consumes angiogenic factors, regions that have a high mass flow rate and faster replenishment of angiogenic factors would stimulate the continued growth of a mature blood vessel.[18,19]

In addition, when only VEGF was incorporated in the hydrogel, no patterning of the neovessels occurred, which suggests the importance of the constant production of multiple growth factors in generating mature and functional blood vessels in the desired patterns. It is also possible that VEGF may be denatured during the in situ cross-linking reaction activated by the high intensity laser. Therefore, live cells may provide an improved method for patterning the neovessels, because of their intrinsic properties of synthesizing and secreting multiple angiogenic factors in a sustained manner. We also hypothesize that the sustained delivery of angiogenic factors increases the vascular size as well as vascular density, although this aspect needs to be confirmed in future studies.[20,21]

8.5 CONCLUSION

In the end, controlling the "bottom-up" emerging behavior of the neovessel formation via "directed top-down" cues using the "living" microvascular stamp can be a major step forward to better understanding and engineering the development of neovessels and further improving treatment of various injuries, traumas, and diseases. For example, neovessels patterned by a microvascular stamp will be discernible from other pre-existing neovessels, so the roles of normal or pathologic extracellular microenvironment in development, homeostasis, and remodeling of neovessels can be better understood. The microvascular stamp can also be implanted in ischemic tissues to engineer mature neovessels with regular spacing and subsequently improve recovery of tissue and organ functions. Finally, the design principles established to assemble the microvascular stamp will be useful in designing a broad array of bioimplants and tissue engineering scaffolds to create "on demand" microvascular networks in an organized fashion.

8.6 ACKNOWLEDGMENTS

This work was supported by US Army Telemedicine & Advanced Technology Research Center (TATRC) (W81XWH-08-1-0701) (R.B. and H.J.K.), National Science Foundation (CAREER: DMR-0847253) (H.J.K.), American Heart Association (Scientist Development Grant 0830468Z) (H.J.K.),National Science Foundation (Science and Technology Center Emergent Behaviors of Integrated Cellular Systems Grant CBET-0939511) (C.D., K.J.H., V.C., C.D., K.J.H., R.B.,, and H.J.K), National Science Foundation IGERT (DGE-0965918) (C.D., K.J.H., R.B., and H.J.K), and NSF CMMI-0952565 (K.J.H.)., National Science Foundation IGERT (DGE-0965918) (C.D., K.J.H., R.B., and H.J.K), and NSF CMMI-0952565 (K.J.H.).

8.7 REFERENCES

1. Belting, M., *et al*. Regulation of angiogenesis by tissue factor cytoplasmic domain signaling. *Nat. Med*. 10, 502-509 (2004).

2. Carmeliet, P., & Jain, R. K. Angiogenesis in cancer and other diseases. *Nature* 407, 249-257 (2000).

3. Dor, Y., Djonov, V. & Keshet, E. Making vascular networks in the adult: branching morphogenesis without a roadmap. *Trends Cell Biol.* 13, 131-136 (2003).

4. Chen, R. R., Silva, E. A., Yuen, W. W. & Mooney, D. J. Spatio-temporal VEGF and PDGF delivery patterns blood vessel formation and maturation. *Pharm. Res.* 24, 258-264 (2007).

5. Silva, E. A., & Mooney, D. J. Effects of VEGF temporal and spatial presentation on angiogenesis. *Biomaterials* 31, 1235-1241 (2010).

6. Kim, S. M., Moo, S. B., & Hwang, S. J. *Tissue Eng. Regen. Med.* 5, 959 (2008).

7. Khademhosseini, A., Langer, R., Borenstein, J. P., & Vacanti, J. P. Microscale technologies for tissue engineering and biology. *Proc. Natl. Acad. Sci. U S A* 103, 2480-2487 (2005).

8. Gbureck, U., Holzel, T., Doillon, C. J., Muller, F. A., & Barralet, J. E. Direct printing of bioceramic implants with spatially localized angiogenic factors. *Adv. Mater.* 19, 795-800 (2007).

9. Barkefors, I., Thorslund, S., Nikolajeff, F., & Kreuger, J. A fluidic device to study directionial angiogenesis in complex tissue and organ culture models. *Lab Chip* 9, 529-535 (2008).

10. DeVolder, R., Bae, H., Lee, J., & Kong, H. Directed blood vessel growth using an angiogenic microfiber/microparticle composite patch. *Adv. Mater.* 23, 3139-3143 (2011).

11. Cha, C., Kim, S. Y., & Kong, H. Decoupled control of stiffness and permeability with a cell-encapsulating poly(ethylene glycol) dimethacrylate hydrogel. *Biomaterials* 31, 4864-4871 (2010).

12. Chan, V., Zorlutuna, P., Jeong, J. H., Kong, H., & Bashir, R. Three-dimensional photopatterning of hydrogels using stereolithography for long-term cell encapsulation. *Lab Chip* 10, 2062-2070 (2010).

13. Staton, C. A., Lewis, C., & Bicknell, R. in *Angiogenesis Assays: A critical appraisal of current techniques*, Wily, New York, Ch. 11 (2007).

14. Grugel, S., Finkenzeller, G., Weindel, K., Barleon, B., & Marme, D. Both v-Ha-Ras and v-Raf stimulate expression of the vascular endothelial growth factor in NIH 3T3 cells. *J. Biol. Chem.* 270, 25915-25919 (1995).

15. Discher, D. E., Mooney D. J., & Zandstra, P. W. Growth factors, matrices, and forces combine and control stem cells. *Science* 324, 1673-1677 (2009).

16. Albrecht, D. R., Underhill, G. H., Wassermann, T. B., Sah, R. L., & Bhatia, S. N. Probing the role of multicellular organization in three-dimensional microenvironments. *Nat. Methods* 3, 369-375 (2006).

17. Wang, J., Gonzalez, A. D., & Ugaz, V. M. Tailoring bulk transport in hydrogels through control of polydispersity in the nanoscale pore size distribution. *Adv. Mater.* 20, 4482-4489 (2008).

18. Adams, R. H., & Alitalo, K. Molecular regulation of angiogenesis and lymphangiogenesis. *Nat. Rev. Mol. Cell Biol.* 8, 464-478 (2007).

19. Conway, E. M., Collen, D., & Carmeliet, P. Molecular mechanisms of blood vessel growth. *Cardiovasc. Res.* 49, 507-521 (2001).

20. Burdick, J. A., Mason, M. N., Hinman, A. D., Thorne, K., & Anseth, K. S. Delivery of osteoinductive growth factors from degradable PEG hydrogels influences osteoblast differentiation and mineralization. *J. Control Release* 83, 53-63 (2002).

21. Lutolf, M. P., & Hubbell, J. A. Synthetic biomaterials as instructive extracellular microenvironments for morphogenesis in tissue engineering. *Nat. Biotechnol.* 23, 47-55 (2005).

8.8 FIGURES AND CAPTIONS

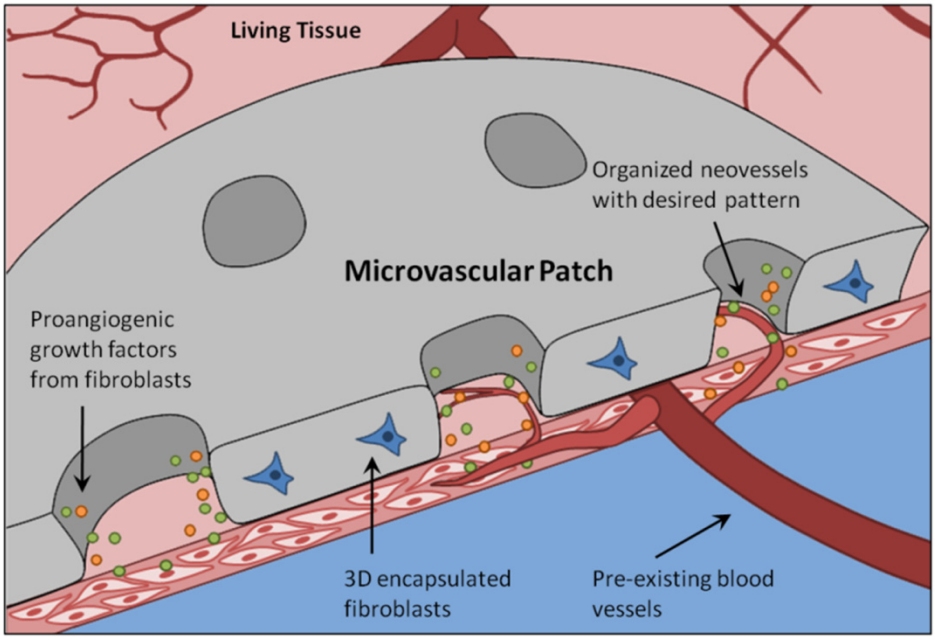

Fig. 8.1 | Schematic of the microvascular stamp. The overall concept of the microvascular stamp is that it releases multiple angiogenic growth factors that are geometrically localized to grow and guide new blood vessels within the same pattern as the stamp. The stamp consists of live cells that secrete angiogenic factors, an engineered hydrogel matrix that promotes cellular expression of angiogenic factors, and a three-dimensional (3D) geometry that localizes the angiogenic factors within the pattern. The stamp is then implanted on a target tissue to create the desired blood vessel pattern, allowing precise control over the density and spacing of the blood vessels.

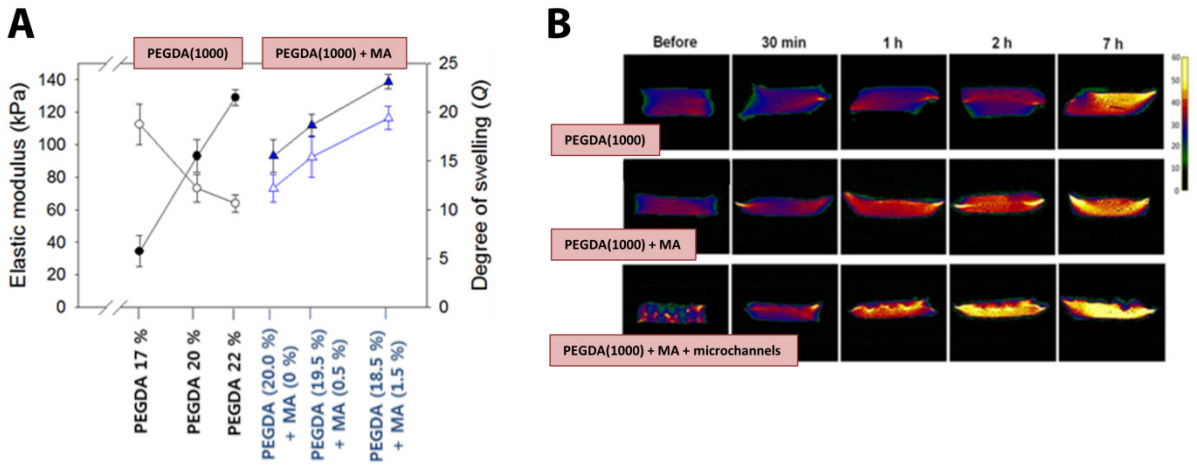

Fig. 8.2 | Characterization of PEGDA and PEGDA-MA hydrogels. The addition of methacrylic alginate (MA) to the PEG-based backbone decoupled elastic modulus from swelling ratio. (**A**) PEGDA hydrogels had a hallmark inverse dependency: as the elastic modulus increased with PEG composition, the swelling ratio decreased. PEGDA-MA hydrogels, however, had a direct dependency: as the elastic modulus increased with MA composition, the swelling ratio also increased. (**B**) Diffusion of water protons into PEGDA and PEGDA-MA hydrogels were visualized with MRI. The pseudo-color represents relative peak intensity of the water protons. The incorporation of both MA and microchannels resulted in higher oxygen diffusion, while maintaining rigidity.

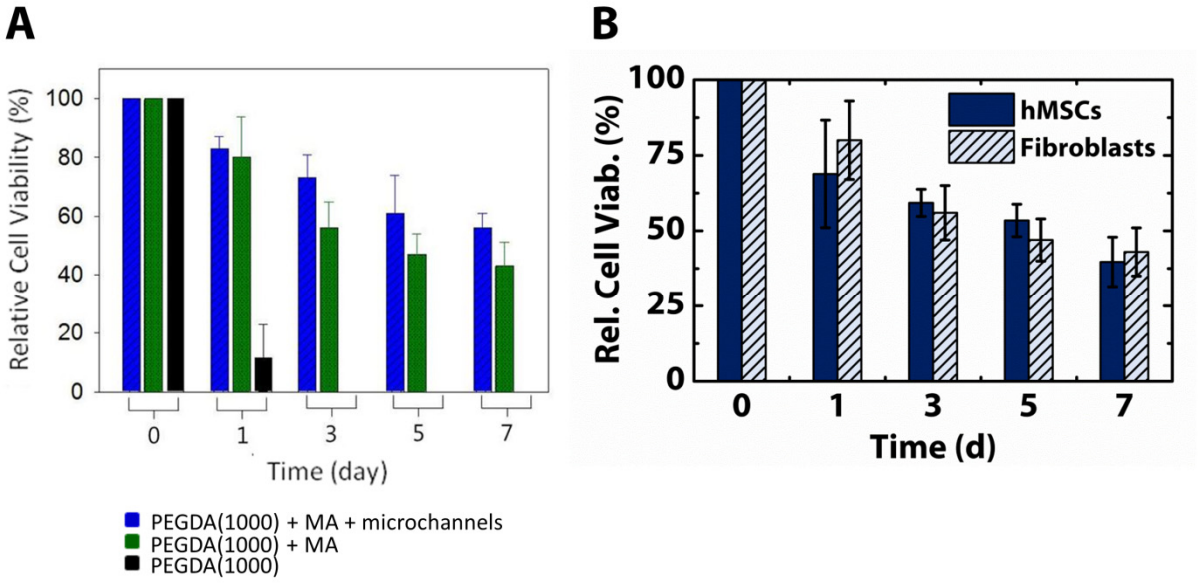

Fig. 8.3 | Viability of cells in PEGDA and PEGDA-MA hydrogels. The relative cell viability was quantified by normalizing the absorbance values of samples treated with MTT reagent to that measured on day 0. (**A**) Viability was evaluated with NIH/3T3 fibroblasts encapsulated in PEGDA (*black*), PEGDA-MA (*green*), and PEGDA-MA + microchannels (*blue*) hydrogels. (**B**) Viability was evaluated with human mesenchymal stem cells (hMSCs) encapsulated in PEGDA-MA + microchannels hydrogels and compared to the results with NIH/3T3 fibroblasts. For both cell types, the addition of MA and microchannels significantly increases the viability over 7 days (*$p<0.05$).

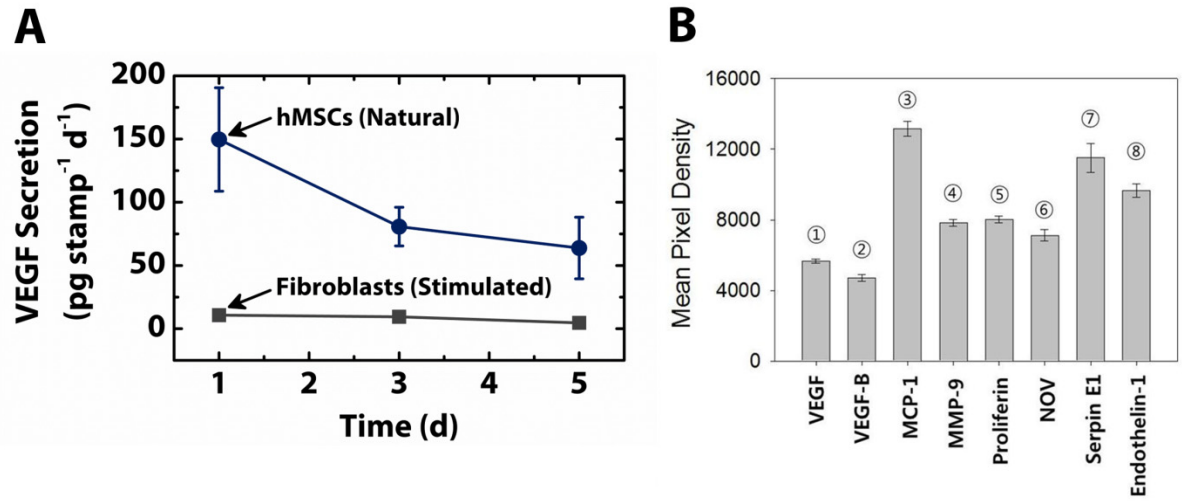

Fig. 8.4 | Secretion of angiogenic growth factors by encapsulated cells. (**A**) The amount of VEGF secreted by hMSCs and NIH/3T3 fibroblasts encapsulated in PEGDA-MA hydrogels were evaluated using a VEGF ELISA kit over 5 days (*$p<0.05$). Fibroblasts were stimulated with 12-O-tetradecanoylphorbol-13-acetate (TPA), a protein kinase C activator, to secrete growth factors. Despite chemical stimulation of fibroblasts, hMSCs naturally secreted higher amounts of VEGF per day. (**B**) An angiogenesis assay kit was used to evaluate the presence of over 55 different angiogenic growth factors to demonstrate the multitude of angiogenic growth factors secreted by the cell-based microvascular stamp.

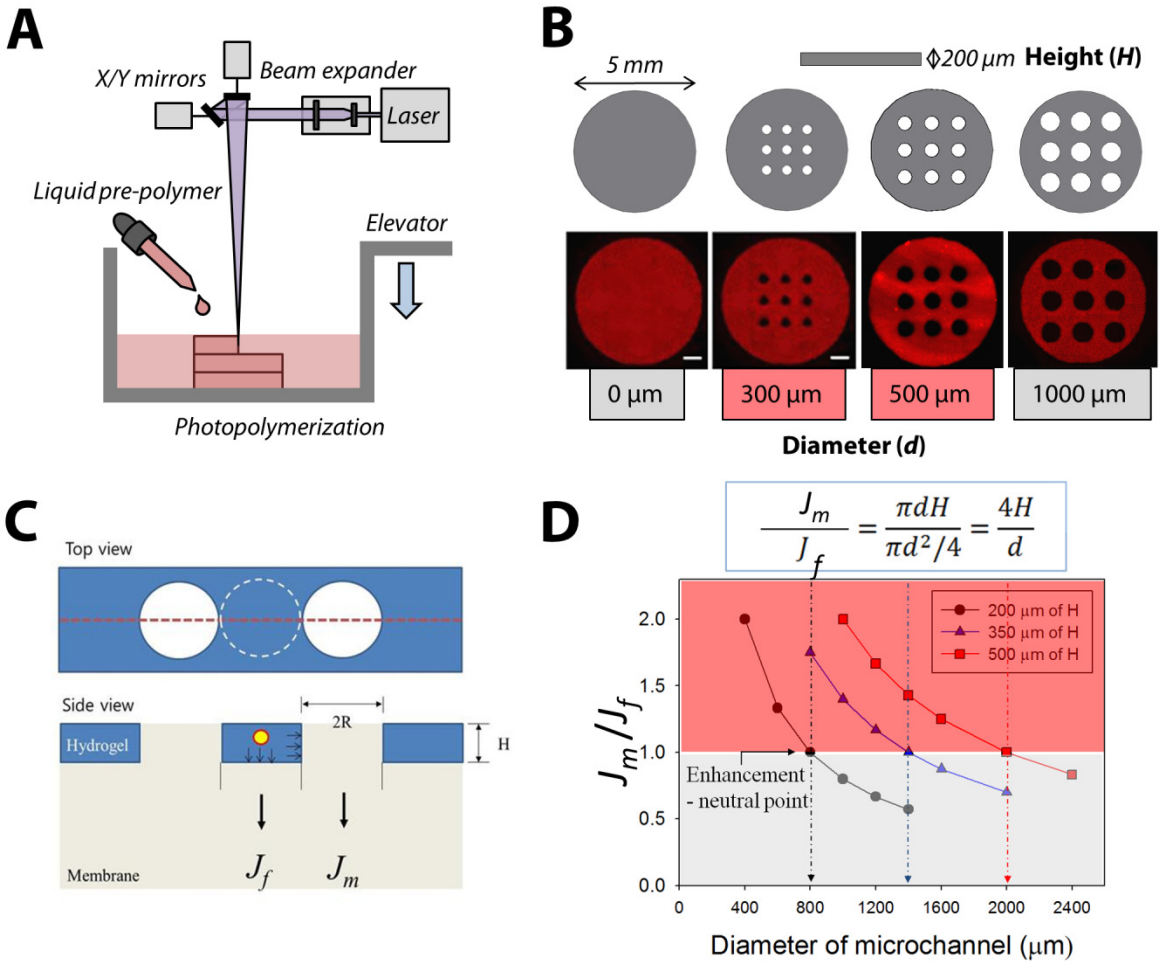

Fig. 8.5 | Fabrication of microvascular stamp with stereolithography. (**A**) Schematic of the stereolithography set up for fabrication of the microvascular stamp. (**B**) Schematic top-view of microvascular stamp assembled with various diameters of microchannels. (**C and D**) The scaling law suggests that the average molar flux (J) delivered to the tissue through the bottom of the channel, *Jchannel*, is enhanced, as the microchannel diameter becomes smaller than 800 μm for a hydrogel with thickness of 200 μm.

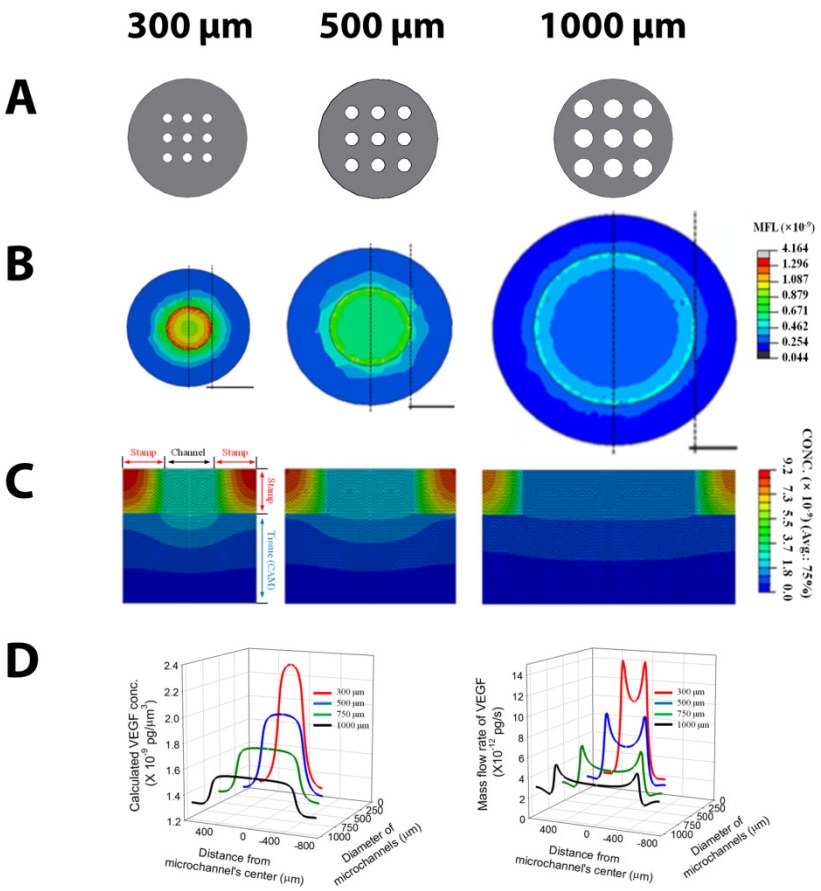

Fig. 8.6 | Numerical analysis of angiogenic growth factor diffusion. (**A**) AutoCAD blueprints for three different microchannel diameters (300 µm, 500 µm, and 1000 µm). (**B**) Numerical analysis of the top view of the mass flow rate of VEGF on a plane 20 µm below the hydrogel stamp-CAM interface. Scale bars represent 300 µm. Plots show the numerical values of VEGF concentration distributions (**C**) Numerical analysis of the cross-sectional contours of VEGF concentration distributions at Day 7. (**D**) VEGF concentration distributions and mass flow rates across the diameter of the channel at 20 µm below the stamp-tissue interface. e) Pictures of the hydrogel stamp with the three different microchannels diameters.

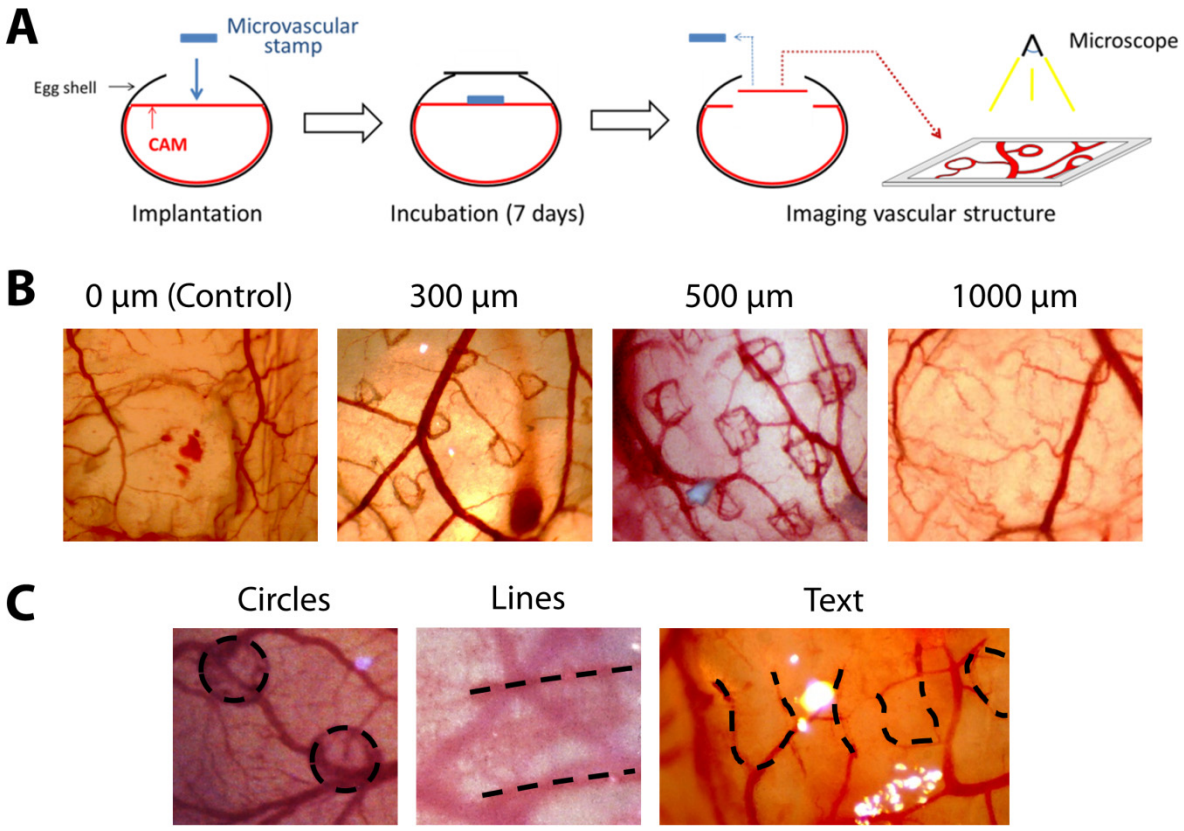

Fig. 8.7 | Formation of patterned blood vessels on chick chorioallantoic membranes. (**A**) Schematic illustrating the blood vessel patterning process: (1) egg shell windowing, (2) microvascular stamp implantation on CAMs, (3) and fixed membrane imaging. (**B**) Bright-field images of new blood vessels formed under PEGDA-MA hydrogels containing microchannels of diameters at 0, 300, 500, and 1,000 μm. (**C**) Bright-field images of new blood vessels formed under PEGDA-MA hydrogels containing circles, lines, and text ('uiuc').

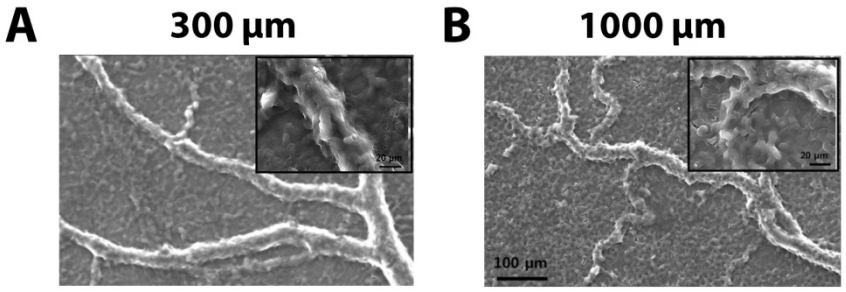

Fig. 8.8 | Images of new blood vessels formed near microchannels. (**A**) SEM image of new blood vessels formed near 300 µm microchannels are straight and directed. (**B**) SEM image of new blood vessels formed near 1000 µm microchannels are winding and tortuous.

CHAPTER 9: CONCLUSION AND FUTURE DIRECTIONS

9.1 CONCLUSION

We demonstrated millimeter-scale "bio-bots" that could walk across surfaces in fluid. The bio-bots were fabricated using a 3D printer and seeded with a sheet of cardiac cells. The contraction (power stroke) and subsequent relaxation of the cell sheet powered the constructs. The bio-bots moved as a result of their simple asymmetric shape, with one long, thin leg resting on a shorter, wider support leg. The bio-bots walked at an average velocity of ~236 $\mu m \cdot s^{-1}$, an average displacement per power stroke of ~354 μm, and an average beating frequency of ~1.5 Hz.

9.2 FUTURE DIRECTIONS

This was an important achievement in our quest to 'forward-engineer' biological machines. We envision that these bio-bots could be integrated with other cell types and clusters that have different functionalities. One compartment in the bio-bot could accommodate for a 'toggle switch' made of neural networks that sense a signal, process that signal, and instruct the sheet of cardiac cells to contract (Fig. 9.1). Another compartment in the bio-bot could accommodate for a cell-based 'factory' with specialized cell clusters that release chemicals into the environment (Fig. 9.2). Below is a short list of targeted goals in our bio-bot roadmap:

- External control of the bio-bots by integrating them with light-driven 'optogenetic' C_2C_{12} skeletal muscle to move/stop, pace, and steer.
- External control of the bio-bots by integrating them with C_2C_{12} skeletal muscle and motor neurons through neuromuscular junctions by innervation.
- Autonomous control of the bio-bots by constructing synthetic gene networks in the neurons to enable a wide range of new programmed cell applications.

The long term goal is to develop millimeter-scale biological machines constructed with intelligent polymers (*i.e.* hydrogels) and living cells that can achieve net motion towards a chemical toxin and subsequently release chemicals to neutralize the toxins.

9.3 FIGURES AND CAPTIONS

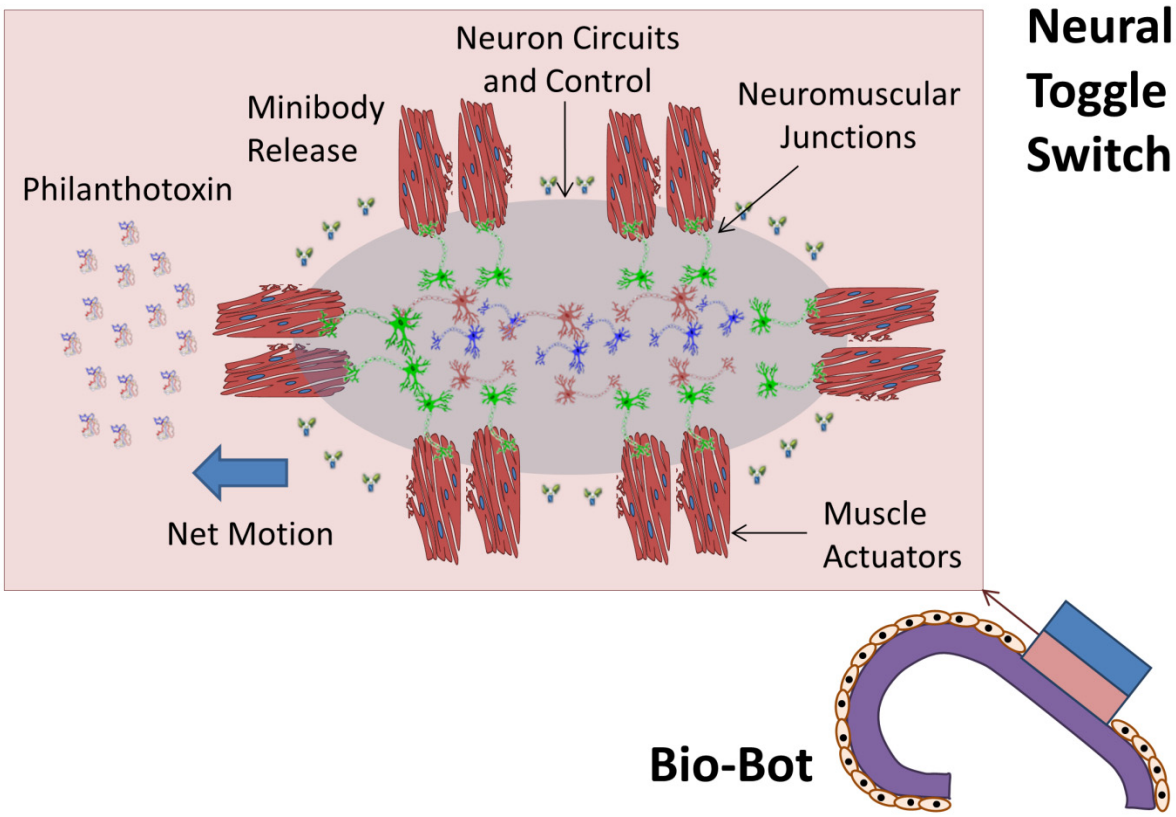

Fig. 9.1 | Schematic of a neural 'toggle switch'. Example of one compartment in the bio-bot that could be used for a 'toggle switch' made of neural networks to sense a signal, process that signal, and instruct the sheet of cardiac cells to contract.

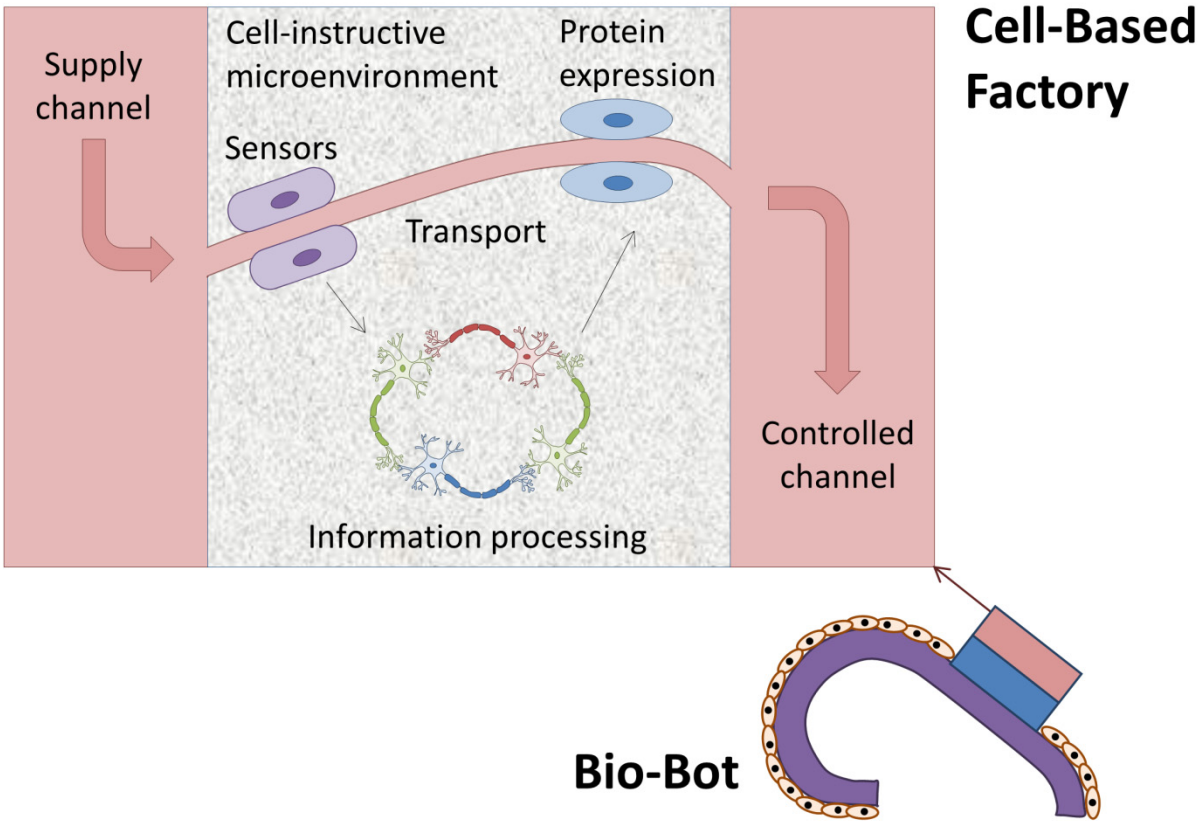

Fig. 9.2 | Schematic of a cell-based 'factory'. Example of another compartment in the bio-bot that could be used for a 'cell-based factory' with specialized cell clusters to release chemicals into the environment.